Reactivity of Reducing Iron Minerals in the Subsurface: Implications for Contaminant Remediation

Part I: Remediation of Technetium by Sulfidated Nano Zerovalent Iron
Part II: Characterization of Reducing Iron Minerals Using Chemical Reactive Probes

By

Dimin Fan

A DISSERTATION

Presented to the Division of Environmental and Biomolecular Systems

the Institute of Environmental Health

and the Oregon Health & Science University

in partial fulfillment of

the requirements for the degree of

Doctor of Philosophy

in

Environmental Science and Engineering

April 2015

INSTITUTE OF ENVIRONMENTAL HEALTH
OREGON HEALTH & SCIENCE UNIVERSITY

CERTIFICATE OF APPROVAL

This is to certify that the Ph.D. dissertation of

Dimin Fan

has been approved

Dr. Paul G. Tratnyek, Thesis Advisor
Professor, Oregon Health & Science University

Dr. Bradley M. Tebo, Thesis Committee Member
Professor, Oregon Health & Science University

Dr. Richard L. Johnson, Thesis Committee Chair
Professor, Oregon Health & Science University

Dr. James E. Szecsody, Thesis Committee Member
Pacific Northwest National Laboratory

Table of Contents

Chapter 2 Reductive Sequestration of Pertechnetate ($^{99}TcO_4^-$) by Nano Zero-Valent Iron (nZVI) Transformed by Abiotic Sulfide...................................52

List of Figures

List of Figures in Appendix

List of Tables in Appendix

ACKNOWLEDGMENTS

The past five and half years just went by in the blink of an eye. The journey was tough but also extremely rewarding. As I am finally close to finish one of the most important milestones in my life and career, I would like to express my sincere gratitude to many people who have helped me along the way. First and foremost, I owe a debt of gratitude to my advisor Dr. Paul Tratnyek for giving me this opportunity to work with him and for his mentorship, patience, and encouragement. I am truly grateful for every opportunity that I have received for being one of his students. I would also like to thank Dr. Brad Tebo, Dr. Rick Johnson, and Dr. Jim Szecsody for their invaluable inputs to my work as my co-advisors and committee members, and Rick, especially for his kindness and time in helping me in the lab on numerous little projects.

Contributions from several people have made my first project possible. Thank Carolyn for organizing the lab space for me to conduct the experiments. Thank Sung-Woo for collecting the preliminary data and personally connecting me with the beamline scientist at SSRL. Without his initiation, the latter part of the project would be so much more difficult than it had been. I am also grateful for all the help I have received from the collaborators at IEH, EMSL and SSRL to conduct the experiments, interpret the data and prepare the manuscripts.

Next, I would like to thank all my labmates in Tratnyek and Johnson lab, who have overlapped with me since my first day here. Special thanks should go to Jim Nurmi, Ali Salter-Blanc, and Miranda Bradley for helping me in the lab, sharing the good and bad, and giving inputs to my work, and Zhenqing Shi, Jing Guo, Shengwen Chen, and Chunhua Xu for giving me numerous genuine and useful advices, and my four summer interns, J.P, Vy, Adrian, and Ginny for their hard work and contributions in the second project.

My time at OHSU would not be so smooth without all the help from staff members, especially Nancy, Nievita from IEH and Alison from the International office. I also want to thank all the IEH students, faculty members for their support and help during the past years.

The final note goes to my family, especially my parents, for their love and support, and Mouzhong Xu, for her company, support, and love during this journey. Without them, I could never be able to go this far by myself.

ABSTRACT

Reactivity of Reducing Iron Minerals in the Subsurface: Implications for Contaminant Remediation

Part I: Remediation of Technetium by Sulfidated Nano Zerovalent Iron
Part II: Characterization of Reducing Iron Minerals Using Chemical Reactive Probes

April 2015

Dimin Fan

Ph.D. Oregon Health & Science University

Directed by: Professor Paul G. Tratnyek

Reducing iron minerals are of broad interest in biogeochemistry and environmental engineering, in part because of their roles in a variety of approaches to remediation of contaminated groundwater. Zerovalent iron (Fe(0)), which is predominantly of anthropogenic origin, and divalent iron minerals (Fe(II)), usually from naturally-occurring biogeochemical processes, together comprise a broad class of the reducing materials that are responsible for most of the contaminant removal by in-situ chemical reduction (ISCR). Regardless of how ISCR is implemented (e.g., injection of ZVI, dithionite, or polysulfide), the physical and chemical properties of the resulting reductants are strongly influenced by

the biogeochemical transformations involving iron and sulfur that are at aqueous mineral interfaces. These processes operate from molecular scale to grain scale, and to pore scale in controlling the contaminant removal and the overall remediation performance. Therefore, from both fundamental and practical point of view, a more comprehensive understanding of the biogeochemical processes that control contaminant fate in ISCR and related scenarios is needed.

The research presented in this dissertation is composed of two parts. **Part I** (**Chapters 2** and **3**) concerns the development of a combined chemical and biological remediation strategy involving the application of nano zerovalent iron (nZVI) to sequester pertechnetate (TcO_4^-), a common radionuclide oxyanion. **Part II** (**Chapters 4** and **5**) concerns the development of a general approach to characterize the thermodynamic, kinetic, and capacity aspects of a broad spectrum of reducing iron minerals in order to better understand their contributions to in-situ chemical reduction.

Part I—Laboratory batch experiments were conducted to investigate the abiotic sulfidation of nZVI and sequestration of Tc by sulfidated nZVI to evaluate the prospect of remediating Tc-contaminated groundwater by adding nZVI to stimulate sulfidic conditions in situ. Complementary solid/surface characterization methods showed that up to 10% of added nZVI was converted to FeS after 24 h exposure to aqueous sulfide (at sulfide to iron ratios above 0.112). The sulfidated nZVI gave faster Tc removal rates than nZVI that was not exposed to sulfide. Evidence by transmission electron microscopy (TEM) showed that the majority of Tc was associated with FeS, and X-ray absorption spectroscopy (XAS) showed there was a complete shift in the Tc sequestration products from TcO_2 to TcS_2 as aqueous sulfide increased from 0 to 1 mM. The stability of the resulting reduced Tc sulfide phases to reoxidation was examined by exposing them to ambient air. Tc sequestered by sulfidated nZVI was reoxidized (to dissolved TcO_4^- in solution) significantly more slowly compared with the reduction products formed by non-sulfidated nZVI. The onset of Tc release occurred after complete consumption of FeS, indicating that oxidation was inhibited partially due to the presence of FeS serving as redox buffer. XAS characterization also revealed a solid state transformation process from TcS_2 to TcO_2 during oxidation, which also contributed to the inhibition of Tc reoxidation.

Part II—A set of chemical reactive probes (CRPs) were used to characterize the thermodynamic and kinetic properties of reducing iron minerals, with the ultimate goal of using them to predict the abiotic natural attenuation of chlorinated ethenes (**Chapter 4**). After equilibration in aqueous media containing various combinations of iron minerals with adsorbed Fe(II), the redox speciation of the thermodynamic CRPs was measured spectrophotometrically, and the results were used to calculate mineral reduction potentials as a function of mineral type, mineral loading, and Fe(II) concentration. The potentials determined by this method (E_{CRP}) were 150–200 mV more negative than the potentials measured by conventional oxidation-reduction potentials with a platinum electrode (E_{Pt}), consistent with the hypothesis that the latter method does not fully represent the mineral reduction potential. E_{CRP} was shown to qualitatively correlate with the rate constants for reduction several model contaminants (4-chloronitrobenzene, carbon tetrachloride, and 2-chloroacetophenone). Further correlation analysis using reduction rate constants compiled from prior studies showed consistent reactivity patterns of three classes of contaminants—including chlorinated ethenes—across the whole range of ISCR relevant reducing mineral minerals, despite the experimental variability of different sources. These results suggest the possibility of using fast reacting CRPs to assess slow abiotic natural attenuation processes from both thermodynamic and kinetic perspectives.

Indigo disulfonate (I2S), one of the thermodynamic CRPs used in **Chapter 4**, was applied as a kinetic and capacity probe to characterize nZVI modified by carboxymethyl cellulose (CMC-nZVI), one of most widely used nZVI formulations in ISCR (**Chapter 5**). The results suggested that I2S is specific to Fe(0) at neutral pHs, providing an operationally easy way to quantify the Fe(0) content in groundwater impacted by nZVI injection. The reaction stoichiometry of I2S to Fe(0) is close to 1.5, suggesting complete oxidation of Fe(0) to Fe(III) because reduction of I2S is a two-electron process. Under the experimental conditions, the kinetics of I2S reduction was described by the second-order kinetic model. I2S was further applied to quantify the corrosion rate of CMC-nZVI in anaerobic water as a function of initial nZVI concentration and pH to simulate likely geochemical scenarios upon nZVI emplacement. The results revealed orders of magnitude faster Fe(0) loss than conventional nZVI, suggesting chemical transformation of CMC-nZVI is sufficiently fast that its “reductant demand” should be a major consideration in design on any application of CMC-nZVI in remediation.

Chapter 1 Introduction: Overview of Biogeochemical Processes of Reducing Iron Minerals and Their Roles in Contaminant Sequestration and Degradation

Background

Groundwater and soil contamination are long-term environmental problems, which pose significant risks to global environment and human health. In south Asia, arsenic contaminated groundwater impacts the drinking water quality of millions of people (*1*). A recent nationwide survey in China revealed heavy metal contamination is widespread of arable soils, raising concerns about food safety (*2*). In the U.S, aquifers under numerous industrial and military facilities are contaminated with hazardous materials, such as radionuclides and chlorinated solvents (*3*). Migration of these contaminants with groundwater can end up releasing the contamination to surface water (*4*) or reach the subsurface underneath the surrounding neighborhoods and communities, posing secondary environmental hazards, such as food web accumulation and vapor intrusion (*5*).

Due to complexity of aquifer and soil matrices, remediation is often challenging and expensive, and restoration to pristine states may require decades or more. Conventional treatment approaches include pump-and-treat for groundwater (*6*) and dig-and-dump for soils, both involving ex-situ treatment and therefore can be more difficult and costly than in situ treatment scenarios. Over the past few decades, most new approaches to groundwater remediation—including both source zones and plumes—have emphasized in-situ treatment with bioremediation (*7*), chemical reduction (*8*), chemical oxidation (*9*), and thermal treatment (*10*). These technologies, collectively, should eventually improve overall outcomes, including more satisfactory end-points at lower financial cost (*11*). As a result, in-situ treatment is gradually emerging as the preferred remedial strategy, while remedies based on pump-and-treat methods have declined substantially over the last thirty years (**Figure 1.1**).

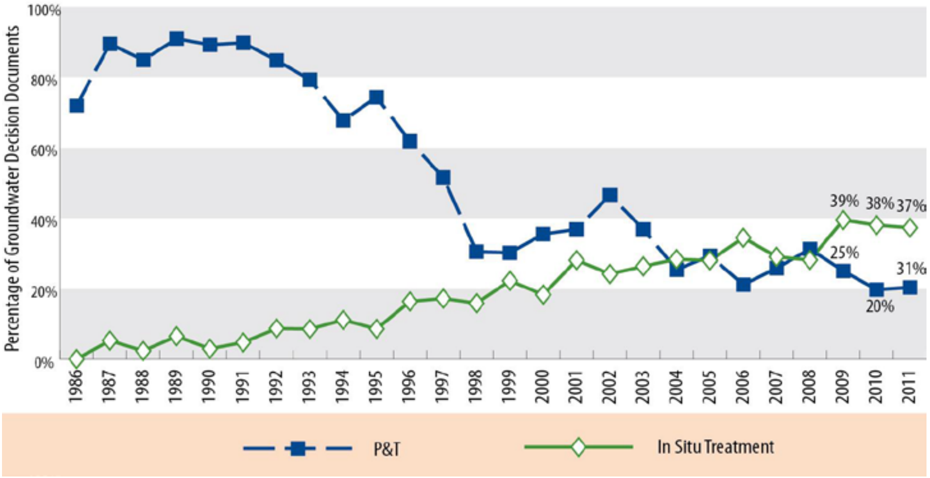

Figure 1.1. Trends in the selection of pump-and-treat vs. in-situ remedies selected for use at EPA superfund sites (source: EPA Superfund Remedy Report, 14th Edition, Nov, 2013).

Among currently favored groundwater treatment technologies, in-situ chemical reduction (ISCR) is relatively new (*8, 12*), but it has attracted increasing interest in recent years. The core concept of ISCR is to promote in-situ abiotic contaminant reduction by directly emplacing chemical reductants into subsurface and/or creating conditions that are favorable for in-situ chemical or biological production of chemical reductants. The first generation of ISCR technology focused mainly on using zerovalent iron (ZVI), as a strong chemical reductant in the form of permeable reactive barrier (PRB) for treating contaminated groundwater plumes. Subsequent developments involving nano zerovalent iron (nZVI) in late 90s initiated a new phase for ISCR by expanding applications to source zone remediation. More recently, recognition that naturally-occurring divalent iron (DVI) minerals can cause abiotic contaminant reduction has further extended the scope of ISCR applications from active remedies based on (n)ZVI technologies to include more passive remedies that rely on natural biogeochemical transformations, such as natural attenuation (*8*). In current groundwater remedial practice, ISCR is often integrated with other remedies, like bioremediation, which takes advantage of synergy between biotic and abiotic processes to achieve the long-term benefits of contaminant attenuation. This has resulted in a variety of hybrid-ISCR based remedies involving microbiological elements, such as BiRD (Biogeochemical Reductive Dechlorination) (**Figure 1.2**).

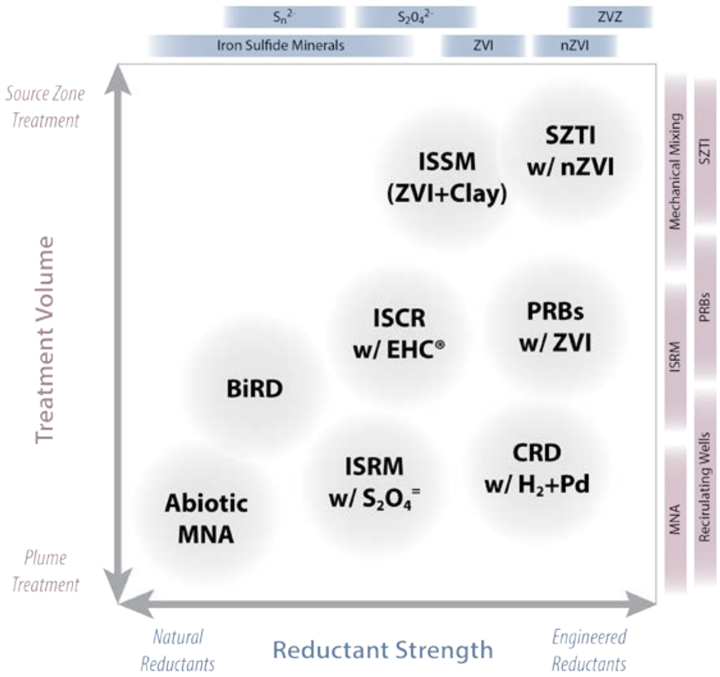

Figure 1.2. Map of ISCR technologies in current practice. The horizontal dimension represents a range of ISCR relevant reductants ordered by their reductant strength. It can be seen that reducing iron minerals are either directly or indirectly involved in every type of ISCR technologies (acronyms) except CRD. Depending on the reducing strength,

the potential applications range from source zone remediation (strong) to plume treatment (weak) (reprinted with permission from Tratnyek, P.G., R.L. Johnson, G.V. Lowry, and R.A. Brown, In situ chemical reduction for source remediation, in *Chlorinated Solvent Source Zone Remediation*. 2014, Springer. p. 307-351. Copyright (2011) Springer).

Reducing iron minerals (including iron sulfides) comprise a major part of the reducing materials that are important in ISCR (*8*, *13*). This is largely due to (*i*) the ubiquitous presence of iron in the environment, which is the fourth most abundant element in the Earth's crust and (*ii*) the high redox activity of iron compared to other abundant elements, such as aluminum and silicate, which are essentially redox inert under typical subsurface conditions. The following sections provide an overview of the fundamental biogeochemical processes of reducing iron minerals in subsurface and the resulted implications for ISCR in contaminant remediation.

1.1. Classification of Reducing Iron Minerals

Based on the valence states of iron, iron based reductant can be divided into two major categories: zerovalent (or elemental) iron (ZVI) and divalent (or ferrous) iron (DVI). The former is generally viewed as an anthropogenic or engineered—as opposed to naturally-occurring—material because the metallic state of iron is unstable under environmental conditions, especially in the presence of oxygen and water. The DVI category includes a broader range of aqueous and solid Fe(II) species, some of which are abundant in anoxic/aquatic environments. Although aqueous Fe(II) reductants, especially Fe(II)-ligand complexes, are known as an important class of DVI reductant (*14*-*16*), the major focus of this work is on solid reductants such as Fe(II) bearing minerals.

1.1.1. Zerovalent Iron

The role of ZVI in reducing halogenated aliphatics in environmental application was first recognized by Gillham and Tratnyek in early 90s (*17-19*). Since then, remediation technologies and products based on ZVI have shown tremendous development, which now are among the most widely-implemented in-situ remedial strategies in subsurface remediation (*20-25*). Despite numerous ZVI formulations and sources, the material is most commonly categorized based on particle size and purity: ranging from the coarse recycled iron "aggregate" from construction applications, to the more-pure, micron-sized high purity ZVI (mZVI) manufactured for powder metallurgy applications, to the most-pure nano sized ZVI (nZVI) that is synthesized for remediation. The former two types are commercially available in bulk at moderate cost, and are used routinely for permeable reactive barriers (PRBs) (*26*), which is the first generation ISCR technology that has been widely used in treating groundwater plumes. PRB technologies involve emplacement of a semi-permeable reactive barrier composed of ZVI (and/or other supporting materials) in the flow path of contaminants. As contaminants flow through the barrier with groundwater, contaminants are degraded or immobilized within the treatment zone due to various biogeochemical processes.

Interest in the smaller forms of ZVI (mZVI and nZVI) reflects the emergence and development of nanotechnology in environmental applications over the past fifteen years (*27-30*). Due to the small particle size and high surface area, nZVI usually shows greater reactivity with contaminants than granular iron. The small particles are also designed to be more amenable for direct subsurface injection in concept, and therefore they are better suited for source zone remediation (*31-33*). Commercial products based on mZVI, such as the proprietary product EHC^{TM} from PeroxyChem (Philadelphia, PA), have already been widely applied in field remediation projects for remediating inorganic metals and DNAPL plumes or sources (*34, 35*). Commercially manufactured nZVI have also been offered, including RNIP (reactive nano iron particle), which was prepared by H_2 reduction under high temperature and pressure (but is no longer available), and Nanofer, developed by NANO IRON, s.r.o (Rajhrad, Czech Republic), which recently has been used in many field applications in European countries. For nZVI prepared on-site and in laboratory, the most frequently used synthesis protocol is aqueous phase reduction of ferrous or ferric salt by borohydride (*36*), which involves addition of aqueous borohydride solution, a strong reductant, to ferric or ferrous iron solution in slightly excess stoichiometric ratios to produce Fe(0) particles.

Despite significant research efforts, full-scale nZVI applications are limited by the poor mobility of nZVI in the subsurface due to the strong tendency of nZVI to agglomerate because of intra-particle magnetic attraction and other forces (*33, 37*) or to sorb onto the surface of soil grains. The presence of various surfactants has been shown to improve the mobility of nZVI in porous media, which has led to development of engineered coating on nZVI by organic polymers, including polyelectrolytes, polysaccharides, and synthetic surfactants (summarized in Tratnyek et al. (*38*)). The additives have been shown to improve nZVI stability and therefore transport and delivery, although most of the evidence for this is obtained from laboratory tests. At the field-scale, synthesis of nZVI by borohydride reduction in the presence of CMC has proven to be effective (*39, 40*). The key part of this protocol is to allow sufficient pre-equilibration between CMC and Fe(II) before borohydride addition. Formation of CMC-Fe(II) complexation leads to nucleation of very small NPs distributed along the CMC polymer. CMC-nZVI has much smaller particle size, better dispersion property, and greater mobility than any other types of nZVI, and therefore has quickly become one of the most widely used formulations of nZVI in recent field applications. A number of field injection trials have been performed and have shown that CMC-nZVI can be distributed into the porous media for 1−2 meter, depending on the particular emplacement method used (*41-43*).

1.1.2. Divalent Iron

Unlike ZVI based reductants, which are primarily of anthropogenic origin, divalent iron (DVI) minerals are widely distributed in anoxic environments as a result of naturally occurring biogeochemical processes (**Section 1.2**) or, engineered interventions intended to generate DVI (e.g., injection of sodium dithionite for “in situ redox manipulation”) (*12*, *44*). The DVI associated with minerals has traditionally been regarded as either adsorbed to the surface (i.e., $Fe(II)_{ads}$ or $Fe(II)_{surf}$) or Fe(II) incorporated into the mineral lattice (i.e., “structural” Fe(II)). The former arises when Fe(II) adsorbs onto Fe(III) oxyhydroxides or oxides, such as goethite or hematite, while the latter is found in pure divalent minerals (e.g., siderite, iron sulfides) or mixed valent minerals (e.g., magnetite and green rust (GR)) (*13*, *45*). Green rust typically has the structure of layered double hydroxide (LDH), in which the interlayer is occupied by anions to neutralize the positive charge resulting from Fe(II) replacement by Fe(III) in hydroxide layers. Depending on the anions present in the interlayers, GR can be further divided into GR-chloride, GR-sulfate, and GR-carbonate. The ideal Fe(II) to Fe(III) ratio is 3 for GR-chloride, and 2 for the latter two formulas. Magnetite, the other mixed-valent mineral, has an Fe(II) to Fe(III) ratio of 0.5 at ideal stoichiometry. In natural environment, however, both green rust and magnetite exhibit remarkable redox flexibility, in which the Fe(II) to Fe(III) ratio can deviate significantly from the ideal stoichiometry, without necessarily resulting in changes in mineral structures (*46-48*). Clays that contain sorbed or structural Fe(II) represent another important group of DVI minerals (*49*, *50*), which, however, are not included here due to limited scope. Overall, the ubiquitous presence and abundance of DVI minerals make them the major component of the intrinsic reductants in iron-rich soils and aquifers.

1.2. Transformations of Reducing Iron Minerals

Biogeochemical transformations of reducing iron minerals are ubiquitous in the subsurface environment, given high redox activity of these mineral phases and their constant interactions with surrounding environmental components, including groundwater constituents, microorganisms, and contaminants. These transformations are mediated by redox reactions (either biotic or abiotic), such as oxidation and reduction, or by non-redox reactions, such as precipitation and recrystallization. The capacity and reactivity of reducing iron minerals—as well as the dynamics of contaminant reduction by these reductants—are expected to be substantially altered as a result of the collective effects of these processes. The key biogeochemical transformation processes involving reducing iron minerals are summarized in **Figure 1.3** and are discussed below. Given that conventionally-defined iron redox cycling only focuses on Fe(II) and Fe(III), but not Fe(0), the following subsections are divided into two parts, similar to **Section 1.2** but focusing on ZVI and DVI, respectively.

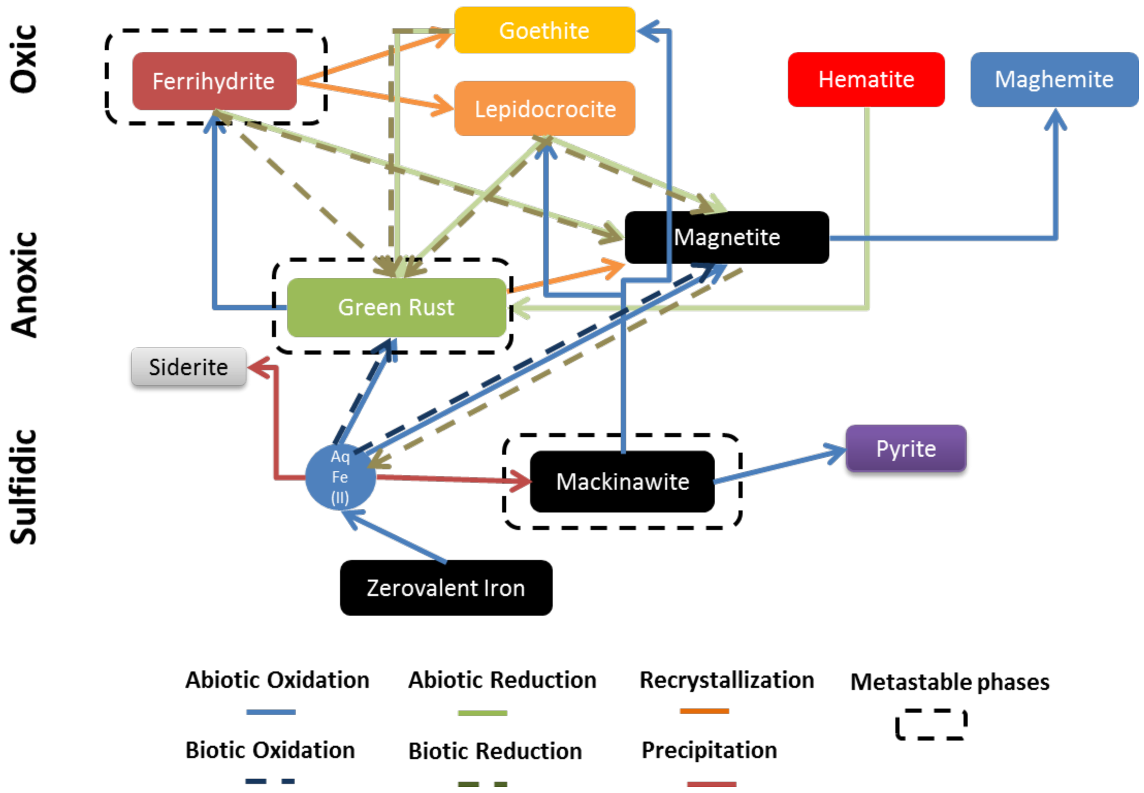

Figure 1.3. Summary of biotic and abiotic transformations of iron mineral phases in subsurface under environmentally-relevant conditions (pH 6–9) (transformation pathways are all suggested based on prior studies).

1.2.1. Zerovalent Iron

The strong reducing strength of ZVI makes it highly susceptible to reactions with a wide range of oxidants, including oxygen, nitrate, and various contaminants, which lead to the formation of dissolved and solid-phase Fe(II) and Fe(III) (*21, 51-53*). For example, nitrate is well known to oxidize ZVI to form surface iron oxides or oxyhydroxides, and this contributes to ZVI passivation (*54, 55*). In the absence of oxygen, ZVI corrosion (oxidation) in water usually is the dominant transformation reaction, even though water is not commonly viewed as an oxidant per se. The processes involved are similar for corrosion of all types of metals, especially ferrigenous metals like steel (*56*), which has been extensively investigated in corrosion literature (*57*). Corrosion of ZVI at low pH yields dissolved Fe(II), hydrogen gas, and hydroxide ion. With pH increasing, Fe(II) precipitates initially as $Fe(OH)_2$. In the presence of common groundwater anions, such as chloride and bicarbonate, the various forms of green rust also form (*58, 59*). Both $Fe(OH)_2$ and green rusts are metastable, which can progressively transform to magnetite (Fe_3O_4), which is thermodynamically more stable (*60*). Magnetite and green rusts have been frequently identified among the transformation (corrosion) products in solid materials recovered from laboratory and field-scale PRBs with granular ZVI without high sulfate concentration in the groundwater (*61-64*).

Apart from abiotic redox reactions, transformation of ZVI can also be influenced by biotic redox reactions. Anaerobic microbial activity is strongly favored in the presence of ZVI because of the highly reducing conditions created by ZVI emplacement and ample H_2 production from ZVI corrosion in water as the electron source for microbial growth (*65-67*). One of the most prominent examples with respect to enhanced microbial activities is the stimulation of bacterial sulfate reduction, evidenced by decreasing groundwater sulfate concentration and increasing population of sulfate reducers down gradient of PRB (*21, 68-70*). Because of the high affinity of sulfide to iron, ZVI and other iron mineral phases can be transformed to highly reactive amorphous iron sulfides (*71-73*). Over time, amorphous iron sulfides further transform to more crystalline phases, such as mackinawite, greigite, and pyrite (*74*), which likely results in less reactivity(*75*).

Similar transformation processes also occur to nZVI, but the smaller particle size and higher surface area are expected to significantly enhance the rates of these transformation reactions (*76*). Therefore capacity (or lifetime) of nZVI is an important operational parameter to characterize in field applications. Several laboratory studies have examined the geochemical transformation of different types of nZVI. For RNIP—the commercial nZVI—significant transformation of Fe(0) to various Fe(II) minerals have been observed after one month exposure to various groundwater anions in batch reactors (*77*). Even in the presence of water, substantial loss of Fe(0) has been observed after prolonged aging (*78, 79*). For nZVI synthesized by borohydride reduction, we showed that around 10% of Fe(0) transformed to FeS after 24-h exposure to Na_2S at pH 7.8 (*80*) (**Chapter 2**). However, it should be noted that the aggregated nZVI used in those studies are not likely to be directly applicable in field injection. Therefore, accommodations may be needed when applying results obtained in batch studies to predict the transport and lifetime of nZVI during field applications.

For CMC-nZVI, oxidation by reactions with the medium and/or contaminants can lead to complete conversion to Fe(III), which we have documented in column study (*81*) and field injection trial (*41*). However, its transformation rates have not been quantified, mainly due to the limitations of current analytical methods to specifically measure Fe(0) in nZVI-containing groundwater samples. In order to resolve this issue, a redox probe based approach was developed in this work, which is presented in **Chapter 5**. It was found that the transformation of CMC-nZVI is much faster than conventional types of nZVI observed in laboratory batch experiments, suggesting that it is necessary to include chemical transformation into the current models that describe transport of CMC-nZVI in subsurface.

1.2.2. Divalent Iron

Naturally-occurring Processes

Under environmental conditions, ZVI is a bulk electron donor only, and is never (re)formed by natural processes, but DVI containing reductants can participate in the cycling between Fe(II) and Fe(III), which are actively mediated by microbial activity (*82*). Under oxic conditions, most DVI minerals are unstable and can be oxidized by oxygen or other oxidants, such as MnO_2, to form Fe(III) oxyhydroxides in aqueous solution at circumneutral pHs or iron(III) oxides from dry oxidation. The particular oxyhydroxides that form depends on many factors, including the concentrations of anions that are present in the medium. For example, it has been shown that increased carbonate concentration during Fe(II) oxidation at neutral pH promotes the formation of goethite over lepidocrocite (*83*, *84*). Microbial iron oxidation is another route for oxidizing Fe(II), mostly dissolved Fe(II), to Fe(III). This reaction is primarily carried out by iron oxidizing bacteria under microaerophilic conditions near the oxic-anoxic interface, in order to compete with the rapid abiotic oxidation of Fe(II) by oxygen (*82*). Under anoxic conditions when nitrate is present, oxidation of Fe(II) (including aqueous but also solid Fe(II)) can be carried out anaerobically by nitrate reducing bacteria (*82*). Indirect abiotic Fe(II) oxidation by nitrite, resulting from biotic nitrate reduction, has recently been shown to coexist with the biotic oxidation (*85*). Microbial oxidation produces a variety of Fe(III) and mixed valent iron minerals, including green rust and magnetite, depending on geochemical conditions (*82*, *86*, *87*). Because green rust and magnetite are reactive towards various groups of contaminants, this process might have important implication in contaminant dynamics at some contaminated sites with high nitrate concentration.

Ferric minerals formed by abiotic or biotic iron oxidation can be re-reduced, under anaerobic conditions, to ferrous via a process mainly known as dissimilatory iron reduction carried out by iron reducing bacteria (*82, 88*). The iron reducing bacteria couple iron reduction with oxidation of organic carbon to acquire energy. This reaction is favored in the environments where oxygen/nitrate depletion has occurred, leaving ferric minerals as the next most favorable terminal electron acceptors for microbial metabolism (*88*). In subsurface environments, this process serves as the major route in producing and regenerating a variety of Fe(II) based reductants and therefore has significant environmental implications in contaminant natural attenuation.

The favorability of iron reduction decreases as Fe(III) minerals become more crystalline (*89*, *90*). For each type of ferric oxide, higher surface area results in faster bioreduction rates (*91*). A number of studies have reported formation of biogenic magnetite or green rust from bioreduction of Fe(III) oxyhydroxides and oxides (*92*-*94*). Magnetite can be further reduced to different ferrous minerals depending on the solution conditions (*95*). Apart from biogenesis, other laboratory studies have also demonstrated abiotic formation of magnetite or green rust by solid state conversion from Fe(III) oxyhydroxide induced by high concentration of aqueous Fe(II) at neutral pHs (*96*-*98*). As with microbial iron reduction, amorphous ferrihydrite and less crystalline lepidocrocite are more susceptible to abiotic transformation compared to goethite of high crystallinity (*97*). The thermodynamically most stable product from the reaction is magnetite, but formation of green rust has been shown to be kinetically favored under certain conditions (likely due to its open layered structure, which is easier to form than denser magnetite particles). Under environmental conditions, conversion of green rust to magnetite is usually observed (*46, 94*), although several studies have found that silicate, phosphate, or extracellular polysaccharide might stabilize green rusts in environment (*86, 99, 100*).

Fe(II) sorbed onto iron oxyhydroxides and oxides is another class of reductants that are likely to form as a result of microbial iron reduction. This group has been extensively characterized because contaminant reduction rates by sorbed Fe(II) are substantially greater compared with aqueous Fe(II) (*101, 102*). Recent studies on the reactivity of adsorbed Fe(II) using Fe^{57} Mössbauer spectroscopy, isotopic solution chemistry, molecular modeling, and time-resolved synchrotron techniques have shown that interfacial electron transfer between sorbed Fe(II) and underlying iron oxides and dynamic phase transformation induced by Fe(II) adsorption (*103-107*). These studies provide new insights that completely alter the traditional conceptual model of discrete Fe(II) sites at the surface of iron(III) oxides. However, the importance of this group of reductants in contaminant remediation in environment remains unknown. Most studies of sorbed Fe(II) were conducted at low Fe(II) concentrations (< 3 mM), to avoid secondary mineral precipitation or phase transformation, which means the results might be most representative of the early stage of iron reduction, which is precursory to the formation of structural Fe(II) minerals, such as magnetite and green rust.

Iron(II) sulfide minerals form primarily in the presence of microbial sulfate reduction, after sulfate has replaced Fe(III) minerals as the most favorable terminal electron acceptor. For groundwater remediation, iron sulfide is considered to be highly reactive to heavy metals, oxyanions, and chlorinated solvents. As a result, remedies based on microbially-facilitated formation of iron sulfide are prevalent. For remediation of chlorinated solvents, this approach has been called BiRD as listed in **Figure 1.2** (*108-*

110). In BiRD, organic carbon, sulfate, and iron oxides are usually amended to the subsurface to form a biowall, another variation of PRB. As sulfidic conditions develop inside the biowall, aqueous sulfide first reductively dissolves Fe(III) oxides, producing Fe(II) and elemental sulfur (*71*). The dissolved Fe(II) reacts with excess aqueous sulfide, leading to formation of amorphous iron sulfide, which—despite being metastable—is moderately persistent in anoxic subsurface environments (*74*). Eventually, amorphous iron sulfide is further transformed to more crystalline mackinawite (FeS), and eventually pyrite (FeS_2) in the presence of excess of H_2S by disproportion reactions (*74*).

Abiotic oxidation of FeS by dissolved oxygen is slower than for Fe(II) oxides partly because of the redox buffer capacity provided by Fe(II) and sulfide. The mechanisms of this oxidation involves oxidation of the Fe(II) and sulfide by independent pathways, leading to the formation of iron (oxyhydr)oxides and elemental sulfur (*111, 112*). The elemental sulfur can be further oxidized to a series of sulfur oxyanions by various sulfur oxidizing bacteria. This process produces sulfuric acid as the product. At many mining sites, the oxidation of pyrite and other metal sulfides is the main cause for acid mine drainage (*113*).

Anthropogenic Manipulation

Although majority of the transformations of DVI reductants are regulated by naturally-occurring abiotic and biotic processes, these processes also can be engineered, to enhance abiotic natural attenuation. The most fully developed example of this involves the injection of sodium dithionite into subsurface to produce DVI containing phases in situ (*114, 115*), which is termed as in-situ redox manipulation (ISRM) (**Figure 1.2**). The resulting DVI phases have been characterized by sequential extraction, before and after dithionite treatment of sediment, and it was found there is significant enhancement in sorbed Fe(II) (1 M $CaCl_2$ extraction) and FeS/CO_3 phases (0.5 M HCl−1 M $CaCl_2$) and decrease in amorphous iron(III) oxides ($NH_2OH \bullet HCl$), suggesting transformation of iron species from the latter to the former (*12*). Formation of magnetite and FeS at the surface of the aquifer materials after treatment by dithionite has been reported by using a suite of surface characterization techniques (*116*).

1.3. Methods for Characterizing Reducing Iron Minerals

The advance of our understanding of reducing iron minerals in the environment primarily relies on a suite of methods to characterize these materials across the range of scales that their effects are expressed. Applied methods range from visual appearance of slurry of sediment to microscopy with sub-nanometer spatial resolution, from electrochemical analysis of bulk mineral redox properties to spectroscopic analysis of speciation at the mineral-water interface, and from spectrophotometric and electrometric methods that are routinely performed in the field to advanced spectroscopy that require transport of samples to specialized facilities. The scope of this dissertation includes many of these techniques, often in combinations that provide complementary information about the properties of the reducing minerals. To provide perspectives on the range of methods used in the following chapters, this section provides an overview of the fundamentals of the techniques and tools that are commonly applied for characterizing reactive iron minerals, with emphasis on the ones that were applied in this work.

1.3.1. Wet Chemistry: Extraction

Extraction is a solution-based approach to convert solid iron into dissolved iron, which is then usually measured by colorimetric iron assays (e.g., 1,10-phenanthraline for ferrous iron and ferrozine for ferrous and ferric iron) or by inductively coupled plasma (ICP) -OES or -MS. Protocols for sequential extraction of iron from soil and sediment samples are well established with slight variations among different studies (*117*, *118*). Extractants with increasing strength are applied to target different iron pools, starting from ion exchangeable Fe or adsorbed Fe (1M $CaCl_2$), to $FeCO_3$+FeS (0.5 M HCl−1 M $CaCl_2$), to amorphous Fe(III) oxide (NH_2•OH, HCl), to crystalline Fe(III) oxide (dithionite-citrate-bicarbonate (DCB) − NH_2•OH, HCl), and to total Fe(III) (5 M HCl). In general, the more redox active the iron phases are, the easier they can be extracted. A number of pure mineral phases have been tested by the extraction protocols, and the selectivity of different extractants to different iron pools was confirmed even though they are purely operationally defined (*117*). However, these solution-based extraction methods are also tedious, and overestimation by acid extraction in the presence of iron sulfide has been reported by one recent study (*119*).

1.3.2. Solid Characterization

Characterization techniques that apply directly to solid samples, can be sensitive to bulk properties or selective (to varying degrees) for the near-surface interface. They also vary greatly in the spatial or temporal resolution of the information they provide. When multiple methods are used in complementary combinations, a more complete understanding of the properties of reducing iron minerals can be obtained. In the summary of solid-phase characterization methods that follows, these techniques are organized in three categories: *physical characterization*, *chemical characterization*, and *reactivity characterization*.

Physical Characterization

The physical properties of reducing iron minerals that are of most relevant to contaminant reduction are *surface area* and *surface charge.* Surface area is the primary determinant of the quantity of reductant available for reaction with contaminants where the reaction occurs at the mineral-water interface. Small particles have large surface area to mass ratio (i.e., specific surface area), so they offer a higher concentration of surface sites to react with contaminants (*81, 120*). In general, the specific surface area (m^2/g) of granular material is inversely correlated with the particle size. If the particle geometry is sufficiently simple (i.e., uniform size and shape, spherical, without significant porosity), the specific surface area can be estimated from the particle size distribution determined by analysis of TEM images. However, the preferred protocol is usually by N_2 or Kr gas adsorption using the theory known as BET (Brunauer, Emmet, and Teller). However, a disadvantage of the BET method is that sample preparation steps—which include heating and drying—can induce changes in the particles, such as aggregation which could cause significant underestimation of surface area by BET (*121*). These sample processing artifacts might be more likely for nanosized materials due to their strong tendency to aggregate into large particles. The specific surface area is commonly used in contaminant reduction studies as a basis for normalizing the observed reduction rate constants (*122, 123*). This allows the reactivity of reductants with the same chemical composition but different sources (e.g., ZVI) to be compared on a relatively uniform basis, thereby making the derived properties—especially surface area normalized rate constants (k_{SA})—more generally useful in assessing the "true" material reactivity (*26, 122, 123*).

Chemical Characterization

Chemical characterization of reducing iron minerals mainly includes crystal structure and chemical speciation. *X-ray diffraction* (XRD) is common and often the most definitive method for identification of specific minerals (based on their crystal structure) (*124*). Samples with high crystallinity exhibit sharp peaks in their diffraction patterns, which can be easily interpreted by matching with the reference minerals included in the database. In contrast, amorphous and poorly crystalline materials, such as the samples described in **Chapters 2 and 3** (*80, 125*), usually give broad and less-well resolved diffraction patterns, and therefore are less useful in definitively identifying the mineral phases.

Mössbauer spectroscopy (MB) is another widely used and powerful method for characterizing the mineralogy of iron reductants. Unlike XRD, MB is well-suited for characterizing samples that are amorphous or poorly crystalline (because the recoil that produces the MB effect is only sensitive to neighboring atoms and not affected by the long range order (*126*). Because Fe(II) and Fe(III) give distinctive features by MB spectroscopy, this method has been used widely for characterizing DVI reductants, such as sorbed Fe(II) (*105*), green rust (*127*), magnetite (*128*), and FeS (*73*). For sorbed Fe(II), the selectivity provided by ^{57}Fe isotopic labeling combined with MB spectroscopy has been used to distinguish surface bound Fe(II) from structural Fe(II) in studies of interfacial electron transfer involving Fe(II) on iron oxides. In addition, several recent studies, including a portion of the work described here (**Chapters 2 and 3**), have used MB spectroscopy to characterize biogeochemical transformations of reducing iron minerals that include iron sulfide and ZVI as it is a highly sensitive technique that can detect even trace amount of speciation change. Fitting of MB spectra allows quantitative differentiation of various iron species in samples composed of multiple transient phases (*80, 111, 125*).

In contrast to XRD and MB spectroscopy, both of which are bulk characterization techniques, *X-ray photoelectron spectroscopy* (XPS) is sensitive only to the outer ~10 nm of the sample surface. This makes XPS a useful technique for mechanistic studies of reducing iron minerals because the majority of interactions between the reductants and environmental components occur at or very near the aqueous solid interface. The resulting changes in surface properties often are too subtle to detect with bulk measurements but sufficiently strong for XPS to detect. For example, in **Chapter 2**, both Mössbauer and XPS were used to characterize nZVI exposed to artificial groundwater for 24 h. While MB spectra only showed subtle difference between exposed nZVI and pristine nZVI, XPS spectra clearly showed the attenuation of two peaks in exposed nZVI, which corresponded to the transformation of surface Fe(0) (**Figure 1.4**). XPS can be performed in two modes. The wide scan mode gives the elemental compositions of the surface, while the narrow scan mode further reveals the speciation of target elements (including oxidation states and chemical bonds). For samples with mixed surface speciation, the narrow scan spectra require deconvolution to quantify contributions from individual species. Identification of these species can be improved by examining the narrow scans of other elements that are likely bonded with iron, such as O, S, or P.

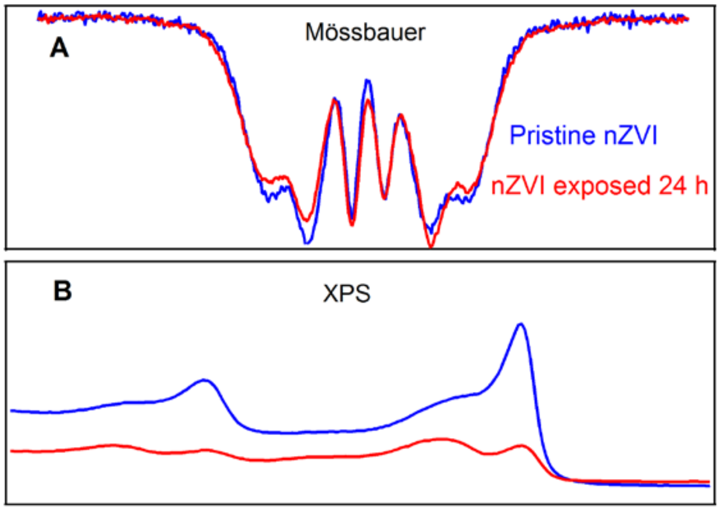

Figure 1.4. Comparison between (**A**) Mössbauer and (**B**) XPS spectra of pristine nZVI and nZVI exposed to artificial groundwater for 24 h (data was extracted from Figures 2.2 and 2.3, and replotted; composition of artificial groundwater is based on Table A.1).

None of the techniques mentioned above offers high spatial resolution information. This information can be obtained by *electron microscopy* coupled with *energy dispersive spectroscopy* (EDS), which is useful in gaining insights on the elemental distribution of reductants at micro- to nano-meter scale. This is essential when the reductants are known or designed to have mixed compositions, such as sulfide transformed nZVI described in **Chapters 2 & 3** or nZVI doped with transition metals (*129*). In addition, electron microscopy is uniquely useful in detecting changes in the morphology of specimens, such as structural breakdown of the oxide film on the ZVI surface, or formation of secondary precipitates.

X-ray absorption spectroscopy (XAS) is a synchrotron based spectroscopy technique that has been extensively used for characterizing the speciation of inorganic elements. XAS spectra are of two types: XANES (X-ray absorption near edge structure) and EXAFS (extended X-ray absorption fine structure). The former is mainly used for identifying the oxidation states of the target elements while the latter provides information on atomic-scale coordination environment of the selected elements (*130*). The major application of XAS in environmental research is to characterize the speciation of trace elements during biogeochemical transformation processes. When used for characterizing iron based reductants, XAS provides similar information as MB spectroscopy, such as valence state of iron, sample composition, but with less precision. In one study, XAS spectra for 27 iron reference minerals were obtained, and it was found that XANES can distinguish different classes of minerals, but not necessarily specific minerals within a class (*131*). In addition, for mixed samples, the sensitivity of XANES varies depending on sample matrix and specific type of minerals (because they have different X-ray absorptivities). Therefore, care must be taken when using XAS spectra to quantify mineral composition. However, recent development in coupling XAS with spatially resolved electron microscopy can provide speciation information with high spatial resolution, and this has been successfully applied in characterizing model biogeochemical matrix (*132-134*).

Reactivity Characterization

The characterization methods classified above as “physical” and “chemical” do not directly reflect mineral “reactivity” with contaminants. Although mineral reactivity is most commonly characterized by the kinetics of contaminant reduction (as discussed in **Sections 1.4 and 1.5),** thermodynamic measurement, such as mineral reduction potential, can also be used as a more generic “reactivity” gauge to characterize the reducing strength of the reductants. As a thermodynamic parameter, reduction *potential* quantifies only the energetic driving force for redox reactions, with more negative potentials favoring reduction and positive potentials favoring oxidation. A summary of standard reduction potentials (at pH 7) of half reactions for many environmentally-relevant redox-active species is given in **Figure 1.5**, including terminal electron acceptors, organic and inorganic contaminants, shuttles, and reductants. Major iron species are listed in the far right column, including several reducing iron minerals, such as Fe(II)/Fe(0). The couple has the reduction potential that is lower than most of the organics and oxyanions. Therefore Fe(0) is considered to be highly reactive towards those contaminants. As a general rule of thumb, the lower the reductant is in the column, the more reactive that reductant is.

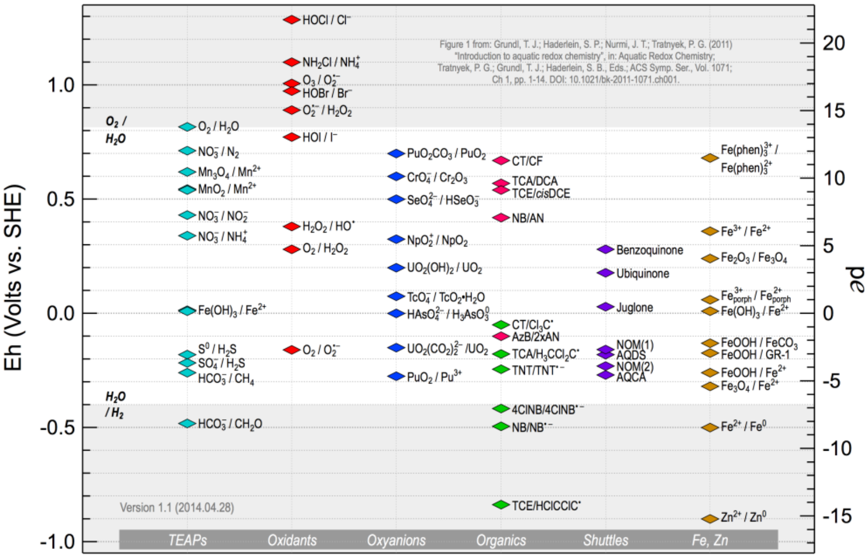

Figure 1 from: Grundl, T. J.; Haderlein, S. P.; Nurmi, J. T.; Tratnyek, P. G. (2011) "Introduction to aquatic redox chemistry", in: Aquatic Redox Chemistry; Tratnyek, P. G.; Grundl, T. J.; Haderlein, S. B., Eds.; ACS Symp. Ser., Vol. 1071; Ch 1, pp. 1-14. DOI: 10.1021/bk-2011-1071.ch001.

Figure 1.5. Redox ladder of six representative groups of environmental redox active species The data are gathered from various sources that include reduction potentials determined by a wide range of methods and theories; values for reducing iron minerals are mostly obtained from (*135, 136*). (reprinted with permission from Grundl, T.J., S.P. Haderlein, J.T. Nurmi, and P.G. Tratnyek, Introduction to aquatic redox chemistry, in *Aquatic Redox Chemistry*, P.G. Tratnyek, T.J. Grundl, and S.B. Haderlein, Editors. 2011, American Chemical Society: Washington, DC. p. 1-14. Copyright (2011) American Chemical Society).

The mineral reduction potential is often measured with a Pt electrode in a well-mixed mineral suspension. This method is largely adapted from widely applied reduction potential measurements in aqueous solution or soil suspensions. However, it should be noted that the measured value, operationally defined as the oxidation-reduction potential (ORP), fundamentally, represent mixed potentials that may include contributions by all the redox active species in the system (*137*), and the relative contributions of the various redox active species are rarely know. In addition, electrode responses to solid phases can vary greatly depending on the physicochemical properties of the materials. These factors make it particularly difficult to quantitatively interpret ORP measurements on suspensions of granular minerals. The most successful and thorough application of ORP to characterizing suspensions of redox-active environmental materials was with the most highly reducing materials (nZVI) under highly-controlled laboratory conditions (*137*). In this case, the measured mixed potentials were interpretable in part because the strongly reducing nZVI dominates the electrode response, and overwhelms the contributions of other aqueous redox species, such as Fe(II). However, in most cases, ORP measurements deviate substantially from the expected values (calculated from thermodynamic properties) because of weak electrode response to mildly-reducing materials or materials of large particle size. Therefore, in most cases, ORP can only be used as a qualitative indicator of redox conditions in mineral suspensions.

The typical way to measure ORP on mineral suspensions involves a commercial combination ORP electrode (with a Pt ring or disk working electrode and reference electrode) into a well-mixed and deoxygenated suspension of the particles and a simple high-impedance potentiometer. A more controlled approach is to use separate working and reference electrodes, so that the working electrode can be polished and cleaned effectively before each measurement in order to produce reproducible data (*137*). This minimizes common issues with combination electrodes such as memory, fouling and poisoning, which often cause inconsistent results.

Another approach to make electrochemical measurements of reduction potentials of fine-grained minerals employs working electrodes made with the mineral sample. For example, powder disc electrodes (PDEs) (*138*) are made by packing the reducing materials into a customized holder supported by a conventional disc electrode underneath. This method is quite flexible and has been used to characterize the electrochemical properties of (n)ZVI, magnetite, and nano Fe/FeS composites(*37, 138-141*). However, it seems likely that only materials with substantial conductivity are suitable for this type of measurement, and therefore limited types of minerals have been tested.

Given these limitations in electrode determination of mineral reduction potential, alternative approaches are needed. The main alternative involves the use of chemical redox probes (CRPs) and redox mediators, which have been employed in several recent studies to determine reduction potentials of the reducing minerals (*142, 143*). In this approach, redox probes/mediators are selected that form reversible redox couples that reach equilibrium rapidly in response to changes in conditions of the test medium (*144*). For probe/mediators that derive from redox indicators, the oxidized and/or reduced forms are easily determined from their strong and distinctive absorbance or fluorescence spectra. The degree of probe reduction can then be calculated based on calibrated absorbance measurements. Assuming that the redox equilibrium is reached between the reductant and the probe, the reduction potential of the reductant can be calculated based on the ratio of oxidized form to the reduced form of the CRPs using the Nernst equation.

Various redox indicators have been used to determine the redox conditions of biological systems or groundwater in the absence of solid phases. For example, redox indicators—representing a range of standard reduction potentials—immobilized on glass beads in a flow-through cell has been successfully used to measure the reduction potential of the progressively more reducing groundwater by UV-Vis spectroscopy (*145, 146*). This approach to progressive reduction of indicators also was used to characterize laboratory simulated iron reducing conditions and sulfate reducing conditions. The quantification of indicator speciation in the presence of solid reductants, however, is complicated by the potential of decolorization by adsorption. This is particularly problematic for positively-charged indicators, which adsorb strongly to surface-water sediments that are high in organic matter (*147*).

1.3.3. Applications to ISCR

Although the methods of characterization discussed above have often been applied in laboratory research to characterize reducing iron minerals, full-scale ISCR remediation projects that have been well characterized are limited to just a few technologies. Foremost among these are ZVI based PRBs, which have been subject to many detailed field studies. A wide range of mineralogical, microscopic, and spectroscopic techniques have been applied to characterizing materials recovered from column or field-scale ZVI based PRBs (*53, 63*). The extensive characterizations are mainly driven by the practical needs to understand the effects of the fundamental biogeochemical transformation on the long-term performance of PRB, which can only be achieved by applying advanced instrumentation. For example, by using XANES and SEM, it was found that chromium was primarily associated with mackinawite as Cr(III) in a ZVI based PRB after 8-year operation, indicating the dominant role of long-term biogeochemical transformation in Cr sequestration (*148*).

Recently, increasing interest in applying nZVI as the primary ISCR remedy in field has highlighted the needs for developing field deployable characterization tools to detect nZVI in order to understand nZVI delivery and performance in subsurface. For nZVI, characterization conducted on-site is particularly beneficial because (*i*) nZVI usually results in rapid changes in redox conditions that require real-time monitoring and (*ii*) nZVI is highly reactive and often present in groundwater at low concentrations, making off-site characterizations less reliable. The unique challenges that arise when characterizing the in situ fate and effects of nZVI, and methods available to meet these challenges, were reviewed in our recent paper by Shi et al.(*81*). In that review, we noted that the two most common measurements made at field sites are total iron and ORP, but neither of these two methods is diagnostic to Fe(0) and could overestimate the delivery of Fe(0) due to interference from other species resulted from nZVI transformation, such as Fe(II) or hydrogen. This issue is addressed in **Chapter 5** where we developed a simple and field-deployable method using a chemical reactive probe (CRP) that is selective to Fe(0) but not to other Fe(II) or Fe(III) species. By measuring the reduction of selected CRP, the Fe(0) content in given groundwater sample can be quantified based on the reaction stoichiometry.

Characterization of DVI minerals as corrosion byproducts of ZVI has been commonly performed on many column- to pilot-scale ZVI based PRB (*51, 149*). The interest has recently renewed in the context of abiotic natural attenuation (NA), as a result of increasing recognition of the effects of DVI minerals in abiotic contaminant reduction (*150*-*155*). However, characterization of DVI minerals in abiotic NA is challenging because (*i*) the quantity of iron phases is much less than ZVI based PRB and (*ii*) it is very difficult to preserve small quantities of highly reactive DVI minerals, such as green rust and FeS, against oxidation during sample collection and transport. The latter issue may be largely overcome by recently developed cryogenic coring technique (*156*, *157*). This expectation is supported by several earlier studies showing storage at frozen temperatures minimizes the sample changes with respect to acid-volatile sulfide (AVS) content and dissolved Fe(II) (*158*). The cryogenic sampling protocol might facilitate applications of solid phase characterizations for DVI minerals given increasing interests in understanding their roles in abiotic NA.

To date, the methods that have been mostly applied for characterizing DVI minerals on field samples include total solid Fe(II) measurements by chemical extraction, XRD, and magnetic susceptibility. One recent study also applied SEM-EDX to study the ferrous iron distribution in low permeability rock matrices that has been exposed to chlorinated solvents (*153*). While each of these methods describes a unique aspect of DVI minerals, they all have their own weakness. For example, total Fe(II) measurement does not differentiate various DVI minerals, which have a wide range of reactivity. XRD, although capable to identifying individual DVI minerals, is less useful for characterizing amorphous phases, which are known to be more reactive with contaminants than crystalline phases. Magnetic susceptibility is based on the assumption that the major DVI pool responsible for abiotic dechlorination is magnetite, which neglects other reactive

DVI minerals such as green rusts and iron sulfides. On top of that, none of these three methods provide a direct measure of redox reactivity. In **Chapter 4**, we explored the possibility of using chemical reactive probes (CRPs) as a way to characterize the reactivity of a wide range of DVI minerals. The CRP methods could even be applied in field using push-pull injection methods (Istok's book) to evaluate the in-situ reactivity of DVI minerals and estimate the potential for abiotic NA.

1.4. Reductive Sequestration of Metal/Metalloid by Reducing Iron Minerals

Sequestration (removal by any process that involves immobilization) of metals/metalloids from aqueous solution by reducing iron minerals has been extensively studied. Adsorption, surface precipitation, reduction, and incorporation are the four main sequestration mechanisms (*130*, *159*-*161*). Among these four, only reduction involves electron transfer from the reductants to the contaminants. Adsorption involves a monolayer of adsorbate (contaminant), forming inner- or outer-sphere complex with mineral surface, whereas surface precipitation involves formation of multiple layers of new phases, which usually contain elements from contaminants and/or minerals. Incorporation into host mineral structure can occur as a result of co-precipitation and recrystallization. For any particular combination of contaminant and reductant, sequestration might result from the collective effects of several mechanisms simultaneously or in sequence, depending on the specific properties of both contaminant and reductant.

1.4.1. Zerovalent Iron

The low reduction potential of Fe(0) provides strong thermodynamic driving forces to reduce a variety of metals and metalloids (**Figure 1.5**). As a result, ZVI based technology (e.g., PRBs) has long been applied for in-situ treatment of groundwater plumes containing heavy metal cations, oxyanions, and radionuclides in North America (*162-164*). Engineered applications in treating municipal or industrial wastewater containing metal/metalloid contaminants by ZVI or nZVI have also become more common, especially in China (*165-167*).

Although reduction is generally considered to be the primary sequestration mechanism in ZVI system, adsorption and co-precipitation are important for a number of contaminants as well. For example, a recent pilot-scale study using nZVI in treating smelting wastewater containing high concentrations of mixed heavy metals/metalloids provides a conceptual illustration of different sequestration mechanisms for different contaminants by (n)ZVI. Essentially the same range of processes apply to groundwater despite significant difference in chemical compositions between wastewater and groundwater (*165*).

Thermodynamic factors play an important role in contaminant sequestration mechanisms by ZVI. For heavy metal cations with standard reduction potentials substantially higher than Fe(0)(such as Cu(II) and Ag(I)), reductive immobilization to lower oxidation states, usually elemental states, are expected. For metal cations with reduction potentials lower than Fe(0), such as Zn(II), adsorption or coprecipitation is the primary removal mechanism. For metals with reduction potentials in between (e.g., Ni(II), Pb(II)), both reduction and adsorption could be important.

A similar classification also applies to interactions of metalloids with ZVI. Mixed sequestration mechanisms are typically observed for arsenic in ZVI system (*168*), which has relatively low reduction potential compared to other oxyanions according to **Figure**

1.5. Reduction, adsorption, and co-precipitation have been shown to contribute to As sequestration simultaneously (*169, 170*). The contribution from each mechanism depends on the mineralogy of surface iron species and environmental conditions. With aged ZVI or in the presence of an oxidant (e.g., dissolved oxygen), adsorption plays a bigger role due to the presence of iron oxides or oxyhydroxides on the surface, while with fresh (n)ZVI under anoxic conditions, reduction to lower oxidation states is expected (*168, 170, 171*). By contrast, for other common oxyanions (e.g., Cr(VI)) and radionuclides (e.g., U(VI), Tc(VII)) with more positive reduction potentials, reduction is the main sequestration mechanism, producing metal hydroxides (e.g., $Cr(OH)_3$) or dioxides (e.g., UO_2) as the reduction products.

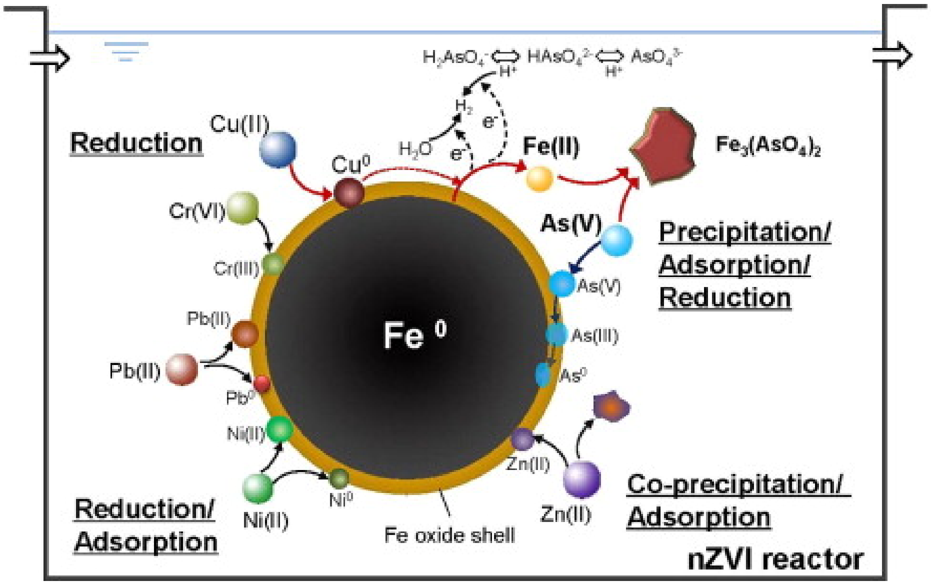

Figure 1.6. Conceptual model of diverse removal mechanisms for different metals and metalloids by nZVI in treating smeltering wastewater (reprinted from Li, S., W. Wang, Y. Liu, and W. Zhang, Zero-valent iron nanoparticles (nZVI) for the treatment of smelting wastewater: A pilot-scale demonstration. *Chemical Engineering Journal*, 2014. **254**: p. 115-123.Copyright (2014) Elsvier B.V.).

1.4.2. Divalent Iron

The long term biogeochemical transformation of Fe(0) leads to significant shifts of the dominant reductant pool from ZVI to DVI. In addition, natural biogeochemical cycling also produces various DVI minerals (**Figure 1.3**). Because DVI minerals are less strong reductants than ZVI, slower sequestration kinetics and lower removal capacities are usually observed (if reduction is the dominant sequestration mechanism). For contaminants that are mainly removed by adsorption, removal may be greater by ZVI that is coated with the most oxide surface area (ref). Moreover, because, as mentioned earlier, DVI is part of the iron redox cycling, sustained reactivity for metal/metalloid sequestration via microbial regeneration are possible.

A decrease in reductant strength can result in changes in sequestration mechanisms for metalloids with low reduction potentials, for reasons similar to those discussed above. For example, reduction of As(V), one of the three sequestration mechanisms by ZVI, has not been observed with green rust and magnetite, which are two most common DVI minerals formed by ZVI corrosion under anoxic conditions (*149, 172*). Instead, As(V) appears to be sequestered predominantly by adsorption as an inner-sphere complex appears to be the dominant process. For contaminants with more positive reduction potentials, like Cr(VI), U(VI), or Tc(VII), the sequestration mechanism and products are not altered with DVI minerals. Numerous studies have shown that Cr(VI) is reduced to Cr(III)(OH)$_3$, U(VI) is reduced to uraninite (U(IV)O$_2$), and Tc(VII) is reduced to Tc(IV)O$_2$ by different DVI minerals, including sorbed Fe(II), green rusts, magnetite or FeS (*101, 102, 173-179*).

Among the various DVI minerals, FeS is of particular interests in sequestration because of its strong affinity with many metals/metalloids to form highly insoluble metal sulfide precipitates, such as Zn, Cu, Ni, Hg, As, etc. (*180, 181*). Therefore, stimulating microbial sulfate reduction by amending sulfate and organic carbon to promote FeS formation is an effective remedial strategy for immobilizing metals/metalloids in contaminated aquifers. Most of the precipitation reactions to form metal sulfides are not redox based. Nevertheless, in the work described in **Chapter 2**, we found a redox based sequestration pathway for $^{99}Tc(VII)O_4^-$ involving FeS, which can potentially be used as a promising remediation strategy for this highly mobile radionuclide (*80*).

1.4.3. Stability

Unlike organic contaminants that can be degraded (sometimes completely mineralized), metals/metalloids are only sequestered, leaving remobilization a potential risk. Remobilization of reduced metals/metalloids often occurs during subsurface redox fluctuations (*182*). For example, when redox conditions change from oxic to anoxic, remobilization of arsenic occurs as a result of desorption during biotic reductive dissolution of ferrihydrite (*183, 184*). By contrast, when anoxic environment becomes oxic, abiotic oxidative dissolution of sulfide minerals can also lead to arsenic remobilization (*112*). Because the majority of the sequestration reactions mediated by reducing iron minerals are reduction, the stability in the presence of natural oxidants is of particular concern.

Common natural oxidants include oxygen, manganese dioxide (MnO_2), and nitrate (NO_3^-). Different metals/metalloids exhibit a wide range of susceptibility to oxidation by different oxidants. For example, $Cr(OH)_3$ is known to be stable in the presence of dissolved oxygen (DO) (*174*), but U(IV)O_2 is readily oxidized to U(VI) by DO (*185*). Biogenic MnO_2, a strong solid oxidant, has been shown to be capable of oxidize a variety of metal hydroxides and oxides, such as Cr(III), U(IV), and Tc(IV), by solid electron transfer (*186-190*). Nitrate by itself does not give abiotic oxidation, but in the presence of nitrate reducing bacteria, oxidation could proceed despite the much slower rates that are reported compared to abiotic oxidation by DO (*191, 192*). Recall that nitrate reducing bacteria can oxidize some divalent iron minerals (**Section 1.2.2**), which might result in release of sequestered trace elements. This pathway might have potentially important implications in contaminant remobilization in anoxic environment.

To mitigate the remobilization of metals and metalloids, several strategies have been investigated, including (*i*) addition of oxygen scavengers to enhance the redox buffer capacity; (*ii*) manipulation of the sequestration pathway to favor the reduction products that are more resistant to oxidation, (*iii*) formation of secondary phases that physically limit oxygen contact, and (*iv*) incorporation of elements into the structure of host minerals. Among these mitigation strategies, relying solely on natural redox buffer capacity is the least effective, because remobilization can only be suppressed if redox buffer capacity is not completely consumed. Naturally-occurring DVI minerals are part of the intrinsic subsurface redox buffer capacity. Among them, iron sulfides are considered to be particularly important because (*i*) sulfide adds additional redox buffer capacity compared to other DVI minerals and (*ii*) many metals or metalloids are sequestered in sulfide forms that co-exist with iron sulfides. Recent studies showed that the presence of FeS significantly inhibits the oxidation of UO_2 until the FeS is fully oxidized and so the redox buffer capacity it provides is exceeded (*111*). Analogous effects of FeS were observed in this work, which are described in **Chapter 3** (*125*). However, in our study, it was additionally found that formation of FeS shifts the speciation of reduced Tc from TcO_2 to TcS_2, which is more resistant to oxidation. Upon oxidation TcS_2 was first converted to TcO_2, which plays a secondary role in slowing Tc oxidation.

Formation of secondary Fe(III)−phosphate phases has been shown to inhibit pyrite oxidation by oxygen and Fe(III) above pH 4 (*193, 194*), which can potentially serve as a way to improve the stability of toxic metals associated with pyrite. The most effective strategy, however, is by incorporation of the contaminants into the crystal structures of host minerals. Tc(IV) incorporation into goethite has been reported but high temperature was used to facilitate this process (*195*). The resulting phase showed limited remobilization during reoxidation by oxygen, Several recent studies have shown incorporation of radionuclides such as U and Tc into the mineral structure during recrystallization from ferrihydrite to more crystalline goethite or magnetite shown in **Figure 1.3**, suggesting incorporation might occur under relevant subsurface conditions (*196-198*).

1.5. Reductive Degradation of Organic Contaminants by Reducing Iron Minerals

Despite the continual emergence of new organic contaminants of concern, common organic contaminants in groundwater, such as chlorinated aliphatic hydrocarbons (CAHs) and nitroaromatic compounds (NACs) are still of the top priority for mitigation due to their wide occurrance and large quantity in subsurface environment. NACs are commonly found in environment as residues from munitions, insecticides, and various other industrial processes, whereas CAHs are widely used as degreasers, cleaning solutions and other industrial processes. With increasing interests in applying ISCR for treating contaminated groundwater over the last two decades, the reduction of different subsets of these two groups of contaminants by a range of reducing iron minerals has been extensively investigated. This section mainly focused on the CAHs due to their environmental persistence as DNAPL (dense non-aqueous phase liquid) in subsurface.

1.5.1. Zerovalent iron

In early 90s, a series of laboratory and field studies reported successful abiotic reduction of CAHs, including both alkanes and alkenes, by ZVI (*17-19*). This finding changed the whole paradigm for remediation of these persistent organic contaminants in subsurface, which was initially thought to be only carried out by microbial reduction (*199*). Driven by the benefits that iron is non-toxic and relatively cheap to apply in large quantity, numerous laboratory and field tests were conducted, aiming to develop and optimize ZVI based remedial technologies for in-situ cleanup of CAHs. Much of this research has been mainly focused on reduction mechanisms, performance enhancement, and performance evaluation.

Reduction Mechanism

The mechanistic aspect of abiotic reduction of CAHs by ZVI has been investigated extensively by analysis of product distributions (*200, 201*), kinetics (*19, 122, 202*), linear free energy relationships (LFERs) (*122, 200, 201, 203*), and more recently, compound specific isotope analysis (*204*). The detailed reaction pathways are complex and vary depending on specific compounds and solution conditions, so only the general conclusions are summarized here. In general, hydrogenolysis and β-elimination represent the major abiotic reduction pathways for chlorinated alkanes and alkenes. Both reaction pathways involve a net gain of two electrons from ZVI to contaminant, resulting in replacement of carbon-bonded chlorine atoms with hydrogen atoms (for hydrogenolysis), or release of two chlorines from adjacent carbons and formation of new C–C bond (for β-elimination). For chlorinated methanes, hydrogenolysis usually is the dominant reduction pathway, which leads to sequentially less chlorinated products (e.g., $CCl_4 \rightarrow CHCl_3 \rightarrow CHCl_2 \rightarrow CH_3Cl$), with each reduction step being less favorable than the ones before. For chlorinated ethanes or ethenes, β-elimination is more important than hydrogenolysis, which leads to fully dechlorinated products (e.g., acetylene, ethene, and ethane) without formation of partially dechlorinated intermediates (e.g., *cis*-DCE, VC) (*202*, *205*). Because partially dechlorinated ethenes are more toxic and persistent than the parent compounds in environment, abiotic reduction by ZVI can be more effective than bioremediation, which tends to favor stepwise hydrogenolysis.

Correlation analysis—including the identification and interpretation of LFERs—is another frequently used approach for investigation of dechlorination mechanisms. The method involves correlating response variables (e.g., measured reduction rate constants normalized by surface area for different compounds) with descriptor variables (e.g., one-electron reduction potentials for these compounds or other molecular descriptors) with a linear relationship (*203*). In early work (*201*), it was reported that the LFER obtained with two-electron reduction potentials of chlorinated ethenes was significantly better than when the one-electron reduction potential was the descriptor variable, which could be the evidence that two-electron dechlorination is dominant for reduction by zerovalent metals. However, these correlations did not show statistically difference between two-electron reduction potential of β-elimination and hydrogenolysis. In a subsequent study using a more complete kinetic dataset (*122*), a more complex non-linear pattern was found. It was suggested that using E_{LUMO} (lowest unoccupied molecular orbital) as the descriptor variable provides better correlation with the kinetic rate constants because it is independent of competing dechlorination pathways (*203*). When applied cautiously, this correlation can be used to estimate the reduction rates for new compounds or compounds whose reduction is too slow to be reliably measured in laboratory (*203*), which has significant implications in predicting the recalcitrance of certain contaminants to dechloriantion by ZVI.

Performance Enhancement

Apart from performance optimization through improved understanding of the fundamental processes, significant efforts have been devoted to enhancement of CAH degradation by ZVI in order to alleviate various limitations to the technology. The enhancement strategies that have received the most attention fall into two categories: material optimization and external amendments.

The most prominent example of ZVI enhancement by material optimization is the emergence and development of nZVI, which becomes a popular research area after the first report of applying laboratory synthesized nZVI for TCE and PCB reduction in 1997 (*36*). The high apparent reactivity of nZVI has been demonstrated in numerous studies of CAH reduction (*79, 206, 207*), which is mainly due to the small particle size and high surface area. Many studies have been focused on development of synthesis protocols that produce nZVI with enhanced reactivity. For example, as an extension of the early work showing improved reactivity of ZVI doped with palladium or other noble metals (*208, 209*), various noble metals have also been added to nZVI (*33, 210*). The resulting bimetallic variations nZVI often give remarkable improvement in reduction kinetics of

CAHs and even some organic contaminants that are not very reactive with bare nZVI, such as polychlorinated dioxins (*211*) and polychlorinated biphenyls (*212*). Metals with more positive reduction potentials, such as Pd, showed greater enhancement in CAH reduction rates than metals with low reduction potentials, such as Cu. This pattern might be explained by galvanic corrosion. The greater the potential difference is between iron and metal, the more favorable the corrosion reaction is. Another example of optimizing performance with modified synthesis protocols is the production of Fe/FeS composite nanoparticle using conventional borohydride reduction process but with addition of dithionite during the synthesis. The resulted material was shown to reduce TCE at faster rates than nZVI synthesized in the absence of dithionite (*129, 213, 214*).

External amendments are modifications to the medium, or system, that are improve remediation performance without changing the intrinsic properties of (n)ZVI. To date, a few promising approaches have been reported, including adding aqueous phase activators, such as Fe(II) or electron-transfer mediators, or supplying external energy, such as ultrasound, low electric current or weak magnetic field (WMF) (reviewed by Guan et al.(*215*)). Although operationally different, the main effect of all these amendments is to counter the passivation effects due to ZVI aging—a common process known to inhibit ZVI reactivity in laboratory and field applications—thereby facilitating electron transfer from Fe(0) to contaminants. For example, the addition of Fe(II) or other divalent cations to aged ZVI completely restored the reactivity of aged ZVI to reduce TCE, and this effect was attributed to enhanced ZVI corrosion induced by locally high proton concentration that results from proton displacement by cation sorption onto surface iron oxides (*216, 217*). Another external modification that enhances contaminant removal rates by ZVI involves the additions of a WMF. These treatments also enhance corrosion rates, as evidenced by increasing amount of Fe(II) produced in the presence of WMF (*218-220*). The WMF effect has not yet been demonstrated with CAHs, but the some aspects of the proposed mechanism of the WMF effect should apply in all ZVI systems.

Performance Evaluation

Given the numerous sources, formulations, and preparation/modification protocols for (n)ZVI that have been investigated to date, it is imperative to have reliable metrics that researchers and practitioners can use to compare and evaluate these materials. From the reactivity perspective, surface area normalized reduction rate constants (k_{SA}) is the most widely used metric, which is calculated by dividing the first-order observed reduction rate constant (k_{obs} h^{-1}) obtained in batch or column experiments with surface area loading (m^2 L^{-1}). Comparisons based on k_{SA} are more representative of the "intrinsic" reactivity because k_{obs} varies linearly with surface area, although other factors can complicate this relationship. For example, when the kinetics for TCE reduction by two most common types of nZVI (RNIP and Fe^{BH}) were compared, it was found that Fe^{BH} gave a ~4 fold higher k_{SA} than RNIP. Surprisingly, the k_{SA} value of RNIP was very similar to those obtained for conventional, micro-sized iron fillings, suggesting there was no difference in the intrinsic reactivity between RNIP and granular iron. The modest reactivity of RNIP was attributed to the dense magnetite surface layer that comprised the passive film on this material. A more systematic approach to such comparison is provided by the meta analysis of the kinetic rate constants, shown in **Figure 1.7**. By plotting the rate constant normalized by surface area (k_{SA}) against the rate constant normalized by mass (k_M) (**Figure 1.7**), experimental and literature data can be evaluated for trends, patterns, or clusters, even in the presence of substantial experimental variability (*221*). **Figure 1.7** shows a version of the k_{SA} vs. k_M plot for carbon tetrachloride reduced by three types of ZVI. It can be easily seen that (*i*) the data cluster into three groups, (*ii*) low purity Fe(0) is the least reactive, and (*iii*) nano Fe (0) is not necessarily more reactive than micro Fe (0) on a surface area normalized basis (because the two have similar ranges of k_{SA}).

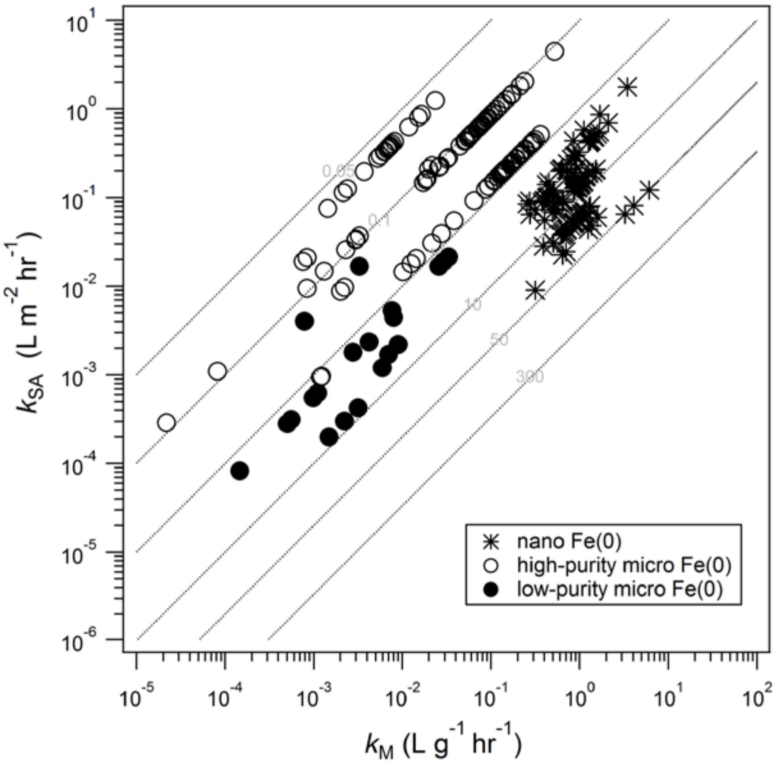

Figure 1.7. Surface area normalized reduction rate constant (k_{SA}) vs. mass normalized reduction rate constant (k_M) plot for carbon tetrachloride reduction by three types of ZVI (reprinted with permission from Tratnyek, P.G., A.J. Salter, J.T. Nurmi, and V. Sarathy, Environmental applications of zerovalent metals: Iron vs. zinc, in *Nanoscale Materials in Chemistry: Environmental Applications*, L.E. Erickson, R.T. Koodali, and R.M. Richards, Editors. 2010, American Chemical Society. p. 165-178.Copyright (2011) American Chemical Society.).

1.5.2. Divalent Iron

The role of divalent iron minerals in reducing chlorinated aliphatics has long been recognized. Many studies showed that sorbed Fe(II) and other DVI minerals can reduce carbon tetrachloride and other halogenated methanes and ethanes.(*45, 120, 222-225*) For Fe(II) sorbed onto goethite, Based on the kinetic modeling, a termolecule two-electron transfer step from two sorbed Fe(II) to one CCl_4 was proposed as the rate limiting step in carbon tetrachloride reduction by Fe(II) sorbed onto goethite (*222*). More recent work, however, by compound specific isotope analysis (CSIA) (*226*) showed that the initial one-electron transfer to form CCl_3• is rate limiting for CCl_4 reduction. A follow-up CSIA study by Zwank et al. on CCl_4 reduction by other types of DVI minerals extended that work to show that CCl_4 reduction by all iron (hydr)oxide minerals appears to have similar isotopic fractionation, suggesting similar reaction mechanisms (whereas reduction by FeS showed a complete different isotopic signature).

By contrast, the reduction of chlorinated ethenes by DVI minerals is less thoroughly studied, in part due to slow reaction (e.g., less than 10% reduction over the course of 6−12 months (*227*)), which makes laboratory measurements difficult. This can be expected as chlorinated ethenes are thermodynamically more difficult to reduce than methanes (**Figure 1.5)**. Despite the slow rates of reduction, dechlorination of chlorinated ethenes by a range of pure synthetic iron mineral phases have been reported, including green rusts, pyrite, mackinawite, and magnetite (*228-232*). Based on the values of k_{SA}, the reactivity of different minerals appear to be ordered by mackinawite > green rust > pyrite > magnetite. The reduction rates were too slow to be measured for Fe(II) sorbed onto iron oxyhydroxide in batch reactor (*227*). However, significant TCE reduction by Fe(II) associated with iron minerals was observed in dithionite treated aquifer materials in column experiments (*12*). In this case, the observed reduction products are mainly acetylene and ethene, suggesting that β-elimination is the dominant reduction mechanism. Several more recent laboratory studies also showed reduction of *cis*-DCE by in-situ precipitation of metastable iron phases, which are formed by mixing Fe(II), S(II), chloride or sulfate at pH 7.8 (*233-235*). According to the speciation modeling, the primary iron phases formed in those studies were green rusts (*235*).

The properties of DVI minerals that control the reactivity have not been well understood, but several important factors are suggested. For sorbed Fe(II), the density of sorbed Fe(II) has been suggested to be the primary determinant, but this conclusion is complicated by the observation that the absence of aqueous Fe(II) appeared to completely inhibit the reduction (*105*). To date, a universal descriptor for all DVI minerals has not been identified. In **Chapter 4**, we showed that the reduction potentials of minerals determined by chemical redox probes (CRPs) qualitatively correlate with the published reduction rate constants for three classes of contaminants by different DVI minerals, suggesting reduction potentials of DVI minerals determined by the CRP method might be an important parameter to evaluate their reactivity to reduce contaminants. This prospect is supported by several prior studies where mineral reduction potentials and contaminant reduction rates are found to be correlated (*47*, *236*). These correlations have potential implication to be used for assessing abiotic reduction of chlorinated ethenes, which is otherwise very difficult to assess due to slow reactions.

Field evidence of reduction of chlorinated ethenes by DVI minerals was first reported in several long-term ZVI based PRB studies where sustained reactivity to reduce TCE or PCE was observed even after extended operation (*21, 68*). Green rusts and iron sulfides are identified as the major mineral phases in these PRBs. In several recent field case studies that applied BiRD (biogeochemical reductive dechlorination) as the main remedy, amorphous iron sulfides are found to be the primary reactive phases to reduce TCE and PCE (*108, 110*). However, the roles of these mineral phases in long-term natural attenuation processes are likely to be more difficult to evaluate because of less availability of reactive minerals and consequently slower reactions. A three-year microcosom study on abiotic dechlorination of *cis*-DCE by contaminated aquifer materials showed substantial reduction (*155*) that was attributed to natural magnetite phase in aquifer materials. A role of DVI minerals in abiotic NA has also been suggested for low permeability rock matrices based on the relation between reduction rates and the amount of ferrous iron in rocks by two recent studies (*152, 153*).

Additional difficulty to evaluate abiotic natural attenuation in field could arise from interference of parallel biotic dechlorination, long being considered as the major component of natural attenuation process (*205*). In these cases, patterns of product formation have been interpreted as evidence for abiotic as opposed to biotic reduction (*154*). For example, the absence of partially dechlorinated intermediates or the presence of acetylene and ethene can be evident for abiotic reduction because the products are mainly produced by β-elimination, which is the dominant pathway for abiotic reduction with DVI. In addition, the concentrations of highly chlorinated ethenes (e.g., PCE or TCE) and daughter products (e.g., *cis*-DCE or VC) tend to decrease at similar rates with distance for abiotic reduction, whereas for biotic reduction, sequential appearance and disappearance of the parent and daughter products are usually observed (*154*, *205*). It should be noted that while abiotic dechlorinations of chlorinated ethenes are slow reactions, the DVI minerals may be regenerated in situ via biogeochemical processes (**Section 1.3**), thereby providing long exposure times to reducing minerals. might suggest their non-trivial roles in the time frame that MNA mostly concerns (e.g., decades or more). Many studies have demonstrated active mineral transformations, but the effects of these processes on abiotic NA, however, have not been fully investigated.

1.6. Effects of Common Environmental Factors on Reactivity of Reducing Iron Minerals

1.6.1. pH

The reactivity of reducing iron minerals is significantly affected by pH. For (n)ZVI, substantial decrease in contaminant reduction rates as pH increases from acidic to basic range has been consistently observed for various inorganic and organic contaminants by numerous studies (*78*, *237*). This is primarily attributed to enhanced Fe(0) corrosion corrosion at low pH and less favorability to form surface passivation layers that inhibit ZVI reactivity. However, aging of ZVI in water naturally produces hydroxide ion that increases aqueous pH. As a result, secondary mineral phases tend to accumulate on ZVI surface over time. In laboratory, decreasing reactivity of nZVI with increasing aging time has been observed due to increasing thickness of Fe_3O_4 layer (*78, 79*). In ZVI-based PRB, high pH can additionally favor precipitates, such as $CaCO_3$, causing PRB cement and loss of permeability.

By contrast, DVI minerals, on the other hand, generally become more reactive with increasing pH. Despite the diversity of DVI minerals, this trend appears to be consistent for all DVI minerals, including sorbed Fe(II), green rust, magnetite, and FeS. For sorbed Fe(II), this pattern has been attributed to increasing the amount of sorbed Fe(II) with increasing pH, which is evidenced by decrease in measured concentrations of dissolved Fe(II). For other divalent minerals, the effect of pH can be attributed to increasing abundance of deprotonated surface Fe(II), which is more reactive than protonated Fe(II) (*238, 239*).

1.6.2. Natural Organic Matter (NOM)

NOM consists of highly complex macromolecules, some of which are redox active due (mainly) to polyphenolic and quinone-like moieties. Apart from being reductants that can generate ferrous iron from iron oxyhydroxide (*240*), NOM can also serve as an electron shuttle by mediating electron transfer between reductants and contaminants. Functional analogues of NOM, such as AQDS, lawsone, and juglone, have been shown to be able to shuttle electrons between the bulk reductants, such as cysteine, sulfide or ZVI, and contaminants, thereby accelerating the contaminant reduction rates (*241-247*).

With (n)ZVI, however, the effect of NOM is generally found to be inhibitory to the removal of both organic contaminants (*38, 247, 248*) and inorganic contaminants (*249, 250*). This inhibition has been attributed to the adsorption of NOM onto the reductant surface. Because the majority of the contaminant reductions by reducing iron minerals are surface mediated, NOM adsorption to redox-active surface may be a general mechanism of inhibiting contaminant reduction by minerals. Interestingly, the opposite effects of NOM on ZVI reactivity have been observed under oxic conditions, where NOMs shuttle electrons from ZVI to oxygen, enhance the production H_2O_2 and Fe^{2+}, and accelerate contaminant degradation by Fenton reaction (*251*). This may arise because the reaction between ZVI and oxygen is not limited by surface sites, and therefore is not affected by NOM adsorption. Although processes that require aerobic conditions are outside the scope of this work, this finding demonstrates the capability of NOM, as a whole complex molecule, in mediating electron transfer in ZVI system.

For ZVI, the inhibitory effects by NOM also apply to non-specific reactions with other environmental oxidants. From this perspective, NOM might be beneficial, especially with nZVI, in that it preserves the reduction capacity of (n)ZVI to reduce contaminants in the long term by limiting fast side reactions with other receptors such as water. This effect is supported by several laboratory studies showing that exposure of nZVI to NOM preserved the total Fe(0) content in water over time (*38*).

Small organic biomolecules secreted by microorganisms have also been shown to enhance reduction rates of organic contaminants by various reducing iron minerals. For example, riboflavin was shown to accelerate carbon tetrachloride reduction by nZVI (*252*). By adding Cobalamin (III) to nanocrystalline FeS, the reduction rate of PCE was enhanced by 145 times (*253*). The roles of these small biomolecules as electron mediators to shuttle electron transfer between contaminant and reductant are expected as many of them have redox active structures such as quinone-like moieties or complexed metal centers.

1.6.3. Groundwater Solutes

The complexity of groundwater chemistry can significantly alter the reactivity of reducing iron minerals. This issue has been investigated extensively for ZVI (*206, 254, 255*). For example, chloride is a well-known corrosion promoter and it increases the reduction rates of a variety of contaminants by ZVI (*256*, *257*). In contrast, other anions are inhibitory. Several well-known inhibitors include nitrate (*55*), silicate (*258, 259*), and phosphate (*260*). Nitrate oxidizes ZVI to form iron oxides, iron oxyhydroxides as passivation layers, which prevents the electron transfer from Fe(0) to contaminants. The latter two anions adsorb or precipitate onto the ZVI surface, hindering electron transfer as well (*258*). Cations such as calcium, magnesium can form precipitates with carbonate at high pHs, which have been frequently caused passivation layers in ZVI based PRB (*261*).

For DVI minerals, research on the effects of groundwater solutes has mainly focused on the stability rather than the reactivity of these minerals, although high ionic strength has been shown to decrease CT reduction rates by nano-magnetite due to induced particle aggregation (*120*). Anions including sulfate, chloride, and carbonate can participate in the formation of green rust. Also, the presence of phosphate and silicate has been shown to stabilize metastable green rusts against transformation to magnetite, but these effects on reactivity with contaminants remain unknown. Effects of transition metal cations on reactivity of DVI minerals to reduce CAHs have been investigated for green rust and iron sulfide (*262-264*). Significant enhancements in reduction rates have been reported, which are attributed to the reduction of transition metal cations to their elemental states or formation of highly reactive metal sulfide precipitates. In any case, the results indicate positive effects of these likely co-contaminants on reduction of chlorinated compounds by natural reducing minerals.

1.7. Summary and Research Needs

The utility of reducing iron minerals for contaminant reduction and sequestration is the central component of ISCR. The knowledge gained from prior studies on a wide range of subjects ranging from fundamental iron biogeochemistry to contaminant degradation by reducing iron minerals has made significant contributions towards understanding the biogeochemical basis of ISCR processes. Over the last twenty years, the family of remediation strategies now known as ISCR has evolved from ZVI based technologies only to a much broader range that includes both ZVI and DVI, which allows more successful integration of ISCR into a wider range of remedies. Nonetheless, research is still needed in order to understand and quantify the roles of ISCR in contaminant attenuation in complex subsurface environment. This will require more fundamental biogeochemical investigations in simple laboratory system, but also the development of conceptual and physical models that can parameterize the fundamental biogeochemical processes into more complex field scenarios.

1.8. Overview of the Dissertation

This dissertation is composed of two major parts, with each part including two chapters. **Part I** presents the development of a remediation strategy that shifts the sequestration pathway of mobile TcO_4^-, a common radionuclide contaminant, from TcO_2 to TcS_2, which is more resistant to reoxidation and therefore offers a more sustainable approach to remediation of Tc-contaminated groundwater. The central premise of this work, as discussed in **Section 1.3.1**, is that application of nZVI in subsurface stimulates biological sulfate reduction, which generates amorphous FeS to reduce Tc to Tc sulfide. Specifically, **Chapter 2** investigates the effects of sulfidation on nZVI properties, the kinetics of Tc reduction by sulfidated nZVI, and the resulting product formation. **Chapter 3** further examines the stability of the Tc sulfide phases formed upon reoxidation. The reoxidation kinetics were compared with solid phase characterizations to provide a mechanistic understanding of the factors that control the oxidation of Tc sulfides. Collectively, these two chapters describe the fundamental biogeochemical basis for remediating Tc contaminated groundwater under sulfidic conditions stimulated by (n)ZVI.

Part II focuses on characterization of the redox properties of reducing iron minerals by using chemical redox probes (CRPs). **Chapter 4** explores the correlations between the mineral reduction properties and contaminant degradation rates, such as TCE. The goal is to estimate the rates of the slow reduction of chlorinated ethenes by reactive minerals based on CRPs that react at faster rates, and therefore provide a more convenient screening tool to assess the potential of natural attenuation processes for chlorinated ethenes. **Chapter 5**, which builds on the work described in **Chapter 4**, develops a novel approach that can diagnostically quantify the Fe(0) content in groundwater samples impacted by nZVI injection by using indigo disulfonate (I2S) as the CRP. This work provides a field-deployable protocol that can definitively quantify Fe(0) content in field samples, which is a significant improvement over methods currently used to characterize the transport (and fate) of nZVI in the field (such as colorimetric methods for total iron and electrode measurements of ORP).

PART I. Remediation of Technetium by Sulfidated Nano Zerovalent Iron

CHAPTER 2. Reductive Sequestration of Pertechnetate ($^{99}TcO_4^-$) by Nano Zero-Valent Iron (nZVI) Transformed by Abiotic Sulfide

CHAPTER 3. Oxidative Remobilization of Technetium Sequestered by Sulfide-Transformed Nano Zerovalent Iron

Chapter 2 Reductive Sequestration of Pertechnetate ($^{99}TcO_4^-$) by Nano Zero-Valent Iron (nZVI) Transformed by Abiotic Sulfide[1]

Dimin Fan, Roberto P. Anitori, Bradley M. Tebo, Paul G. Tratnyek, Juan S. Lezama Pacheco, Ravi K. Kukkadapu, Mark H. Engelhard, Mark E. Bowden, Libor Kovarik, Bruce W. Arey

2.1. Abstract

Under anoxic conditions, soluble $^{99}TcO_4^-$ can be reduced to less soluble $TcO_2{\bullet}nH_2O$, but the oxide is highly susceptible to reoxidation. Here we investigate an alternative strategy for remediation of Tc-contaminated groundwater whereby sequestration as Tc sulfide is favored by sulfidic conditions stimulated by nano zero-valent iron (nZVI). nZVI was pre-exposed to increasing concentrations of sulfide in simulated Hanford groundwater for 24 h to mimic the onset of aquifer biotic sulfate reduction. Solid-phase characterizations of the sulfidated nZVI confirmed the formation of nanocrystalline FeS phases, but higher S/Fe ratios (> 0.112) did not result in the formation of significantly more FeS. The kinetics of Tc sequestration by these materials showed faster Tc removal rates with increasing S/Fe between S/Fe = 0–0.056, but decreasing Tc removal rates with S/Fe > 0.224. The more favorable Tc removal kinetics

---

[1] Reprint with permission from Fan, D.; Anitori, R. P.; Tebo, B. M.; Tratnyek, P. G.; Lezama Pacheco, J. S.; Kukkadapu, R. K.; Engelhard, M. H.; Bowden, M. E.; Kovarik, L.; Arey, B. W. Reductive sequestration of pertechnetate ($^{99}TcO_4^-$) by nano zerovalent iron (nZVI) transformed by abiotic sulfide, *Environ. Sci. Technol.* **2013**, *47*, 5302-5310. Copyright 2011 American Chemical Society.

at low S/Fe could be due to a higher affinity of TcO_4^- for FeS than iron oxides, and electron microscopy confirmed that the majority of the Tc was associated with FeS phases. The inhibition of Tc removal at high S/Fe appears to have been caused by excess HS^-. X-ray absorption spectroscopy revealed that as S/Fe increased, the pathway for Tc(IV) formation shifted from $TcO_2 \bullet nH_2O$ to TcS_2. The most substantial change of Tc speciation occurred at low S/Fe, coinciding with therapid increase in Tc removal rate. This agreement further confirms the importance of FeS in Tc sequestration.

2.2. Introduction

Technetium 99 (^{99}Tc) is a weak β-emitting isotope, mainly generated from nuclear fission processes of uranium-235 and plutonium-239. Its long half-life (2.13×10^5 years) and high mobility in oxic subsurface environments (as the pertechnetate anion, $Tc^{VII}O_4^-$) make it a high priority among radionuclides that require control and remediation at U.S. Department of Energy sites. Under anoxic conditions and in the absence of strong complexing ligands, such as carbonate and humic substances (*265*, *266*), aqueous TcO_4^- is readily reduced to the much less soluble $Tc^{IV}O_2 \bullet nH_2O$. This reduction can occur by various abiotic and biotic processes (reviewed by Icenhower et al. (*177*) and O'Loughlin et al. (*267*)). To date, most research has focused on using biogenic or abiogenic reactive Fe(II) species (aqueous, sorbed, or structural) as the reductant (*101, 102, 268, 269*). The rationale for this focus is partly because of the natural abundance of iron oxides, and—in particular—the concurrency of Tc reduction and iron reduction observed under natural redox gradients (*270*). However, the long-term stability of Tc phases sequestered under iron reducing conditions is uncertain due to the susceptibility of $TcO_2 \bullet nH_2O$ to reoxidation by oxygen (or nitrate) and subsequent release of TcO_4^- back into the aqueous phase (*191*). Although several studies have reported that the association of Tc with iron oxide minerals by chemical adsorption (*101*) or structural incorporation (*195*) can significantly lower the rate of Tc^{IV} oxidation, the adequacy of these mechanisms for long-term stabilization of Tc in natural sediments is unproven, especially where it is likely to be limited due to heterogeneity of the sediments and other factors.

An alternative strategy to mitigate Tc reoxidation is to sequester Tc in a sulfide-rich environment that will favor the formation of Tc sulfide phases. Laboratory studies have demonstrated that Tc can be immobilized by Na_2S under simulated field conditions of nuclear waste tank repositories (high pH and ionic strength) (*271-273*). The resulting solid was characterized as Tc_2S_7, which was proposed to have a Tc^{IV} oxidation state, even though the stoichiometry appears to suggest Tc^{VII}. More recently, based on rigorous EXAFS fitting, Lukens et al. (*272*) suggested that the solid is more accurately characterized asTc_3S_{10}. Synthetic mackinawite (FeS) can also sequester Tc via reduction and coprecipitation, forming phases of which the composition is still uncertain (*274-276*). Although complete understanding of these Tc/S phases is yet to be achieved, preliminary evidence from several studies suggested that Tc sequestered under sulfidic conditions is more recalcitrant to oxidation (*40, 272, 276*).

Sulfidic conditions in a subsurface environment can be created by either direct injection of H_2S or HS^- or stimulated *in-situ* by microbial sulfate reduction. Injection of H_2S gas has been successfully used to treat Cr(VI)-contaminated sediment (*277*), but its effectiveness for sequestering Tc at groundwater pHs is low (*271, 273*). Stimulating *in-situ* sulfidogenesis is potentially a more environmentally benign (sustainable) approach to this treatement. However, the formation of Tc sulfides along natural redox gradients may be limited by prior (up-gradient or earlier) Tc reduction to $TcO_2 \bullet nH_2O$ under iron reducing conditions. This may also explain why no evidence has been reported for Tc sulfides in naturally-developed sulfate reducing sediments (*270, 278*). Maximizing the potential for Tc sulfide formation requires a strong reducing agent to rapidly establish sulfidic conditions and thereby minimize the interference from iron reduction.

Emplacing (nano) zero-valent iron (nZVI) in the presence of sufficient quantities of SO_4^{2-} into the subsurface is a promising approach for achieving these conditions because (*i*) (n)ZVI will abiotically scavenge alternative electron acceptors (e.g., O_2 and NO_3^-) but not SO_4^{2-}, and (*ii*) the H_2 generated by Fe^0 dissolution provides an electron donor that is readily utilized by many sulfate reducers (*66*, *67*). These collateral microbiological effects of (n)ZVI have frequently been documented in both laboratory experiments (*51, 68, 70, 71, 279*) and pilot- to field-scale applications (i.e., permeable reactive barriers (PRB)) (*21, 65, 69*). During microbial sulfate reduction, iron sulfides are also expected to form, and these may provide secondary phases—in addition to (n)ZVI—that react with Tc. The most extensively studied iron sulfide phase is nanocrystalline mackinawite (amorphous FeS), commonly considered to be the first iron sulfide phase formed in sulfidic environments (*74, 121, 280*). Mackinawite is highly reactive towards various heavy metals (*181, 281*), chlorinated solvents (*282*, *283*), and oxyanions (*176, 284*, *285*). Therefore, it is expected to play an important role in contaminant degradation/sequestration in sulfidic environments.

The objective of this study was to provide the fundamental geochemical understanding of Tc sequestration during the development of sulfidogenic conditions in the presence of nZVI. Abiotic sulfide was used to simulate biotic sulfate reduction. **Figure 2.1** presents a conceptual model of Tc sequestration pathways in three sequential scenarios: (*I*) the pre-sulfate reduction stage; (*II*) the initial stage of sulfate reduction, and (*III*) the end stage of sulfate reduction. We hypothesized that as sulfate reduction develops, the reactive phases (mineral or aqueous) that are responsible for Tc sequestration evolve, leading to different sequestration pathways and products. By combining wet chemical analysis with electron microscopy, synchrotron X-ray absorption spectroscopy, and other methods, we examined the change of host mineral phases during sulfidation, Tc sequestration kinetics under incremental S/Fe ratios, and further elucidated sequestration pathways, Tc distribution, phase compositions, and the local coordination environment of Tc within the final Tc-Fe-S solids.

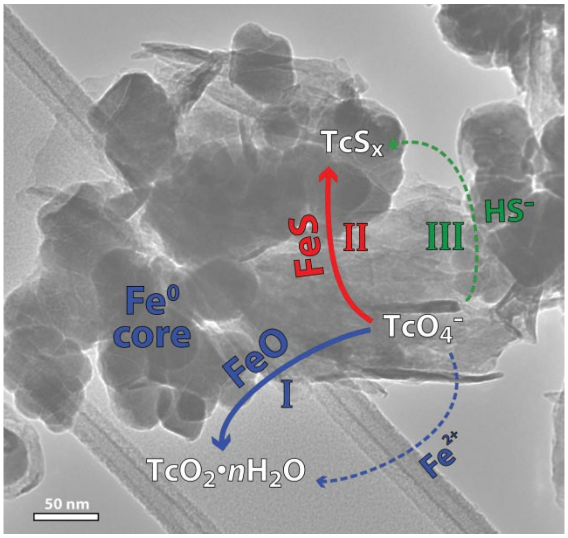

Figure 2.1. Conceptual model of Tc sequestration pathways under sulfidogenic conditions stimulated by nano zero-valent iron (nZVI). Processes (I), (II), and (III) represent the pre-, initial, and end stages of sulfate reduction, respectively (Solid arrows: reaction with mineral phases; Dashed arrows: reaction with aqueous species).

2.3. Experimental

2.3.1. Reagents

$FeCl_3 \bullet 6H_2O$, $NaBH_4$, Na_2S, and methanol were ACS grade. All reagents were used as received without further purification. ^{99}Tc was obtained as concentrated stock solution of ammonium pertechnetate (NH_4TcO_4) from Pacific Northwest National Laboratory. ^{99}Tc is a radioactive beta emitter (half-life 2.13×10^5 years; $E_{max} = 294$ keV) and was handled in a properly equipped radioactive laboratory.

2.3.2. Preparation of nZVI

Sulfur-free nZVI particles were synthesized using a modified version of the borohydride reduction method (*36*). Briefly, $FeCl_3 \bullet 6H_2O$ (2.43 g) was dissolved in 500 mL 7:3 (v/v) deionized deoxygenated (DI/DO) water/methanol. $NaBH_4$ (1.42 g) was dissolved in 40 mL DI/DO water and continuously introduced to the $FeCl_3$ solution via a 0.5 mm I.D. plastic tubing with a syringe pump (KD Scientific, Holliston, MA) at 2 mL min^{-1}, while the resulting suspension was vigorously mixed by a homogenizer (Kinematica, Bohemia, NY). After introducing $NaBH_4$, the solution was allowed to sit for 15 min for H_2 bubbles to dissipate. All of the above steps were carried out under an inert gas stream (N_2 or Ar). The suspension was then transferred to an anaerobic chamber (95% N_2/5% H_2). Solid nZVI particles were recovered by flash drying, as previously described (*286*).

2.3.3. Sulfidation

Pre-equilibration between nZVI and sulfide was carried out in 120 mL glass serum bottles. All procedures below were carried out in the anaerobic chamber except otherwise mentioned, dry nZVI particles (0.02 g) were weighed into each bottle. The bottles were then filled with 20 mL deoxygenated Hanford synthetic groundwater (HS300) buffered at pH 7.9 by 30 mM HEPES (the detailed HS300 recipe is given in **Appendix A** in **Table A.1.**). The bottles were sonicated in a water bath for 5 min to disperse the nZVI particles. The volume of HS300 was then adjusted up to 100 mL (0.2 g L^{-1} nZVI). A 0.2 M sulfide stock solution was prepared by dissolving anhydrous Na_2S in deoxygenated HS300 and aliquoted to each bottle to achieve concentrations varying incrementally from 0 to 4 mM, thus providing S/Fe molar ratios ranging from 0 to 1.12. At high sulfide doses, 6 M HCl was added to titrate the pH back to 7.9. The bottles were then sealed with grommet septum stoppers (Bellco Glass, Vineland, NJ), taken out of the anaerobic chamber and placed in a shaker (150 rpm) at 27 ± 0.5 ºC for pre-equilibration, during which time the aqueous sulfide concentration (< 0.2 μm) was measured intermittently by the methylene blue colorimetric method (# 8131) using a Hach DR700 colorimeter (Hach, Loveland, CO).

2.3.4. Tc Reduction

After 1 day pre-equilibration, 10 mL of nZVI/sulfide suspension was withdrawn from the serum bottle and transferred to a 15 mL serum vial in the anaerobic chamber, TcO_4^- stock solution was then added to achieve a final concentration of 6 μM. The reactors were sealed by a 20 mm septum (SUN SRi, Rockwood, TN) and placed on an end-to-end rotator (20 rpm). Tc concentration in the aqueous phase (< 0.2 μm) was monitored periodically by liquid scintillation counting (Beckman, Brea, CA). In selected experiments, 0.02 μm filtration was used in order to separate the colloidal phase of Tc from the dissolved phase. Controls included reactors with HS300/Tc but no sulfide, and HS300/Tc with 4 mM sulfide.

2.3.5. Solid Characterization.

The bulk mineralogy of sulfidated nZVI was characterized by micro X-ray diffraction (µXRD) and Mössbauer spectroscopy. The near-surface composition of sulfidated nZVI during reaction with different amounts of sulfide was analyzed by X-ray photoelectron spectroscopy (XPS). In order to recover sufficient quantities of solids for these bulk analyses, 0.5 g L^{-1} nZVI and proportionally higher sulfide doses (to keep the S/Fe comparable with batch experiment) were used. The microscopic structure of the mineral phase was examined by scanning electron microscopy (SEM) and transmission electron microscopy (TEM) with energy dispersive X-ray spectroscopy (EDX). For SEM and TEM of Tc-containing samples, lower nZVI (0.2 g L^{-1} nZVI) and sulfide doses, but higher Tc concentrations (50 µM) were used in order to detect Tc by EDX. Details of these solid phase characterizations are given in **Appendix A**.

2.3.6. X-ray Absorption Spectroscopy

Tc K-edge XAS for Tc sequestered by nZVI (0.5 g L^{-1}) and increasing sulfide (0–10 mM) were collected in fluorescence mode at the Stanford Synchrotron Radiation Lightsource (SSRL) on beamline 4-1 and 11-2. EXAFS spectra were analyzed using SixPack, Athena, and Artemis interfaces to the IFEFFIT package (*287*). Backscattering phase and amplitude functions required for fitting of spectra were obtained from FEFF8 (*288*). Details of XAS are given in **Appendix A.**

2.4. Results and Discussion

2.4.1. Characterization of Pristine nZVI

The sulfur-free nZVI particles synthesized by borohydride reduction form chain-like structures, and individual particles have an average diameter of 30–60 nm with a well-defined core-shell structure (**Figure A.1A**), both of which are the typical features of nZVI produced by this method.(*20, 37, 289*) While the core is mainly composed of Fe^0, the 2–3 nm thick shell appears to be composed of amorphous Fe oxides—based on the XPS Fe 2p narrow region spectra (**Figure 2.3A**)—and boron, which is evident in the XPS wide survey scans (**Appendix A**, **Table A.2**) and presumably results from the incorporation of iron boride in the outer shell as byproducts during the synthesis (*290*). The XPS spectrum is also consistent with the spectrum previously reported for a similar type of nZVI (*37*). Mossbauer spectroscopic measurements further indicated that the shell is not composed mainly of magnetite (**Figure 2.2A**), as noted previously for nZVI synthesized by H_2 reduction (e.g., RNIP) (*37*). Both the μXRD and Mössbauer spectra of freshly-prepared nZVI suggest that the pristine nZVI is largely amorphous, which has not been reported in prior studies for similar types of nZVI. These differences and their possible explanations are summarized in Appendix A (**Table A.3**), but further investigation of this was outside the scope of this study. Finally, BET N_2-gas adsorption measurements showed that the material had a surface area of ~20 m^2 g^{-1}, which is within the typical range for this type of material (*20*, *291*).

2.4.2 Sulfidation of nZVI

At low S/Fe (≤ 0.112), aqueous sulfide was removed to below the detection limit within 5 min after sulfide addition (**Figure A.3**). However, at relatively high S/Fe (0.224

and 0.56), the kinetics of sulfide removal from solution exhibited two phases, with about half of the input sulfide removed rapidly followed by a gradual decrease over a much longer period (**Figure A.3**). The initial, fast stage likely corresponds to instantaneous sulfide adsorption onto the nZVI surface, forming a surface complex of Fe(II)–HS^- (*72*). A similar process has been postulated to be the initial step in mackinawite formation on iron oxides in natural sulfidic environments (*74, 280*). The later stage of sulfide removal reflects relatively slow formation of FeS precipitates. At S/Fe = 0.56, significant residual aqueous sulfide was detected even after 150 days of exposure, indicating incomplete transformation of nZVI to FeS.

The μXRD data shows that sulfidation at S/Fe = 0.112 resulted in the emergence of poorly crystalline mackinawite (**Appendix A**, **Figure A.2C**). The mackinawite diffraction pattern observed was slightly different from that observed for bulk crystalline mackinawite, with an expanded *c* parameter that is consistent with disordered or nanocrystalline materials described previously (*121, 292*). Mössbauer spectra further confirmed that the bulk phases were mainly composed of residual nZVI (amorphous Fe^0) and secondary mackinawite (**Figure 2.2**). However, fitting the Mössbauer spectra gave a negligible increase in the percentage of mackinawite when S/Fe increased ten-fold from 0.112 to 1.12 (**Figure 2.2**). Likewise, XPS wide survey scans showed the surface atomic ratio of sulfide leveling off at S/Fe ≥ 0.112 (**Table A.2**). This apparent inhibition of sulfide uptake is likely caused by a decrease in available Fe/FeO surface sites due to the formation of FeS. This is evidenced by the attenuation of broad Fe(II)–O peaks around 710 and 723 eV and evolution of sharp Fe(II)–S peaks around 706 and 719 eV when S/Fe increased from 0 to 0.112 in the XPS narrow region spectra of Fe 2p (**Figure 2.3A**). Note that the overlap of Fe(0) and Fe(II)–S peaks prevents quantifying these two species separately, but parallel S 2p spectra confirmed that the enhanced peaks were largely due to the formation of FeS (**Figure 2.3B**). Alternatively, particle aggregation—either originating with pristine nZVI or further induced by sulfidation—may also decrease the availability of surface sites to react with sulfide, and thereby possibly contribute to limiting sulfide uptake. This effect has been reported to significantly suppress sulfide uptake by aggregated Ag nanoparticles (NPs) relative to well-dispersed NPs.(*293*) TEMs of nZVI sulfidated at S/Fe = 0.112 revealed that FeS deposition onto the surfaces of nZVI appears to be highly non-uniform and there does not leave a well-defined Fe^0/FeS core-shell structure upon sulfidation. Instead, laminar FeS appears to grow out of the original nZVI particles, forming distinct phases that are closely associated with material retaining the original nZVI structure (**Appendix A**, **Figure A.1C**).

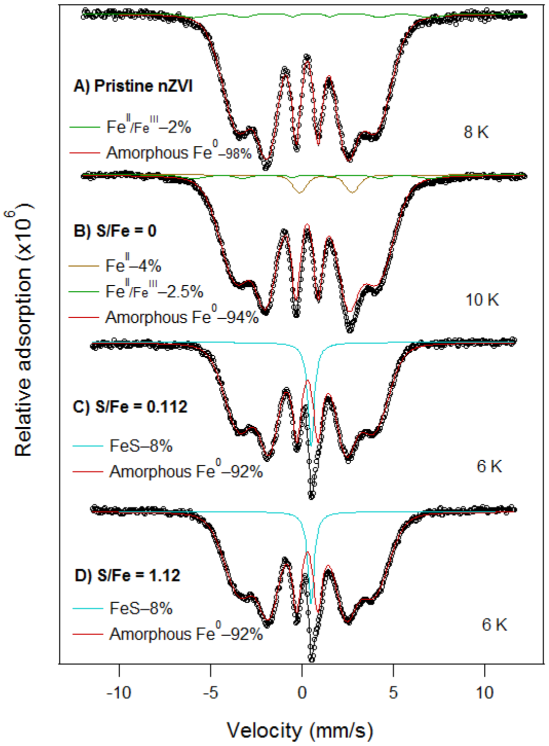

Figure 2.2. Experimental and modeled Mössbauer spectra of (**A**) pristine, (**B–D**) nZVI exposed to 0 mM, 1 mM, and 10 mM sulfide, in HS300 for 24 hrs. A small amount of Fe(II) noted in (**B**) is presumably due to oxidation in the simulant.

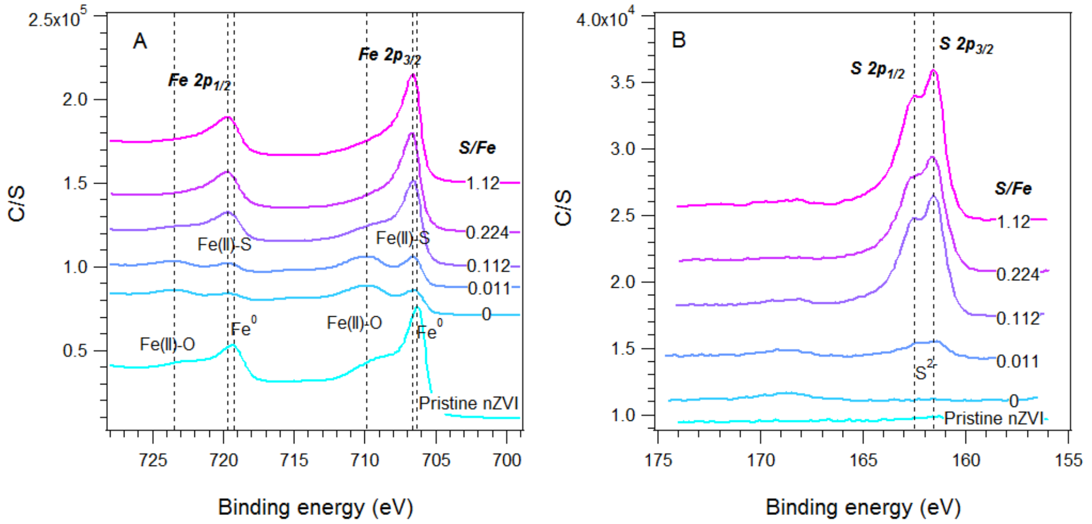

Figure 2.3. XPS (**A**) Fe 2p and (**B**) S 2p narrow region spectra of 0.5 g L^{-1} nZVI pre-exposed to increasing sulfide concentrations (0–10 mM) for one day in HS300 artificial groundwater (Fe peak assignments, represented by dashed lines, were based on literature values summarized by Mullet et al. (*73*) and Descostes et al. (*294*)).

2.4.3. Tc Sequestration Kinetics

Aqueous TcO_4^- was rapidly removed from solution at all values of S/Fe except 0 and 1.12 (**Figure 2.4A**). However, the kinetics of this reaction were not entirely pseudo first-order because of tailing that appears to approach a limiting value after ~1 hr. Therefore, the TcO_4^- removal rates were quantified using only the initial, linear portion of the concentration vs. time plots. **Figure 2.4B** shows the initial Tc immobilization rate (left axis) and residual sulfide concentration measured before Tc addition (right axis) vs. S/Fe in each experiment. As S/Fe increased from 0 to 0.045, the Tc disappearance rate increased. The reaction rate was too fast to be accurately determined from the data obtained at S/Fe = 0.056 and 0.224, but higher values of S/Fe resulted in decreased Tc removal rates. The high Tc removal rate observed at low S/Fe ratios can be explained by either enhanced nZVI corrosion due to sulfide facilitated corrosion (*141*) and/or increasing formation of reactive FeS. Both of these two mechanisms have been invoked to explain the enhanced reactivity of sulfidated ZVI with chlorinated solvents (e.g., carbon tetrachloride and trichloroethylene) (*24, 70, 282*). In the present study, however, the latter mechanism is considered more likely because mackinawite has been shown to be a highly reactive phase with a wide range of inorganic oxyanions, including TcO_4^-. This hypothesis is also backed by the correlation between enhanced Tc removal rate and the increasing amount of surface FeS observed by XPS (**Figure 2.3**) as S/Fe increased from 0 to 0.112. Further evidence for this interpretation is provided by the XAS data presented below.

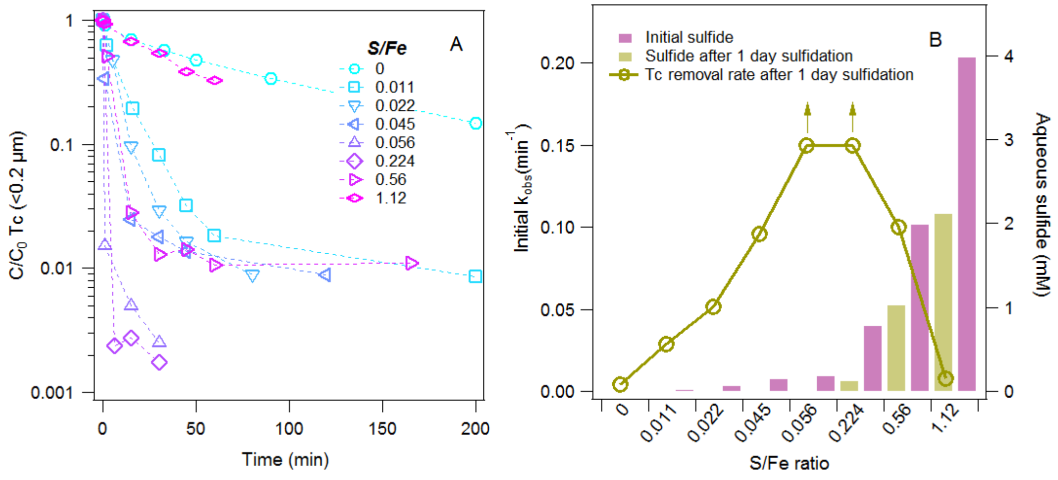

Figure 2.4. (**A**) Tc reduction kinetics at increasing S/Fe ratios after 1 day pre-exposure of nZVI to sulfide (n = 2); (**B**) Aqueous sulfide concentrations and initial Tc removal rate constants after 1 day pre-exposure of nZVI to various concentrations of sulfide (upward arrows represent lower limits because the reduction rate was too fast to be determined from the data).

At high S/Fe, the inhibition of Tc removal correlates well with the residual aqueous sulfide concentration. As S/Fe increased from 0.224 to 1.12, the reaction rate decreased significantly while the aqueous sulfide concentration increased from ~0.2 to ~2 mM (**Figure 2.4B**), indicating that the inhibition is likely caused by aqueous sulfide. To verify this, additional experiments were performed that showed removal of excess aqueous sulfide before Tc addition restored faster Tc removal (**Figure A.5**). Inhibition by sulfide has been previously observed for adsorption of molybdate onto pyrite (FeS_2) (*295*), which was interpreted as a result of sulfide competing for adsorption sites and/or the formation of Mo-S complexes. Direct interaction between TcO_4^- and aqueous sulfide has been reported to form Tc_2S_7 (or Tc_3S_{10}) solids at acidic or basic pHs (*271*, *273*). However, at neutral pHs that are similar to our experimental conditions, it was found that Tc removal—in a way that is consistent with our observations—was negligible (*271*, *273*).

We note that these studies quantified "aqueous Tc" by measuring Tc in either supernatant after centrifugation (*271*) or 0.45 μm filtrate (*273*), both of which may not be sufficient to differentiate truly dissolved TcO_4^- from colloidal Tc_2S_7 (*296*). To test this, we compared Tc concentration after 0.2 and 0.02 μm filtration when TcO_4^- was reacted with 0 and 4 mM sulfide (**Figure A.6**). In the absence of sulfide, Tc activity was kept unchanged in 0.2 μm filtrate and only slightly decreased in 0.02 μm filtrate after 96 hr reaction. By contrast, in the presence of 4 mM sulfide, Tc activity decreased by 15% in 0.2 μm filtrate and by 35 % in 0.02 μm filtrate, which indicates the formation and growth of Tc sulfide, most likely Tc_2S_7, colloids. However, it is worth noting that the time required to form significant quantities of colloidal Tc is considerably longer than the batch reaction time (**Figure A.6**). Therefore, the contributions of this reaction to the overall TcO_4^- removal, even at high S/Fe, might be limited, and the possibility that other factors contributed to the observed inhibition of Tc removal, such as sulfide competing for reaction sites, cannot be excluded.

2.4.4. Microscopy

The Tc distribution between the mineral phases was examined by TEM at S/Fe = 0.112. This ratio was chosen because *(i)* characterizations on sulfidated nZVI suggest that at S/Fe = 0.112, a significant amount of FeS is formed, but it is still much less abundant than residual nZVI phases (therefore, if FeS is indeed more important for Tc sequestration, as indicated by kinetic data, Tc should be partitioned preferentially to FeS, even though it is less abundant), and *(ii)* at S/Fe = 0.112, no excess aqueous sulfide was present (**Figure A.3**), and therefore interference by reaction between Tc and HS^- is minimized. **Figure 2.5A** shows the morphology of sulfidated nZVI after reacting with

TcO_4^-. Consistent with microscopy on sulfidated nZVI that was not reacted with Tc (**Figure A.1C**), two morphologically-distinct phases were present: aggregated particles that retain similar structure to pristine nZVI and a laminar phase that is most likely mackinawite. A third type of structure that was frequently encountered, but not observed in samples without Tc, was the hollow structures shown in **Figure A.8C**. Similar looking structures have been observed when Cu^0 NPs transform to sulfide-deficient Cu_xS NPs under bench-simulated sulfate reducing conditions (*297*). Dispersed copper sulfide NPs that are more sulfide-rich were also observed. The authors suggested that the hollow structures might be a result of direct transformation of the zero-valent metal NPs due to a counter-diffusion phenomenon known as nanoscale Kirkendall effect (*298*), whereas the dispersed NPs probably form by aqueous phase precipitation. Similar mechanisms might apply in the present study, given that the EDX spectra suggest that the laminar phase is more sulfide-rich than the hollow particles (data not shown). The absence of the hollow structures in the samples not exposed to Tc might be related to the lack of “aging” (Tc samples were kept in aqueous suspension for two months before being prepared for TEM, whereas samples without Tc were recovered as solid powder immediately after 1 day of sulfidation).

Despite the highly heterogeneous morphology formed upon nZVI sulfidation, Tc appears to be mainly associated with the FeS phase. **Figure 2.5B** shows the representative EDX spectra for nZVI-like and FeS phases. It can be seen that the FeS phase contains substantially more Tc than the nZVI-like phase. Although the level of Tc in the FeS phase was found to vary, up to 4% of Tc (atomic ratio) was detected in several locations. The preferential association of Tc with FeS further supports the hypothesis that

FeS formed during sulfidation is mainly responsible for the increasing trend in Tc removal rates observed at low S/Fe ratios.

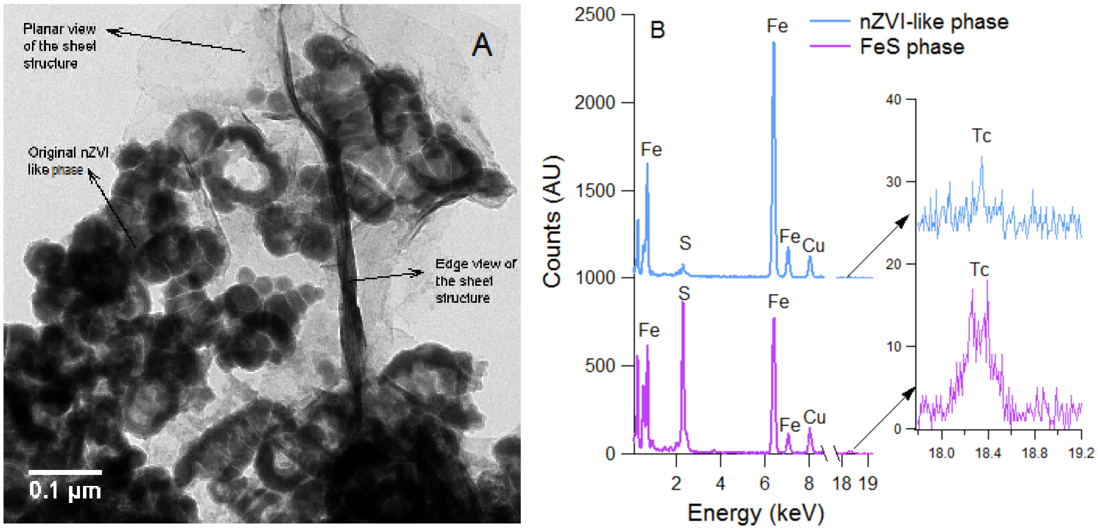

Figure 2.5. (**A**) Transmission electron micrograph of sulfidated nZVI exposed to TcO_4^-; (**B**) representative EDX spectra of Fe-rich and S-rich area with enlarged spectra showing Tc ([nZVI] = 0.2 g L^{-1}; [S^{2-}] = 0.4 mM).

2.4.5. X-ray Absorption Spectroscopy

To better characterize the state of the sequestered Tc, Tc K-edge XAS data were obtained on solids recovered for each S/Fe ratio. The XANES spectra did not show the diagnostic pre-edge peak of TcO_4^- in any of the samples, suggesting that TcO_4^- was absent. The Tc absorption edge decreased steeply from ca. 21.060 keV to ca. 21.054 keV as S/Fe increased from 0 to 0.056, but gradually leveled off above 0.056 (**Figure 2.6**). Given that the position of Tc K-edge absorption edge does not always correspond to the oxidation state of this element (*299, 300*), this two-phase trend most likely reflects changes in Tc speciation rather than its oxidation state. This interpretation is further supported by the EXAFS data in **Figure 2.6**, which shows a clear progression of Tc speciation from one pattern to the other with increasing S/Fe. The shell-by-shell EXAFS fit was further conducted for Tc reduced at S/Fe = 0 and 1.12, respectively, as two end-members (at S/Fe = 1.12, we only consider the speciation of Tc reacted with mineral phases because the contribution from colloidal Tc to the overall speciation of reduced Tc is small). The fitting results are summarized in **Table A.4**. In the absence of sulfide, Tc has an inner shell coordination with 6 O atoms at a distance of 2.02 Å, which agrees well with the structure of $Tc^{IV}O_2 \bullet nH_2O$. Different from previously reported EXAFS fit for Tc reduced by different nZVI under simulated waste conditions,(*301*) the best fit to our data was obtained with Tc (instead of Fe) as neighboring metal atoms in the 2nd shell. At S/Fe = 1.12, Tc is surrounded by 6 S atoms, 2 at 2.30 Å and the other 4 at 2.47 Å. The fit is similar to the crystallographic data for TcS_2 (*302*), although the S coordination number and distance are not entirely consistent. Compared with previous studies on Tc speciation after reacting with synthetic FeS, our finding generally agrees with the TcS_2-like phases reported by Wharton et al. (*276*) and not the $TcO_2 \bullet nH_2O$ reported by Liu et al. (*274*). The reason for the inconsistency requires further investigation, but likely involves the high concentration of TcO_4^- used by Liu et al. (150 μM) and differences in the surface properties of FeS.

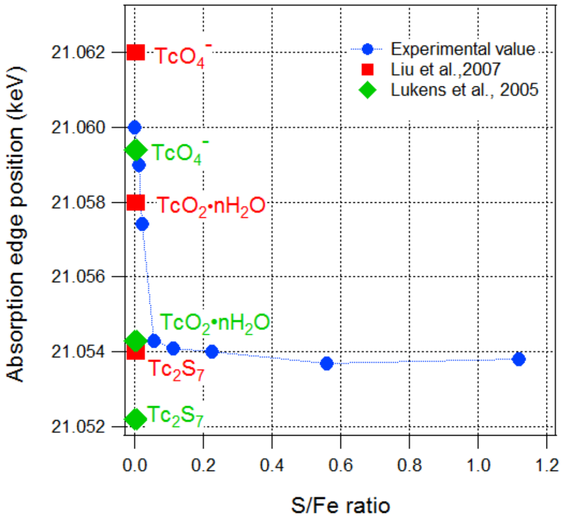

Figure 2.6. Tc K-edge adsorption edge position of Tc immobilized at incremental S/Fe ratios (blue solid dots) vs. the first inflection point of TcO_4^-, TcO_2, and Tc_2S_7 reported in previous studies(*271, 272*) (TcS_2 is not included because TcS_2 was reported only in Wharton et al.(*276*) and the value of its edge position (and the values of other comparable Tc compounds) is about 20 eV lower than values reported in other studies).

By taking the two spectra at S/Fe = 0 and 1.12 as principal components (or "end-members"), the relative proportions of $TcO_2•nH_2O$ to TcS_2 can be estimated by linear combination fitting (LCF) to the EXAFS spectra of different S/Fe ratios (**Figure 2.7**). **Figure 2.8** plots the LCF results at incremental S/Fe ratios. As S/Fe increased, the portion of the high S/Fe end-member (TcS_2) generally increased while the portion of low S/Fe end-member ($TcO_2•nH_2O$) decreased. At S/Fe = 0.011, about one third of the reduced Tc speciation can be accounted for by the TcS_2, despite only trace amounts of surface FeS detected by XPS (**Figure 2.3A**). Taken together, these data suggest that FeS has a higher affinity for TcO_4^- than do nZVI/Fe oxides. In light of this result, it is noteworthy that the most substantial change in Tc speciation (by EXAFS)—the steep drop in the Tc absorption edge (by XANES)—occurred concurrently with the rapid increase of initial Tc removal rates at low S/Fe ratios. The agreement between the XAS and kinetic data again supports the conclusion that the increasing Tc removal rate during the initial stage of sulfidation is due to the rapid shift of Tc sequestration pathway from reduction by nZVI to reduction by FeS (**Figure 2.1**). As sulfidation proceeds, surface FeS apparently becomes the dominant mineral phase for Tc sequestration because Tc EXAFS spectra from above S/Fe = 0.112 were nearly identical to the high S/Fe end-member.

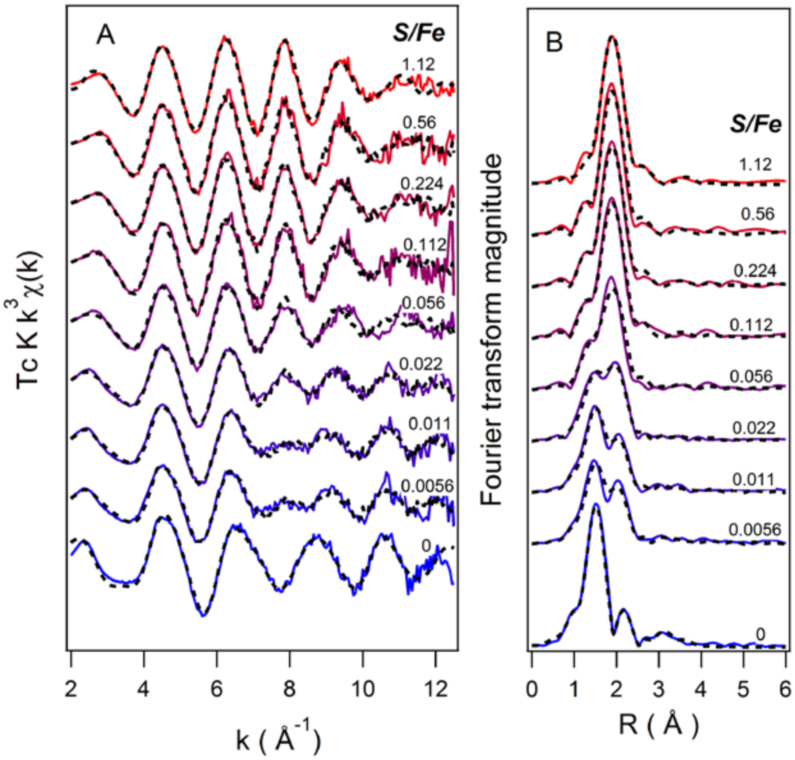

Figure 2.7. (**A**) Tc K-edge EXAFS and (**B**) the respective Fourier transform of Tc reduced at increasing S/Fe ratios.Experimental data are represented with circles. Fits are shown as solid lines (shell-by-shell fit for S/Fe = 0 and 1.12 and linear combination fit for all other S/Fe ratios in-between).

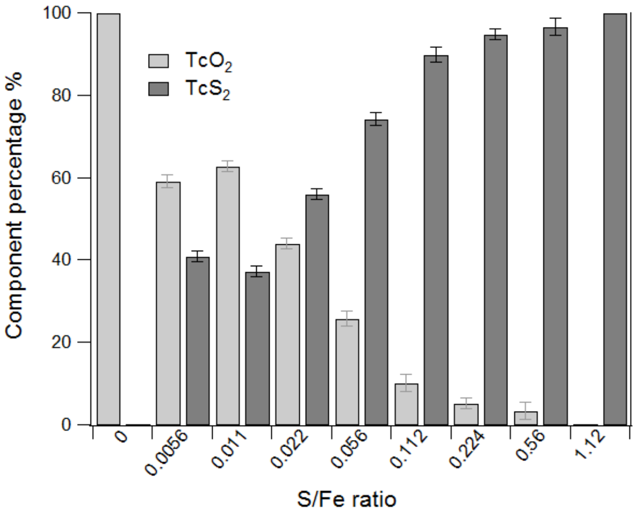

Figure 2.8. Tc speciation at different S/Fe ratios based on linear combination fitting of Tc EXAFS (**Figure 2.7**) using the spectra at S/Fe = 0 and 1.12 as two end-members.

2.4.6. Implications for Tc sequestration in the subsurface

The results presented here demonstrate that sulfidation of nZVI, although forming highly heterogeneous mineral surfaces, can direct TcO_4^- sequestration products from Tc^{IV} oxide (pathway I in **Figure 2.1**) to Tc^{IV} sulfide phases (pathway II in **Figure 2.1**) under groundwater conditions. Given the typically low TcO_4^- concentration in groundwater (even as a contaminant < 10^{-5} M), and the high affinity of TcO_4^- for FeS, it can be expected that sulfidic conditions will favor sequestration of Tc as Tc sulfides rather than Tc oxides, even at the early stage of microbial sulfate reduction. Other reducing iron phases—such as residual nZVI or secondary Fe(II) minerals formed from reaction of nZVI with groundwater constituents—reduce TcO_4^- readily, but nevertheless are outcompeted by FeS. As sulfate reduction proceeds, these iron phases (and possibly other naturally-abundant Fe oxide minerals) will undergo further sulfidation to provide additional FeS capacity for Tc sequestration. At the same time, the formation of iron sulfides will lower the free aqueous sulfide concentration, thereby decreasing the possibility of forming potentially mobile colloidal Tc sulfide phases (pathway III in **Figure 2.1**). Furthermore, in forthcoming work from this project (*303*), it was observed that the amendment of sediment with nZVI and sulfide considerably enhanced the Tc removal rate (compared with nZVI without sediment). In that work, the Tc speciation has not yet been determined, but preliminary observations are consistent with the conclusions of this study.

In contrast to conventional (n)ZVI applications, where the Fe^0 directly reduces target contaminants, this study demonstrates a scenario where the main goal of adding nZVI is conditioning and sustaining a sufficiently reducing environment to favor microbial sulfate reduction. In actual remedial practice, however, direct reduction of TcO_4^- to TcO_2 by nZVI could be the dominant sequestration pathway before microbial sulfate reduction is established (pathway I in **Figure 2.1**). Solid-to-solid transformation from $TcO_2 \bullet nH_2O$ to Tc sulfide, although thermodynamically possible (**Figure A.13**), proceeds at a slow rate (based on additional XAS results shown in **Figure A.12**). Therefore, field-scale application of nZVI for the remediation of Tc may require some direct introduction of sulfide to minimize the initial formation of TcO_2, such as by pre-treating nZVI with aqueous sulfide. This study shows that a small amount of added sulfide may be sufficient to alter the dominant sequestration pathway, and at the same time, not substantially inhibit the ability of the nZVI to condition the subsurface to a sufficiently reducing environment.

There are many additional uncertainties to be addressed before up-scaling such a remediation strategy, including how to effectively deliver nZVI in the subsurface environment (*304*), the effects of physical heterogeneity of the subsurface on Tc sequestration, and the effects of interactions between Tc and natural organic matter (especially thiol moieties) on Tc sequestration in sulfidic environment (*305*). Many of these topics have been examined previously or are under investigation currently, but are beyond the scope of this study. Regardless, the present study suggests an effective alternative for Tc sequestration. Also, further oxidation experiments that we have performed show that Tc sulfide phases have considerably slower reoxidation rate compared to Tc oxide phases formed in the absence of sulfide (details will be presented elsewhere), suggesting the potential advantage of using this strategy over current efforts that rely mostly on natural attenuation processes, where Tc oxides are the dominant reduced phases.

2.5. Acknowledgments

This material is based on work supported by the Subsurface Biogeochemical Research Program of the U.S. Department of Energy, Award Number DE-SC0001376. This report has not been subject to review by the DOE and therefore does not necessarily reflect agency views and no official endorsements should be inferred.

Mössbauer, XPS, μXRD, SEM, and TEM/EDS were performed using using the Environmental Molecular Sciences Laboratory (EMSL), a national scientific user facility sponsored by the Department of Energy's Office of Biological and Environmental Research and located at Pacific Northwest National Laboratory. XAS was carried out at the Stanford Synchrotron Radiation Lightsource, a Directorate of SLAC National

Accelerator Laboratory and an Office of Science User Facility operated for the U.S. Department of Energy Office of Science by Stanford University. The authors would like to thank Alice Dohnalkova and Charles Resch for EM sample preparation, Sung-Woo Lee for preliminary XAS data collection and discussion, Ninian Blackburn for fitting preliminary XAS data, Danielle Jansik and James Szecsody for general discussions, and Wayne Lukens for providing XAS spectra for Tc model compounds and advice regarding the XAS fitting.

Chapter 3 Oxidative Remobilization of Technetium Sequestered by Sulfide-Transformed Nano Zerovalent Iron[2]

Dimin Fan, Roberto P. Anitori, Bradley M. Tebo, Paul G. Tratnyek, Juan S. Lezama Pacheco, Ravi K. Kukkadapu, Libor Kovarik, Mark H. Engelhard, Mark E. Bowden

3.1. Abstract

Our previous study showed that formation of TcS_2-like phases is favored over TcO_2 under sulfidic conditions stimulated by nano zerovalent iron. This study further investigates the stability of Tc(IV) sulfide upon reoxidation by solution chemistry, solid phase characterization, and X-ray absorption spectroscopy. Tc dissolution data showed that Tc(VII) reduced by sulfide-transformed nZVI has substantially slower reoxidation kinetics than Tc(VII) reduced by nZVI only. The initial inhibition of Tc(IV) dissolution at S/Fe = 0.112 is due to the redox buffer capacity of FeS, which is evidenced by the parallel trends in oxidation-reduction potentials (ORP) and Tc dissolution kinetics. The role of FeS in inhibiting Tc oxidation is further supported by the Mössbauer spectroscopy and micro X-ray diffraction data at S/Fe = 0.112, showing persistence of FeS after 24-h oxidation but complete oxidation after 120-h oxidation. X-ray absorption spectroscopy

---

[2] Reprint with permission from Fan, D.; Anitori, R. P.; Tebo, B. M.; Tratnyek, P. G.; Lezama Pacheco, J. S.; Kukkadapu, R. K.; Kovarik, L.; Engelhard, M. H.; Bowden, M. E.Oxidative remobilization of technetium sequestered by sulfide-transformed nano zerovalent iron, *Environ. Sci. Technol.* **2014**, *48*, 7409-7417. Copyright 2011 American Chemical Society.

data for S/Fe = 0.011 showed significantly increasing percentages of TcS_2 in the solid phase after 24-h oxidation, indicating stronger resistance of TcS_2 to oxidation. At S/Fe = 0.112, the XAS results revealed significant transformation of Tc speciation from TcS_2 to TcO_2 after 120-h oxidation. Given that no apparent Tc dissolution occurred during this period, the speciation transformation might play a secondary role in hindering Tc oxidation. Collectively, the results indicate that sequestrating Tc as TcS_2 under stimulated sulfate reduction is a promising strategy to improve the long-term stability of reduced Tc in subsurface remediation.

3.2. Introduction

Technetium-99 (^{99}Tc) is a common radioactive contaminant of groundwater at nuclear waste reprocessing sites (*306, 307*). The environmental risk of Tc arises primarily from its long half-life and high mobility as pertechnetate oxyanion ($Tc^{VII}O_4^-$) under oxic groundwater conditions (*177*). Under anoxic conditions, the solubility and mobility of Tc are much less because $Tc^{VII}O_4^-$ is readily reduced to the relatively insoluble oxide, $Tc^{IV}O_2\bullet nH_2O$ (log $K_{sp} = -8.4$ (*266*)) by a variety of abiotic and biotic processes. Many studies have suggested that dissimilatory iron reduction is the predominant biogeochemical process mediating the reductive sequestration of Tc (*269, 308-310*) and that enhanced rates of Tc sequestration can be achieved with abiotic reductants like adsorbed Fe(II) (*101, 102, 178, 268, 311*) or Fe^0 (*301*). The resulting $Tc^{IV}O_2\bullet nH_2O$ can be sequestered by adsorption onto mineral surfaces (*101*), incorporation into mineral lattice structures (*195*), or association with organic matter (*265*).

The long-term benefit of Tc sequestration by reduction, however, remains uncertain due to the high susceptibility of $Tc^{IV}O_2 \bullet nH_2O$ to reoxidation. The reoxidation of reduced Tc oxide occurs when oxic groundwater or seawater intrudes into anoxic aquifers contaminated with Tc (*312*), or when Tc-bounded sediments are re-suspended above the oxic-anoxic interface during seasonal redox cycling of the subsurface (*191*). Although oxygen is generally considered to be the major cause of Tc reoxidation, other naturally-occurring oxidants can also oxidize Tc(IV). Such oxidants include nitrate (*191, 192*), which is a common co-contaminant with Tc, and Mn(IV) oxides, which is an oxidant mainly of biogenic origin that recently has received substantial interests for its role in oxidizing UO_2 (*185, 313-316*). The former process is coupled with microbial nitrate reduction with Tc(IV) oxide as the electron donor, while the latter reaction is mediated via solid-phase electron transfer (*315, 316*). Nevertheless, the rate of Tc reoxidation driven by these processes—at least as observed at the laboratory scale —is much slower than O_2-promoted oxidation (*192*).

Enhanced stability of reduced Tc oxides against reoxidation has been observed when they are closely associated with host minerals (*101, 195, 317*). This benefit was attributed to (*i*) formation of a protective layer that physically blocks oxygen diffusion to $Tc^{IV}O_2 \bullet nH_2O$ and (*ii*) additional redox buffer capacity provided by host minerals (e.g., scavenging of potential oxidants of Tc by structural Fe(II)), and (*iii*) incorporation of Tc(IV) into the lattice structures of the host minerals. However, the extent of stabilization varies substantially among different studies and appears to depend on the physical and chemical properties of host minerals and the specific experimental conditions under which reduced Tc is formed. For example, Frederickson et al. (*317*) compared the reoxidation rates of Tc reduced by two different iron-reducing sediments, and found a significantly slower Tc reoxidation rate for one material. They postulated that the slower and incomplete Tc oxidation was due to limited oxygen diffusion to Tc protected within aggregates that were only present in the less reactive sediment. In another study, Um et al. (*195*) reported that Tc(IV) reduced by Fe(II)-sorbed goethite exhibited strong resistance to reoxidation. However, in their experiments, the Tc-goethite mixture was annealed at 80 ºC for 7 days to promote Tc substitution and incorporation into goethite structure. In general, Tc reduced by anaerobic sediments in microcosm studies seems to be more susceptible to oxidation than Tc reduced by pure or synthetic minerals. It is likely that the heterogeneity of natural sediments may favor the prevalence of labile Tc-mineral associations (e.g., physical adsorption) as opposed to relatively more stable associations with pure mineral phases (e.g., chemical adsorption or incorporation).

Given the high susceptibility of Tc oxides to oxidation, we have investigated an alternative strategy to sequester Tc as Tc sulfide by stimulating sulfidic conditions with nano zerovalent iron (nZVI). We recently showed that the sequestered Tc formed in this way is mainly composed of TcS_2-like phases (*80*). Another recent study also reported the presence of TcS_2-like phases in microbially-reduced hyporheic zone sediment, demonstrating the presence of Tc sulfide under less extreme environmental conditions (*232*). Based on previous studies conducted under various conditions (mostly high pH and ionic strength to simulate waste leachate), reduced Tc sulfide phases, including TcS_2 and Tc_2S_7, appeared to be more resistant against oxidation (*271, 272, 318*). The reoxidation rates of Tc_2S_7 by O_2 reported by Lukens et al. (*272*) and Liu et al. (*271*) are substantially slower than that of $TcO_2 \bullet nH_2O$ reported elsewhere (*191, 317*). It was also shown that the TcS_2–like phases formed by co-precipitation with FeS transformed to $TcO_2 \bullet nH_2O$ without being further oxidized to Tc(VII) in damp air (*318*). Given the similar size of Tc(IV) and Fe(III) and the octahedral binding structure of both atoms to oxygen, the authors suggested that possible incorporation of Tc(IV) into the lattice structure of goethite—the oxidation product of FeS—stabilizes Tc(IV).

As a follow up to our previous work showing facile reductive sequestration of Tc by nZVI under sulfidic conditions (*80*), this study was performed to investigate the stability of the sequestration products with respect to oxidative dissolution. The primary goal was to characterize the changes in speciation of Tc during the reoxidation process under environmentally relevant conditions. However, because our prior work had demonstrated that secondary FeS (formed during sulfidation) is an important sink for Tc sequestration, this study also addressed changes in the host mineral composition (e.g., FeS) during oxygenation of the sample and its effects on Tc remobilization. The results confirm that reduced S containing phases of Tc and Fe contribute to the stability of Tc sequestration products, and therefore that this might form the basis for an improved strategy for remediation of technetium contaminated groundwater.

3.3. Experimental

3.3.1. Chemical Reagents

All reagents were reagent grade and used as received without further purification. ^{99}Tc was obtained as concentrated stock solution of ammonium pertechnetate (NH_4TcO_4) from Pacific Northwest National Laboratory. ^{99}Tc is a radioactive beta emitter (half-life =

2.13×10^5 years; E_{max} = 294 KeV) and was handled in a properly equipped radioactive laboratory.

3.3.2. Tc Reoxidation Experiments

Tc reoxidation was conducted following the conclusion of Tc reduction experiments. The latter were carried out as described previously (*80*). Briefly, freshly-prepared nZVI (0.2–0.5 g L^{-1}) was pre-equilibrated with various concentrations of sulfide (S/Fe molar ratio = 0–1.12) in 10 mL deoxygenated artificial Hanford groundwater HS300(*319*) (pH buffered at 7.8 with 30 mM HEPES, Chemical compositions shown in **Table A.1** in **Appendix A**) under anaerobic conditions for 24 h. TcO_4^- was then added to a final concentration of 6 μM. After >99% removal of aqueous Tc (< 0.2 μm fraction), the reactors were left aging for different periods of time (7 days or 9 months) before reoxidation was initiated.

The reoxidation experiments were carried out by bubbling 0.2 μm filtered air into a water trap bottle, which then passed to the suspension via a 21 gauge needle through a butyl rubber septum (Bellco Glass; Vineland, NJ). The air bubbling rate (~2–3 bubbles/sec) was adjusted to provide gentle mixing of the solid and aqueous phases. No additional mixing was applied. For sampling, 0.3 mL of suspension was withdrawn from the reactor and passed through a 0.2 μm filter pre-flushed with N_2, and the Tc concentration in the filtrate was measured by liquid scintillation counter (Beckman; Brea, CA). Water loss due to evaporation was monitored by weighing reactors between each sampling and was found to be negligible.

3.3.3. Reoxidation of Host Minerals

To understand the evolution of host mineral phases during reoxidation, parallel Tc-free reoxidation experiments were conducted after 0.5 g L^{-1} nZVI was equilibrated with 0 and 1 mM sulfide for 7 days (S/Fe = 0 and 0.112). The procedure was the same as for the Tc reoxidation experiments except that a large volume 50 mL reactor was used in order to provide a sufficient quantity of solids for material characterizations. During oxidation, the oxidation-reduction potential (ORP) of the suspension was measured intermittently with a Pt microelectrode with Ag/AgCl as a reference electrode. After 0, 24, 120, and 312 h of oxidation, the reactors were sacrificed and the solids were recovered by vacuum filtration inside an anaerobic chamber following the procedure described elsewhere (*286*). The solids were then sealed under N_2 atmosphere and delivered to the Environmental Molecular Sciences Laboratory (EMSL, Richland, WA) for characterization.

3.3.4. Solid Phase Characterization.

Preliminary characterization by Mössbauer spectroscopy on oxidized samples, with or without exposure to Tc, showed that Tc at the concentration used in this study has no detectable effect on the oxidation products of the host minerals. Therefore, further solid phase analysis was done with Tc-free samples for convenience. The bulk mineralogy of sulfidated nZVI throughout the oxidation process was characterized by micro X-ray diffraction (μXRD) and Mössbauer spectroscopy. The near-surface composition of the material was analyzed by X-ray photoelectron spectroscopy (XPS). The microscopic structures of the mineral phase were examined by transmission electron microscopy (TEM) with energy dispersive X-ray spectroscopy (EDS). Details for these methods are given in **Appendix A**.

3.3.5. X-ray Absorption Spectroscopy

Samples were prepared with the solids containing Tc freshly reduced by 0.5 g L^{-1} nZVI that was pre-treated with 0, 0.1, and 1 mM sulfide (S/Fe: 0, 0.011, and 0.112) in 50 mL batch reactors. The reduced solids were further oxidized for 0, 24,120, and 312 h, 7 days after Tc reduction completed. After oxidation, the solids were recovered by centrifugation and then loaded as a concentrated slurry/paste into single slot Teflon holders. The holders were then sealed with a single layer of Kapton tape and further contained inside a heat-sealed polypropylene bag. Additional samples that were aged in solution were also prepared for XAS following the same procedure. Details of those samples are given in **Appendix B**. Loaded samples were kept in an anaerobic chamber prior to the measurements.

3.4. Results and Discussion

3.4.1. Tc Reoxidation Kinetics

The reoxidation kinetics of freshly-reduced Tc in 10 mL batch reactors is shown in **Figure 3.1A**. In the absence of sulfide, aqueous Tc rapidly increased during the initial 20-h oxygenation, presumably due to oxidative dissolution. After 20-h oxidation, the aqueous Tc appearance rate slowed, and appeared to gradually approach a plateau by 312-h oxidation. By the end of the experiments, approximately 30% of the Tc still remained associated with the solid phases, possibly because residual Tc phases that were more resistant to oxidation formed as oxidation progressed. This could be due to either

Tc incorporation into the lattice structures of oxidized Fe mineral phases (*195*, *318*) or formation of secondary iron minerals that protect reduced Tc from oxidation. In the presence of sulfide, the Tc reappearance rate was significantly slower compared to the absence of sulfide. However, among three different S/Fe ratios (0.055, 0.224, and 1.12) that were tested initially, no appreciable difference of aqueous Tc concentration after 312-h oxidation was observed.

The trend in reoxidation kinetics observed in the presence and absence of sulfide is consistent with the speciation of reduced Tc produced across a range of S/Fe ratios that was reported in our reduction study (*80*). In that work, we showed that TcO_4^- was directly reduced by nZVI to $TcO_2 \bullet nH_2O$ in the absence of sulfide. With increasing sulfide doses—even at relatively low S/Fe ratios—a TcS_2-like phase quickly became the dominant reduced Tc species due to the high affinity of FeS for TcO_4^-. The slower kinetics of Tc reoxidation in the presence of sulfide appears to confirm the hypothesis that TcS_2-like phases are more resistant to oxidation than TcO_2. The lack of difference in Tc reoxidation kinetics at three S/Fe ratios also agrees with the finding that TcS_2 is the major component of reduced Tc species above S/Fe = 0.05 (*80*).

To test the effects of aging, reoxidation was also conducted on reduced Tc that was aged for 9 months (**Figure 3.1B**). Similar to freshly reduced samples, no appreciable difference in reoxidation kinetics was observed at S/Fe ratios above 0.044. However, at the two lowest S/Fe ratios tested (0.011 and 0.022)—where the percentage of TcO_2 formed was significantly higher (*80*)—Tc reoxidation was correspondingly faster and the kinetics seems to be positively correlated with the S/Fe ratio. This further indicates that TcS_2 is less labile to oxidation compared to TcO_2. It is noteworthy that the nZVI only sample aged for 9 month had slower reoxidation kinetics than S/Fe = 0.011 and 0.022. This result was not replicated and the reasons for it were not investigated, but it could arise from geochemical stabilization developed during aging process. In fact, all of the 9-month aged samples at S/Fe > 0.044 had considerably slower reoxidation kinetics (Figure 1B) than their freshly reduced counterparts (**Figure 3.1A**).

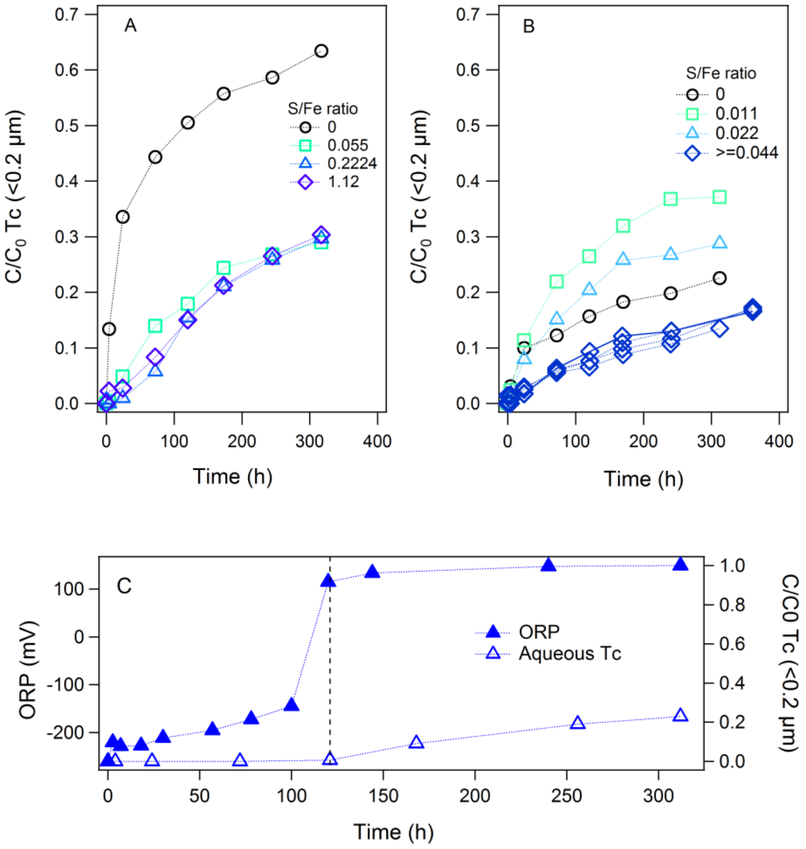

Figure 3.1. (**A**) Aqueous Tc reappearance kinetics of 7-day aged samples in 10-mL batches; (**B**) Tc reoxidation kinetics of 9-month aged samples in 10-mL batches; (**C**) ORP and aqueous Tc concentration vs. time during reoxidation in the 50 mL batch reactor at S/Fe = 0.112 aged for 7 days.

Close inspection of the reoxidation kinetics of fresh samples (**Figure 3.1A**) shows that at relatively high S/Fe ratios (S/Fe = 0.22 and 1.12), there was an initial lag period of about 24 h during which little aqueous Tc was detected. By contrast, a relatively large fraction of reduced Tc was remobilized within 2 hours after O_2 introduction in the absence of sulfide. A lag phase was also observed for uraninite oxidation in the presence of FeS (*111*), and was attributed mainly to FeS being a redox buffer that scavenged dissolved O_2 (although the possibility of oxidized U being re-reduced by Fe(II) was not excluded). Given that our previous study demonstrated that FeS is formed and this phase is responsible for sequestration of Tc as TcS_2 (*80*), the observed lag in initial Tc oxidation is most likely caused by FeS. It is also worth noting that the two highest S/Fe ratios did not result in longer lag phases, which is consistent with our prior finding (*80*) that FeS formation was inhibited at higher S/Fe ratios, presumably due to limited nZVI surface sites.

Parallel measurements of ORP and Tc dissolution in the 50 mL batch reactor (for the purpose of preparing XAS samples) at S/Fe = 0.112 further confirms the role of FeS in inhibiting initial Tc oxidation by showing that (*i*) the lag period where Tc dissolution was inhibited was extended to ~120 h (compared to ~20 h in 10 mL batches), presumably because of the higher quantity of FeS in the larger reactor (**Figure 3.1C**); and (*ii*) the onset of active Tc dissolution occurred after a sharp rise in ORP from −150 mV to 100 mV around 120 h (**Figure 3.1C**). Although interpreting ORP data in our system is complicated by the presence of both dissolved and solid phase redox-active species (*137*), the steep ORP rise at 120 h most likely reflects the depletion of reducing capacity contributed by nZVI and FeS due to reaction with dissolved oxygen. In fact, analogous ORP profiles have been observed in other studies where FeS was oxidized by oxygen (*111, 320*), and a similar concurrency between sharply increased ORP and uranium remobilization has been observed (*111*).

3.4.2. Oxidation of Host Mineral Phases.

Further investigation into the mineralogical transformations of the host minerals during oxidation was conducted at S/Fe = 0 and 0.112. Because the main focus of this study was on sulfidated nZVI, all characterizations of unsulfidated nZVI (S/Fe = 0) for comparison are presented in the **Appendix B** (**Figure B.1–B.2**). The S/Fe ratio of 0.112 was chosen because our reduction study showed that this is the optimal S/Fe ratio in batch experiments to maximize FeS formation of FeS (higher S/Fe ratio did not result in more FeS formation) and to sequester Tc primarily as TcS_2 (*80*).

The µXRD of all oxidized samples was dominated by broad and indistinct features (**Figure B.1**), in agreement with amorphous nature of the fully reduced starting material (*80*). Minor peaks due to the following phases were also evident (**Figure B.1B**): (*i*) mackinawite in 0, and 24 h samples, (*ii*) vivianite in 120 h sample (due to 1.5 mM phosphate in HS300), and (*iii*) broad peaks due to ferrihydrite-like mineral in 24, 120, and 312 h samples (ferrihydrite-like mineral content increased with oxidation time). Mössbauer spectroscopy measurements were used to quantify *bulk* changes in both nZVI and FeS components, together with evolved oxidized Fe mineral phases, during oxidation (**Figures 3.2A–D**). Prior to oxidation, the bulk solid was composed of ~8% mackinawite—the low spin (LS) Fe(II)-tetrahedral-compound shown as red singlet—and 92% nZVI, based on the Mössbauer characterization in our previous study (also shown in **Figure 3.2A**) (*80*).

After 24-h oxidation, the FeS singlet retained in the 20-K Mössbauer spectrum (**Figure 3.2B**), and the presence of FeS was further confirmed by multiple peaks that match mackinawite in µXRD (**Figure B.1B**) and by TEM-EDS, showing the presence of typical FeS morphology with a S/Fe ratio close to 1 (**Figure B.5A**). Nevertheless, XPS survey scan data on the 24-h oxidized sample indicated significant decrease of S^{2-} intensity (**Figure 3.2E**) and the Fe 2p narrow spectra (**Figure B.4A**) also showed strong attenuation of the Fe(II)-S peak around 706.6 eV, both of which suggest the disappearance of reduced sulfide near the mineral surface. These results are consistent with prior studies showing significant FeS dissolution at the beginning of oxidation around acidic to neutral pH values (*112*). A qualitative Mössbauer modeled fit (**Figure B.3**) further revealed possible Fe(III) structures that might result from structural and surface oxidation of FeS (*111*).

The main oxidized Fe species emerged after 24-h oxidation was high spin (HS) Fe(II), represented by a broad Fe(II) doublet in the 20-K Mössbauer spectrum (**Figure 3.2B**). The formation of Fe(II) primarily resulted from oxidation of nZVI as the reduction in the percentage of nZVI (from 92% to 45%) corresponded well with the formation of HS Fe(II) (39%), although a small fraction of Fe(II) could also have resulted from FeS oxidation. The nature of this HS Fe(II) phase, however, remains unclear. The XPS survey scan of the 24-h oxidation sample showed a large increase of P and O near the surface with decreased Fe (**Figures 3.2E and 3.2F**). Additionally, TEM (**Figure 3.2I**) showed that the exterior of mineral aggregates was mostly composed of less electron dense materials, which are enriched in P and Ca relative to the interior regions that are Fe rich (see EDS spectra, **Figure B.5A**). However, no vivianite ($Fe_3(PO_4)_2 \cdot 8H_2O$) peaks were identified by µXRD (**Figure B.1**). It is possible that at the early stage of oxidation, secondary mineral phases formed by dissolution, oxidation and re-precipitation still mostly preserve the amorphous or nanocrystalline nature of the starting material. A small percentage of ferryhydrite (4%) was also identified by the modeled Mössbauer spectrum (the broad sextet in **Figure 3.2B**), presumably due to oxidation.

Further oxidation to 120 h resulted in more complete oxidation of host minerals. The fitting of the Mössbauer 20-K spectrum indicated that the percentage of ferrihydrite increased to 73% while the HS Fe(II) percentage decreased to 20% (**Figure 3.2C**). The residual high spin Fe(II) underwent further crystallization to form vivianite, which is supported by Mössbauer fitting parameters (**Table B.2**) and µXRD (**Figure B.1B**). A third component resembled the singlet feature of low spin Fe(II)S, but FeS peaks were not evident in the µXRD pattern (**Figure B.1B**). Further examination of the Mössbauer fitting parameters showed slight deviations from the FeS component in the 0 and 24-h oxidized samples (**Table B.2**). TEM (**Figure 3.2J**) showed that apart from the major structure that is composed of poorly crystalline small particle (presumably ferrihydrite based on the µXRD data), a small fraction of the solid materials exhibit the distinctive ribbon-like structure that is typical of mackinawite (**Figure 3.2J** & **Figure B.5C**). The EDS, however, showed only Fe and O as the main elements with no or very low levels of sulfur (**Figure B.5B**). It is possible that these structures were some transient phases of FeS oxidation (which likely caused the unidentified Mössbauer component with similar singlet shape to FeS in the 120-h oxidation sample) and had yet to be transformed to more stable phases. This might also indicate that the Fe atoms in nZVI and FeS were oxidized to different phases. By 312-h oxidation, the solid phase was nearly completely transformed to ferrihydrite, based on Mössbauer (**Figure 3.2D**) and µXRD data (**Figure B.1B**).

Despite FeS only being a minor component of sulfidated nZVI (8% of the total solid based on Mössbauer fitting of the 0-h oxidation sample), its oxidation plays an important role in Tc remobilization because it is the major mineral phase that associated with Tc sulfide (*80*). The effect of the oxidation of iron sulfide minerals on contaminant remobilization, including heavy metals and oxyanions, has been the subject of many studies (*111, 112, 321-324*). Among various biotic and abiotic oxidizing agents, oxygen is of particular interest due to its ubiquitous role in chemical oxidation. The general consensus on the mechanism of abiotic oxidation of FeS by oxygen is that iron and sulfur undergo independent oxidations to form Fe (oxyhdr)oxide and elemental sulfur (polysulfide) as the main products, respectively. At neutral pHs, the oxidation of FeS was suggested to proceed via solution phase oxidation and solid phase mediated oxidation mechanisms (*111, 112*). Given that our study was conducted under comparable conditions (e.g., near neutral pH), it is expected that the oxidation of FeS component in the current study follows the same pathway, despite the lack of complementary solution chemistry data. The absence of a strong polysulfide/elemental sulfur signal in our S2p XPS narrow scan (**Figure B.4B**) could be because these spectra were collected at room temperature, which can cause sublimation of S^0 under high vacuum (*325*). The difference in the iron mineralogy of the final oxidation product between this study and prior work might be largely due to variations in geochemical conditions (e.g., aqueous constituents).

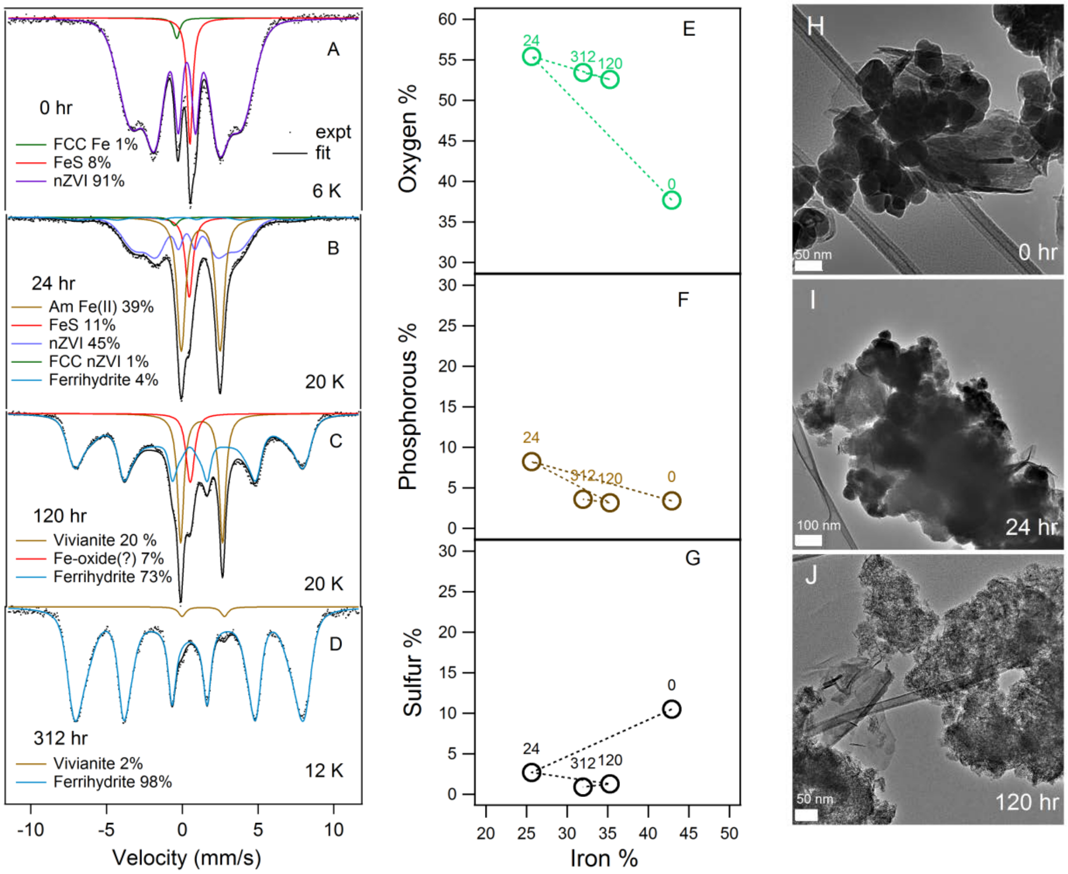

Figure 3.2. Solid phase characterizations of sulfidated nZVI (S/Fe = 0.112) during oxidation. Left panel: Experimental and modeled Mössbauer spectra of sulfidated nZVI after (**A**) 0, (**B**) 24, (**C**) 120, and (**D**) 312-h oxidation (FCC: face cubic center); Middle panel: XPS wide survey plot of surface atomic percentage of (**E**) oxygen, (**F**) phosphorous, (**G**) sulfur vs. Fe during oxidation (numbers in E, F and G represent oxidation time; Sulfur refers exclusively to S^{2-}); Right panel: transmission electron micrographs of sulfidated nZVI after (**H**) 0, (**I**) 24, and (**J**) 120-hr oxidation (associated EDS spectra are presented together with TEMs in **Figure B.5**). All data for the 0-hr oxidized sample are adopted from Fan et al. (*80*).

3.4.3. Evolution of Tc Speciation

Both Tc reappearance kinetics and mineral characterizations suggest that the redox buffer capacity of sulfidated nZVI plays a key role in inhibiting initial Tc reoxidation. However, slower Tc reoxidation was also observed at the final stage of the batch experiments with sulfidated nZVI, even when the redox buffer capacity should have been depleted by extended exposure to oxygen (**Figure 3.1A**). Recalling that the reduction study showed that Tc was sequestered mainly as TcS_2 in the presence of sulfide (*80*), it is possible that Tc speciation might be another reason for slower Tc reoxidation in the presence of sulfidated nZVI.

To further investigate the factor(s) that regulates Tc remobilization, X-ray absorption spectroscopy (XAS) measurements were performed to probe the change in speciation of reduced Tc during reoxidation. Tc K-edge data were collected on the solids of S/Fe = 0, 0.011, and 0.112 recovered after 0, 24, 120, and 312-h oxidation. In the absence of sulfide, both XANES (**Figure B.6A**) and EXAFS (**Figure B.6B**) showed that solid Tc speciation (S/Fe = 0) remained nearly unchanged throughout the oxidation process. Because the aqueous phase was mostly removed during XAS sample preparation, no oxidized Tc ($Tc(VII)O_4^-$) was observed (in contrast to the results described in Lukens et al.(*272*)). The Tc speciation was consistent with $TcO_2{\bullet}2H_2O$ shown in the reduction study (*80*), along with many prior studies (*101*, *301*, *326*).

The Tc reduction study showed that the speciation of reduced Tc at different S/Fe ratios can be represented by a mixture of TcO_2 and TcS_2, and that the Tc absorption edge position can be used as an indicator to qualitatively assess the respective content of TcS_2 and TcO_2 in a given mixture (because the former has about 6 eV lower absorption edge than the latter, even though both are Tc(IV) species) (*80*). In this study, at S/Fe =0.011, the Tc absorption edge decreased from ca. 21059.2 to ca. 21056.6 eV after 24-h oxidation (**Figure 3.3**). This shift in the absorption edge position suggests an increasing percentage of TcS_2 after 24-h oxidation. This was further confirmed by increasing intensity for Tc–S binding in the Fourier transformed EXAFS (**Figure 3.4B**) and higher TcS_2 content based on linear combination fitting (**Figure 3.4C**). Given that little inhibition of Tc dissolution was observed at low S/Fe ratios—presumably due to minimal FeS formation—the increase in the TcS_2 percentage likely suggests that more TcO_2 relative to TcS_2 was oxidized to aqueous Tc(VII). After 120-h oxidation, the absorption edge, however, increased back to the level similar to that seen in the 0-h oxidation sample and the Tc–S peak attenuated in the Fourier transformed EXAFS spectrum (**Figure 3.4B**), indicating that TcS_2 was gradually oxidized (or transformed), leaving higher TcO_2 percentage in the solid phase.

At S/Fe = 0.112, the fully reduced Tc was mainly present as TcS_2 (> 90% based on LCF of EXAFS data in **Figure 3.4C**). The initial 24-h oxidation resulted in little change of the overall Tc speciation as the absorption edge position remained at 21053 eV (**Figure 3.3**) and the EXAFS of the 0-h and 24-h oxidation samples were almost identical (**Figure 3.4A**). Because no significant Tc dissolution occurred during the initial 24 hours (**Figure 3.1C**), little or no speciation change indicates that the presence of redox buffer capacity protected reduced Tc from oxidation. This is consistent with the solid phase characterization, showing substantial surface oxidation of the host minerals during the initial 24 hours (**Figures 3.2E–G**). After 120-h oxidation, a significant change of solid Tc speciation was evident by XAS: (*i*) the absorption edge position increased by ~2 eV (**Figure 3.3**); and (*ii*) the Fourier transformed EXAFS showed notable enhancement of the Tc–O peak at the expense of a decreasing Tc–S peak (**Figure 3.4B**). Recall that the kinetic data still did not show elevated aqueous Tc concentration by this time point. Therefore, the substantially increasing percentage of TcO_2 in the solid phase could only have resulted from a change of Tc speciation in TcS_2 to TcO_2. A similar transformation from Tc sulfide to Tc oxide was reported for the oxidation of TcS_2-like phases in damp air in the presence of FeS (*318*). However, in contrast with that study, where Tc(IV) was shown to be eventually incorporated into goethite structure, we found little evidence of Tc incorporation into the iron oxide or ferrihydrite mineral in this study (including Fe(II) in the 2nd shell did not significantly improved the overall fitting). In addition, the EXAFS data showed a significant level of TcS_2 present in the solid phase after 312-h oxidation (data not shown), which implies that the transformation in speciation provided only a secondary barrier that partially inhibited Tc oxidation. Once the transformation began, TcO_2 became readily available for further oxidation.

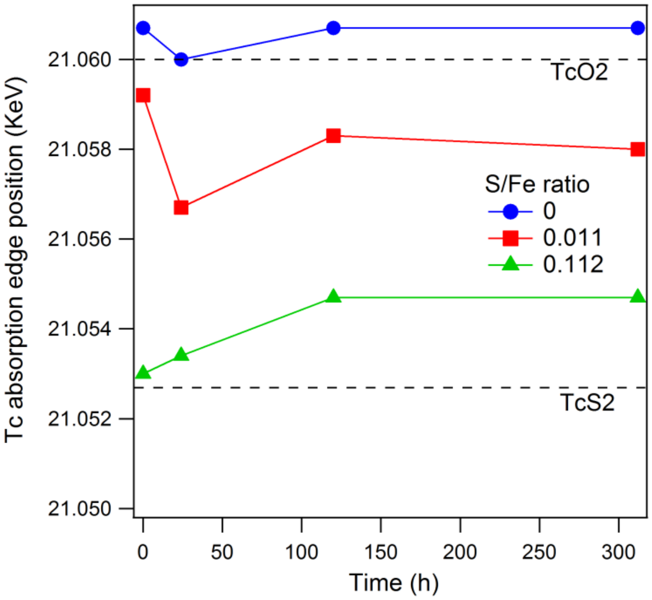

Figure 3.3. Tc XANES absorption edge positions during oxidation at S/Fe = 0, 0.011, and 0.112 (The values for the 0-hr oxidized samples, TcO_2, and TcS_2 (dashed lines) are adopted from our Tc reduction study(*80*)).

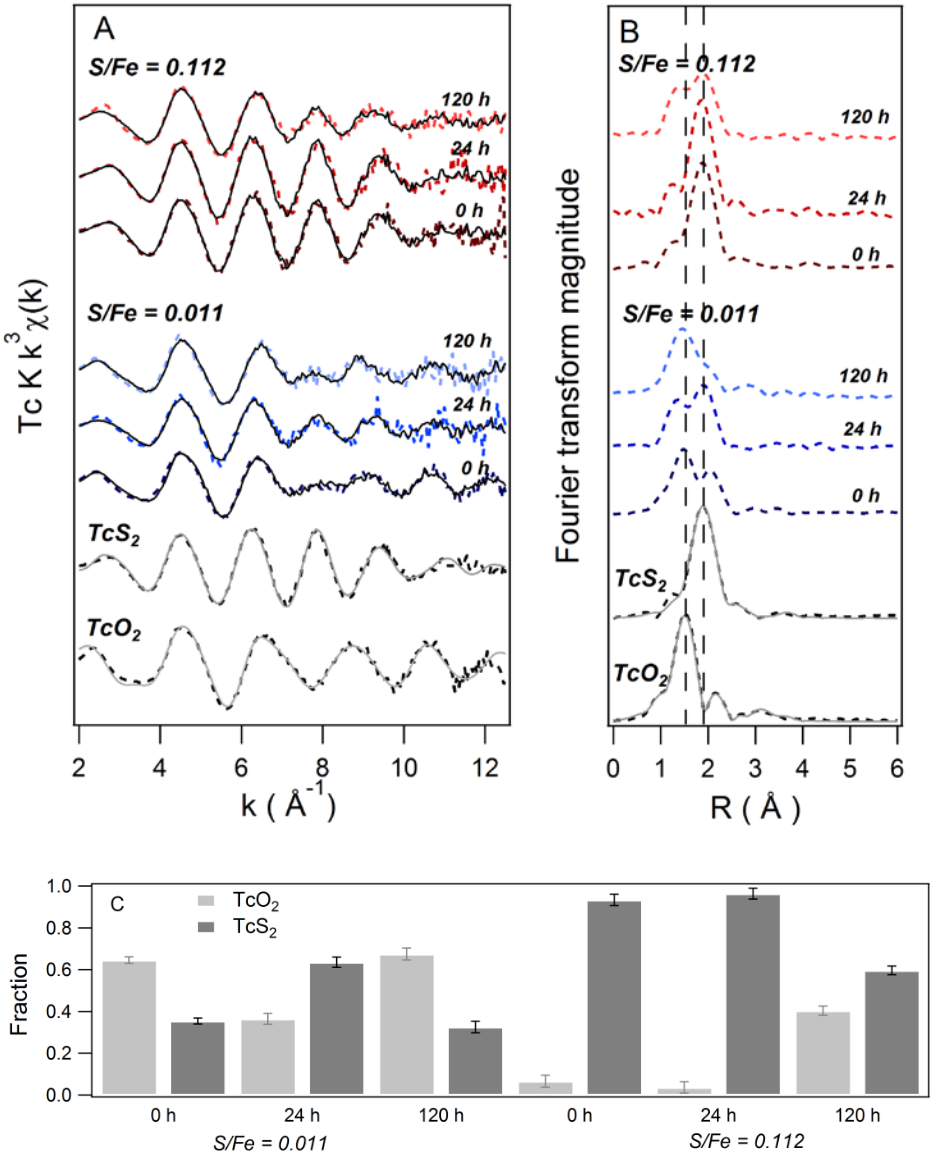

Figure 3.4. Tc K-edge (**A**) EXAFS and (**B**) the Fourier transformed EXAFS after 0, 24, and 120 h oxidation at S/Fe ratio = 0.011 and 0.112. Experimental data are shown by dashed lines and EXAFS fits are shown by solid lines. Vertical dashed lines in **B** denote the positions of first shell Tc–O and Tc–S binding. (**C**) Fraction of Tc speciation during oxidation at S/Fe = 0.011 and 0.112 based on linear combination fitting of EXAFS data (Tc reduced at S/Fe=0 (TcO_2) and Tc reduced at S/Fe=1.12 (TcS_2) and their respective shell-by-shell fitting were used as reference spectra.(*80*) Data for 0-h oxidized sample are adopted from the Tc reduction study (*80*). Linear combination fitting of EXAFS of oxidized Tc at S/Fe = 0.011 and 0.112 was done using TcS_2 and TcO_2 as principle components).

3.4.4. Implications

Under the batch experimental conditions of this study, oxygenation of materials containing reduced Tc resulted in considerably less release of $Tc^{VII}O_4^-$ when the Tc had been sequestered under sulfidic conditions. However, the practical benefit of creating sulfidic conditions to sequester Tc as TcS_2 will depend on whether recalcitrance of TcS_2 to oxidation can be maintained over the long-term under field-scale remediation conditions. It should be recognized that the batch experiments used in this study represented a worst case scenario in which Tc oxidation is favored by (*i*) unlimited oxygen supply, (*ii*) no mass transport limitations, and (*iii*) limited redox buffer capacity of FeS. These conditions usually do not apply in the subsurface, which might make sequestration of Tc as TcS_2 more favorable under more realistic conditions. For example, the contact between reduced Tc and dissolved oxygen is likely to be limited by diffusion in vadose zone and low-flow groundwater system. Formation of secondary precipitates from iron oxidation and reprecipitation may further protect Tc from oxidation by increasing the thickness of the diffusion barrier. This effect might also explain the relatively stronger resistance to oxidation of aged samples observed in the present study. Dissolved oxygen concentration is likely to be limited due to upstream aerobic respiration by microorganisms, provided sufficient organic matter is present in aquifers. In fact, implementation of ZVI in combination with organic materials into the subsurface to stimulate in-situ chemical and biological reduction has become a widely applied strategy in field remediation. With respect to the redox buffer capacity, given the general abundance of iron bearing minerals in the subsurface, the sulfidation process of these mineral phases could result in greater redox buffer capacity. Although the extent of protection exerted by these natural processes is not yet clearly understood, field data tends to show substantially less Tc mobilization than prediction derived from laboratory tests, even for TcO_2 (*327*).

It should be further noted that even though the high reactivity of iron sulfides for a variety of groups of subsurface contaminants has long been recognized (*141, 176, 282, 284, 328, 329*). FeS is commonly not considered to be stable in oxic environments. The current study may overestimate the stability of FeS and associated TcS_2 by not considering other biogeochemical processes that can oxidize FeS, such as microbially-mediated oxidation (e.g., by Fe-oxidizing bacteria or nitrate-reducing bacteria) or abiotic oxidation by naturally-occurring MnO_2 (*330*). Both of these processes have been shown to play significant roles in controlling the speciation and availability of trace metals in specific types of environments (*316, 322, 323*), but their effects on Tc remobilization remain to be examined. Another important biogeochemical process that merits further investigation is pyritization, not only because pyrite is the ultimate sink for iron and sulfur in sulfidic environments (*74*), but also because pyrite is generally considered to be less susceptible to oxidation than mackinawite. Furthermore, effective approaches to inhibit pyrite oxidation have been proposed by many prior studies (*193, 194, 331*), which might be proved to be useful for further stabilization of reduced Tc sulfide.

3.5. Acknowledgments

This material is based on work supported by the Subsurface Biogeochemical Research Program of the U.S. Department of Energy, Award Number DE-SC0001376. This report has not been subject to review by the DOE and therefore does not necessarily reflect agency views and no official endorsements should be inferred.

Mössbauer, XPS, μXRD, and TEM/EDS were performed using the Environmental Molecular Sciences Laboratory (EMSL), a national scientific user facility sponsored by the Department of Energy's Office of Biological and Environmental Research and located at Pacific Northwest National Laboratory. XAS was carried out at the Stanford Synchrotron Radiation Lightsource, a Directorate of SLAC National Accelerator Laboratory and an Office of Science User Facility operated for the U.S. Department of Energy Office of Science by Stanford University. The authors would like to thank Sung-Woo Lee for preliminary XAS data collection and discussion, Danielle Jansik and James Szecsody for general discussions.

PART II. Characterization of Reducing Iron Minerals Using Chemical Reactive Probes

CHAPTER 4. Assessing the Potential for Abiotic Natural Attenuation of Contaminants by Reducing Iron Minerals

CHAPTER 5. Characterizing the Reactivity and Transformation of Carboxymethyl Cellulose Modified Nano Zerovalent Iron Using Chemical Redox Probe: A Field Deployable Approach

Chapter 4 Assessing the Potential for Abiotic Natural Attenuation of Contaminants by Reducing Iron Minerals[3]

Dimin Fan, Adrian. W. Hinkle, Richard L. Johnson, and Paul G. Tratnyek

4.1. Abstract

Despite increasing recognition that natural attenuation (NA) of chlorinated solvents involves abiotic as well as biotic degradation processes, current approaches to assessing the potential for abiotic NA are inadequate. Recognizing that reducing iron minerals play a major role in contaminant reduction by abiotic NA, this study set out to explore the use of chemical reactive probes (CRPs) to characterize the thermodynamic and kinetic aspects of contaminant reduction by these phases. A set of thermodynamic CRPs were selected and used to determine the reduction potentials (E_{CRP}) by spectrophotometric determination of CRP speciation at equilibrium, and calculations using the Nernst equation. The measured E_{CRP} were found to vary upon mineral type, Fe(II) concentration, and mineral loading. Reduction potentials were also measured electrochemically with a Pt rotating disc electrode (RDE) (E_{Pt}). Despite showing a trend consistent with E_{CRP}, E_{Pt} values were 150─200 mV more positive than E_{CRP}, likely due to the poor electrode responses to reducing iron minerals. The reduction experiments of three different kinetic CRPs by four iron oxides at 1mM Fe(II) concentration showed that the observed reduction rate constants in general followed the order of mineral reduction

---

[3] Prepared as a research paper to be submitted to *Environmental Science & Technology*

potential, although kinetic effects were also observed, likely resulting from intrinsic differences between different minerals. Combination of experimentally measured reduction rate constants with published rate constants, including chlorinated ethenes, showed qualitatively consistent reactivity pattern between the kinetic CRPs and chlorinated ethenes, indicating the potential utility of CRPs in assessment of abiotic NA.

4.2. Introduction

Abiotic reduction of chlorinated ethenes (e.g., trichloroethylene) by naturally-occurring reducing iron minerals (including iron oxides and sulfides) has been identified as a potentially important component in monitored natural attenuation (NA) (*8, 154, 332*). Reduction of chlorinated ethenes has been reported in laboratory batch experiments using minerals prepared by chemical synthesis (*151, 227, 228*), in-situ precipitation (*233-235*), and with materials obtained directly from contaminated subsurface (*152, 153, 155*). However, the rates of these reactions are slow and therefore difficult to quantify, making it impractical to use them directly for assessing the potential for abiotic NA in the field.

One alternative approach involves exploring correlations between the contaminant reduction rates (measured under optimized conditions) with properties of aquifer materials that are easier to measure, such as total solid ferrous iron and magnetic susceptibility (*154, 155, 332*). However, the scientific basis for using these indirect methods to assess the potential for abiotic NA has not been thoroughly evaluated and there are reasons to expect they will have limited generality. For example, total Fe(II) determined on the solids (after acid digestion) represents the overall reductant capacity but does not differentiate between the various ferrous minerals that might possess a wide range of reactivity. Magnetic susceptibility measurement primarily reflect magnetite while other reactive iron phases that could contribute to dechlorination—such as green rusts (*151, 227*) or iron sulfide (*230, 283*)—are not represented. In addition, neither of these approaches provides direct assessment regarding the “true” reactivity of the reductants.

The reactivity of these reducing iron minerals has been extensively studied with contaminants that are much easier to reduce, such as nitroaromatics or chlorinated alkanes. Therefore it is possible that these compounds might serve as kinetic probes to provide a more efficient, general and practical approach to assess the mineral reactivity in abiotic NA. To date, the utility of kinetic probes has been mostly explored on identifying predominant reductants in natural samples by comparing the reactivity patterns (e.g., kinetics) of probe compounds between natural samples and model systems (*225, 333, 334*). For this purpose, probe selection is commonly limited to one class of contaminants. However, to assess abiotic NA, reactivity pattern needs to be compared across several classes of contaminants, including chlorinated ethenes, which has not been fully investigated.

A prototype of this analysis has been conducted by Elsner et al. (*45*), where they examined the reactivity of Fe(II) sorbed onto the surface of a series of iron minerals with three probe compounds: hexachloroethane (HCA), 4-chloronitrobenzene (4Cl-NB), and 4-chlorophenyl hydroxylamine. A qualitatively consistent reactivity pattern was observed between HCA and 4Cl-NB with different minerals, even though the two compounds belong to different classes of reducible contaminants and were reduced at rates that differed by almost 3~4 orders (normalized by surface area). They further cautiously proposed that HCA might be used as a kinetic probe for TCE as these two compounds exhibit similar reactivity pattern with magnetite, green rust, and iron sulfides, based on TCE reduction data reported by other studies (*151, 228*).

One fundamental question—which would justify using kinetic probes to assess abiotic NA but was not fully addressed by Elsner et al. (*45*)—is the identification of which mineral properties control the observed, overall rates of contaminant reduction. This issue is challenging because most contaminant reduction experiments have not been designed in a way that facilitates comparison between different minerals. Perhaps, more importantly, it is due to the diversity of reducing iron minerals, which results in the lack of a universal descriptor for reducing iron minerals. For Fe(II) sorbed onto iron oxides, a number of studies have suggested that the mineral reactivity correlates with the density of the sorbed Fe(II) (*45*). However, the interpretation of $\mathrm{Fe(II)}_{\mathrm{ads}}$ values estimated from traditional measurements is complicated by electron transfer from adsorbed Fe(II) into the bulk materials and that aqueous Fe(II) appears to be needed for maintaining mineral reactivity (*105*). For mixed valent iron oxides, such as magnetite or green rust, the ratio of Fe(II) to Fe(III) has been shown to affect the reduction kinetics of contaminants (*140*).

In an analogous reducing system with aqueous Fe(II)-organic ligand complexes as the reductants, a linear free energy relationship (LEFR) is obtained between reduction rate constants of oxime carbamate pesticides and the one electron reduction potentials of Fe(II)/Fe(III) redox couples (*14*). In this case, thermodynamic reduction potentials of the reductants determine their reactivity with the contaminants. An analogous LFER is less likely to work in heterogeneous systems, with reducing iron minerals, but, the mineral reduction potential is still expected to be the major determinant of mineral reactivity because it dictates the thermodynamic driving force of the reduction for given contaminants (*335*).

Nevertheless, reliable data on mineral reduction potentials under appropriate conditions is largely lacking. Conventional electrode potential measurements of oxidation-reduction potential (ORP) on mineral suspensions are common (*137*), but the measured values represent mixed potentials that are likely to be influenced by other factors such as mass transport, aggregation, and secondary redox-active species (*81, 137*). The "standard" reduction potentials for iron oxide/Fe(II) couples that appear in some tabulations (*82*) are based on calculations with thermodynamic data from calorimetry, and therefore may not be representative of the phases controlling solution phase speciation. Mineral reduction potentials, such as Fe(II) sorbed to iron oxides, have also been estimated with LFERs developed for aqueous Fe(II)-ligand complex (*336*). However, the predicted potentials vary substantially with contaminants used in the training data set (*336*).

Another approach to measuring the reduction potentials of reducing iron minerals involves using redox indicator or shuttle compounds that provides a redox couple that rapidly and reversibly equilibrates with the bulk redox active minerals in solution (*145*). If the redox couple behavior of indicator or shuttle is sufficiently ideal, then its speciation can be determined—e.g., spectrophotometrically—and used to calculate a redox potential for the system with the Nernst equation. Many redox indicators have been used to characterize the redox states of a variety of biogeochemical systems, including groundwater (*145, 146*), soil suspensions (*159*), and anaerobic sediments (*144, 147*). Some of these indicator/probes are the same as, or similar to, established electron transfer mediators (i.e., “ETMs” or “shuttles”) (*337*). The shuttle compounds have been widely used in studies of redox based biogeochemical processes, especially those involving iron (*241, 247, 338, 339*).

To explore the fundamental relationships between mineral reduction potentials and contaminant reduction kinetics, the present study applied redox indicator approach to systematically measure the reduction potentials of a range of reducing iron minerals. We, then, used the measured reduction potentials to correlate with the reduction kinetics of several probe contaminants with minerals that cover a range of reduction potentials to identify reactivity patterns. The redox indicators and probe contaminants represent *thermodynamic* and *kinetic* aspects of the system reactivity, respectively, and together are defined as *chemical reactive probes* (CRPs). Finally, we analyzed the reactivity data by combining our measured kinetic rate constants with prior reported rate constants for various contaminants including chlorinated ethenes, to examine whether a general pattern can be developed—despite different experimental conditions—to characterize abiotic NA processes.

4.3. Experimental

4.3.1. Chemical Reagents

All chemical regents were ACS reagent grade and used as received without further purification. Resorufin (Rsf) was acquired from Sigma Aldrich as sodium salt with 98% purity. 5,5'-indigodisulfonate (I2S) and 9,10-anthraquinone-2-sulfonate (AQS) were purchased from TCI America (Portland, OR), as disodium salt with greater than 95% purity. 9,10-anthraquinone-2,6-disulfonate (AQDS) was purchased from Combi-Blocks as disodium salt with 98% purity (San Diego, CA).

4.3.2. Preparation of Mineral Suspensions.

Goethite (GT), hematite (HT), and lepidocrocite (LP) were acquired from Bayferrox (Burgettstown, PA). These materials have been extensively characterized with respect to contaminant reduction by sorbed Fe(II) (*45*, *204*, *224*, *226*, *340*, *341*), and therefore were selected as model systems for studying sorbed Fe (II) onto iron oxides. Iron oxide suspensions were prepared by agitating powders in deionized water (DIW) overnight, vacuum filtered and resuspended in DIW. The suspensions were then deoxygenated by sparging with N_2 for 2 hours and stored in a N_2 filled anaerobic chamber (No H_2, $O_2 < 0.8$ ppm). Magnetite, sulfate green rust (GR-SO_4), chloride green rust (GR-Cl), and mackinawite (FeS) were synthesized inside the anaerobic chamber using well-established co-precipitation protocols adapted or modified from prior studies (detailed descriptions are provided in **Appendix C**). The resulting suspensions of the synthesized particles were centrifuged under N_2 atmosphere, washed with deoxygenated DIW (DO/DIW) at least three times, and resuspended in DO/DIW for batch experiments.

To prepare Fe(II) sorbed onto the three commercial iron oxides and synthetic magnetite, different amounts of Fe(II) stock solution (~100 mM) were added to the mineral suspensions with pH kept around 7.24 (or as noted) by 10 mM HEPES (initially adjusted with NaOH/HCl, as necessary) in amber serum bottles. The bottles were then crimp sealed and placed on an end-over-end rotator for ~20 h equilibration (t_{eq}).

4.3.3. Selection of Thermodynamic CRPs

The criteria for selecting thermodynamic CRPs used in this study included (*i*) standard reduction potentials that cover the redox range of expected potentials for the minerals and (*ii*) compatibility with subsurface solid matrix (e.g., minimal adsorption) such that they can eventually be applied to characterize porous media. The latter critically led us to exclude positively charged redox dyes, which have been successfully used in aqueous systems, but that are expected to sorb strongly to aquifer and sediment solids because the surfaces are mostly negatively charged (*147*). The four redox probes selected were resorufin (*Rsf*), and disulfonate (*I2S*), anthraquinone disulfonate (*AQDS*), and monosulfonate (*AQS*). All probes except Rsf are negatively charged due to the sulfonate groups, while Rsf is neutral but relatively hydrophobic. Although majority of the iron minerals included in this study commonly have PZC above pH 7, so they presumably have significant positive charge, the high solubility of the sulfonated CRPs resulted in negligible sorption in most cases. The standard reduction potentials of these probes at pH 7 range from −46 mV to −229 mV are given in **Table C.1**. Other properties of the probes (both oxidized and reduced forms), such as maximum absorption wavelength, molar absorptivity, and pKa's are also given in **Table C.1**.

4.3.4. Assay of Thermodynamic CRPs

The reactions of the redox probes with reducing mineral suspensions were evaluated by three types of experiments: (*i*) fixed loading of iron oxides with Fe(II) dose varied from 0.2 to 1.0 mM, and (*ii*) fixed dose of Fe(II) with varied mineral loadings, and (*iii*) varied mineral loadings without Fe(II). The first two sets were used to study Fe(II) sorbed onto iron oxides and the last set was used for magnetite, green rusts and FeS. Reactions between redox probes and minerals were carried out in 10 mL amber serum vials to avoid photo reactions involving the probes or Fe(II). Aliquots of deoxygenated probe stock solutions (~1 mM) were added to 5 mL mineral suspensions inside the anaerobic chamber, thereby giving an initial concentration of ~20 μM for Rsf and I2S and ~90 µM for AQS and AQDS. The reaction vials were crimp sealed with 20 mm viton septa (Sigma Aldrich) and placed on an end-over-end rotator overnight (45 rpm, t_{react}=20 h). Sample aliquots of 5 mL were then filtered by 0.2 µm nylon filters (Fisher) inside the anaerobic chamber. The first mL of filtrate was discarded and the rest was collected in 1-cm path length glass (for Rsf and I2S) or quartz (for AQS and AQDS) cuvettes, which were sealed by screw caps with 4 mm viton linings. The sealed cuvettes were removed from the anaerobic chamber and the absorbance spectra of the reduced probes were immediately measured with a UV−Vis spectrophotometer (Varian Bio 5). The reduced probes were then reoxidized by briefly exposing to ambient air to accurately determine the initial probe concentrations and assess probe adsorption.

4.3.5. Electrochemical Measurements

ORP measurements were performed following the protocols developed in our previous study with suspensions of nano zerovalent iron (nZVI) (*137*). A two electrode system was used with a 3 mm Pt rotating disc electrode (RDE) as the working electrode and an Ag/AgCl electrode (3 M KCl filling) as the reference electrode. Before each set of experiments, the Pt electrode was polished to avoid electrode fouling or memory effects, which are common causes for inconsistent results with a commercial ORP electrode. The experiments were carried out in a 10-mL electrochemical cell that was purged with Ar gas for at least 10 minutes before the mineral suspension was introduced. Aliquots of the suspension were withdrawn with a 10-mL syringe inside the anaerobic chamber, taken out of the chamber, and immediately injected into the electrochemical cell. The Pt electrode was immersed into the suspension and rotating at 2000 rpm to maintain mixing. The ORP data was recorded using an Autolab PGSTAT30 (EcoChemie, Utrecht, The

Netherlands) for 30 minutes, during which the headspace was continuously purged with Ar to maintain anoxic conditions.

4.3.5. Reduction of Kinetic CRPs

Three probe contaminants commonly used for characterizing reactivity of iron minerals were selected for batch tests, including carbon tetrachloride (CT), 4-chloronitrobenzene (4Cl-NB), and 2-chloroacetophenone (2-CAP) for majority of the minerals. All preparations were conducted in the anaerobic chamber unless otherwise mentioned. For volatile compounds including CT and TCE, an aliquot of stock solution was added into a ~19 mL mineral suspension in a 20 mL serum vial to an initial concentration of ~10 µM with minimum headspace. The vial was immediately crimp sealed with a viton septum, transferred out of the anaerobic chamber, and placed on an orbital shaker at 125 rpm in dark at 23ºC. At each sampling point, 0.25 mL mineral suspension was withdrawn after injecting 0.3 mL N_2 into the vial using a gas-tight glass syringe. The mineral suspension was injected into a headspace vial containing 2 mL DIW. After brief vortex, 100 µL headspace was sampled and VOCs were measured by a HP5890 gas chromatography equipped with an electron capture detector.

For 4Cl-NB and 2-CAP, the reactions were carried out in 60 mL amber serum bottles, crimp sealed with viton septa, containing an initial concentration of ~10 µM and ~50 µM, respectively. The reactors were mixed on the orbital shaker at 125 rpm at 23ºC. At each sampling time point, 2.5 mL aliquot was withdrawn and filtered by a 0.20 µm filter. The resulting filtrates were analyzed for disappearance of parent compounds by high performance liquid chromatography (HPLC).

4.4. Results and Discussion

4.4.1. Quantification of Thermodynamic CRPs

Building on the protocol developed and validated by Orsetti et al.(*142*) the amount of probe reduction by minerals was quantified based on the absorbance difference of the oxidized form before and after reoxidation at maximum absorbance wavelengths for each probe (in most cases). Interference from Fe(III) (due to oxidation of aqueous Fe(II)) was found negligible because the reoxidation of the reduced probes is much faster (a few seconds) than Fe(II) oxidation at neutral pH ($t_{1/2}$ = ~3 min).

4.4.2. Reduction of Thermodynamic CRPs by Fe(II) containing minerals

In preliminary experiments, each of the redox indicators was reacted with 1 mM aqueous Fe(II) in the absence of iron minerals. The absorbance spectra after 24 h reaction showed that Rsf was completely reduced, I2S was slightly reduced, and AQDS and AQS were not reduced significantly (data not shown). The pattern is consistent with the order of the redox potentials of the probes (Rsf > I2S > AQDS > AQS) and that aqueous Fe(II) is only a relatively weak reductant.

The range of CRP reactivity in the presence of Fe(II) and oxides was studied by varying several experimental variables, including mineral type, mineral loading, and initial Fe(II) concentration. Typical absorbance spectra measured are presented in **Figure 4.1** using lepidocrocite (LP) and 0.5 mM Fe(II) as an example. Each panel (except **Panel A**) shows three spectra for each probe: (*i*) before reoxidation, (*ii*) after reoxidation, and (*iii*) without oxide and Fe(II) (i.e., the buffer only control). In this case, adsorption of the probe was found to be significant only for Rsf, because the absorbance after reoxidation of the reduced Rsf was no difference from the reduced one. Our protocol cannot identify the redox states of sorbed Rsf, but we believe that the adsorbed Rsf is in the reduced form because no Rsf disappearance was found with LP + 0.2 mM Fe(II) compared to HEPES only (**Figure 4.1A**). If we consider Rsf is completely reduced by LP + 0.5 mM Fe(II), the pattern is then clear that the extent of probe reduction followed the order of Rsf > I2S > AQDS > AQS (**Figures 4. 1B–4.1D**), which is consistent with the order of reduction potentials of these three probes (cf., **Table C.1**).

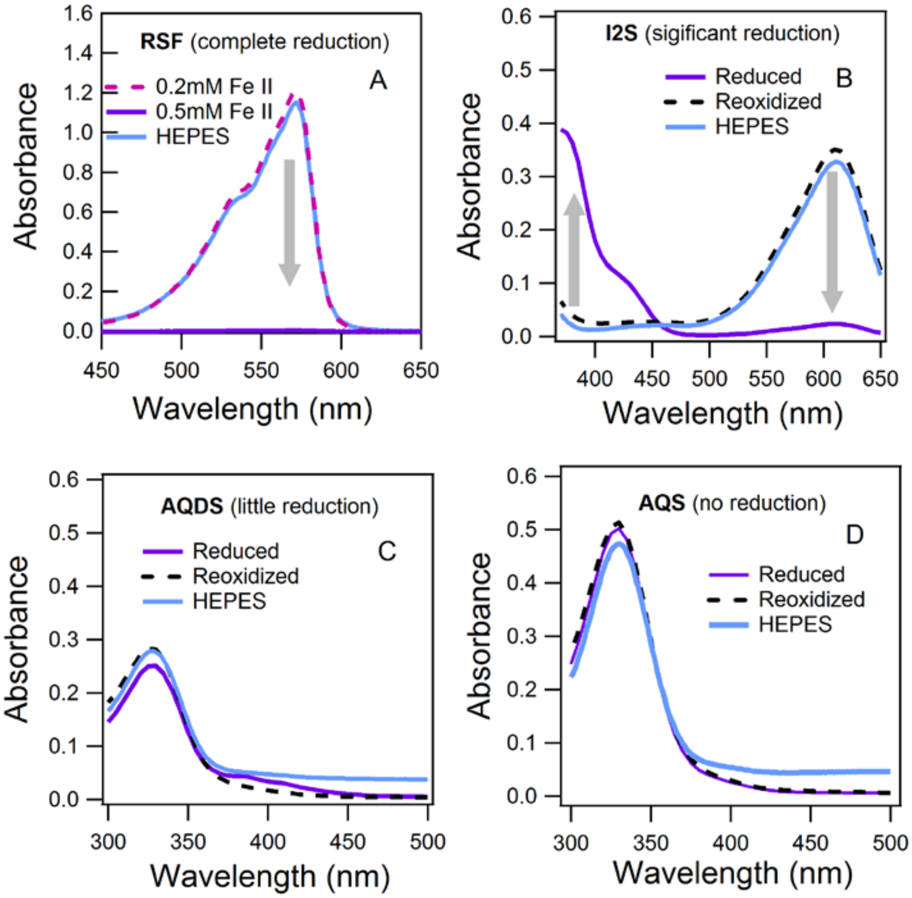

Figure 4.1. Absorbance spectra of (**A**) RSF, (**B**) I2S, (**C**) AQDS, and (**D**) AQS after reduction by lepidocrocite (LP) + 0.5 mM Fe(II), after exposing to ambient air and in HEPES only control (In panel A, no recovery of reduced rsf was observed after reoxidation. We additionally showed no disappearance of Rsf with LP + 0.2 mM Fe(II), suggesting reduced Rsf is likely adsorbed).

The effects of mineral type, mineral loading, and Fe(II) concentration on probe reduction are presented in **Figure 4.2** (only showing the spectra of reduced CRPs). **Figure 4.2A** shows that the extent of AQDS reduction varied among different iron oxides with 1 mM Fe(II) loading, ranging from no reduction for hematite, to partial reduction for lepidocrocite and magnetite, and to complete reduction for goethite. However, as goethite loading decreased from 3.0 to 0.3 g/L with 1 mM Fe(II) concentration, the amount of AQDS reduction decreased (**Figure 4.2B**). Comparison between **Figure 4.2C** and **4**.**2D** shows that partial reduction of AQS occurs over the entire Fe(II) range for magnetite, but only at the highest Fe(II) for goethite, which again implies that there are intrinsic differences among different underlying solid minerals. The combinations of probe and minerals over the range of experimental conditions tested in this study are summarized in **Table C.2**.

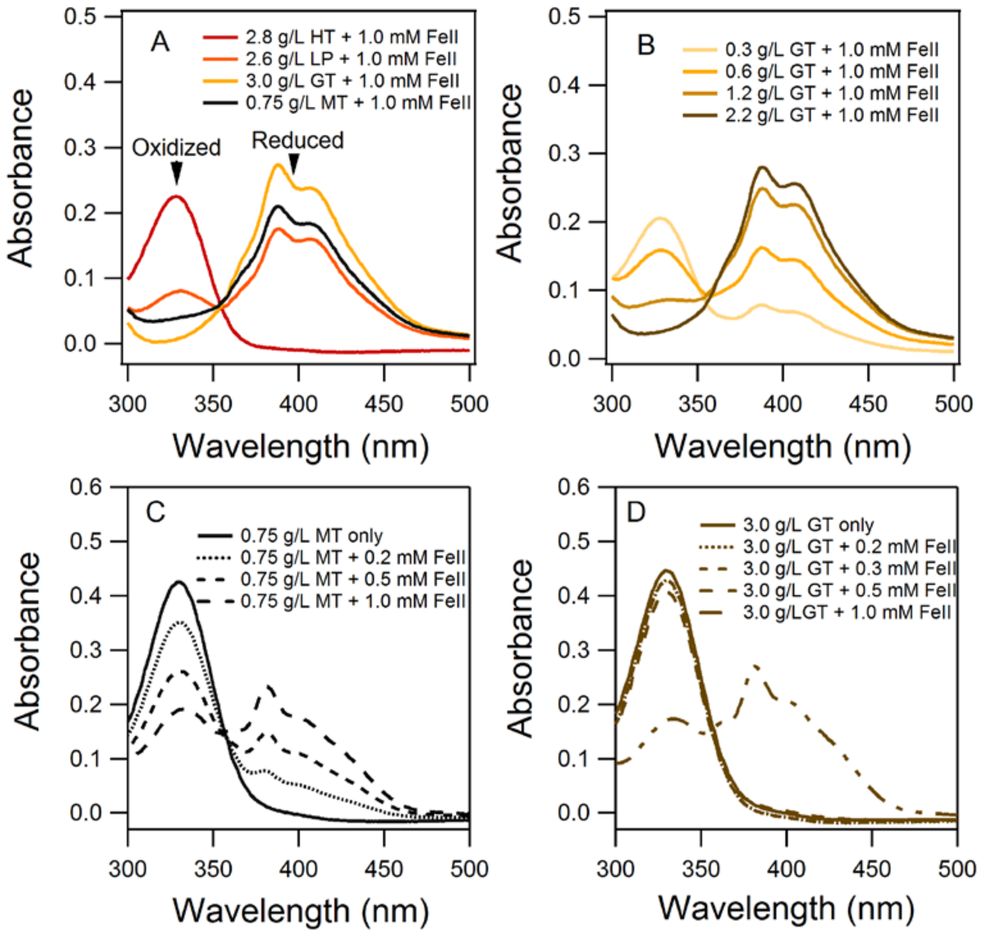

Figure 4.2. The effects of (**A**) oxide type, (**B**) goethite loading, (**C**) Fe(II) loading (magnetite), and (**D**) Fe(II) loading (goethite) on reduction of redox indicators by Fe(II) + iron oxide suspensions ([CRP] = ~90 µM, pH = 7.2 with 10 mM HEPES, t_{eq} = 20 h, t_{react} = 20 h, AQDS for (A) and (B); AQS for (C) and (D)).

4.4.3. Reduction Potential of Minerals Determined by Thermodynamic CRPs

The survey of probe reduction results represented by **Figure 4.2** was used to match appropriate CRPs for calculating reduction potentials for the various minerals. The reduction potential calculations require quantification of reduced and oxidized probe concentrations, which were determined from the absorbance spectra based on calibration curves. Probe results were not used if they gave too much (**Figure 4.1A**) or too little (**Figure 4.1D**) reduction, which we defined as 95% and 5%, respectively, for operational purposes. The matches between probe and reductant that we deemed suitable are summarized in **Table C.2**.

Assuming that equilibrium was reached between the oxide/Fe(II) system and the CRPs, reduction potentials were calculated from the CRP data (E_{CRP}), using the measured concentrations of oxidized and reduced forms of the CRP, the CRP's standard reduction potentials, and the Nernst equation (Eq.1). Note that the half-reactions involving these probes are pH dependent, and the calculations performed here were all done for pH 7.2. Additional pH effects due to the pKa's of specific oxidized and reduced forms of the CRPs are minimal near neutral pH (*142*, *342*) and therefore were neglected. For the conditions and assumptions that apply to this work, equation 1 can be further simplified to equation 2.

$$E_{\mathrm{CRP}} = E^0 + \frac{\mathrm{R}T}{2\mathrm{F}} \ln\left(\left[\mathrm{H}^+\right]^2 + K_{\mathrm{r1}}\left[\mathrm{H}^+\right] + K_{\mathrm{r1}}K_{\mathrm{r2}}\right) + \frac{\mathrm{R}T}{2\mathrm{F}} \ln\left(\frac{\left[\mathrm{CRP}_{\mathrm{ox}}\right]}{\left[\mathrm{CRP}_{\mathrm{red}}\right]}\right) \tag{1}$$

$$E_{\mathrm{CRP}} = E_7^0 + \frac{\mathrm{R}T}{\mathrm{F}}\, p\mathrm{H} + \frac{\mathrm{R}T}{2\mathrm{F}} \ln\left(\frac{\left[\mathrm{CRP}_{ox}\right]}{\left[\mathrm{CRP}_{red}\right]}\right) \tag{2}$$

Where E_7^0 is the standard reduction potential of the probe at pH 7, R is the gas constant, T is temperature, F is the Faraday constant, and [CRP_{ox}] and [CRP_{red}] are the concentrations of oxidized and reduced forms of the probe after reduction.

The mineral reduction potentials (E_{CRP}) calculated using eq. 2 are given in **Table C.3** and summarized in **Figure 4.3**. In **Figure 4.3**, each type of minerals tested is represented as a category (column), which is composed of several sub columns. Each sub column contains a series of mineral reduction potentials (horizontal markers) determined with one varied parameter (e.g., Fe(II) dose, mineral loading), which is indicated with bold labels above the corresponding sub column. At the lowest Fe(II) concentration tested (0.2 mM), reduction potentials are not available for hematite, lepidocrocite, and goethite because no probe reduction occurred, suggesting that their reduction potentials are out of the range of potentials that are accessible by the probes used in this study. With increasing Fe(II), the calculated reduction potentials decreased, as expected, for all oxides (**Figure 4.3**), but goethite gave a much wider range of potentials than hematite and lepidocrocite. Magnetite (0.75 g/L) without Fe(II) gave a negative potential around −180 mV, likely due to structural Fe(II), but only dropped ~30 mV as aqueous Fe(II) increased from 0.2 to 1.0 mM.

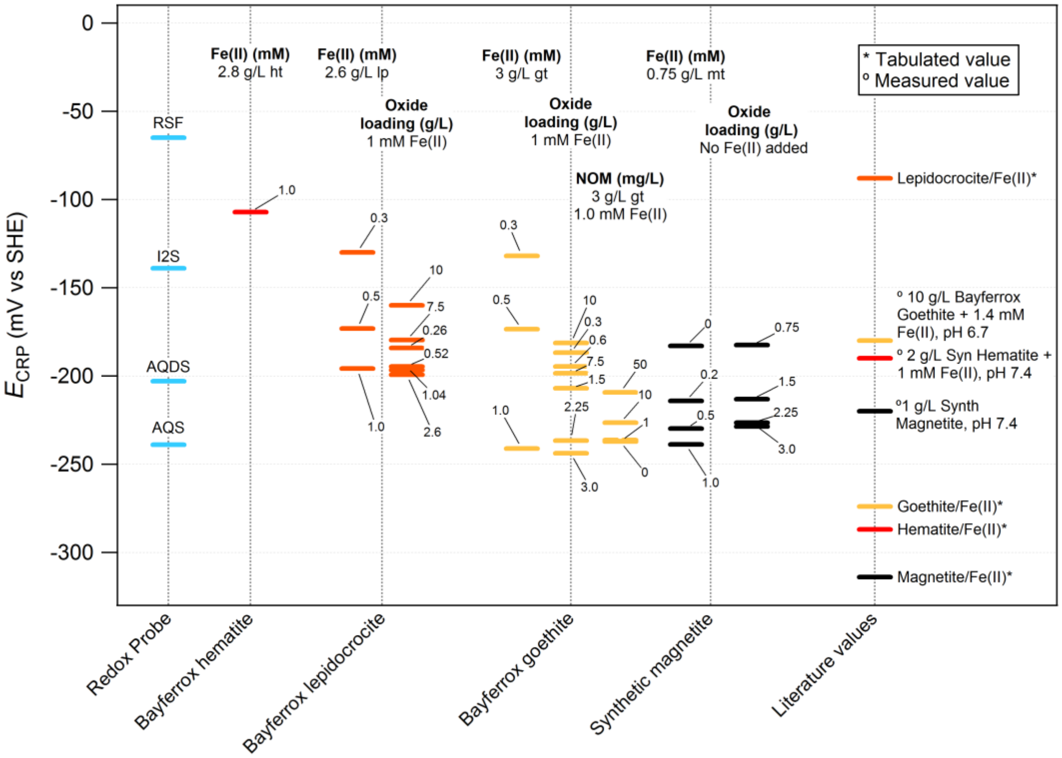

Figure 4.3. Summary of E_{CRP} values determined by redox indicators for different reducing iron minerals under various conditions (the specific value of the varied parameter is given at a tag on each E_{CRP} marker; the regular annotation above each sub

column indicates the constant experimental parameter used in that series of experiments; The reduction potentials of four redox indicators at pH 7.2 are plotted in the left most column for reference and the reduction potentials reported by prior studies are plotted in the right most column for comparison; Tabulated values are based on (*82*) and measured values are based on Orsetti et al.,(*142*) and Gorski (*143*)).

A particularly interesting trend in E_{CRP} was obtained by varying the mineral loading (with constant Fe(II) dose), which is shown in **Figure 4.4** for lepidocrocite and goethite with 1 mM initial Fe(II) concentration. The E_{CRP} (left axis), along with aqueous Fe(II) measured after 20 hr equilibration with the oxide but immediately before probe addition (right axis), is plotted as a function of increasing mineral loading. Constant initial Fe(II) allows differentiation of the effects of aqueous and solid Fe(II) on E_{CRP}. Aqueous Fe(II), as expected, showed monotonic decrease as mineral loading increased (**Figure 4.4**), because there was more iron oxide surface area to adsorb Fe(II). By contrast, the trend in E_{CRP} was bimodal with a minimum reduction potential at about 3 g/L for goethite and 2.7 g/L for lepidocrocite. This trend cannot be explained by the changes of either quantity of sorbed Fe(II) or density of sorbed Fe(II) because both of them were monotonic with Fe(II) dose. Instead, the observed pattern suggests that both aqueous and solid Fe(II) contribute to determining E_{CRP}. This result may be analogous to those reported in several recent studies of Fe(II) adsorption onto iron oxides where it was concluded that excess aqueous Fe(II) significantly lowered the contaminant reduction rates by sorbed Fe(II) onto Fe(III) oxides (*105, 222*).

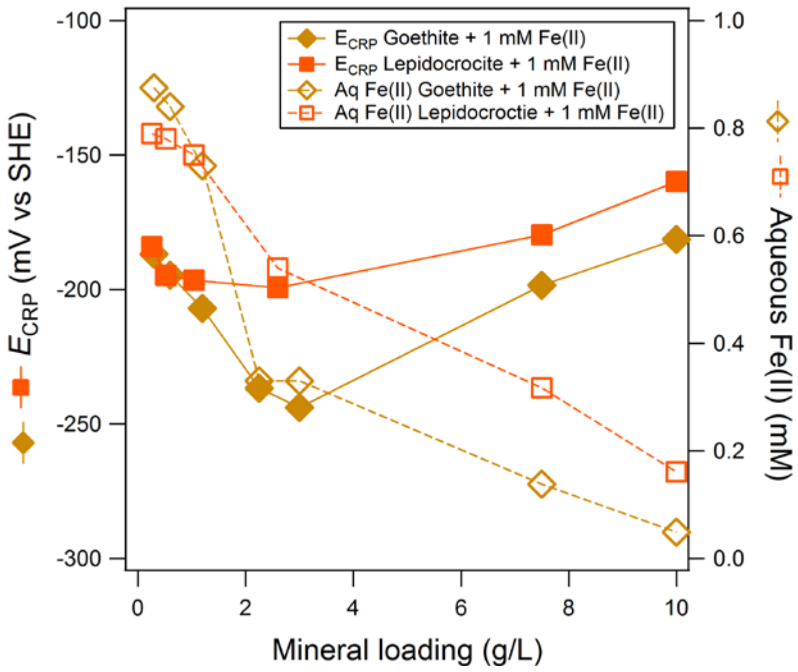

Figure 4.4. E_{CRP} (left) and aqueous Fe(II) (right) as a function of mineral loading for goethite and lepidocrocite at 1 mM Fe(II) loading (E_{CRP} values were taken from Figure 4.3, pH = 7.2, t_{eq} = 20 h, t_{react} = 20 h).

4.4.4. Comparison with Prior Literature

For comparison with the potentials obtained in this study, previously reported reduction potentials for Fe(II) based minerals were compiled and summarized in **Table C.4–C.7** and **Figure 4.3**. The measured potentials for Fe(II) adsorbed onto goethite reported by Orsetti et al.(*142*) and for Fe(II) adsorbed synthetic hematite and magnetite reported by Gorski (*143*) are of particular interest for two reasons. First, both studies used redox mediators to facilitate equilibration with surface species, as we did in this study, and therefore the reduction potentials were calculated based on the same principle. Secondly, the mineral phases used in those studies are the same as some of those used in this study (for goethite, we used the same product from Bayferrox as Orsetti et al. (*142*) and for magnetite, we based our synthesis on the recipe described in Gorski (*143*)).

In general, E_{CRP} values obtained in this study agree well with the previous values various redox indicators and reported as E_h. For example, the E_h for 10 g/L goethite with 1.4 mM Fe(II) determined by AQDS at pH 6.7 ranged from −180 to −160 mV (*143*), which agrees well with the value of −181 mV that was measured in this study for 10 g/L goethite with 1 mM Fe(II) at pH 7.2 (**Figure 4.3**). The E_h of stoichiometric magnetite at pH 7.4 measured by viologen (*143*) also falls into the range of magnetite reported here. By contrast, the synthetic hematite showed a much lower reduction potential than the Bayferrox hematite (*143*), presumably because the two materials differed greatly in preparation method, degree of crystallinity, degree of hydration, etc.. This is also consistent with the substantially faster reduction of CT obtained with synthetic hematite (*343*) than Bayferrox hematite (*224*).

4.4.5. Comparison with Electrochemically Measured ORP

For comparison with the values of E_{CRP} summarized in **Figure 4.3**, conventional ORP measurements were made by open circuit chronopotentiometry (CP) on suspensions of hematite, lepidocrocite, goethite, and magnetite with a range of initial Fe(II) concentrations. The ORP vs time profiles obtained by CP are shown in **Figure C.2A.** For each time series, the lowest ORP value (ORP_{min}) was selected because ORP rebound eventually occurred in most cases (**Figure C.2A**), likely due to intrusion of trace quantities of oxygen intrusion into the electrochemical cell, as we discussed previously(*137*). Plotting the data for ORP_{min} vs. Fe(II) concentration (**Figure C.2B**) shows several trends that were qualitativly consistent with E_{CRP}: (*i*) ORP_{min} followed the same order as hematite > lepidocrocite > goethite, (*ii*) the ORP_{min} of goethite covered a wider redox range with increasing Fe(II) than other oxides, and (*iii*) the decrease in

ORP_{min} of magnetite with Fe(II) was small. However, quantitatively, the electrochemically-measured reduction potentials, E_{Pt} (derived from ORP_{min}) where more positive than the E_{CRP} by about 150–200 mV (**Figure C.2C**). It is worth noting that the ORP_{min} of mt + 1 mM Fe(II) was ca. 50 mV more negative than that of gt + 1 mM Fe(II), but the E_{CRP} values were very close between the two as shown in **Figure 4.3**. This is likely due to better conductivity and small particle size of magnetite, resulting improved electrode response. In fact, magnetite at all Fe(II) concentrations gave the least difference between the two measurements (closest to the 1:1 diagonol line).

The overall interpretation of ORP results reported here is consistent with prior studies suggesting conventional electrode potential measurements of ORP are not sufficient for quantitative determination of reduction potentials of sorbed Fe(II) mineral suspension. As indicated in our earlier papers empolying ORP to detect nZVI(*81*, *137*), particle size, aggregation, reductant strength, and solution species all affect electrode response. For Fe(II) containing minerals, which are much weaker reductants than nZVI, electrode responses are less likely to be dominated by the solid reductants and interference from other factors might be more significant.

4.4.6. Kinetic CRPs and Links to Mineral Reduction Potential

The kinetics of reduction of 4Cl-NB, 2-CAP and CT were measured for various combinations of Fe(II) and iron oxides, and other Fe(II) bearing minerals (summarized **Table C.3**) with conventional batch experiments. 4Cl-NB and CT have been widely used as probe compounds in studies of the reactivity of reduced iron minerals, and 2-CAP has been as a probe for to identify reductants and reduction pathways (*344*). Data on a variety of mineral phases were included, representing a range of reduction potentials (e.g., as measured by *E_{CRP}*) to test for general trends in reduction rate constants of CRPs versus mineral reduction potentials. The reduction of the three probes were fit to pseudo-first order kinetics, after excluding deviations (tailing) that was were observed towards the end of the experiments in a few cases (**Figure C.3**). No additional effort was made to quantify the reduction products, as the reduction pathways for these probe compounds have been investigated in detail in prior studies (*45*, *344*, *345*).

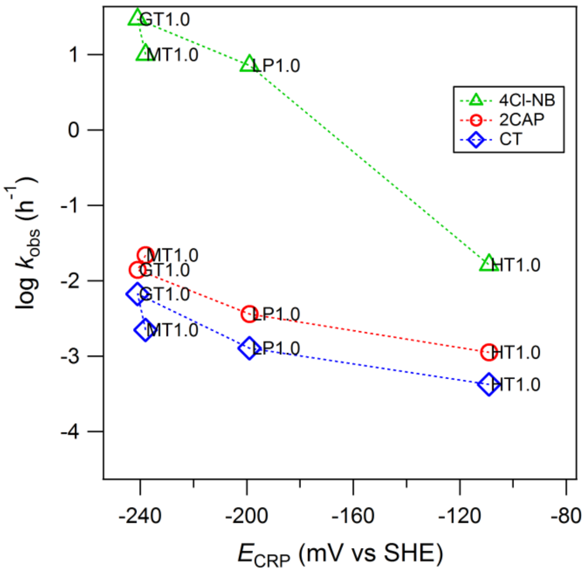

Figure 4.5. Pseudo-first order reduction rate constants (k_{obs}) of 4Cl-NB, 2-CAP, and CT by reducing iron minerals as a function of mineral reduction potentials determined by thermodynamic CRPs (E_{CRP}) (oxide type and Fe(II) concentration for each data point are annotated next to the marker).

Figure 4.5 presents the measured reduction rate constants (k_{obs}) for three kinetic CRPs with respect to the mineral reduction potentials (E_{CRP}) determined by the redox indicators. In general, a consistent trend was observed with respect to both contaminant/probe and iron oxide: k_{obs} for the three probe/contaminants followed 4Cl-NB >> 2CAP >CT and increased as the E_{CRP} of the mineral became more negative.

However, within these trends, kinetic effects arising from specific mineral-contaminant interactions are also apparent. For example, the reduction rate constants of CT by GT+1.0 mM Fe(II) was ~4 times faster than MT+1.0 mM Fe(II), even though their reduction potentials (E_{CRP}) only differed by 5 mV (**Figure 4.3**). In the case for 2-CAP reduction, however, the reverse order of reactivity was observed with magnetite and goethite. It is well known that heterogeneous reduction depends on surface properties. For different contaminants, specific surface interactions may vary among different minerals even though their reduction potentials are similar. This suggests that LFERs for contaminant reduction kinetics by minerals maybe be significantly more difficult to establish than those for solution phase reductants (like aqueous Fe(II)-ligand complex (*14, 15*)).

The reduction rate constants of CT and 4Cl-NB measured in this study were combined with other kinetic data from previous studies for reduction of nitroaromatics (represented by NB and 4Cl-NB), chlorinated alkanes (represented by CT and HCA), and chlorinated ethenes (represented by TCE and PCE) and are summarized in Tables **C.4─C.7**. This compilation provides a sufficiently large kinetic dataset to allow a comprehensive meta-analysis of the reduction kinetics of contaminants by reducing iron minerals. The whole dataset is shown in **Figure 4.6A** as log of the mass normalized reduction rate constants (log k_M) of each type of the contaminant reduced by each type of the minerals. The x-axis is ordered by the apparent reactivity of reducing minerals ranking from low (left) to high (right). First, it can be seen that that the k_M values measured in this study (solid symbols) are within the range reported by prior work. As expected, various degrees of data scattering were observed among different studies, due to the diversity in experimental conditions, including mineral sources, pretreatment, addition of Fe(II), buffer selection or pH, etc. For example, the primary cause for scatter k_M in data for CT reduction by magnetite appears to be the different synthesis recipes adopted by different studies (**Table C.4**), whereas the major factor that results in scatter k_M for chlorinated ethene reduction by FeS appears to be whether freeze drying is used in mineral pretreatment (**Table C.7**). Despite this high degree of variability in k_M due to operational conditions, the data for each class of contaminants form relatively confined clusters with positive slopes (i.e., faster reduction rates by more strongly reducing minerals). Three parallel dashed lines are drawn to emphasize these general trends in the data. The vertical separation on the bands defined by classes of contaminants indicates that reduction rate constants of nitroaromatics generally are more than two orders of magnitude faster than chlorinated alkanes, and the chlorinated alkanes are at least another two orders of magnitude faster than chlorinated ethenes.

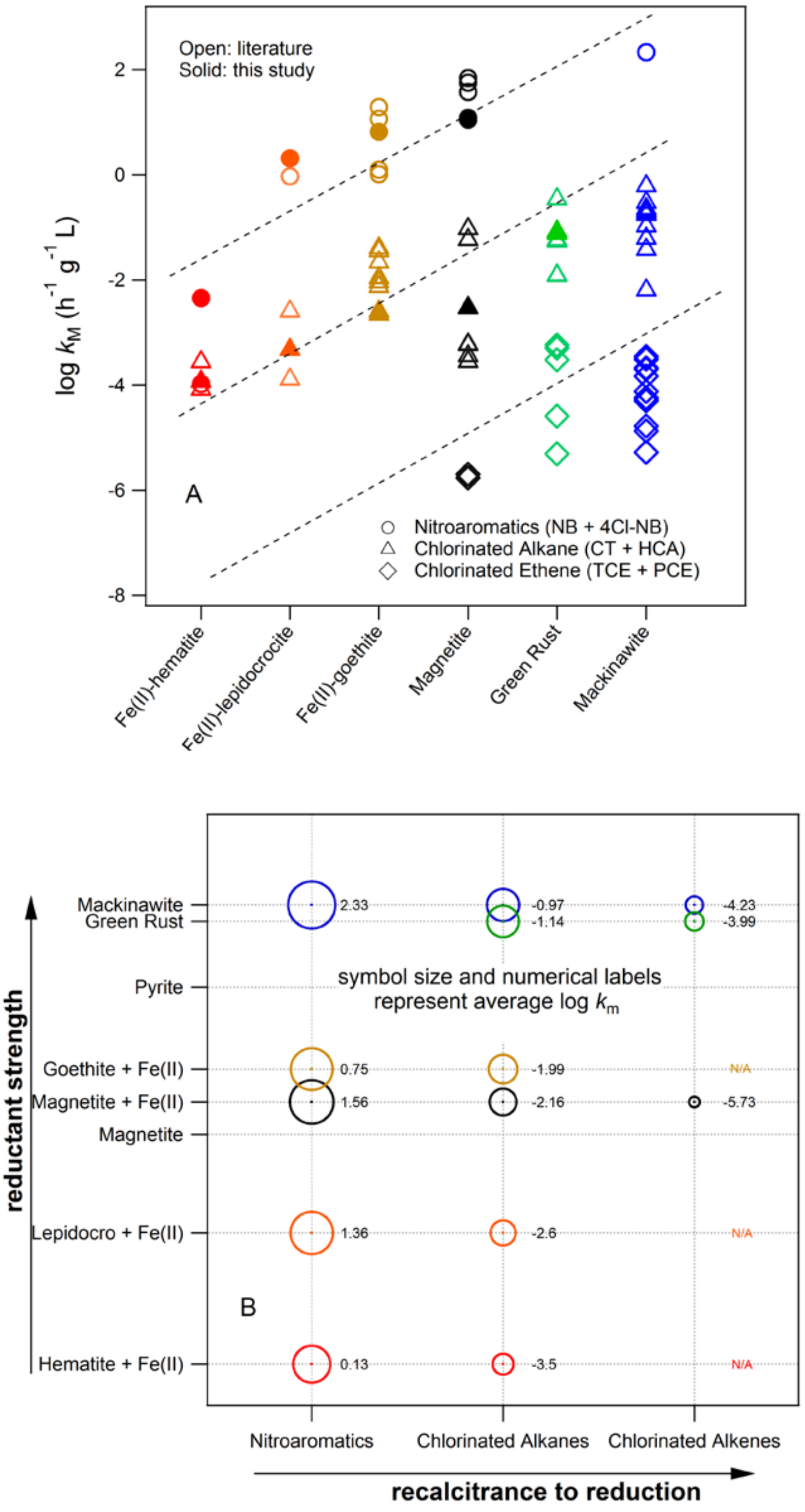

Figure 4.6. (**A**) Mass normalized reduction rate constants (k_M) of kinetic CRPs (including nitroaromatics and chlorinated alkanes) and chlorinated ethenes with various reducing

iron minerals (open symbol: value reported in literature; solid symbol: value determined in this study). (**B**) Bubble plot of average log k_M values (size of the bubble) for each combination of contaminant and mineral obtained in literature with respect to the mineral reduction potential determined by thermodynamic CRPs. (y-axis).

We further investigated whether the reactivity pattern identified by the kinetic CRPs can be explained by the mineral reduction potentials determined by thermodynamic CRPs. To incorporate data from prior work, we assumed that the values of E_{CRP} obtained in this study are representative of the minerals used in prior studies. This assumption is reasonable given overlap between the mineral phases used in this study (both commercial and synthesized) with the materials commonly used in other work. This allowed us to combine new and literature data on a quantitative axis for mineral reduction potential, as shown in **Figure 4.6B**. This "bubble plot" ranks the reduction rate constants of three classes of contaminants (x-axis) based on the E_{CRP} measured by the thermodynamic CRPs (y-axis). For simplicity, (*i*) the reported log k_M values for each combination of contaminant and mineral summarized in **Figure 4.6A** were averaged, which is represented by the size of the bubble; and (*ii*) only one E_{CRP} value was assigned to each mineral as an approximation based on measured or extrapolated values from the probe measurements, despite that the reduction potential should be represented by a range of values depending on various factors (**Figure 4.3**).

Decreasing circle size along the horizontal axis is another presentation showing decreasing k_M from nitroaromatics to chlorinated alkanes, then to chlorinated ethenes. More interesting (perhaps less apparent) is the second pattern along the y-axis. For all three contaminants, the reduction rates (the bubble size) decrease as the reduction potential of minerals become more positive, which is consistent with the experimental data shown in **Figure 4.5**. It should be noted that the reduction potentials of FeS and green rust are below the range of the CRPs we selected, but are expected to be much lower than other iron oxides due to higher Fe(II) percentage as well as based on electrode measurements by several prior studies (*58, 100*). In general, it appears to be true that the lower the mineral reduction potentials are the higher rates of abiotic reduction are. Fe(II) sorbed onto iron oxides that have no data reported for reduction of chlorinated ethenes are also the ones with more positive reduction potentials. However, the lack of laboratory measured reduction does not necessarily mean their negligible effects in long-term abiotic NA in field because the time frame for NA is usually much longer than that can be used for reliable kinetic measurement in laboratory. For this reason, the option for relying on fast reacting CRPs is appealing if a quantitative relationship can be further developed between the reduction of CRPs and chlorinated ethenes by reducing iron minerals.

4.6.7. Implications

The CRP-based methods developed in this study can be used in laboratory studies of fundamental aspects of redox reactions involving reducing iron minerals. The qualitatively consistent trends between experimentally measured reduction rate constants of kinetics CRPs and the mineral reduction potentials determined by thermodynamic CRPs suggests a promising linkage between the two core concepts involved in abiotic contaminant reduction. This result is further supported by comparison with previously published literature data, which shows conforms to the same pattern of reactivity with different minerals (and their corresponding reduction potentials) among three classes of contaminants, despite significant degree of experimental variability.

To apply CRPs in natural medium to assess abiotic natural attenuation, further validation with subsurface materials is necessary to confirm whether the reactivity patterns observed with the model mineral systems exist with the field samples. Although the thermodynamic CRPs were selected with consideration of their compatibilities with subsurface matrix materials, the overall behavior of thermodynamic CRPs in complex environmental samples may differ from the results obtained in this model system studies, for several reasons. For example, dissolved Fe(II) concentration in the field rarely exceed 5 mg/L, which is about 5-fold lower than the Fe(II) concentration used in model mineral suspension. In contrast, Fe(II) associated with mineral solids might be higher in natural materials due to the higher solid to water ratio. A field study that concluded abiotic NA of *cis*-DCE was occurring by naturally-occurring magnetite estimated the loading of magnetite to be10 g/L based on magnetic susceptibility (*155*). In low permeability zones, the solid Fe(II) content can reach up to a few mmole per gram, Therefore the Fe(II) loading in pore space (mmole/L) could be much higher given the porosity is much lower in rock matrix (*153*). Under such conditions, in a highly heterogeneous system, it is possible that the CRPs used to characterize reducing conditions thermodynamically, might be useful to characterize the kinetics of reduction processes as well.

Compared with the proposed application of thermodynamic CRPs, kinetic applications of CRPs are more similar to methods that currently are in use. Although validation of the conceptual models with field samples is currently limited by the data availability, the reactivity pattern observed with chemically synthesized reductants should extend to environmental reductants provided the same thermodynamic principles that control the reduction processes. As the next step, field samples from sites with demonstrated abiotic NA might be good candidates for further investigation.

4.5. Acknowledgments

This material is based on work supported by the Strategic Environmental Research and Developmental Program of the U.S. Department of Defense, Award Number ER-2308.

Chapter 5 Characterizing the Reactivity and Transformation of Carboxymethyl Cellulose Modified Nano Zerovalent Iron Using Chemical Redox Probe: A Field Deployable Approach[4]

Dimin Fan, Shengwen Chen, Richard L. Johnson, and Paul G. Tratnyek

5.1. Abstract

Nano zerovalent iron synthesized with carboxymethylcellulose (CMC-nZVI) has emerged as a leading formulation of nZVI for in-situ groundwater remediation, mainly because of the stability and mobility of its suspensions. However, the fate of CMC-nZVI remains poorly characterized, in part because the available characterization methods are inadequate. Most of the frequently used methods to detect nZVI impacted zones, such as total iron concentration and oxidation-reduction potential (ORP), are not specific for nZVI (because they are influenced by ZVI-related species such as Fe(II) and H_2). This study demonstrates a simple and specific colorimetric approach for detection and characterization of CMC-nZVI using indigo disulfonate (I2S) as a chemical redox probe (CRP). The apparent stoichiometric ratio of reaction between I2S and nZVI was measured to be 1.45±0.033, which suggests that I2S reduction to the dihydro-product is coupled to complete oxidation of nZVI to Fe(III). To describe the kinetics of I2S reduction, a second-order kinetic model was required because the concentrations of I2S and nZVI were comparable to each other. At neutral pH, I2S reduction in the presence of

---

[4] Prepared as a research paper to be submitted to *Environmental Science & Technology*

CMC-nZVI was selective for Fe(0) because aqueous Fe(II) reduced I2S at very slow rates ($t_{1/2}$ > 24 h). However, adding Fe(II) to CMC-nZVI gave enhanced I2S reduction rates, likely due to enhanced corrosion induced by Fe(II). The consumption of Fe(0) in CMC-nZVI by anaerobic corrosion was quantified using I2S and found to be orders of magnitude faster than previously reported values for conventional nZVI. The effect of this reductant demand was accelerated by dilution and lowing of the pH. Overall, these results provide basis for developing a novel and field-deployable method for characterizing nZVI in field applications.

5.2. Introduction

Biogeochemical transformations of engineered nanomaterials (ENMs) significantly affect their fate, transport, and reactivity in environment (*76, 78*). Nano zerovalent iron (nZVI) is unique among ENMs in that it is deliberately released into the environment under conditions that take advantage of its high reactivity (e.g., for reduction of contaminants in groundwater). Due to its high reactivity under relevant environmental conditions, biogeochemical transformations of nZVI result in substantial "aging" of the material. This process affects the kinetics, capacity, and pathways by which it interacts with contaminants (*78, 79*). For example, detailed studies of the aging products formed from RNIP—one of the first commercial nZVI products for remediation—showed significant loss of Fe(0) and formation of other iron mineral phases after one month exposure to anoxic water (*38*, *78*, *79*) and common groundwater constituents (*80*). Using another commonly studied type of nZVI (synthesized with borohydride), we showed that sulfidic groundwater conditions result in formation of iron sulfides, which completely shifts the sequestration pathway for technetium (*80*, *125*).

However, these and most other studies of nZVI transformation (or aging) have been conducted in batch systems without the stabilizers used to make nZVI useful in field applications, which leaves considerable uncertainty regarding the fate of stabilized nZVI under field conditions.

Many methods for improving the stability of nZVI suspensions have been investigated (*38, 39, 346, 347*), but the most widely used method for field-scale groundwater remediation applications involves nZVI synthesized in the presence of carboxymethyl cellulose (CMC) (*41-43, 348*). Despite extensive characterization of the physical properties of CMC-nZVI, its chemical transformations after emplacement have received little attention. Several field studies have noted transformation of CMC-nZVI after emplacement, including oxidation to Fe(III) (*41*) or Fe(0) loss (*349*), but the results are mostly descriptive. The lack of quantitative data on the chemical transformation of CMC-nZVI is in large part due to limitations of the conventional tools for characterizing CMC-nZVI. The quasi-liquid character (*350*) of CMC-nZVI suspensions, which significantly improves the mobility of this type of ENM, also makes conventional methods of analyzing the solution and solid phases (e.g., X-ray absorption spectroscopy (*137*), X-ray diffraction (*137*)) inapplicable because the aqueous and solid phases cannot be separated or even concentrated by filtration or centrifugation.

To date, most studies have used total iron measurement to track the transport of CMC-nZVI. Some rely on indirect indicators of nZVI that arise from reactions of nZVI with the medium after emplacement, such as oxidation-reduction potential measurement (ORP) (*137*). Both methods are widely used in the field because they are operationally easy and the data are intuitive to interpret, but neither of them is specific to nZVI. Total iron measurement, by definition, does not differentiate various iron species among Fe(0), Fe(II) and Fe(III), whereas ORP measurement with a platinum (Pt) electrode gives mixed potentials due to its response to multiple electroactive species (*137*). As a result, potentials measured under complex geochemical conditions are not adequate to differentiate Fe(II) from nZVI, especially at low nZVI concentrations and when hydrogen is present. In a recent field-scale injection study (*41*), direct spectrophotometric measurements on groundwater samples impacted by CMC-nZVI was used to distinguish reduced and oxidized forms of nZVI. However, this approach cannot differentiate dissolved Fe(II), one of the major products of nZVI corrosion under anoxic conditions, from Fe(0) and its response to other transformation products from nZVI (e.g., iron sulfides) is unknown.

Methods for determining Fe(0) in (n)ZVI suspensions from measurements of H_2 production have been described by Liu et al. and Reardon et al. (*78, 337*). These methods involve digestion of ZVI by acidification, followed by measurement of the produced H_2 by volumetric determination or by gas chromatography. These approaches are applicable to laboratory studies as well as ex situ analysis of samples taken during field demonstrations, but work best at relatively high doses of nZVI (on the order of g/L). In field applications of nZVI, high concentrations fo Fe(0) are only expected in slurry prior to injection and maybe in samples collected close to injection with respect to both space and time. For a groundwater sample containing 100 mg/L Fe(0), to get a 50 mL H_2 evolution would require acid digestion of ca.1.2 L sample, which is not operationally practical. Much lower concentrations of dissolved H_2 can be measured by gas chromatography, but precautions must be ensured that the analyzed samples are representative of the field conditions. Given the high reactivity of nZVI, any analysis method that involves sample transport is likely to give results conflated with effects of aging the nZVI.

In this study, we describe a simple and yet powerful, potentially field-deployable method for determining nZVI concentration and reactivity using indigo 5,5’-disulfonate (I2S) as a chemical redox probe (CRP). Although I2S and other redox active dyes have long been used in characterizing the redox properties of geochemical systems (*144, 337*), most of these studies have been focused on using probe equilibrium to describe the thermodynamic conditions of the system. In nZVI containing systems, characterizing thermodynamic conditions is less useful because (*i*) the relevant species (Fe(0), Fe(II), Fe(III), H_2, and etc.) are far from equilibrium with each other, and (*ii*) any Fe(0) containing system has more than enough thermodynamic potential to effect reduction of most contaminants. Instead, kinetic and capacity considerations are of more interest and more useful in evaluating field implementations because these aspects are directly determinative of the rate and extent of contaminant degradation that can be achieved. In the present study, we designed the experiments in such a way that I2S, a traditional thermodynamic probe, serves mainly as a CRP for kinetic and a capacity aspects of CMC-nZVI transformation and reactivity, thereby providing new insights into the factors that control the overall performance of ZVI and other remediation technologies based on chemical reduction.

5.3. Experimental

5.3.1. Chemical Reagents

All chemical regents except indigo 5,5’-disulfonate (I2S) were ACS reagent grade and used as received without further purification. I2S was purchased from TCI America (Portland, OR), as the disodium salt, 95% purity.

5.3.2. Synthesis of CMC-nZVI

CMC-stabilized nZVI suspensions were synthesized following the procedure we used in Johnson et al.,(*41*) which was based on the method developed by He et al.(*39*) The suspension was prepared in 50 mL batches in a 120 mL serum bottle, while purging the suspension with N_2 purge throughout the synthesis process. Starting with a CMC solution (0.5%, w/w) prepared in DI water, $FeSO_4 \bullet 7H_2O$ salt was added to give an Fe(II) concentration of 1 g/L. The solution was mixed for 10 min to allow Fe(II)–CMC complex development. A 10-mL solution containing 0.0675 g of $NaBH_4$ (twice the stoichiometric amount needed to completely reduce Fe(II) to Fe(0)) was then introduced into the Fe(II)–CMC solution dropwise with continuous swirling by hand. After completion of $NaBH_4$ addition, the reaction was given additional 10 min for H_2 evolution to cease. The bottle containing the nZVI suspension was then crimp sealed and moved into an anaerobic chamber (100% N_2, $O_2 < 0.8$ ppm). The suspension was prepared daily and used immediately.

5.3.3. CMC-nZVI Incubations

Several experimental variables—including CMC-nZVI concentration, pH, and aging time—were chosen to simulate the scenarios that are likely to result in transformation of CMC-nZVI during its transport in the subsurface. Accordingly, CMC-nZVI suspension (1 g/L) was diluted to target concentrations with DO/DI water and 10 mM HEPES buffer into 12 mL serum vials, adjusted to various solution conditions, and crimp sealed. The incubation time varied up to 30 h, which was chosen to represent the initial time period of rapid reactions when CMC-nZVI is first introduced into the subsurface (based on the results of the pilot injection we described in Johnson et al. (*41*))

5.3.4. Probe Assay

At each sampling point, the incubated CMC-nZVI suspension was further diluted with DO/DI to give 2–10 mg/L total iron with a final volume of 3.8 mL inside a 1 cm cuvette. 10 mM HEPES buffer was included at this step because it was necessary to avoid pH effects on probe reduction rate and absorbtivity of the probe. The cuvette was sealed with a viton-lined screw cap. Aliquots of ~4 mM I2S stock solution were withdrawn with a 1-mL plastic syringe. Then the cuvette and the syringe were transferred out of the anaerobic chamber. Because the oxidized form of I2S has maximum absorbance wavelength at 610 nm (**Appendix D, Figure D.1**), the initial absorbance at 610 nm contributed by CMC-nZVI was measured (Lambda 20 UV-vis spectrophotometer). The probe solution (~0.17 mL) was then injected into the cuvette through the septum to make an initial I2S concentration around 140 µM. The cuvette was mixed by hand for 5 sec and placed into the UV-Vis spectrophotometer. The decrease in absorbance at 610 nm was recorded as a function of time (10–15 min). After the reduction step, the solution was reoxidized by brief exposure to ambient air and the absorbance was measured again in order to determine the exact initial I2S concentration.

5.3.5. Transmission Electron Microscopy

Samples for TEM were prepared by applying a 5 µL drop of CMC-nZVI suspension onto a Cu-carbon grid and letting it dry overnight in the anaerobic chamber on a filter paper. The samples were then sealed under N_2 and transported to the imaging facility. During the sample loading, there was approximately 1 min exposure to the ambient atmosphere. The TEM images were taken by FEI Tecnai F-20 Transmission electron microscope.

5.4. Results and Discussion

5.4.1 Probe Properties

The oxidized form of I2S ($I2S_{ox}$) is bright blue (λ_{max} = 610 nm) and the reduced form ($I2S_{red}$) is pale yellow (λ_{max} = 407 nm) at neutral pHs. The absorbance spectra of the oxidized and reduced forms are shown in **Figure D.1**. The standard reduction potential of I2S at pH = 7 is −0.125 V vs SHE,(*342*) and therefore the reduction of I2S by nZVI is thermodynamically strongly favorable given the much lower reduction potential of Fe(0)/Fe(II) couple (−0.410 V vs SHE at pH = 7). At the concentrations used in this study (~140 µM), the reduction of I2S is easily detected by the visible change from blue to yellow.

Scheme 5.1. Two-electron reduction reaction of indigo disulfonate.

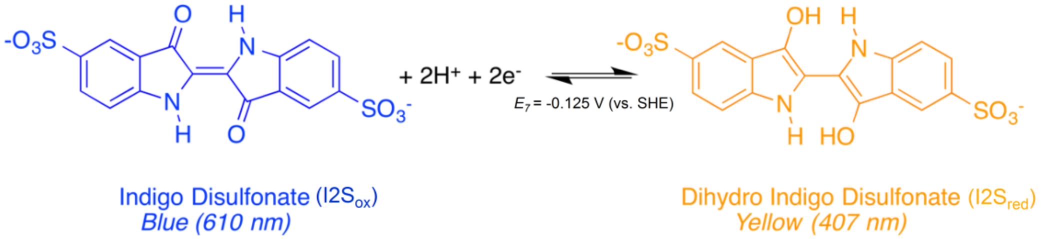

5.4.2. Determining Apparent Stoichiometry

As shown in **Scheme 5.1**, the reduction of I2S to the dihydro-form involves two electrons and two protons. If Fe(II) is the end product of nZVI oxidation, a 1-to-1 stoichiometric ratio between I2S reduced and CMC-nZVI oxidized is expected. To examine the reaction stoichiometry, the molar ratio of nZVI (defined by the total iron) to I2S was varied from 0.25 to 1.25 with a fixed I2S concentration of ~140 µM. Dilution of nZVI to concentrations in the µM range is necessary to (*i*) slow the initial rate of I2S reduction and (*ii*) minimize interference from the absorbance of CMC-nZVI at the monitored wavelength.

Figure 5.1A shows the change of absorbance due to reduction of $I2S_{ox}$ over time at different CMC-nZVI concentrations. At the highest nZVI concentration (10 mg/L), the absorbance decreased quickly, but then plateaued out at about 0.1. In contrast, at nZVI concentrations below 5 mg/L, the absorbance decreased more slowly and leveled out at higher plateaus. At high iron doses, the bright yellow color of the aqueous phase was consistent with full conversion to $I2S_{red}$, so the plateau in absorbance at 610 nm must be due to excess nZVI. At lower nZVI doses (2 and 4 mg/L), the blue color of the aqueous phase indicates complete consumption of nZVI, so the plateaus observed in these experiments must be due to excess $I2S_{ox}$.

To quantify the I2S concentration, absorptivity at 610 nm was determined for individual species that could potentially contribute to suspension absorbance, including $I2S_{ox}$, $I2S_{red}$, nZVI, Fe(II), and $nZVI_{ox}$. The results showed that $I2S_{ox}$ contributes the majority of the absorbance at 610 nm and nZVI contributes less than 10%. Neither $I2S_{red}$ nor $nZVI_{ox}$ absorbed measurably at that wavelength (**Figure D.2**). Therefore, for each

I2S reduction experiment, if I2S was in excess, the amount of I2S reduction was determined by the difference between initial absorbance of I2S and plateau absorbance, whereas nZVI was determined based on initial absorbance before I2S addition. In contrast, if nZVI was in excess, the amount of CMC-nZVI oxidation was calculated based on the difference between initial absorbance before I2S injection and the final absorbance (because $I2S_{red}$ showed little absorbance at 610 nm). For the majority of experiments, a smaller dose of nZVI was used to leave excess $I2S_{ox}$, because the larger absorptivity $I2S_{ox}$ gave more reliable measurements. Plotting the amount of I2S reduction against the amount of nZVI oxidation for each experiment (**Figure 5.1B**), shows that reacted I2S and nZVI correlate linearly with the slope of 1.45±0.033. This ratio is significantly greater than the 1-to-1 stoichiometry assuming Fe(II) is the oxidation end point. In addition, this relationship appears to apply to both freshly prepared and aged samples.

Since reoxidation of the aqueous suspension at the end of the experiments showed complete recovery of the initial absorbance at 610 nm, adsorption of $I2S_{ox}$ to the solids was not responsible for a greater than expected disappearance of $I2S_{ox}$. Thus, other reductants must be contributing, which could include residual $NaBH_4$ from the nZVI synthesis and aqueous Fe(II) or Fe(II) solid phases generated by nZVI oxidation. Unreacted $NaBH_4$ is expected to be minimal as the borohydride was dosed exactly twice as much as the Fe(II) concentration to ensure complete consumption during synthesis. The possibility of reduction by aqueous Fe(II) was excluded, as well, because it reduced I2S at a much slower rate at pH 7.2 (**Figure D.3**), which leaves solid phase Fe(II) as the only likely candidate. Although no direct evidence regarding the speciation of solid-phase Fe(II)—e.g., Fe(II) minerals or Fe(II) sorbed onto Fe(III) oxides—was obtained in this study, its presence and role in reducing I2S are supported by the electron equivalence calculations described above. Recall that the apparent reaction ratio between I2S and nZVI was close to 1.5 (**Figure 5. 2B**). Given that the reduction of 1.5 mole I2S$_{ox}$ requires three moles of electron, this ratio of 1.5 can only be met if three moles of electron are solely supplied by one mole of nZVI, which indicates complete oxidation of Fe(0) to Fe(III). Since oxidation of Fe(0) to Fe(III) proceeds via Fe(II) but aqueous Fe(II) hardly reduces I2S at the observed rates, solid Fe(II) must be formed as an intermediate.

The reason that the calculated stoichiometry was slightly less than 1.5 is likely due to the parallel reaction of nZVI with water during I2S reduction. Control experiments without adding I2S showed up to 10 % CMC-nZVI consumption by DO/DI water at pH 7.2 after 15 min exposure to water (**Figure D.3**). Although adjusting reaction pH to 8.5 appears to inhibit nZVI dissolution (**Figure D.3**), additional experiments found that aqueous Fe(II) caused fast and appreciable I2S reduction only at pH 8.5 (**Figure D.4**). For freshly-prepared nZVI, this reaction is not expected to produce substantial interference as dissolved Fe(II) should be minimal (see discussion below). However, it will compromise the diagnostic response of I2S to nZVI in the field because aqueous Fe(II) is almost certain to coexist with nZVI as the major corrosion product.

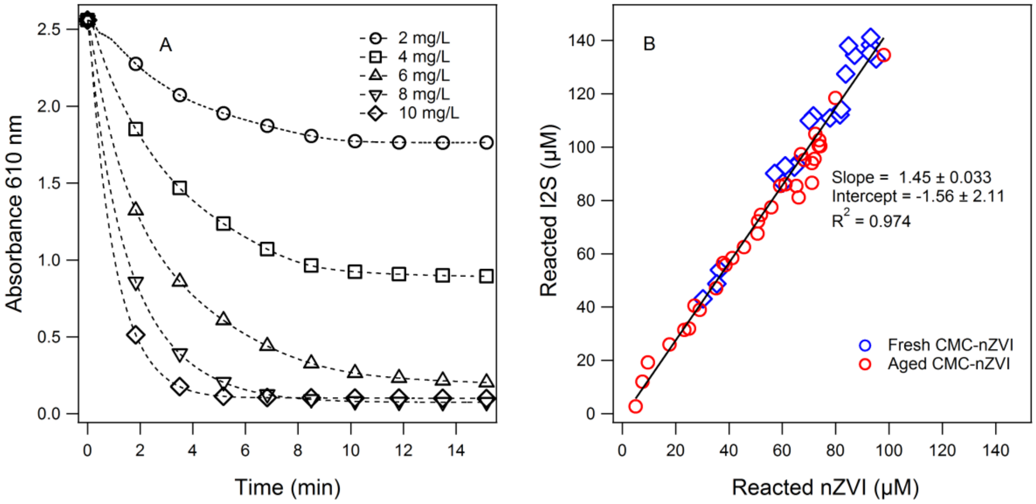

Figure 5.1. Determination of the apparent stoichiometry of I2S reaction with nZVI: (**A**) decrease in aqueous absorbance at 610 nm due to reduction of I2S$_{ox}$ by freshly-prepared 1 g/L CMC-nZVI diluted to initial concentrations from 2 to 10 mg/L (Absorbance was measured in a sealed glass cuvette with 1-cm path length. Data was recorded continuously but markers are shown every 1000 data points), (**B**) Correlation between the amount of I2S reduction and nZVI oxidation for fresh and aged CMC-nZVI (Open symbols are experimental data with each point derived from an individual I2S reduction curve exemplified in **A** and solid line is linear fit).

5.4.3. Fitting Second Order Kinetics

As neither nZVI nor I2S was in greater excess, the requirement for commonly-applied pseudo first-order was not met (*338*). Instead, the second-order kinetic model was adopted based on a previous study on reduction of lepidocrocite by anthrohydroquinone disulfonate (AH$_2$DS), which shows similar characteristics to I2S reduction by nZVI (*338*). Several simplifying assumptions were made: (*i*) Fe(0) and intermediate solid phase Fe(II) were treated as a single reductant, (*ii*) the reaction rate was first order with respect to both nZVI and I2S, and (*iii*) the stoichiometric ratio between I2S and nZVI was 1.5 based on determined reaction stoichiometry. The overall reaction is expressed by eq 1:

$$2\mathrm{Fe}^0 + 3[\mathrm{I2S}_{\mathrm{ox}}] + 6\mathrm{H}_2\mathrm{O} \rightarrow 2\mathrm{Fe}^{3+} + 3[\mathrm{I2S}_{\mathrm{rd}}] + 6\mathrm{OH}^- \qquad (1)$$

where $[\mathrm{I2S}_{\mathrm{ox}}]$ is the oxidized form and $[\mathrm{I2S}_{\mathrm{rd}}]$ is the reduced form. The reaction rate (*r*) is described by eq 2:

$$\mathrm{r} = \frac{\mathrm{d}[\mathrm{I2S}_{\mathrm{ox}}]}{\mathrm{dt}} = \mathrm{k}[\mathrm{I2S}_{\mathrm{ox}}][\mathrm{nZVI}] \qquad (2)$$

where $[\mathrm{I2S}_{\mathrm{ox}}]$ is the concentration of oxidized I2S, *k* is the second order reaction rate constant ($\mu\mathrm{M}^{-1}\ \mathrm{min}^{-1}$), [nZVI] is the concentration of nZVI. The concentration of $\mathrm{I2S}_{\mathrm{ox}}$ at any given time can be obtained by solving eq 2, as shown in eq 3:

$$[\mathrm{I2S}_{\mathrm{ox}}]_t = [\mathrm{I2S}_{\mathrm{ox}}]_0 - \frac{1.5 \times [\mathrm{I2S}_{\mathrm{ox}}]_0 \times [\mathrm{nZVI}]_0 \times (\mathrm{e}^{[\mathrm{nZVI}]_0 \mathrm{kt}} - \mathrm{e}^{2/3[\mathrm{I2S}_{\mathrm{ox}}]0\mathrm{kt}})}{1.5 \times [\mathrm{nZVI}]_0 \times \mathrm{e}^{[\mathrm{nZVI}]_0 \mathrm{kt}} - [\mathrm{I2S}_{\mathrm{ox}}] \times \mathrm{e}^{2/3[\mathrm{I2S}_{\mathrm{ox}}]\mathrm{kt}}} \qquad (3)$$

where $[\mathrm{I2S}_{\mathrm{ox}}]_0$ is the initial oxidized I2S concentration, $[\mathrm{nZVI}]_0$ is the amount of nZVI reacted, and *k* is the second-order reaction constant. The latter two parameters were determined by fitting.

As can be seen from **Figure 5.2A**, this approach fit the data very well, indicating that second-order kinetic model is adequate for describing the kinetics of I2S reduction by CMC-nZVI. Slight discrepancies between the fitting and the experimental data towards the end may reflect errors introduced by (*i*) small contributions of nZVI (< 5%) to the overall absorbance (**Figure D.2**), which was not included when calculating I2S concentrations, or (*ii*) the simplified assumption by mathematically treating nZVI and solid Fe(II) as a single reductant. We chose only to fit the data where nZVI was completely consumed (2 and 4 mg/L total iron) because (*i*) as stated earlier the amount of I2S reduction can be more accurately determined than the amount of nZVI oxidation due to high absorptivity of oxidized I2S and (*ii*) excess nZVI leaves uncertainty with respect to the first hypothesis for applying the second order kinetic model.

Another way to examine the fitting quality is to compare the molar concentration of reacted nZVI determined by fitting ($[nZVI]_0$ in eq. 3) and calculated based on initial absorbance before I2S addition for the subset of the data we fit (**Figure 5.2B)**. It can be seen that the fitted values, in general, agree well with the calculated values, further suggesting that the second-order kinetic model is appropriate to describe the kinetics of I2S reduction by CMC-nZVI under the experimental conditions investigated here.

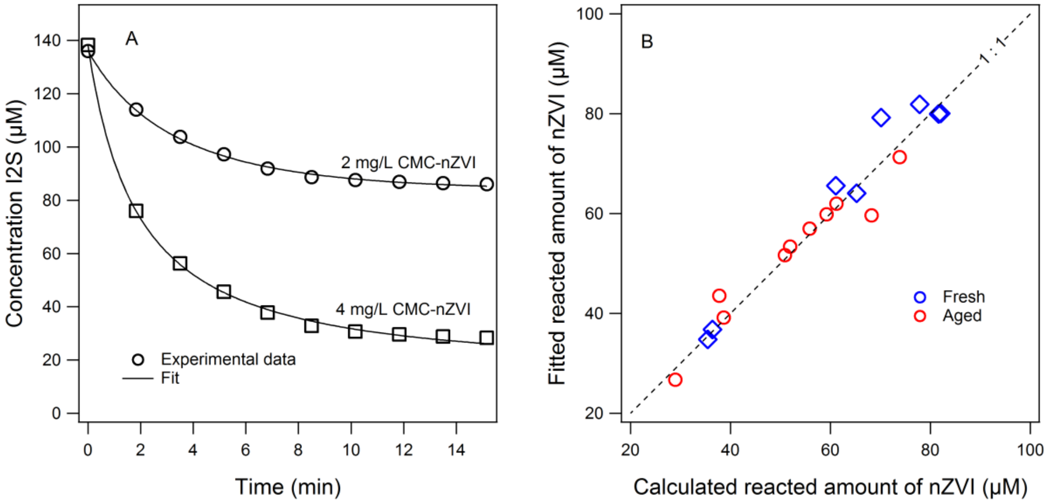

Figure 5.2. Second-order kinetic modeling of I2S reduction: (**A**) Fitting of representative data for I2S reduction by freshly-prepared CMC-nZVI diluted to 2 and 4 mg/L in pH 7.2 HEPES buffer (the concentration was calculated based on the absorbance data shown in **Figure 5.1A**), (**B**) Correlation between reacted nZVI determined by fitting and reacted nZVI determined by absorbance.

5.4.4. Distinguishing Fe(II) from Fe(0)

The negligible rate of I2S reduction by aqueous Fe(II) alone at pH 7.2 (**Figure D.3**) suggests that I2S may be used as a chemical redox probe (CRP) to distinguish aqueous Fe(II) from Fe(0), which is a prerequisite for quantifying Fe(0) content. **Figure 5.3A** shows the reduction of I2S at pH 7.2 by mixtures composed of different proportions of aqueous Fe(II) and CMC-nZVI, all with 10 mg/L total iron concentration. For comparison, data obtained at the same nZVI concentrations but without added aqueous Fe(II) are also included in the figure. It can be seen that with the same total iron concentration, a higher proportion of nZVI results in more I2S reduction. Aqueous Fe(II) did not appear to provide additional reduction capacity, as the I2S reduction with or without added Fe(II) reached similar plateau concentrations for all nZVI concentrations. The amount of I2S reduction is approximately 1.5 times greater than the amount of nZVI oxidation in these experiments—consistent with the reaction stoichiometry determined above—further confirming that aqueous Fe(II) is not directly responsible for reduction of I2S.

Figure 5.3A also shows that adding Fe(II) to CMC-nZVI resulted in faster I2S reduction rates than CMC-nZVI without Fe(II), especially at the lower nZVI concentrations (2 and 4 mg/L). Further experiments were conducted using 4 mg/L nZVI with added Fe(II) from 0 to 15 mg/L and the data was also fitted to the second-order kinetics (**Figure 5.3B**) with the rate constants plotted against aqueous Fe(II) in **Figure 5.3C** (left axis). Clearly, increasing aqueous Fe(II) progressively increased the rate of I2S reduction rates. The fitted results also revealed a subtle decrease of the amount of I2S reduction with increasing Fe(II) (right axis in **Figure 5.3C**), indicating that the presence of Fe(II) might slightly enhance the reaction rate of nZVI with water as well, resulting in less Fe(0) to reduce I2S. The enhanced reaction rates by Fe(II) is consistent with several previous studies showing that the presence of Fe(II) contributes to depassivation of aged ZVI by adsorption of Fe(II) to the oxide film, thereby enhancing the reduction rate of target contaminants (*351*). Under the strictly anoxic conditions of this study, there should be little if any Fe(III) oxide on the unreacted nZVI. This suggests that the positive effects of aqueous Fe(II) on enhancing reduction rates of probes/contaminants might apply in non-aged (n)ZVI systems as well.

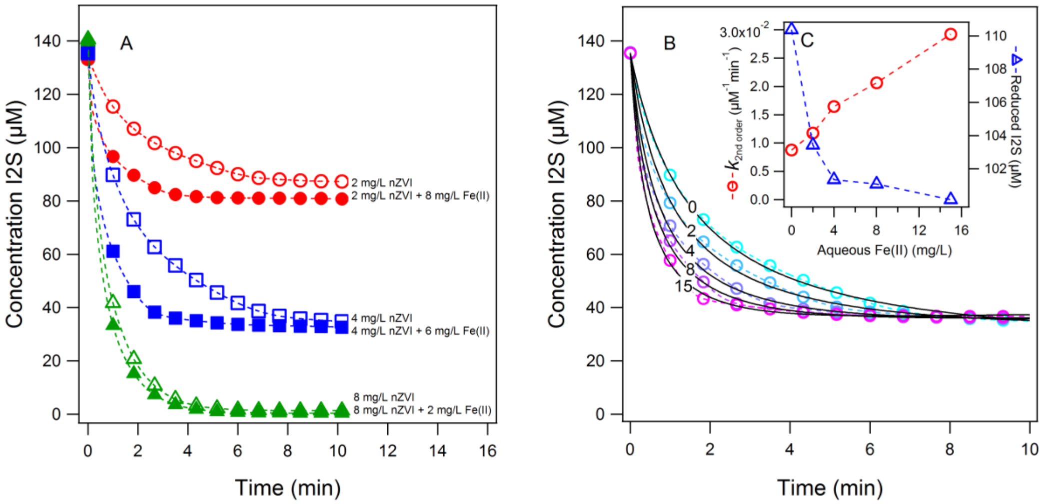

Figure 5.3. Distinguishing Fe(II) from Fe(0) by I2S: (**A**) I2S reduction by mixtures of Fe(II) and CMC-nZVI with the total iron concentration of 10 mg/L and equal concentrations of nZVI without Fe(II). (**B**) I2S reduction by 4 mg/L CMC-nZVI with aqueous Fe(II) concentrations from 0 to 15 mg/L (open symbols are experimental data, and solid lines are second-order kinetic fits). (**C**) Second-order rate constant (left axis) and reduction capacity (right axis) extracted from fitting the data in **Figure 5.3B**.

5.4.5. Quantifying nZVI Lifetime in Water

One of the practical issues that can be addressed by using I2S as a CRP concerns the corrosion of nZVI in water, which can be a major source of demand on the capacity of ZVI to affect contaminant reduction. Compared to conventional H_2 measurement, which either requires substantial samples or off site gas chromatography, reaction with I2S only requires small sample volume (<1 mL) and can be performed on site, and therefore is more suitable for quantifying Fe(0) recovered from subsurface after injection.

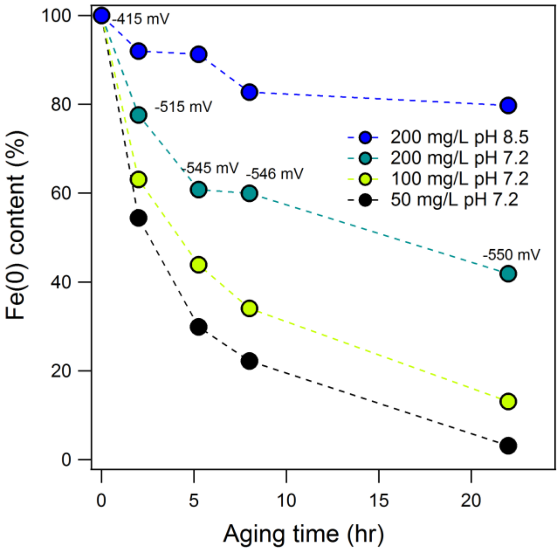

Figure 5.4. Quantifying nZVI lifetime by I2S: kinetics of Fe(0) loss in water with 50, 100, and 200 mg/L initial nZVI concentrations in 10 mM HEPES buffer of pH 7.2 and 200 mg/L initial nZVI concentration in 10 mM HEPES buffer of pH 8.5 (each data point was determined by I2S reduction by nZVI sampled at that time point diluted to 4 mg/L total iron).

To test the applicability of I2S in quantifying Fe(0) reaction with water, the loss of Fe(0) as a function of time at different initial nZVI concentrations (50, 100, and 200 mg/L) and pHs (7.2 and 8.5) was measured, which is shown in **Figure 5.4**. The concentration and pH ranges were chosen because dilution and pH decrease occur during/after injection of nZVI. Field studies of nZVI transport after injection show decreased nZVI delivery with increasing distance from the injection point, due to combined effects of dilution, adsorption, dispersion, and reaction (*41*). pH decrease following the initial rise in monitoring well after nZVI injection has also been observed in field studies (*349*).

With increasing initial concentration of nZVI, the rate of Fe(0) consumption decreased (**Figure 5.4**). At 50 and 100 mg/L CMC-nZVI concentration, nearly 50% of the Fe(0) was oxidized (by H_2O, under strictly anaerobic condition) within 3 hrs. This result suggests that there should be substantial consumption of ZVI over the timeframe of typical laboratory experiment, but this reductant demand has been neglected in prior studies (*352*, *353*). Given the large difference in terms of reactivity between Fe(0) and Fe(II), relying on total Fe measurement as the main parameter to characterize nZVI transport may significantly overestimate the quantity of Fe(0) delivered and the potential for contaminant reduction.

The kinetics of nZVI consumption were fitted to pseudo-first order kinetics and the k_{obs} values obtained for Fe(0) loss (0.72–3.60 d^{-1}, depending on initial nZVI concentration) is several orders of magnitude greater than previously reported oxidation rates for commercial nZVI in anoxic water, determined by measuring H_2 evolution (6×10^{-3} d^{-1} for RNIP (*78*) to 2.72×10^{-2} d^{-1} for NANOFER (*354*)). The large difference in oxidation rates by water between CMC-nZVI and other types of nZVI is likely due to greater dispersion of CMC-nZVI (or less aggregation), which expose more surface area to react with water.

Another variable shown in **Figure 5.4** is the pH. It can be seen that Fe(0) loss at 200 mg/L was significantly slower in pH 8.5 HEPES than in pH 7.2 HEPES. Slower Fe(0) loss was also observed for original CMC-nZVI suspension, which had high concentration (1 g/L) and high pH, and for 200 mg/L nZVI aged in DO/DI water without buffer (**Figure D.5**). It is worth noting that for the latter experiment, initial Fe(0) loss was still fast (slope similar to 200 mg/L nZVI in pH 7.2 buffer) but inhibition gradually developed, presumably due to the pH increase caused by reaction with unbuffered water (pH ~9 at the end of experiment). These results are consistent with a previous study that showed H_2 production for RINP was inhibited at high pH (*78*). In that study, the formation of iron oxides such as Fe_3O_4 or green rust was invoked as a potential explanation for suppressing H_2 production. While Fe_3O_4 formation was highly plausible in that study (e.g., by the Shickorr reaction (*81*)), it is uncertain whether the same process is responsible for the decreasing Fe(0) loss at higher pH in this study. Considering electron equivalence, reduction of one mole of I2S by Fe_3O_4, would require a stoichiometry of 1:2, corresponding to 6 mole of Fe(0). If a significant amount of Fe_3O_4 is forming during the aging process, the ratio between I2S and nZVI should be substantially lower than 1.5. However, the ratio remained around 1.4 over the course of experiment at pH 8.5 without a notable decreasing trend (data not shown). Nevertheless, the possibility of forming a thin layer of Fe_3O_4 —which might not alter the observed stoichiometry detectably— cannot be excluded. Detailed characterization of surface layer mineralogy would be needed to address this issue, but was not performed as part of this study.

Oxidation reduction potential (ORP), another commonly used indicator for nZVI in studies of emplacement and transport (*81*), was also measured in this study using a combination ORP electrode for 200 mg/L nZVI in pH 7.2 buffer. These data (shown as annotations in **Figure 5.4**) show a trend that is opposite to that of the Fe(0) content determined by I2S reduction. In general, more positive ORPs are expected with lower nZVI concentrtions, although a number of complicating effects have been identified (*81, 137*). In this case, despite 20% Fe^0 loss during the first 2 hours, the ORP value dropped about 100 mV to −550 mV, possibly due to the sensitivity of the Pt electrode to dissolved

H_2, which increased due to the oxidation of nZVI by water. The ORP decreased further and then reached a plateau, which also is not consistent with the continuous loss of Fe(0). The fact that we did not observe this behavior in our early study(*137*) might be due to much slower reaction of RNIP with water and constant headspace purging to displace H_2 during measurement, both resulting in less interference from H_2. Based on the extensive discussion presented in that study, the failure of our ORP data to correlate to Fe(0) content is most likely due to the shifts in the relative contributions of the other species that contribute to the mixed potentials measured by the electrode (mainly Fe(II) and H_2). Therefore, under field conditions, ORP measured with a conventional Pt electrode should be cautiously used as a qualitative instead of quantitative indicator of nZVI presence.

5.4.6. Microscopy Evidence

TEM images of selected samples were obtained, in order to provide visual evidence to support the interpretations made based on the probe results described above. The probe data shown in **Figure 5.4** and **Figure D.5** indicated after 24 h aging, the original CMC-nZVI and 200 mg/L CMC-nZVI in DO/DI water had significantly less Fe(0) loss than 200 mg/L CMC-nZVI in pH 7.2 HEPES buffer. Here we compared TEMs obtained for these three conditions. **Figure 5.5A** shows that despite 24-h aging, the morphology of the original CMC-nZVI particles was consistent with that reported in prior studies (*349*). The individual nZVI particles appear as dark spheres with diameter ranging from 20 to 60 nm (**Figure 5.5A**). For 200 mg/L nZVI aged in DO/DI water for 24 h, however, the integrity of individual particles was substantially degraded (**Figure 5.5B**). Given that the initial pH was similar (above 9) between original CMC-nZVI and 200 mg/L CMC-nZVI in DO/DI water, the most likely remaining cause of this morphological change is the concentration of nZVI. In a previous field study, little morphological change was found between injected CMC-nZVI and CMC-nZVI recovered from adjacent monitoring well after 5 h injection (*349*). The difference could be due to the effects of water chemistry of that specific site, which is not included in the scope of this study.

For nZVI aged in pH 7.2 buffer, two types of structures can be seen in the TEMs. One type showed similar morphology to the original nZVI but the interior was less well defined (Inset in **Figure 5.5C**). The other type, observed only in HEPES buffer at pH 7.2, consists of chain-like aggregate composed of very fine particles (< 5 nm). It remains unclear whether the latter particular morphology originated from the suspension or precipitated on the grid during the drying process. We speculate the latter might be the case because formation of ferrous hydroxide is not favored at this pH even when 200 mg/L Fe(0) is completely converted to Fe(II). The absence of this type of structure in the other two samples further suggested this fine structure might indeed result from artifacts of dissolved Fe(II), which is not favored at high pH. This supports our interpretation that fast corrosion at neutral pH produces dissolved Fe(II), which results in less I2S reduction capacity (**Figure D.5**). In the last sample, where 100 mg/L nZVI was completely consumed by adding high dose of I2S (**Figure 5.5D**), the original nZVI structure was not observed at all. Instead, <10 nm particles were prevalent, presumably as the iron(III) oxide particles.

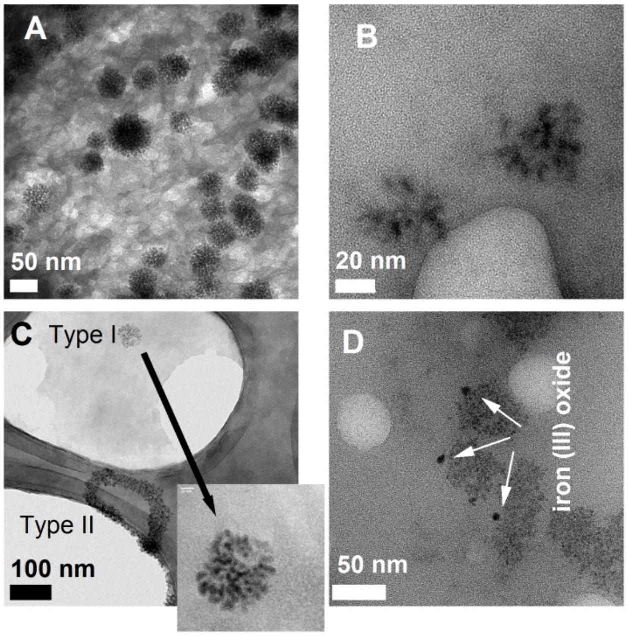

Figure 5.5. Transmission electron micrographs of CMC-nZVI (**A**) original CMC-nZVI aged for 24 h, (**B**) 200 mg/L CMC-nZVI aged for 24 h in DO/DI water, (**C**) 200 mg/L CMC-nZVI aged for 24 h in pH 7.2 HEPES buffer, and (**D**) 100 mg/L CMC-nZVI after complete oxidation by I2S.

5.4.7. Implications for Field Applications

The major advantage of using I2S as a CRP to characterize nZVI, compared with the total iron and ORP measurements, is the selectivity of I2S to Fe(0) but not to other redox active species. The rapid reduction of I2S by nZVI minimizes the interference from I2S reduction by other coexisting dissolved reductants (e.g., Fe(II)), which reduce I2S at much slower rates. This selectivity for Fe(0) could be especially useful in characterization of field deployments of nZVI, where the presence of multiple redox active species and complex water chemistry are expected to compromise the ability of conventional methods to detect nZVI. In addition, successful quantification will allow incorporation of transformation element to the current reactive-transport model of nZVI to better predict nZVI delivery in column studies and field applications.

Although measuring the initial absorbance of nZVI suspension without I2S can be used to quantify nZVI concentration in laboratory (**Figure D.2)**, it will likely be less reliable in field applications because of interference from background turbidity or absorbance in natural groundwater samples. The CPR approach, on the other hand, is less susceptible to interference by background absorbance because only absorbance reduction is required for calculating nZVI concentration.

A simple protocol for field deployment is to inject a known volume of water sample containing nZVI into a deoxygenated and buffered solution with known concentration of I2S in a sealed vial. After injection, the absorbance change at 610 nm can be readily recorded by a portable spectrophotometer. Assuming the stoichiometric ratio calculated in **Figure 5.1B**, the concentration range of nZVI should be diluted to less than half of the initial I2S concentration to ensure complete consumption of nZVI. An appropriate dilution factor can be pre-determined by estimating the initial nZVI concentration in the water samples by either total iron or absorbance measurement.

The CRP approach can also be applied in a broader context to improve the future design of nZVI for higher compatibility in field applications. Currently, the application of nZVI for large-scale groundwater remediation is limited by the limited transport and longevity of nZVI. During the process of nZVI design and synthesis, these two objectives often compete with one another and are difficult to reconcile. CMC-nZVI illustrates this dilemma by showing substantially enhanced mobility, but orders of magnitude shorter lifetime in groundwater than conventional types of nZVI. Refining nZVI formulations to achieve balance between these two aspects should be the focus of the next phase nZVI development. During this process, the reactions with I2S (and potentially other CRPs) could serve as an easy and quick assay to more efficiently assess the reactive transformations of nZVI and their effects on nZVI lifetime in laboratory, and thereby providing guidance on improved design of nZVI to achieve field applicability. In addition, the fast reduction of the probe compound might allow the rate constants to be developed to "higher order of use", such as correlating with relatively slow kinetics of contaminant reduction, and hence to quickly screen the reactivity of nZVI to target contaminants.

5.5. Acknowledgments

This material is based on work supported by the Strategic Environmental Research and Developmental Program of the U.S. Department of Defense, Award Number ER-2308. The authors would like to thank Andrew Barnum at Portland State University for performing the transmission electron microscopy.

Chapter 6 Summary

The work presented in this dissertation spans a wide range of redox processes involving reducing iron materials that are relevant to contaminant fate and remediation. The scope of the reducing materials, and conditions, addressed in this work covers most scenarios included within in-situ chemical reduction (ISCR), which is a classification of remediation technologies that has emerged over the last twenty years. The two parts of this work address remediation of inorganic radionuclides and chlorinated solvents, respectively, by ISCR. The emphasis of **Part I** is mainly on the fundamental biogeochemistry of a particular remedial strategy, whereas **Part II** is focused on developing broadly-applicable tools for characterizing redox conditions and processes involved in all ISCR-related remedial strategies.

In **Chapter 2**, it was shown that sulfide modified (sulfidated) nano zerovalent iron (nZVI) reduces TcO4 preferentially TcS_2 rather than TcO_2 (which is the primary sequestration product under non-sulfide reducing conditions). The mineral phase that is most responsible for the shift of reduction pathways is iron sulfide (FeS, mackinawite), which is the main product of reaction between nZVI and aqueous sulfide. Multiple lines of evidence were provided—including reduction kinetics, microscopy, X-ray absorbance spectroscopy, and geochemical modeling—to support these conclusions. The implications of these results to remediation of Tc-contaminated field sites are compelling:

suggesting that addition of (n)ZVI could be used to stimulate sulfidogenesis in order affect sequestration of Tc in a form that is resist to oxidative remobilization.

Based on the results reported in **Chapter 2** and the central premise that TcS_2 is less susceptible to oxidative remobilization than TcO_2, the work described in **Chapter 3** was further performed to investigate the stability of reduced TcS_2 in the presence of oxygen by kinetic measurement and spectroscopic characterization. The results showed slower reoxidation kinetics in the presence of sulfide, although complete inhibition of the reaction was not achieved. The major factors that contribute to the slower Tc oxidation rates are that (*i*) the presence of FeS as redox buffer capacity to consume oxygen and (*ii*) solid state transformation from TcS_2 to TcO_2.

Chapter 4 concerns the development of alternative tools for assessing to prospects of abiotic natural attenuation of chlorinated ethenes by abiotic natural attenuation (i.e., by reduction with iron minerals). The approach taken used chemical reactive probes (CRPs) to characterize the thermodynamic and kinetic characteristics of reducing iron minerals to so that these properties could be related to measurements of abiotic contaminant reduction. The reduction potentials of minerals (with an without adsorbed Fe(II)) determined by thermodynamic CRPs were found to be better descriptors than conventional electrode potential measurements. The mineral reduction potentials correlate broadly with the reduction rate constants of several kinetic CRPs. A similar pattern in reactivity was identified in a more extensive kinetic dataset that includes both the experimentally determined rate constant from this study and rate constant compiled from previously reported studies. This finding suggests that thermodynamic and kinetic CRPs for relatively rapid assays to screen natural materials for the prospect of abiotic natural attenuation of chlorinated ethenes, which occurs at orders of magnitude slower rates.

Building on the work described in Chapter 4, Chapter 5 develops the CRP approach to address a specific challenge involving characterizing the fate and transport of carboxymethylcelluse stabilized zerovalent iron (CMC-nZVI), which is one of the most widely studied forms of nZVI for remediation. Indigo disulfonate (I2S) was selected as the CRP for this purpose, in part because its environmental redox properties are well known (including Chapter 4) but also that it is widely available and non-toxic. .Most importantly, however, I2S is effectively selective for Fe(0) because other reductants (even adsorbed Fe(II)) react with it much more slowly than Fe(0). The allows the probe to distinguish Fe(0) from other dissolved/solid Fe species in groundwater samples, which is otherwise very difficult due to small particle size of the nanoparticles. The reaction stoichiometry between I2S and Fe(0) is 1.45, from which the Fe(0) content can be determined. The reaction kinetics were described with a second-order kinetic model, which can be used to indicate various surface activation and passivation processes. This approach was used to quantify the corrosion rates of CMC-nZVI in anaerobic water, which was found to be orders of magnitude faster than conventional nZVI. This result indicates that chemical transformation should be considered as an important factor in future studies involving CMC-nZVI due to its high reactivity.

Bibliography

1. Smith, A.H., E.O. Lingas, and M. Rahman, Contamination of drinking-water by arsenic in Bangladesh: a public health emergency. *Bulletin of the World Health Organization*, 2000. **78**: p. 1093-1103.

2. Niu, L., F. Yang, C. Xu, H. Yang, and W. Liu, Status of metal accumulation in farmland soils across China: From distribution to risk assessment. *Environmental Pollution*, 2013. **176**: p. 55-62.

3. Moran, M.J., J.S. Zogorski, and P.J. Squillace, Chlorinated solvents in groundwater of the United States. *Environ. Sci. Technol.*, 2006. **41**: p. 74-81.

4. Moser, D.P., J.K. Fredrickson, D.R. Geist, E.V. Arntzen, A.D. Peacock, S.-M.W. Li, T. Spadoni, and J.P. McKinley, Biogeochemical processes and microbial characteristics across groundwater-surface water boundaries of the Hanford Reach of the Columbia River. *Environ. Sci. Technol.*, 2003. **37**: p. 5127-5134.

5. DeVaull, G.E., Indoor vapor intrusion with oxygen-limited biodegradation for a subsurface gasoline source. *Environ. Sci. Technol.*, 2007. **41**: p. 3241-3248.

6. Mackay, D.M. and J.A. Cherry, Groundwater contamination: pump-and-treat remediation. *Environ. Sci. Technol.*, 1989. **23**: p. 630-636.

7. Stroo, H.F., M.R. West, B.H. Kueper, R.C. Borden, D.W. Major, and C.H. Ward, In situ bioremediation of chlorinated ethene source zones, in *Chlorinated Solvent Source Zone Remediation*. 2014, Springer. p. 395-457.

8. Tratnyek, P.G., R.L. Johnson, G.V. Lowry, and R.A. Brown, In situ chemical reduction for source remediation, in *Chlorinated Solvent Source Zone Remediation*. 2014, Springer. p. 307-351.

9. Siegrist, R.L., M. Crimi, N.R. Thomson, W.S. Clayton, and M.C. Marley, In situ chemical oxidation, in *Chlorinated Solvent Source Zone Remediation*. 2014, Springer. p. 253-305.

10. Beyke, G. and D. Fleming, In situ thermal remediation of DNAPL and LNAPL using electrical resistance heating. *Remed J,* 2005. **15**: p. 5-22.

11. Stroo, H.F., M. Unger, C.H. Ward, M.C. Kavanaugh, C. Vogel, A. Leeson, J.A. Marqusee, and B.P. Smith, Peer reviewed: Remediating chlorinated solvent source zones. *Environ. Sci. Technol.*, 2003. **37**: p. 224A-230A.

12. Szecsody, J.E., J.S. Fruchter, M.D. Williams, V.R. Vermeul, and D. Sklarew, In Situ Chemical Reduction of Aquifer Sediments: Enhancement of Reactive Iron Phases and TCE Dechlorination. *Environ. Sci. Technol.*, 2004. **38**: p. 4656-4663.

13. Cundy, A.B., L. Hopkinson, and R.L.D. Whitby, Use of iron-based technologies in contaminated land and groundwater remediation: A review. *Science of The Total Environment*, 2008. **400**: p. 42-51.

14. Strathmann, T.J. and A.T. Stone, Reduction of oxamyl and related pesticides by FeII: influence of organic ligands and natural organic matter. *Environ. Sci. Technol.*, 2002. **36**: p. 5172-5183.

15. Strathmann, T., J. , Redox reactivity of organically complexed iron(II) species with aquatic contaminants, in *Aquatic Redox Chemistry*. 2011, American Chemical Society. p. 283-313.

16. Buerge, I.J. and S.J. Hug, Influence of organic ligands on chromium (VI) reduction by iron (II). *Environ. Sci. Technol.*, 1998. **32**: p. 2092-2099.

17. Orth, W.S. and R.W. Gillham, Dechlorination of Trichloroethene in Aqueous Solution Using Fe0. *Environ. Sci. Technol.*, 1995. **30**: p. 66-71.

18. Gillham, R.W. and S.F. O'Hannesin, Enhanced degradation of halogenated aliphatics by zero-valent iron. *Ground Water*, 1994. **32**: p. 958-967.

19. Matheson, L.J. and P.G. Tratnyek, Reductive dehalogenation of chlorinated methanes by iron metal. *Environ. Sci. Technol.*, 1994. **28**: p. 2045-2053.

20. Li, X., D.W. Elliott, and W. Zhang, Zero-valent iron nanoparticles for abatement of environmental pollutants: materials and engineering aspects. *Crit. Rev. Solid State Mater. Sci.*, 2006. **31**: p. 111-122.

21. Phillips, D.H., N.T. Van, L. Bastiaens, M.I. Russell, K. Dickson, S. Plant, J.M.E. Ahad, T. Newton, T. Elliot, and R.M. Kalin, Ten year performance evaluation of a field-scale zero-valent iron permeable reactive barrier installed to remediate trichloroethene contaminated groundwater. *Environ. Sci. Technol.*, 2010. **44**: p. 3861-3869.

22. Velimirovic, M., T. Tosco, M. Uyttebroek, M. Luna, F. Gastone, C. De Boer, N. Klaas, H. Sapion, H. Eisenmann, P.-O. Larsson, J. Braun, R. Sethi, and L. Bastiaens, Field assessment of guar gum stabilized microscale zerovalent iron particles for in-situ remediation of 1,1,1-trichloroethane. *J. Contam. Hydro.*, 2014. **164**: p. 88-99.

23. Bennett, P., F. He, D. Zhao, B. Aiken, and L. Feldman, In situ testing of metallic iron nanoparticle mobility and reactivity in a shallow granular aquifer. *J. Contam. Hydro.*, 2010. **116**: p. 35-46.

24. Fagerlund, F., T.H. Illangasekare, T. Phenrat, H.J. Kim, and G.V. Lowry, PCE dissolution and simultaneous dechlorination by nanoscale zero-valent iron particles in a DNAPL source zone. *J. Contam. Hydro.*, 2012. **131**: p. 9-28.

25. Mueller, N.C., J. Braun, J. Bruns, M. Černík, P. Rissing, D. Rickerby, and B. Nowack, Application of nanoscale zero valent iron (NZVI) for groundwater remediation in Europe. *Environmental Science and Pollution Research*, 2012. **19**: p. 550-558.

26. Tratnyek, P.G., T.L. Johnson, M.M. Scherer, and G.R. Eykholt, Remediating ground water with zero‐valent metals: chemical considerations in barrier design. *Ground Water Monit. R.*, 1997. **17**: p. 108-114.

27. Zhang, W., Nanoscale iron particles for environmental remediation: an overview. *J. Nanopart. Res.*, 2003. **5**: p. 323-332.

28. Zhang, W. and D.W. Elliott, Applications of iron nanoparticles for groundwater remediation. *Remed J*, 2006. **16**: p. 7-21.

29. Tratnyek, P.G. and R.L. Johnson, Nanotechnologies for environmental cleanup. *Nano today*, 2006. **1**: p. 44-48.

30. Karn, B., T. Kuiken, and M. Otto, Nanotechnology and in situ remediation: a review of the benefits and potential risks. *Environ. Health Perspect.*, 2009: p. 1823-1831.

31. Taghavy, A., J. Costanza, K.D. Pennell, and L.M. Abriola, Effectiveness of nanoscale zero-valent iron for treatment of a PCE–DNAPL source zone. *J. Contam. Hydro.*, 2010. **118**: p. 128-142.

32. Henn, K.W. and D.W. Waddill, Utilization of nanoscale zero-valent iron for source remediation—A case study. *Remed J*, 2006. **16**: p. 57-77.

33. O'Carroll, D., B. Sleep, M. Krol, H. Boparai, and C. Kocur, Nanoscale zero valent iron and bimetallic particles for contaminated site remediation. *Adv. Water Resour.*, 2013. **51**: p. 104-122.

34. Peale, J.G.D., E. Bakkom, F. Lakhwala, J. Mueller, and J. Molin, TCE plume remediation via ISCR ‐ enhanced bioremediation utilizing EHC® and KB ‐ 1®. *Remed J*, 2008. **18**: p. 19-31.

35. Peale, J.G.D., J. Mueller, and J. Molin, Successful ISCR ‐ enhanced bioremediation of a TCE DNAPL source utilizing EHC® and KB ‐ 1®. *Remed J*, 2010. **20**: p. 63-81.

36. Wang, C. and W. Zhang, Synthesizing nanoscale iron particles for rapid and complete dechlorination of TCE and PCBs. *Environ. Sci. Technol.*, 1997. **31**: p. 2154-2156.

37. Nurmi, J.T., P.G. Tratnyek, V. Sarathy, D.R. Baer, J.E. Amonette, K. Pecher, C. Wang, J.C. Linehan, D.W. Matson, R.L. Penn, and M.D. Driessen, Characterization and properties of metallic iron nanoparticles: spectroscopy, electrochemistry, and kinetics. *Environ. Sci. Technol.*, 2005. **39**: p. 1221-1230.

38. Tratnyek, P., G. , A. Salter-Blanc, J. , J. Nurmi, T. , J. Amonette, E. , J. Liu, C. Wang, A. Dohnalkova, and D. Baer, R., Reactivity of zerovalent metals in aquatic media: effects of organic surface coatings, in *Aquatic Redox Chemistry*. 2011, American Chemical Society. p. 381-406.

39. He, F. and D. Zhao, Manipulating the size and dispersibility of zerovalent iron nanoparticles by use of carboxymethyl cellulose stabilizers. *Environ. Sci. Technol.*, 2007. **41**: p. 6216-6221.

40. He, F., D. Zhao, J. Liu, and C.B. Roberts, Stabilization of Fe-Pd nanoparticles with sodium carboxymethyl cellulose for enhanced transport and dechlorination of trichloroethylene in soil and groundwater. *Ind. Eng. Chem.Res*, 2007. **46**: p. 29-34.

41. Johnson, R.L., J.T. Nurmi, G. O'Brien Johnson, D. Fan, R. O'Brien Johnson, Z. Shi, J. Salter-Blanc Alexandra, P.G. Tratnyek, and G.V. Lowry, Field-scale transport and transformation of carboxymethylcellulose-stabilized nano zero-valent iron. *Environ. Sci. Technol.*, 2013. **47**: p. 1573-1580.

42. Kocur, C.M., D.M. O'Carroll, and B.E. Sleep, Impact of nZVI stability on mobility in porous media. *J. Contam. Hydro.*, 2013. **145**: p. 17-25.

43. Krol, M.M., A.J. Oleniuk, C.M. Kocur, B.E. Sleep, P. Bennett, Z. Xiong, and D.M. O'Carroll, A field-validated model for in situ transport of polymer-stabilized nZVI and implications for subsurface injection. *Environ. Sci. Technol.*, 2013. **47**: p. 7332-7340.

44. Ludwig, R.D., C. Su, T.R. Lee, R.T. Wilkin, S.D. Acree, R.R. Ross, and A. Keeley, In situ chemical reduction of Cr(VI) in groundwater using a combination of ferrous sulfate and sodium dithionite: A field investigation. *Environ. Sci. Technol.*, 2007. **41**: p. 5299-5305.

45. Elsner, M., R.P. Schwarzenbach, and S.B. Haderlein, Reactivity of Fe (II)-bearing minerals toward reductive transformation of organic contaminants. *Environ. Sci. Technol.*, 2004. **38**: p. 799-807.

46. Sumoondur, A., S. Shaw, I. Ahmed, and L.G. Benning, Green rust as a precursor for magnetite: an in situ synchrotron based study. *Mineral. Mag,*, 2008. **72**: p. 201-204.

47. Gorski, C.A. and M.M. Scherer, Influence of magnetite stoichiometry on FeII uptake and nitrobenzene reduction. *Environ. Sci. Technol.*, 2009. **43**: p. 3675-3680.

48. Pearce, C.I., O. Qafoku, J. Liu, E. Arenholz, S.M. Heald, R.K. Kukkadapu, C.A. Gorski, C.M.B. Henderson, and K.M. Rosso, Synthesis and properties of titanomagnetite (Fe 3− xTixO 4) nanoparticles: A tunable solid-state Fe (II/III) redox system. *Journal of Colloid and Interface Science*, 2012. **387**: p. 24-38.

49. Neumann, A., M. Sander, and T. Hofstetter, B. , Redox properties of structural Fe in smectite clay minerals, in *Aquatic Redox Chemistry*. 2011, American Chemical Society. p. 361-379.

50. Soltermann, D., M.M. Fernandes, B. Baeyens, R. Dähn, J. Miehé-Brendlé, B. Wehrli, and M.H. Bradbury, Fe (II) sorption on a synthetic montmorillonite. A combined macroscopic and spectroscopic study. *Environ. Sci. Technol.*, 2013. **47**: p. 6978-6986.

51. Gu, B., T.J. Phelps, L. Liang, M.J. Dickey, Y. Roh, B.L. Kinsall, A.V. Palumbo, and G.K. Jacobs, Biogeochemical dynamics in zero-valent Iron columns: implications for permeable reactive barriers. *Environ. Sci. Technol.*, 1999. **33**: p. 2170-2177.

52. Farrell, J., M. Kason, N. Melitas, and T. Li, Investigation of the long-term performance of zero-valent iron for reductive dechlorination of trichloroethylene. *Environ. Sci. Technol.*, 2000. **34**: p. 514-521.

53. Furukawa, Y., J.-w. Kim, J. Watkins, and R.T. Wilkin, Formation of ferrihydrite and associated iron corrosion products in permeable reactive barriers of zero-valent iron. *Environ. Sci. Technol.*, 2002. **36**: p. 5469-5475.

54. Ritter, K., M.S. Odziemkowski, R. Simpgraga, R.W. Gillham, and D.E. Irish, An in situ study of the effect of nitrate on the reduction of trichloroethylene by granular iron. *J. Contam. Hydro.*, 2003. **65**: p. 121-136.

55. Mishra, D. and J. Farrell, Understanding nitrate reactions with zerovalent iron using tafel analysis and electrochemical impedance spectroscopy. *Environ. Sci. Technol.*, 2004. **39**: p. 645-650.

56. Tratnyek, P.G., Putting corrosion to use: Remediation of contaminated groundwater with zero-valent metals. *Chemistry & Industry*, 1996: p. 499-503.

57. McNeill, L.S. and M. Edwards, Iron pipe corrosion in distribution systems. *Journal (American Water Works Association)*, 2001: p. 88-100.

58. Refait, P.H., M. Abdelmoula, and J.M.R. GÉnin, Mechanisms of formation and structure of green rust one in aqueous corrosion of iron in the presence of chloride ions. *Corros. Sci.*, 1998. **40**: p. 1547-1560.

59. Refait, P., S.H. Drissi, J. Pytkiewicz, and J.M.R. Génin, The anionic species competition in iron aqueous corrosion: Role of various green rust compounds. *Corros. Sci.*, 1997. **39**: p. 1699-1710.

60. Odziemkowski, M.S., T.T. Schuhmacher, R.W. Gillham, and E.J. Reardon, Mechanism of oxide film formation on iron in simulating groundwater solutions: Raman spectroscopic studies. *Corros. Sci.*, 1998. **40**: p. 371-389.

61. Roh, Y., S. Lee, and M. Elless, Characterization of corrosion products in the permeable reactive barriers. *Environ. Geol.*, 2000. **40**: p. 184-194.

62. Wilkin, R.T., R.W. Puls, and G.W. Sewell, Long‐term performance of permeable reactive barriers using zero‐valent iron: Geochemical and microbiological effects. *Groundwater*, 2003. **41**: p. 493-503.

63. Kohn, T., K.J.T. Livi, A.L. Roberts, and P.J. Vikesland, Longevity of granular iron in groundwater treatment processes: corrosion product development. *Environ. Sci. Technol.*, 2005. **39**: p. 2867-2879.

64. Puls, R.W., D.W. Blowes, and R.W. Gillham, Long-term performance monitoring for a permeable reactive barrier at the US Coast Guard Support Center, Elizabeth City, North Carolina. *J. Hazard. Mater.*, 1999. **68**: p. 109-124.

65. Gu, B., D.B. Watson, L. Wu, D.H. Phillips, D.C. White, and J. Zhou, Microbiological characteristics in a zero-valent iron reactive barrier. *Environ. Monit. Assess.*, 2002. **77**: p. 293-309.

66. Scherer, M.M., S. Richter, L.V. Richard, and A.P.J. J., Chemistry and microbiology of permeable reactive barriers for in situ groundwater clean up. *Crit. Rev. Env. Sci. Tec.*, 2000. **30**: p. 363-411.

67. Liamleam, W. and A. Annachhatre, Electron donors for biological sulfate reduction. *Biotechnol. Adv.*, 2007. **25**: p. 452-463.

68. Van Nooten, T., D. Springael, and L. Baktiaens, Positive impact of microorganisms on the performance of laboratory-scale permeable reactive iron barriers. *Environ. Sci. Technol.*, 2008 **42**: p. 1680-1686.

69. Van Nooten, T., D. Springael, and L. Bastiaens, Microbial community characterization in a pilot-scale permeable reactive iron barrier. *Environ. Eng. Sci.*, 2010. **27**: p. 287-292.

70. Van Nooten, T.L., F.; Dries, J.; Pirard, E.; Springael, D.; Bastiaens, L., Impact of microbial activities on the mineralogy and performance of column-scale permeable reactive iron barriers operation under two different conditions. *Environ. Sci. Technol.*, 2007. **41**: p. 5274-5230.

71. Hellige, K., K. Pollok, P. Larese-Casanova, T. Behrends, and S. Peiffer, Pathways of ferrous iron mineral formation upon sulfidation of lepidocrocite surfaces. *Geochim. Cosmochim. Acta*, 2012. **81**: p. 69-81.

72. Hansson, E.B., M.S. Odziemkowski, and R.W. Gillham, Formation of poorly crystalline iron monosulfides: surface redox reactions on high purity iron, spectroelectrochemical studies. *Corros. Sci.*, 2006. **48**: p. 3767-3783.

73. Mullet, S. Boursiquot, M. Abdelmoula, J. Genin, and J. Ehrhardt, Surface chemistry and structural properties of mackinawite prepared by reaction of sulfide ions with metallic iron. *Geochim. Cosmochim. Acta,* 2002. **66**: p. 829-836.

74. Morse, J.W., F.J. Millero, J.C. Cornwell, and D. Rickard, The chemistry of the hydrogen sulfide and iron sulfide systems in natural waters. *Earth-Sci. Rev.*, 1987. **24**: p. 1-42.

75. Whiting, K., P.J. Evans, C. Lebrón, B. Henry, J.T. Wilson, and E. Becvar, Factors controlling in situ biogeochemical transformation of trichloroethene: Field survey. *Ground Water Monit. R.*, 2014. **34**: p. 79-94.

76. Lowry, G.V., K.B. Gregory, S.C. Apte, and J.R. Lead, Transformations of nanomaterials in the environment. *Environ. Sci. Technol.*, 2012. **46**: p. 6893-6899.

77. Reinsch, B.C., B. Forsberg, R.L. Penn, C.S. Kim, and G.V. Lowry, Chemical transformations during aging of zerovalent iron nanoparticles in the presence of common groundwater dissolved constituents. *Environ. Sci. Technol.*, 2010. **44**: p. 3455-3461.

78. Liu, Y. and G.V. Lowry, Effect of particle age (Fe^0 content) and solution pH on nZVI reactivity: H_2 evolution and TCE dechlorination. *Environ. Sci. Technol.*, 2006. **40**: p. 6085-6090.

79. Sarathy, V., P.G. Tratnyek, J.T. Nurmi, D.R. Baer, J.E. Amonette, C. Chun, R.L. Penn, and E.J. Reardon, Aging of iron nanoparticles in aqueous solution: effects on structure and reactivity. *J. Phys. Chem. C*, 2008. **112**: p. 2286-2293.

80. Fan, D., R.P. Anitori, B.M. Tebo, P.G. Tratnyek, J.S. Lezama Pacheco, R.K. Kukkadapu, M.H. Engelhard, M.E. Bowden, L. Kovarik, and B.W. Arey, Reductive sequestration of pertechnetate ($^{99}TcO_4^-$) by nano zero-valent iron (nZVI) transformed by abiotic sulfide. *Environ. Sci. Technol.*, 2013. **47**: p. 5302-5310.

81. Shi, Z., D. Fan, R.L. Johnson, P.G. Tratnyek , J.T. Nurmi , Y. Wu, and K.H. Williams, Methods for characterizing the fate and effects of nano zerovalent iron during groundwater remediation. *J. Contam. Hydro.*, 2015: p. Accepted.

82. Weber, K.A., L.A. Achenbach, and J.D. Coates, Microorganisms pumping iron: anaerobic microbial iron oxidation and reduction. *Nat Rev Micro*, 2006. **4**: p. 752-764.

83. Carlson, L. and U. Scewertmann, The effect of CO_2 and oxidation rate on the formation of goethite versus lepidocrocite from an Fe(II) system at pH 6 and 7 *Clay Miner.*, 1990. **25**: p. 65-71.

84. Larese-Casanova, P., A. Kappler, and S.B. Haderlein, Heterogeneous oxidation of Fe(II) on iron oxides in aqueous systems: Identification and controls of Fe(III) product formation. *Geochim. Cosmochim. Acta*, 2012. **91**: p. 171-186.

85. Etique, M., F.P.A. Jorand, A. Zegeye, B. Grégoire, C. Despas, and C. Ruby, Abiotic process for Fe(II) oxidation and green rust mineralization driven by a heterotrophic nitrate reducing bacteria (*Klebsiella mobilis*). *Environ. Sci. Technol.*, 2014. **48**: p. 3742-3751.

86. Zegeye, A., M. Etique, C. Carteret, C. Ruby, P. Schaaf, and G. Francius, Origin of the differential nanoscale reactivity of biologically and chemically formed green rust crystals investigated by chemical force spectroscopy. *J. Phys. Chem. C*, 2014. **118**: p. 5978-5987.

87. Chaudhuri, S.K., J.G. Lack, and J.D. Coates, Biogenic magnetite formation through anaerobic biooxidation of Fe(II). *Appl. Environ. Microbe.*, 2001. **67**: p. 2844-2848.

88. Roden, E., Microbial iron-redox cycling in subsurface environments. *Biochemical Society Transactions*, 2012. **40**: p. 1249.

89. Bonneville, S., P. Van Cappellen, and T. Behrends, Microbial reduction of iron(III) oxyhydroxides: effects of mineral solubility and availability. *Chem. Geol.*, 2004. **212**: p. 255-268.

90. Bonneville, S., T. Behrends, and P. Van Cappellen, Solubility and dissimilatory reduction kinetics of iron(III) oxyhydroxides: A linear free energy relationship. *Geochim. Cosmochim. Acta*, 2009. **73**: p. 5273-5282.

91. Roden, E.E. and J.M. Zachara, Microbial reduction of crystalline iron (III) oxides: Influence of oxide surface area and potential for cell growth. *Environ. Sci. Technol.*, 1996. **30**: p. 1618-1628.

92. Hansel, C.M., S.G. Benner, J. Neiss, A. Dohnalkova, R.K. Kukkadapu, and S. Fendorf, Secondary mineralization pathways induced by dissimilatory iron reduction of ferrihydrite under advective flow. *Geochim. Cosmochim. Acta*, 2003. **67**: p. 2977-2992.

93. Lovley, D., Magnetite formation during microbial dissimilatory iron reduction, in *Iron Biominerals*, R. Frankel and R. Blakemore, Editors. 1991, Springer US. p. 151-166.

94. Ona-Nguema, G., M. Abdelmoula, F. Jorand, O. Benali, J.-C. Block, and J.-M.R. Génin, Iron(II,III) hydroxycarbonate green tust formation and stabilization from lepidocrocite bioreduction. *Environ. Sci. Technol.*, 2001. **36**: p. 16-20.

95. Dong, H., J.K. Fredrickson, D.W. Kennedy, J.M. Zachara, R.K. Kukkadapu, and T.C. Onstott, Mineral transformations associated with the microbial reduction of magnetite. *Chem. Geol.*, 2000. **169**: p. 299-318.

96. Wang, Y., G. Morin, G. Ona-Nguema, and G.E. Brown, Arsenic (III) and Arsenic (V) speciation during transformation of lepidocrocite to magnetite. *Environ. Sci. Technol.*, 2014.

97. Usman, M., K. Hanna, M. Abdelmoula, A. Zegeye, P. Faure, and C. Ruby, Formation of green rust via mineralogical transformation of ferric oxides (ferrihydrite, goethite and hematite). *Appl. Clay Sci.*, 2012. **64**: p. 38-43.

98. Hansel, C.M., S.G. Benner, and S. Fendorf, Competing Fe (II)-induced mineralization pathways of ferrihydrite. *Environ. Sci. Technol.*, 2005. **39**: p. 7147-7153.

99. Hansen, H.C.B., Composition, stabilization, and light absorption of Fe (II) Fe (III) hydroxycarbonate(green rust). *Clay Miner.*, 1989. **24**: p. 663-9.

100. Ruby, C., A. Géhin, R. Aissa, J. Ghanbaja, M. Abdelmoula, and J.-M. Génin, Chemical stability of hydroxysulphate green rust synthetised in the presence of foreign anions: carbonate, phosphate and silicate. *Hyperfine Interact.*, 2006. **167**: p. 803-807.

101. Zachara, J.M., S.M. Heald, B. Jeon, R.K. Kukkadapu, C. Liu, J.P. McKinley, A.C. Dohnalkova, and D.A. Moore, Reduction of pertechnetate [Tc(VII)] by aqueous Fe(II) and the nature of solid phase redox products. *Geochim. Cosmochim. Acta*, 2007. **71**: p. 2137-2157.

102. Peretyazhko, T., J.M. Zachara, S.M. Heald, B.-H. Jeon, R.K. Kukkadapu, C. Liu, D. Moore, and C.T. Resch, Heterogeneous reduction of Tc(VII) by Fe(II) at the solid-water interface. *Geochim. Cosmochim. Acta*, 2009. **72**: p. 1521-1539.

103. Pedersen, H.D., D. Postma, R. Jakobsen, and O. Larsen, Fast transformation of iron oxyhydroxides by the catalytic action of aqueous Fe(II). *Geochim. Cosmochim. Acta*, 2005. **69**: p. 3967-3977.

104. Tishchenko, V., C. Meile, M.M. Scherer, T.S. Pasakarnis, and A. Thompson, Fe2+ catalyzed iron atom exchange and re-crystallization in a tropical soil. *Geochim. Cosmochim. Acta*, 2015. **148**: p. 191-202.

105. Williams, A.G.B. and M.M. Scherer, Spectroscopic evidence for Fe(II)−Fe(III) electron transfer at the iron oxide−water interface. *Environ. Sci. Technol.*, 2004. **38**: p. 4782-4790.

106. Katz, J.E., X. Zhang, K. Attenkofer, K.W. Chapman, C. Frandsen, P. Zarzycki, K.M. Rosso, R.W. Falcone, G.A. Waychunas, and B. Gilbert, Electron small

polarons and their mobility in iron (oxyhydr)oxide nanoparticles. *Science*, 2012. **337**: p. 1200-1203.

107. Boland, D.D., R.N. Collins, C.J. Miller, C.J. Glover, and T.D. Waite, Effect of solution and solid-phase conditions on the Fe (II)-accelerated transformation of ferrihydrite to lepidocrocite and goethite. *Environ. Sci. Technol.*, 2014. **48**: p. 5477-5485.

108. Evans, P.J., D. Nguyen, R.W. Chappell, K. Whiting, J. Gillette, A. Bodour, and J.T. Wilson, Factors controlling in situ biogeochemical transformation of trichloroethene: column study. *Ground Water Monit. R.*, 2014. **34**: p. 65-78.

109. He, Y.T., J.T. Wilson, and R.T. Wilkin, Transformation of Reactive Iron Minerals in a Permeable Reactive Barrier (Biowall) Used to Treat TCE in Groundwater. *Environ. Sci. Technol.*, 2008. **42**: p. 6690-6696.

110. Kennedy, L.G., J.W. Everett, E. Becvar, and D. DeFeo, Field-scale demonstration of induced biogeochemical reductive dechlorination at Dover Air Force Base, Dover, Delaware. *J. Contam. Hydro.*, 2006. **88**: p. 119-136.

111. Bi, Y., S.P. Hyun, R. Kukkadapu, and K.F. Hayes, Oxidative dissolution of UO_2 in a simulated groundwater containing synthetic nanocrystalline mackinawite. *Geochim. Cosmochim. Acta*, 2012. **102**: p. 175-190.

112. Jeong, H.Y., Y. Han, S.W. Park, and K.F. Hayes, Aerobic oxidation of mackinawite (FeS) and its environmental implication for arsenic mobilization. *Geochim. Cosmochim. Acta*, 2010. **74**: p. 3182-3198.

113. Evangelou, V.P. and Y.L. Zhang, A review: Pyrite oxidation mechanisms and acid mine drainage prevention. *Crit. Rev. Env. Sci. Tec.*, 1995. **25**: p. 141-199.

114. Amonette, J., J. Szecsody, H. Schaef, Y. Gorby, J. Fruchter, and J. Templeton, Abiotic reduction of aquifer materials by dithionite: A promising in-situ remediation technology. 1994, Pacific Northwest Lab., Richland, WA (United States). Funding organisation: USDOE, Washington, DC (United States).

115. Fruchter, J.S., C.R. Cole, M.D. Williams, V.R. Vermeul, J.E. Amonette, J.E. Szecsody, J.D. Istok, and M. Humphrey, Creation of a subsurface permeable treatment zone for aqueous chromate contamination using in situ redox manipulation. *Ground Water Monit. R.*, 2000. **20**: p. 66-77.

116. Langell, M.A., E. Kadossov, H. Boparai, and P. Shea, Effect of sodium dithionite on the surface composition of iron-containing aquifer sediment. *Surface and Interface Analysis*, 2009. **41**: p. 941-950.

117. Poulton, S.W. and D.E. Canfield, Development of a sequential extraction procedure for iron: implications for iron partitioning in continentally derived particulates. *Chem. Geol.*, 2005. **214**: p. 209-221.

118. Gleyzes, C., S. Tellier, and M. Astruc, Fractionation studies of trace elements in contaminated soils and sediments: a review of sequential extraction procedures. *TrAC Trends in Analytical Chemistry*, 2002. **21**: p. 451-467.

119. Kwon, M.J., J.-S. Yang, M.J. Shim, M.I. Boyanov, K.M. Kemner, and E.J. O'Loughlin, Acid extraction overestimates the total Fe (II) in the presence of iron (hydr) oxide and sulfide minerals. *Environmental Science & Technology Letters*, 2014. **1**: p. 310-314.

120. Vikesland, P.J., A.M. Heathcock, R.L. Rebodos, and K.E. Makus, Particle size and aggregation effects on magnetite reactivity toward carbon tetrachloride. *Environ. Sci. Technol.*, 2007. **41**: p. 5277-5283.

121. Jeong, H.Y., J.H. Lee, and K.F. Hayes, Characterization of synthetic nanocrystalline mackinawite: crystal structure, particle size and specific surface area. *Geochim. Cosmochim. Acta*, 2008. **72**: p. 493-505.

122. Johnson, T.L., M.M. Scherer, and P.G. Tratnyek, Kinetics of halogenated organic compound degradation by iron metal. *Environ. Sci. Technol.*, 1996. **30**: p. 2634-2640.

123. Miehr, R., P.G. Tratnyek, J.Z. Bandstra, M.M. Scherer, M.J. Alowitz, and E.J. Bylaska, Diversity of contaminant reduction reactions by zerovalent iron: Role of the reductate. *Environ. Sci. Technol.*, 2004. **38**: p. 139-147.

124. Schwertmann, U. and R.M. Cornell, Iron oxides in the laboratory. 2008: John Wiley & Sons.

125. Fan, D., R.P. Anitori, B.M. Tebo, P.G. Tratnyek, J.S. Lezama Pacheco, R.K. Kukkadapu, L. Kovarik, M.H. Engelhard, and M.E. Bowden, Oxidative remobilization of technetium sequestered by sulfide-transformed nano zerovalent iron. *Environ. Sci. Technol.*, 2014. **48**: p. 7409–7417.

126. Tominaga, T. and Y. Minai, Applications of Mössbauer spectroscopy to environmental and geochemical studies. 1984: CRC Press.

127. Refait, P., C. Bon, L. Simon, G. Bourrié, F. Trolard, J. Bessiere, and J. Genin, Chemical composition and Gibbs standard free energy of formation of Fe (II)-Fe (III) hydroxysulphate green rust and Fe (II) hydroxide. *Clay Miner.*, 1999. **34**: p. 499-510.

128. Gorski, C.A. and M.M. Scherer, Determination of nanoparticulate magnetite stoichiometry by Mössbauer spectroscopy, acidic dissolution, and powder X-ray diffraction: A critical review. *Am. Mineral.*, 2010. **95**: p. 1017-1026.

129. Kim, E.-J., J.-H. Kim, Y.-S. Chang, D. Turcio-Ortega, and P.G. Tratnyek, Effects of metal ions on the reactivity and corrosion electrochemistry of Fe/FeS nanoparticles. *Environ. Sci. Technol.*, 2014. **48**: p. 4002-4011.

130. Sparks, D.L., Environmental soil chemistry. 2003: Academic press.

131. O'Day, P.A., N. Rivera, R. Root, and S.A. Carroll, X-ray absorption spectroscopic study of Fe reference compounds for the analysis of natural sediments. *Am. Mineral.*, 2004. **89**: p. 572-585.

132. Pallud, C., M. Kausch, S. Fendorf, and C. Meile, Spatial patterns and modeling of reductive ferrihydrite transformation observed in artificial soil aggregates. *Environ. Sci. Technol.*, 2010. **44**: p. 74-79.

133. Pallud, C., Y. Masue-Slowey, and S. Fendorf, Aggregate-scale spatial heterogeneity in reductive transformation of ferrihydrite resulting from coupled biogeochemical and physical processes. *Geochim. Cosmochim. Acta*, 2010. **74**: p. 2811-2825.

134. Mayhew, L.E., S.M. Webb, and A.S. Templeton, Microscale imaging and identification of fe speciation and distribution during fluid-mineral reactions under highly reducing conditions. *Environ. Sci. Technol.*, 2011. **45**: p. 4468-4474.

135. Amonette, J.E., Iron redox chemistry of clays and oxides: Environmental applications, in *Electrochemistry of Clays*, A. Fitch, Editor. 2002, Clay Minerals Society: Aurora, CO. p. 89-147.

136. Langmuir, D., Aqueous environmental geochemistry. 1997, Upper Saddle River, NJ: Prentice Hall.

137. Shi, Z., J.T. Nurmi, and P.G. Tratnyek, Effects of nano zero-valent iron (nZVI) on oxidation-reduction potential (ORP). *Environ. Sci. Technol.*, 2011. **45**: p. 1586-1592.

138. Nurmi, J.T., J.Z. Bandstra, and P.G. Tratnyek, Packed powder electrodes for characterizing the reactivity of granular iron in borate solutions. *Journal of the Electrochemical Society*, 2004. **151**: p. B347-B353.

139. Nurmi, J.T. and P.G. Tratnyek, Electrochemical studies of packed iron powder electrodes: Effects of common constituents of natural waters on corrosion potential. *Corros. Sci.*, 2008. **50**: p. 144-154.

140. Gorski, C.A., J.T. Nurmi, P.G. Tratnyek, T.B. Hofstetter, and M.M. Scherer, Redox behavior of magnetite: Implications for contaminant reduction. *Environ. Sci. Technol.*, 2009. **44**: p. 55-60.

141. Turcio-Ortega, D., D. Fan, P.G. Tratnyek, E.-J. Kim, and Y.-S. Chang, Reactivity of Fe/FeS nanoparticles: Electrolyte composition effects on corrosion electrochemistry. *Environ. Sci. Technol.*, 2012. **46**: p. 12484-12492.

142. Orsetti, S., C. Laskov, and S.B. Haderlein, Electron transfer between iron minerals and quinones: estimating the reduction potential of the Fe (II)-goethite surface from AQDS speciation. *Environ. Sci. Technol.*, 2013. **47**: p. 14161-14168.

143. Gorski, C.A., Redox behavior of magnetite in the environment: moving towards a semiconductor model, *PhD Thesis*, 2009, University of Iowa

144. Tratnyek, P., T. Reilkoff, A. Lemon, M. Scherer, B. Balko, L. Feik, and B. Henegar, Visualizing redox chemistry: probing environmental oxidation–reduction reactions with indicator dyes. *Chem. Educator*, 2001. **6**: p. 172-179.

145. Jones, B.D., J.D. Ingle, and Jr, Evaluation of immobilized redox indicators as reversible, in situ redox sensors for determining Fe(III)-reducing conditions in environmental samples. *Talanta*, 2001. **55**: p. 699-714.

146. Jones, B.D. and J.D. Ingle Jr, Evaluation of redox indicators for determining sulfate-reducing and dechlorinating conditions. *Water Res.*, 2005. **39**: p. 4343-4354.

147. Tratnyek, P.G. and N.L. Wolfe, Characterization of the reducing properties of anaerobic sediment slurries using redox indicators. *Environ. Toxicol. Chem.*, 1990. **9**: p. 289-295.

148. Wilkin, R.T., C. Su, R.G. Ford, and C.J. Paul, Chromium-removal processes during groundwater remediation by a zerovalent iron permeable reactive barrier. *Environ. Sci. Technol.*, 2005. **39**: p. 4599-4605.

149. Su, C. and R.W. Puls, Significance of iron (II, III) hydroxycarbonate green rust in arsenic remediation using zerovalent iron in laboratory column tests. *Environ. Sci. Technol.*, 2004. **38**: p. 5224-5231.

150. Liang, X., Y. Dong, T. Kuder, L.R. Krumholz, R.P. Philp, and E.C. Butler, Distinguishing abiotic and biotic transformation of tetrachloroethylene and trichloroethylene by stable carbon isotope fractionation. *Environ. Sci. Technol.*, 2007. **41**: p. 7094-7100.

151. Lee, W. and B. Batchelor, Abiotic reductive dechlorination of chlorinated ethylenes by iron-bearing soil minerals. 2. green rust. *Environ. Sci. Technol.*, 2002. **36**: p. 5348-5354.

152. Darlington, R., L.G. Lehmicke, R.G. Andrachek, and D.L. Freedman, Anaerobic abiotic transformations of cis-1, 2-dichloroethene in fractured sandstone. *Chemosphere*, 2013. **90**: p. 2226-2232.

153. Schaefer, C.E., R.M. Towne, D.R. Lippincott, P.J. Lacombe, M.E. Bishop, and H. Dong, Abiotic dechlorination in rock matrices impacted by long-term exposure to TCE. *Chemosphere*, 2015. **119**: p. 744-749.

154. Brown, R.A., J.T. Wilson, and M. Ferrey, Monitored natural attenuation forum: The case for abiotic MNA. *Remed J*, 2007. **17**: p. 127-137.

155. Ferrey, M.L., R.T. Wilkin, R.G. Ford, and J.T. Wilson, Nonbiological removal of cis-dichloroethylene and 1, 1-dichloroethylene in aquifer sediment containing magnetite. *Environ. Sci. Technol.*, 2004. **38**: p. 1746-1752.

156. Johnson, R.L., C.N. Brow, R.O.B. Johnson, and H.M. Simon, Cryogenic core collection and preservation of subsurface samples for biomolecular analysis. *Ground Water Monit. R.*, 2013. **33**: p. 38-43.

157. Brow, C.N., R.O.B. Johnson, M. Xu, R.L. Johnson, and H.M. Simon, Effects of cryogenic preservation and storage on the molecular characteristics of microorganisms in sediments. *Environ. Sci. Technol.*, 2010. **44**: p. 8243-8247.

158. Wilkin, R.T., Mineralogical preservation of solid samples collected from anoxic subsurface environments. *Groundwater Research and Issues*, 2008: p. 185.

159. McBride, M.B., Environmental chemistry of soils. 1994: Oxford university press.

160. Brown, G.E., A.L. Foster, and J.D. Ostergren, Mineral surfaces and bioavailability of heavy metals: a molecular-scale perspective. *Proc. Natl. Acad. Sci. USA*, 1999. **96**: p. 3388-3395.

161. Borch, T., R. Kretzschmar, A. Kappler, P.V. Cappellen, M. Ginder-Vogel, A. Voegelin, and K. Campbell, Biogeochemical redox processes and their impact on contaminant dynamics. *Environ. Sci. Technol.*, 2009. **44**: p. 15-23.

162. Ludwig, R.D., D.J.A. Smyth, D.W. Blowes, L.E. Spink, R.T. Wilkin, D.G. Jewett, and C.J. Weisener, Treatment of arsenic, heavy metals, and acidity using a mixed ZVI-compost PRB. *Environ. Sci. Technol.*, 2009. **43**: p. 1970-1976.

163. Naftz, D., S.J. Morrison, C.C. Fuller, and J.A. Davis, Handbook of groundwater remediation using permeable reactive barriers: applications to radionuclides, trace metals, and nutrients. 2002: Academic Press.

164. Obiri-Nyarko, F., S.J. Grajales-Mesa, and G. Malina, An overview of permeable reactive barriers for in situ sustainable groundwater remediation. *Chemosphere*, 2014. **111**: p. 243-259.

165. Li, S., W. Wang, Y. Liu, and W. Zhang, Zero-valent iron nanoparticles (nZVI) for the treatment of smelting wastewater: A pilot-scale demonstration. *Chem. Eng. J.*, 2014. **254**: p. 115-123.

166. Chen, S.-S., C.-Y. Cheng, C.-W. Li, P.-H. Chai, and Y.-M. Chang, Reduction of chromate from electroplating wastewater from pH 1 to 2 using fluidized zero valent iron process. *J. Hazard. Mater.*, 2007. **142**: p. 362-367.

167. Fu, F., D.D. Dionysiou, and H. Liu, The use of zero-valent iron for groundwater remediation and wastewater treatment: a review. *J. Hazard. Mater.*, 2014. **267**: p. 194-205.

168. Kanel, S.R., J.-M. Grenèche, and H. Choi, Arsenic(V) removal from groundwater using nano scale zero-valent iron as a colloidal reactive barrier material. *Environ. Sci. Technol.*, 2006. **40**: p. 2045-2050.

169. Su, C. and R.W. Puls, Arsenate and arsenite removal by zerovalent iron: kinetics, redox transformation, and implications for in situ groundwater remediation. *Environ. Sci. Technol.*, 2001. **35**: p. 1487-1492.

170. Mondal, P., S. Bhowmick, N. Jullok, W. Ye, W. Van Renterghem, S. Van den Berghe, and B. Van der Bruggen, Behavior of As (V) with ZVI–H_2O system and the reduction to As (0). *J. Phys. Chem. C*, 2014. **118**: p. 21614-21621.

171. Ramos, M.A., W. Yan, X. Li, B.E. Koel, and W. Zhang, Simultaneous oxidation and reduction of arsenic by zero-valent iron nanoparticles: understanding the significance of the core− shell structure. *J. Phys. Chem. C*, 2009. **113**: p. 14591-14594.

172. Jönsson, J. and D.M. Sherman, Sorption of As (III) and As (V) to siderite, green rust (fougerite) and magnetite: Implications for arsenic release in anoxic groundwaters. *Chem. Geol.*, 2008. **255**: p. 173-181.

173. Dhal, B., H.N. Thatoi, N.N. Das, and B.D. Pandey, Chemical and microbial remediation of hexavalent chromium from contaminated soil and mining/metallurgical solid waste: A review. *J. Hazard. Mater.*, 2013. **250–251**: p. 272-291.

174. Fendorf, S., B.W. Wielinga, and C.M. Hansel, Chromium transformations in natural environments: the role of biological and abiological processes in chromium(VI) reduction. *Int. Geol. Rev.*, 2000. **42**: p. 691-701.

175. Buerge, I.J. and S.J. Hug, Influence of mineral surfaces on chromium(VI) reduction by iron(II). *Environ. Sci. Technol.*, 1999. **33**: p. 4285-4291.

176. Hyun, S.P., J.A. Davis, K. Sun, and K.F. Hayes, Uranium(VI) reduction by iron(II) monosulfide mackinawite. *Environ. Sci. Technol.*, 2012. **46**: p. 3369-3376.

177. Icenhower, J.P., N.P. Qafoku, J.M. Zachara, and W.J. Martin, The biogeochemistry of technetium: A review of the behavior of an artificial element in the natural environment. *Am. J. Sci.*, 2010. **310**: p. 721-752.

178. Peretyazhko, T., J.M. Zachara, S.M. Heald, R.K. Kukkadapu, C. Liu, A.E. Plymale, and C.T. Resch, Reduction of Tc(VII) by Fe(II) sorbed on Al (hydr)oxides. *Environ. Sci. Technol.*, 2008. **42**: p. 5499-5506.

179. Peretyazhko, T.S., J.M. Zachara, R.K. Kukkadapu, S.M. Heald, I.V. Kutnyakov, C.T. Resch, B.W. Arey, C.M. Wang, L. Kovarik, J.L. Phillips, and D.A. Moore, Pertechnetate (TcO_4^-) reduction by reactive ferrous iron forms in naturally anoxic, redox transition zone sediments from the Hanford Site, USA. *Geochim. Cosmochim. Acta*, 2012. **92**: p. 48-66.

180. Gallegos, T.J., S.P. Hyun, and K.F. Hayes, Spectroscopic investigation of the uptake of arsenite from solution by synthetic mackinawite. *Environ. Sci. Technol.*, 2007. **41**: p. 7781-7786.

181. Jeong, H.Y., K. Sun, and K.F. Hayes, Microscopic and spectroscopic characterization of Hg(II) immobilization by mackinawite. *Environ. Sci. Technol.*, 2010. **44**: p. 7476-7683.

182. Couture, R.-M., L. Charlet, E. Markelova, B.t. Madé, and C.T. Parsons, On–Off mobilization of contaminants in soils during redox oscillations. *Environ. Sci. Technol.*, 2015.

183. Islam, F.S., A.G. Gault, C. Boothman, D.A. Polya, J.M. Charnock, D. Chatterjee, and J.R. Lloyd, Role of metal-reducing bacteria in arsenic release from Bengal delta sediments. *Nature*, 2004. **430**: p. 68-71.

184. Zobrist, J., P.R. Dowdle, J.A. Davis, and R.S. Oremland, Mobilization of arsenite by dissimilatory reduction of adsorbed arsenate. *Environ. Sci. Technol.*, 2000. **34**: p. 4747-4753.

185. Bargar, J.R., K.H. Williams, K.M. Campbell, P.E. Long, J.E. Stubbs, E.I. Suvorova, J.S. Lezama-Pacheco, D.S. Alessi, M. Stylo, S.M. Webb, J.A. Davis, D.E. Giammar, L.Y. Blue, and R. Bernier-Latmani, Uranium redox transition pathways in acetate-amended sediments. *Proc. Natl. Acad. Sci. USA*, 2013. **110**: p. 4506-4511.

186. Landrot, G., M. Ginder-Vogel, K. Livi, J.P. Fitts, and D.L. Sparks, Chromium (III) oxidation by three poorly-crystalline manganese (IV) oxides. 1. Chromium (III)-oxidizing capacity. *Environ. Sci. Technol.*, 2012. **46**: p. 11594-11600.

187. Landrot, G., M. Ginder-Vogel, K. Livi, J.P. Fitts, and D.L. Sparks, Chromium (III) oxidation by three poorly crystalline manganese (IV) oxides. 2. Solid phase analyses. *Environ. Sci. Technol.*, 2012. **46**: p. 11601-11609.

188. Wang, Z. and E. Acosta, Formulation design for target delivery of iron nanoparticles to TCE zones. *J. Contam. Hydro.*, 2013. **155**: p. 9-19.

189. Plathe, K.L., S.-W. Lee, B.M. Tebo, J.R. Bargar, and R. Bernier-Latmani, Impact of microbial Mn oxidation on the remobilization of bioreduced U (IV). *Environ. Sci. Technol.*, 2013. **47**: p. 3606-3613.

190. Jaisi, D.P., H. Dong, A.E. Plymale, J.K. Fredrickson, J.M. Zachara, S. Heald, and C. Liu, Reduction and long-term immobilization of technetium by Fe (II) associated with clay mineral nontronite. *Chem. Geol.*, 2009. **264**: p. 127-138.

191. McBeth, J.M., G. Lear, and J.R. Lloyd, Technetium reduction and reoxidation in aquifer sediments. *Geomicrobiol. J.*, 2007. **24**: p. 189-197.

192. Burke, I.T., C. Boothman, J.R. Lloyd, F.R. Livens, J.M. Charnock, J.M. McBeth, R.J.G. Mortimer, and K. Morris, Reoxidation behavior of technetium, iron, and sulfur in estuarine sediments. *Environ. Sci. Technol.*, 2006. **40**: p. 3529-3535.

193. Elsetinow, A.R., M.A.A. Schoonen, and D.R. Strongin, Aqueous geochemical and surface science investigation of the effect of phosphate on pyrite oxidation. *Environ. Sci. Technol.*, 2001. **35**: p. 2252-2257.

194. Kargbo, D.M., G. Atallah, and S. Chatterjee, Inhibition of pyrite oxidation by a phospholipid in the presence of silicate. *Environ. Sci. Technol.*, 2004. **38**: p. 3432-3441.

195. Um, W., H. Chang, J.P. Icenhower, W.W. Lukens, R.J. Serne, N.P. Qafoku, J. Westsik, J. H., E.C. Buck, and S.C. Smith, Immobilization of 99-technetium (VII) by Fe(II)-goethite and limited reoxidation. *Environ. Sci. Technol.*, 2011. **45**: p. 4904-4913.

196. Marshall, T.A., K. Morris, G.T. Law, F.R. Livens, J.F.W. Mosselmans, P. Bots, and S. Shaw, Incorporation of uranium into hematite during crystallization from ferrihydrite. *Environ. Sci. Technol.*, 2014. **48**: p. 3724-3731.

197. Marshall, T.A., K. Morris, G.T.W. Law, J.F.W. Mosselmans, P. Bots, S.A. Parry, and S. Shaw, Incorporation and retention of 99-Tc(IV) in magnetite under high pH conditions. *Environ. Sci. Technol.*, 2014. **48**: p. 11853-11862.

198. Nico, P.S., B.D. Stewart, and S. Fendorf, Incorporation of oxidized uranium into Fe (hydr) oxides during Fe (II) catalyzed remineralization. *Environ. Sci. Technol.*, 2009. **43**: p. 7391-7396.

199. Vogel, T.M., C.S. Criddle, and P.L. McCarty, ES&T critical reviews: transformations of halogenated aliphatic compounds. *Environ. Sci. Technol.*, 1987. **21**: p. 722-736.

200. Arnold, W.A. and A.L. Roberts, Pathways and kinetics of chlorinated ethylene and chlorinated acetylene reaction with Fe (0) particles. *Environ. Sci. Technol.*, 2000. **34**: p. 1794-1805.

201. Roberts, A.L., L.A. Totten, W.A. Arnold, D.R. Burris, and T.J. Campbell, Reductive elimination of chlorinated ethylenes by zero-valent metals. *Environ. Sci. Technol.*, 1996. **30**: p. 2654-2659.

202. Hara, J., H. Ito, K. Suto, C. Inoue, and T. Chida, Kinetics of trichloroethene dechlorination with iron powder. *Water Res.*, 2005. **39**: p. 1165-1173.

203. Scherer, M.M., B.A. Balko, D.A. Gallagher, and P.G. Tratnyek, Correlation analysis of rate constants for dechlorination by zero-valent iron. *Environ. Sci. Technol.*, 1998. **32**: p. 3026-3033.

204. Elsner, M., M. Chartrand, N. VanStone, G. Lacrampe Couloume, and B. Sherwood Lollar, Identifying abiotic chlorinated ethene degradation: characteristic isotope patterns in reaction products with nanoscale zero-valent iron. *Environ. Sci. Technol.*, 2008. **42**: p. 5963-5970.

205. Brown, R.A., J.G. Mueller, A.G. Seech, J.K. Henderson, and J.T. Wilson, Interactions between biological and abiotic pathways in the reduction of chlorinated solvents. *Remed J*, 2009. **20**: p. 9-20.

206. Liu, Y., T. Phenrat, and G.V. Lowry, Effect of TCE concentration and dissolved groundwater solutes on NZVI-promoted TCE dechlorination and H2 evolution. *Environ. Sci. Technol.*, 2007. **41**: p. 7881-7887.

207. He, F., D. Zhao, and C. Paul, Field assessment of carboxymethyl cellulose stabilized iron nanoparticles for in situ destruction of chlorinated solvents in source zones. *Water Res.*, 2010. **44**: p. 2360-2370.

208. Liang, L., N. Korte, J. Goodlaxson, J. Clausen, Q. Fernando, and R. Muftikian, Byproduct Formation During the Reduction of TCE by Zero ‐ Valence Iron and Palladized Iron. *Ground Water Monit. R.*, 1997. **17**: p. 122-127.

209. Cwiertny, D.M., S.J. Bransfield, K.J. Livi, D.H. Fairbrother, and A.L. Roberts, Exploring the influence of granular iron additives on 1, 1, 1-trichloroethane reduction. *Environ. Sci. Technol.*, 2006. **40**: p. 6837-6843.

210. Schrick, B., J.L. Blough, A.D. Jones, and T.E. Mallouk, Hydrodechlorination of trichloroethylene to hydrocarbons using bimetallic nickel-iron nanoparticles. *Chem. Mater.*, 2002. **14**: p. 5140-5147.

211. Kim, J.-H., P.G. Tratnyek, and Y.-S. Chang, Rapid dechlorination of polychlorinated dibenzo-p-dioxins by bimetallic and nanosized zerovalent iron. *Environ. Sci. Technol.*, 2008. **42**: p. 4106-4112.

212. Zhuang, Y., S. Ahn, A.L. Seyfferth, Y. Masue-Slowey, S. Fendorf, and R.G. Luthy, Dehalogenation of polybrominated diphenyl ethers and polychlorinated biphenyl by bimetallic, impregnated, and nanoscale zerovalent iron. *Environ. Sci. Technol.*, 2011. **45**: p. 4896-4903.

213. Kim, E.-J., J.-H. Kim, A.-M. Azad, and Y.-S. Chang, Facile synthesis and characterization of Fe/FeS nanoparticles for environmental applications. *ACS Appl. Mater. Inter.*, 2011. **3**: p. 1457-1462.

214. Kim, E.-J., K. Murugesan, J.-H. Kim, P.G. Tratnyek, and Y.-S. Chang, Remediation of trichloroethylene by FeS-coated iron nanoparticles in simulated and real groundwater: Effects of water chemistry. *Ind. Eng. Chem.Res*, 2013. **52**: p. 9343-9350.

215. Guan, X., Y. Sun, H. Qin, J. Li, I.M. Lo, D. He, and H. Dong, The Limitations of Applying Zero-Valent Iron Technology in Contaminants Sequestration and the Corresponding Countermeasures: The Development in Zero-Valent Iron Technology in the Last Two Decades (1994-2014). *Water Res.*, 2015.

216. Liu, T., X. Li, and T.D. Waite, Depassivation of aged Fe0 by ferrous ions: implications to contaminant degradation. *Environ. Sci. Technol.*, 2013. **47**: p. 13712-13720.

217. Liu, T., X. Li, and T.D. Waite, Depassivation of aged Fe0 by divalent cations: correlation between contaminant degradation and surface complexation constants. *Environ. Sci. Technol.*, 2014.

218. Chen, L., S. Jin, P.H. Fallgren, N.G. Swoboda-Colberg, F. Liu, and P.J.S. Colberg, Electrochemical depassivation of zero-valent iron for trichloroethene reduction. *Occurrence and fate of emerging contaminants in municipal wastewater treatment systems*, 2012. **239–240**: p. 265-269.

219. Liang, L., X. Guan, Z. Shi, J. Li, Y. Wu, and P.G. Tratnyek, Coupled effects of aging and weak magnetic fields on sequestration of selenite by zero-valent iron. *Environ. Sci. Technol.*, 2014. **48**: p. 6326-6334.

220. Liang, L., W. Sun, X. Guan, Y. Huang, W. Choi, H. Bao, L. Li, and Z. Jiang, Weak magnetic field significantly enhances selenite removal kinetics by zero valent iron. *Water Res.*, 2014. **49**: p. 371-380.

221. Tratnyek, P.G., A.J. Salter, J.T. Nurmi, and V. Sarathy, Environmental applications of zerovalent metals: Iron vs. zinc, in *Nanoscale Materials in Chemistry: Environmental Applications*, L.E. Erickson, R.T. Koodali, and R.M. Richards, Editors. 2010, American Chemical Society. p. 165-178.

222. Amonette, J.E., D.J. Workman, D.W. Kennedy, J.S. Fruchter, and Y.A. Gorby, Dechlorination of carbon tetrachloride by Fe (II) associated with goethite. *Environ. Sci. Technol.*, 2000. **34**: p. 4606-4613.

223. Maithreepala, R. and R.-a. Doong, Synergistic effect of copper ion on the reductive dechlorination of carbon tetrachloride by surface-bound Fe (II) associated with goethite. *Environ. Sci. Technol.*, 2004. **38**: p. 260-268.

224. Zwank, L., M. Elsner, A. Aeberhard, R.P. Schwarzenbach, and S.B. Haderlein, Carbon isotope fractionation in the reductive dehalogenation of carbon tetrachloride at iron (hydr) oxide and iron sulfide minerals. *Environ. Sci. Technol.*, 2005. **39**: p. 5634-5641.

225. Kenneke, J.F. and E.J. Weber, Reductive dehalogenation of halomethanes in iron- and sulfate-reducing sediments. 1. Reactivity pattern analysis. *Environ. Sci. Technol.*, 2003. **37**: p. 713-720.

226. Elsner, M., S.B. Haderlein, T. Kellerhals, S. Luzi, L. Zwank, W. Angst, and R.P. Schwarzenbach, Mechanisms and products of surface-mediated reductive dehalogenation of carbon tetrachloride by Fe (II) on goethite. *Environ. Sci. Technol.*, 2004. **38**: p. 2058-2066.

227. Liang, X., R. Paul Philp, and E.C. Butler, Kinetic and isotope analyses of tetrachloroethylene and trichloroethylene degradation by model Fe(II)-bearing minerals. *Chemosphere*, 2009. **75**: p. 63-69.

228. Lee, W. and B. Batchelor, Abiotic reductive dechlorination of chlorinated ethylenes by iron-bearing soil minerals. 1. pyrite and magnetite. *Environ. Sci. Technol.*, 2002. **36**: p. 5147-5154.

229. Lee, W. and B. Batchelor, Reductive capacity of natural reductants. *Environ. Sci. Technol.*, 2003. **37**: p. 535-541.

230. Butler, E.C. and K.F. Hayes, Factors influencing rates and products in the transformation of trichloroethylene by iron sulfide and iron metal. *Environ. Sci. Technol.*, 2001. **35**: p. 3884-3891.

231. Butler, E.C. and K.F. Hayes, Kinetics of the transformation of trichloroethylene and tetrachloroethylene by iron sulfide. *Environ. Sci. Technol.*, 1999. **33**: p. 2021-2027.

232. Dong, Y., X. Liang, L.R. Krumholz, R.P. Philp, and E.C. Butler, The relative contributions of abiotic and microbial processes to the transformation of tetrachloroethylene and trichloroethylene in anaerobic microcosms. *Environ. Sci. Technol.*, 2008. **43**: p. 690-697.

233. Jeong, H.Y., K. Anantharaman, Y.-S. Han, and K.F. Hayes, Abiotic reductive dechlorination of cis-dichloroethylene by Fe species formed during iron-or sulfate-reduction. *Environ. Sci. Technol.*, 2011. **45**: p. 5186-5194.

234. Han, Y.-S., S.P. Hyun, H.Y. Jeong, and K.F. Hayes, Kinetic study of cis-dichloroethylene (cis-DCE) and vinyl chloride (VC) dechlorination using green rusts formed under varying conditions. *Water Res.*, 2012. **46**: p. 6339-6350.

235. Jeong, H.Y., K. Anantharaman, S.P. Hyun, M. Son, and K.F. Hayes, pH impact on reductive dechlorination of cis-dichloroethylene by Fe precipitates: An X-ray absorption spectroscopy study. *Water Res.*, 2013. **47**: p. 6639-6649.

236. Colón, D., E.J. Weber, and J.L. Anderson, QSAR study of the reduction of nitroaromatics by Fe (II) species. *Environ. Sci. Technol.*, 2006. **40**: p. 4976-4982.

237. Chen, J.-L., S.R. Al-Abed, J.A. Ryan, and Z. Li, Effects of pH on dechlorination of trichloroethylene by zero-valent iron. *J. Hazard. Mater.*, 2001. **83**: p. 243-254.

238. Danielsen, K.M. and K.F. Hayes, pH dependence of carbon tetrachloride reductive dechlorination by magnetite. *Environ. Sci. Technol.*, 2004. **38**: p. 4745-4752.

239. Butler, E.C. and K.F. Hayes, Effects of solution composition and pH on the reductive dechlorination of hexachloroethane by iron sulfide. *Environ. Sci. Technol.*, 1998. **32**: p. 1276-1284.

240. Chen, J., B. Gu, R.A. Royer, and W.D. Burgos, The roles of natural organic matter in chemical and microbial reduction of ferric iron. *Science of the Total Environment*, 2003. **307**: p. 167-178.

241. Schwarzenbach, R.P., R. Stierli, K. Lanz, and J. Zeyer, Quinone and iron porphyrin mediated reduction of nitroaromatic compounds in homogeneous aqueous solution. *Environ. Sci. Technol.*, 1990. **24**: p. 1566-1574.

242. Perlinger, J.A., J. Buschmann, W. Angst, and R.P. Schwarzenbach, Iron porphyrin and mercaptojuglone mediated reduction of polyhalogenated methanes and ethanes in homogeneous aqueous solution. *Environ. Sci. Technol.*, 1998. **32**: p. 2431-2437.

243. Dunnivant, F.M., R.P. Schwarzenbach, and D.L. Macalady, Reduction of substituted nitrobenzenes in aqueous solutions containing natural organic matter. *Environ. Sci. Technol.*, 1992. **26**: p. 2133-2141.

244. Buschmann, J., W. Angst, and R.P. Schwarzenbach, Iron porphyrin and cysteine mediated reduction of ten polyhalogenated methanes in homogeneous aqueous solution: Product analyses and mechanistic considerations. *Environ. Sci. Technol.*, 1999. **33**: p. 1015-1020.

245. Sposito, G., Electron shuttling by natural organic matter: twenty years after, in *Aquatic Redox Chemistry*. 2011, American Chemical Society. p. 113-127.

246. Van der Zee, F.P. and F.J. Cervantes, Impact and application of electron shuttles on the redox (bio) transformation of contaminants: a review. *Biotechnol. Adv.*, 2009. **27**: p. 256-277.

247. Tratnyek, P.G., M.M. Scherer, B. Deng, and S. Hu, Effects of natural organic matter, anthropogenic surfactants, and model quinones on the reduction of contaminants by zero-valent iron. *Water Res.*, 2001. **35**: p. 4435-4443.

248. Chen, J., Z. Xiu, G.V. Lowry, and P.J. Alvarez, Effect of natural organic matter on toxicity and reactivity of nano-scale zero-valent iron. *Water Res.*, 2011. **45**: p. 1995-2001.

249. Dries, J., L. Bastiaens, D. Springael, S. Kuypers, S.N. Agathos, and L. Diels, Effect of humic acids on heavy metal removal by zero-valent iron in batch and continuous flow column systems. *Water Res.*, 2005. **39**: p. 3531-3540.

250. Giasuddin, A.B., S.R. Kanel, and H. Choi, Adsorption of humic acid onto nanoscale zerovalent iron and its effect on arsenic removal. *Environ. Sci. Technol.*, 2007. **41**: p. 2022-2027.

251. Kang, S.-H. and W. Choi, Oxidative degradation of organic compounds using zero-valent iron in the presence of natural organic matter serving as an electron shuttle. *Environ. Sci. Technol.*, 2008. **43**: p. 878-883.

252. Bae, S. and W. Lee, Influence of riboflavin on nanoscale zero-valent iron reactivity during the degradation of carbon tetrachloride. *Environ. Sci. Technol.*, 2014. **48**: p. 2368-2376.

253. Kim, S., T. Park, and W. Lee, Enhanced reductive dechlorination of tetrachloroethene by nano-sized mackinawite with cyanocobalamin in a highly alkaline condition. *Journal of environmental management*, 2015. **151**: p. 378-385.

254. Klausen, J., P.J. Vikesland, T. Kohn, D.R. Burris, W.P. Ball, and A.L. Roberts, Longevity of granular iron in groundwater treatment processes: solution

composition effects on reduction of organohalides and nitroaromatic compounds. *Environ. Sci. Technol.*, 2003. **37**: p. 1208-1218.

255. Jia, H., C. Gu, H. Li, X. Fan, S. Li, and C. Wang, Effect of groundwater geochemistry on pentachlorophenol remediation by smectite-templated nanosized Pd0/Fe0. *Environmental Science and Pollution Research*, 2012. **19**: p. 3498-3505.

256. Kim, J.S., P.J. Shea, J.E. Yang, and J.-E. Kim, Halide salts accelerate degradation of high explosives by zerovalent iron. *Environmental pollution*, 2007. **147**: p. 634-641.

257. Hernandez, R., M. Zappi, and C.-H. Kuo, Chloride effect on TNT degradation by zerovalent iron or zinc during water treatment. *Environ. Sci. Technol.*, 2004. **38**: p. 5157-5163.

258. Kohn, T. and A.L. Roberts, The effect of silica on the degradation of organohalides in granular iron columns. *J. Contam. Hydro.*, 2006. **83**: p. 70-88.

259. Lim, T.-T. and B.-W. Zhu, Effects of anions on the kinetics and reactivity of nanoscale Pd/Fe in trichlorobenzene dechlorination. *Chemosphere*, 2008. **73**: p. 1471-1477.

260. Lim, T.-T., J. Feng, and B.-W. Zhu, Kinetic and mechanistic examinations of reductive transformation pathways of brominated methanes with nano-scale Fe and Ni/Fe particles. *Water Res.*, 2007. **41**: p. 875-883.

261. Jeen, S.-W., J.L. Jambor, D.W. Blowes, and R.W. Gillham, Precipitates on granular iron in solutions containing calcium carbonate with trichloroethene and hexavalent chromium. *Environ. Sci. Technol.*, 2007. **41**: p. 1989-1994.

262. Jeong, H.Y. and K.F. Hayes, Impact of transition metals on reductive dechlorination rate of hexachloroethane by mackinawite. *Environ. Sci. Technol.*, 2003. **37**: p. 4650-4655.

263. Maithreepala, R. and R.-a. Doong, Enhanced dechlorination of chlorinated methanes and ethenes by chloride green rust in the presence of copper (II). *Environ. Sci. Technol.*, 2005. **39**: p. 4082-4090.

264. O'Loughlin, E.J., K.M. Kemner, and D.R. Burris, Effects of AgI, AuIII, and CuII on the reductive dechlorination of carbon tetrachloride by green rust. *Environ. Sci. Technol.*, 2003. **37**: p. 2905-2912.

265. Maes, A., K. Geraedts, C. Bruggeman, J. Vancluysen, A. Rossberg, and C. Hennig, Evidence for the interaction of technetium colloids with humic substances by X-ray absorption spectroscopy. *Environ. Sci. Technol.*, 2004. **38**: p. 2044-2051.

266. Rard, J.A., Current status of the thermodynamic data for technetium and its compounds and aqueous species. *J. Nucl. Radiochem. Sci.*, 2005. **6**: p. 197-204.

267. O'Loughlin, E.J., M.I. Boyanov, D.A. Antonopoulos, and K.M. Kemner, Redox processes affecting the speciation of technetium, uranium, neptunium, and plutonium in aquatic and terrestrial environments, in *Aquatic Redox Chemistry*, P.G. Tratnyek, T.J. Grundl, and S.B. Haderlein, Editors. 2011, American Chemical Society: Washington, DC. p. 477-517.

268. Cui, D. and T.E. Eriksen, Reduction of pertecnnetate in solution by heterogeneou electron transfer from Fe(II)-containing geological material. *Environ. Sci. Technol.*, 1996. **30**: p. 2263-2269.

269. Plymale, A.E., J.K. Fredrickson, J.M. Zachara, A.C. Dohnalkova, S.M. Heald, D.A. Moore, D.W. Kennedy, M.J. Marshall, C. Wang, C.T. Resch, and P. Nachimuthu, Competitive reduction of pertechnetate ($^{99}TcO_4^-$) by dissimilatory metal reducing bacteria and biogenic Fe (II). *Environ. Sci. Technol.*, 2011. **45**: p. 951-957.

270. Burke, I.T., C. Boothman, J.R. Lloyd, R.J.G. Mortimer, F.R. Livens, and K. Morris, Effects of progressive anoxia on the solubility of technetium in sediments. *Environ. Sci. Technol.*, 2005. **39**: p. 4109-4116.

271. Liu, Y., J. Terry, and S. Jurisson, Pertechnetate immobilization in aqueous media with hydrogen sulfide under anaerobic and aerobic environments. *Radiochim. Acta*, 2007. **95**: p. 717-725.

272. Lukens, W.W., J.J. Bucher, D.K. Shuh, and N.M. Edelstein, Evolution of technetium speciation in reducing grout. *Environ. Sci. Technol.*, 2005. **39**: p. 8064-8070.

273. Kunze, S., V. Neck, K. Gompper, and T. Fanghanel, Studies on the immobilization of technetium under near field geochemical conditions. *Radiochim. Acta*, 1996. **74**: p. 159-163.

274. Liu, Y., J. Terry, and S. Jurrison, Pertechnetate immobilization with amorphous iron sulfide. *Radiochim. Acta*, 2008. **96**.

275. Watson, J.H.P., I.W. Croudace, P.E. Warwick, P.A.B. James, J.M. Charnock, and D.C. Ellwood, Adsorption of radioactive metals by strongly magnetic iron sulfide nanoparticles produced by sulfate-reducing bacteria. *Separ. Sci. Technol.*, 2001. **36**: p. 2571-2607.

276. Wharton, M.J.A., B.; Charnock, J. M.; Livens, F. R.; Pattrick, R. A. D.; Collision, D., An X-ray absorption spectroscopy study of the copreipitation of Tc and Re with mackinawite (FeS). *Appl. Geochem.*, 2000. **15**: p. 347-354.

277. Thornton, E.C. and J.E. Amonette, Hydrogen sulfide gas treatment of Cr(VI)-contaminated sediment samples from a plating-waste disposal site: implications for in-situ remediation. *Environ. Sci. Technol.*, 1999. **33**: p. 4096-4101.

278. Keith-Roach, M.J., K. Morris, and H. Dahlgaard, An investigation into technetium binding in sediments. *Mar. Chem.*, 2003. **81**: p. 149-162.

279. Kirschling, T.L., K.B. Gregory, E.G. Minkley, Jr., G.V. Lowry, and R.D. Tilton, Impact of nanoscale zero valent iron on geochemistry and microbial populations in trichloroethylene contaminated aquifer materials. *Environ. Sci. Technol.*, 2010. **44**: p. 3474-3480.

280. Rickard, D. and G.W. Luther III, Chemistry of iron sulfides. *Chem. Rev.*, 2007. **107**: p. 514-562.

281. Coles, C.A., S.R. Rao, and R.N. Yong, Lead and cadmium interactions with mackinawite: retention mechanisms and the role of pH. *Environ. Sci. Technol.*, 2000. **34**: p. 996-1000.

282. Bulter, E.C. and K.F. Hayes, Factors influencing rates and products in the transformation of trichloroethylene by iron sulfide and iron metal. *Environ. Sci. Technol.*, 2001. **35**: p. 3884-3891.

283. He, Y.T., J.T. Wilson, and R.T. Wilkin, Impact of iron sulfide transformation on trichloroethylene degradation. *Geochim. Cosmochim. Acta*, 2010. **74**: p. 2025-2039.

284. Scheinost, A.C. and L. Charlet, Selenite reduction by mackinawite, magnetite and siderite: XAS characterization of nanosized redox products. *Environ. Sci. Technol.*, 2008. **42**: p. 1984-1989.

285. Wolthers, M., L. Charlet, C.H. van Der Weijden, P.R. van der Linde, and D. Rickard, Arsenic mobility in the ambient sulfidic environment: sorption of

arsenic(V) and arsenic(III) onto disordered mackinawite. *Geochim. Cosmochim. Acta*, 2005. **69**: p. 3483-3492.

286. Nurmi, J., V. Sarathy, P. Tratnyek, D. Baer, J. Amonette, and A. Karkamkar, Recovery of iron/iron oxide nanoparticles from solution: comparison of methods and their effects. *J. Nanopart. Res.*, 2011. **13**: p. 1937-1952.

287. Ravel, B. and M. Newville, ATHENA, ARTEMIS, HEPHAESTUS: data analysis for X-ray absorption spectroscopy using IFEFFIT. *J. Synchrotron Radiat.*, 2005. **12**: p. 537-541.

288. Rehr, J.J., R.C. Albers, and S.I. Zabinsky, High-order multiple-scattering calculations of x-ray-absorption fine structure. *Phys. Rev. Lett.*, 1992. **69**: p. 3397-3400.

289. Baer, D.R., P.G. Tratnyek, Y. Qiang, J.E. Amonette, J. Linehan, V. Sarathy, J.T. Nurmi, C. Wang, and J. Anthony, Synthesis, characterization, and properties of zero-valent iron nanoparticles, in *Environmental Applications of Nanomaterials: Synthesis, Sorbents, and Sensors*, G.E. Fryxell, Editor. 2007, Imperial College Press: London. p. 49-86.

290. Glavee, G.N., K.J. Klabunde, C.M. Sorensen, and G.C. Hadjipanayis, Chemistry of borohydride reduction of iron(II) and iron(III) ions in aqueous and nonaqueous media - formation of nanoscale Fe, FeB, and Fe_2B powders. *Inorg. Chem.*, 1995. **34**: p. 28-35.

291. Wang, Q., S. Snyder, J. Kim, and H. Choi, Aqueous ethanol modified nanoscale zerovalent iron in bromate reduction: synthesis, characterization, and reactivity. *Environ. Sci. Technol.*, 2009. **43**: p. 3292-3299.

292. Wolthers, M.t., S.J.V.d. Gaast, and D. Rickard, The structure of disordered mackinawite. *Am. Mineral.*, 2003. **88**: p. 2007-2015.

293. Reinsch, B.C., C. Levard, Z. Li, R. Ma, A. Wise, K.B. Gregory, G.E. Brown, and G.V. Lowry, Sulfidation of silver nanoparticles decreases Escherichia coli growth inhibition. *Environ. Sci. Technol.*, 2012. **46**: p. 6992-7000.

294. Descostes, M., F. Mercier, N. Thromat, C. Beaucaire, and M. Gautier-Soyer, Use of XPS in the determination of chemical environment and oxidation state of iron and sulfur samples: constitution of a data basis in binding energies for Fe and S reference compounds and applications to the evidence of surface species of an oxidized pyrite in a carbonate medium. *Appl. Surf. Sci.*, 2000. **165**: p. 288-302.

295. Bostick, B.C., S. Fendorf, and G.R. Helz, Differential adsorption of molybdate and tetrathiomolybdate on pyrite (FeS_2). *Environ. Sci. Technol.*, 2002. **37**: p. 285-291.

296. Saiki, Y., M. Fukuzaki, T. Sekine, Y. Kino, and H. Kudo, Technetium(VII) sulfide colloid growing observed by laser-induced photoacoustic spectroscopy. *J. Radioanal. Nucl. Chem*, 2003. **255**: p. 101-104.

297. Weber, F.-A., A. Voegelin, R. Kaegi, and R. Kretzschmar, Contaminant mobilization by metallic copper and metal sulphide colloids in flooded soil. *Nat. Geosci.*, 2009. **2**: p. 267-271.

298. Yin, Y., R.M. Rioux, C.K. Erdonmez, S. Hughes, G.A. Somorjai, and A.P. Alivisatos, Formation of hollow nanocrystals through the nanoscale Kirkendall effect. *Science*, 2004. **304**: p. 711-714.

299. Almahamid, I., J.C. Bryan, J.J. Bucher, A.K. Burrell, N.M. Edelstein, E.A. Hudson, N. Kaltsoyannis, W.W. Lukens, and H. Nitsche, Electronic and structural investigations of technetium compounds by x-ray absorption spectroscopy. *Inorg. Chem.*, 1995. **34**: p. 193-198.

300. Terry, J., B. Grzenia, D. Papagiannopoulou, J. Kyger, S. Jurisson, and J.D. Robertson, Structural determination of Tc radiopharmaceuticals and compounds using x-ray absorption spectroscopy. *J. Radioanal. Nucl. Chem*, 2005. **263**: p. 531-537.

301. Darab, J.G., A.B. Amonette, D.S.D. Burke, R.D. Orr, S.M. Ponder, B. Schrick, T.E. Mallouk, W.W. Lukens, D.L. Caulder, and D.K. Shuh, Removal of Pertechnetate from Simulated Nuclear Waste Streams Using Supported Zerovalent Iron. *Chem. Mater.*, 2007. **19**: p. 5703-5713.

302. Lamfers, H.J., A. Meetsma, G.A. Wiegers, and J.L. de Boer, The crystal structure of some rhenium and technetium dichalcogenides. *J. Alloy Compd.*, 1996. **241**: p. 34-39.

303. Jansik, D., J. Szecsody, and J. Istok, Treatment of pertechnetate by nano zero-valent iron and sulfide: column scale studies. *J. Contam. Hydro.*, In preparation.

304. Stroo, H.F., A. Leeson, J.A. Marqusee, P.C. Johnson, C.H. Ward, M.C. Kavanaugh, T.C. Sale, C.J. Newell, K.D. Pennell, and C.A. Lebrón, Chlorinated ethene source remediation: Lessons learned. *Environ. Sci. Technol.*, 2012. **46**: p. 6438-6447.

305. Liu, Y., J. Terry, and S.S. Jurisson, Potential interferences on the pertechnetate-sulfide immobilization reaction. *Radiochim. Acta*, 2009. **97**: p. 33-41.

306. Jones, T.E., R. Khaleel, D.A. Myers, J.W. Shade, and M.I. Wood, A summary and evaluation of Hanford site tank farm subsurface contamination. 1998, Lockheed Martin Hanford: Richland, WA.

307. Beasley, T.M., P.R. Dixon, and L.J. Mann, ^{99}Tc, ^{236}U, and ^{237}Np in the Snake River Plain aquifer at the Idaho National Engineering and Environmental Laboratory, Idaho Falls, Idaho. *Environ. Sci. Technol.*, 1998. **32**: p. 3875-3881.

308. Fredrickson, J.K., J.M. Zachara, D.W. Kennedy, R.K. Kukkadapu, J.P. McKinley, S.M. Heald, C. Liu, and A.E. Plymale, Reduction of TcO_4^- by sediment-associated biogenic Fe(II). *Geochim. Cosmochim. Acta*, 2004. **68**: p. 3171-3187.

309. Lloyd, J.R., V.A. Sole, C.V.G. Van Praagh, and D.R. Lovley, Direct and Fe(II)-mediated reduction of technetium by Fe(III)-reducing bacteria. *Appl. Environ. Microbe.*, 2000. **66**: p. 3743-3749.

310. Pearce, C.I., J. Liu, D.R. Baer, O. Qafoku, S.M. Heald, E. Arenholz, A.E. Grosz, J.P. McKinley, C.T. Resch, M.E. Bowden, M.H. Engelhard, and K.M. Rosso, Characterization of natural titanomagnetites ($Fe_{3-x}Ti_xO_4$) for studying heterogeneous electron transfer to Tc(VII) in the Hanford subsurface. *Geochim. Cosmochim. Acta*, 2014. **128**: p. 114-127.

311. Szecsody, J.E., D.P. Jansik, J.P. McKinley, and N.J. Hess, Influence of alkaline co-contaminants on technetium mobility in vadose zone sediments. *J. Environ. Radioactiv.*, 2014. **135**: p. 147-160.

312. Eagling, J., P.J. Worsfold, W.H. Blake, and M.J. Keith-Roach, Mobilization of technetium from reduced sediments under seawater inundation and intrusion scenarios. *Environ. Sci. Technol.*, 2012. **46**: p. 11798-11803.

313. Chinni, S., C.R. Anderson, K.-U. Ulrich, D.E. Giammar, and B.M. Tebo, Indirect UO_2 oxidation by Mn(II)-oxidizing spores of *Bacillus* sp. strain SG-1 and the effect of U and Mn concentrations. *Environ. Sci. Technol.*, 2008. **42**: p. 8709-8714.

314. Liu, C., J.M. Zachara, J.K. Fredrickson, D.W. Kennedy, and A. Dohnalkova, Modeling the inhibition of the bacterial reduction of U(VI) by β-MnO_2(s). *Environ. Sci. Technol.*, 2002. **36**: p. 1452-1459.

315. Fredrickson, J.K., J.M. Zachara, D.W. Kennedy, C. Liu, M.C. Duff, D.B. Hunter, and A. Dohnalkova, Influence of Mn oxides on the reduction of uranium(VI) by the metal-reducing bacterium *Shewanella putrefaciens. Geochim. Cosmochim. Acta*, 2002. **66**: p. 3247-3262.

316. Wang, Z., S. Lee, P. Kapoor, B.M. Tebo, and D.E. Giammar, Uraninite oxidation and dissolution induced by manganese oxide: a redox reacton between two insoluble minerals. *Geochim. Cosmochim. Acta*, 2013. **100**: p. 24-40.

317. Fredrickson, J.K., J.M. Zachara, A.E. Plymale, S.M. Heald, J.P. McKinley, D.W. Kennedy, C. Liu, and P. Nachimuthu, Oxidative dissolution of potential of biogenic and abiogenic TcO_2 in subsurface sediments. *Geochim. Cosmochim. Acta*, 2009. **73**: p. 2299-2313.

318. Livens, F.R., M.J. Jones, A.J. Hynes, J.M. Charnock, and J.F.W. Mosselmans, X-ray absorption spectroscopy studies of reactions of technetium, uranium and neptunium with mackinawite. *J. Environ. Radioactiv.*, 2004. **74**: p. 211-219.

319. Lee, J.-H., J.K. Fredrickson, R.K. Kukkadapu, M.I. Boyanov, K.M. Kemner, X. Lin, D.W. Kennedy, B.N. Bjornstad, A.E. Konopka, D.A. Moore, C.T. Resch, and J.L. Phillips, Microbial reductive transformation of phyllosilicate Fe(III) and U(VI) in fluvial subsurface sediments. *Environ. Sci. Technol.*, 2012. **46**: p. 3721-3730.

320. Jeong, H.Y., Y. Han, and K.F. Hayes, X-ray absorption and X-ray photoelectron spectroscopic study of arsenic mobilization during mackinawite (FeS) oxidation. *Environ. Sci. Technol.*, 2010. **44**: p. 955-961.

321. Holmes, J., Fate of incoporated metals during mackinawite oxidaiton in sea water. *Appl. Geochem.*, 1999. **14**: p. 277-281.

322. Schippers, A. and B.B. Jørgensen, Oxidation of pyrite and iron sulfide by manganese dioxide in marine sediments. *Geochim. Cosmochim. Acta*, 2001. **65**: p. 915-922.

323. Schippers, A. and W. Sand, Bacterial leaching of metal sulfides proceeds by two indirect mechanisms via thiosulfate or via polysulfides and sulfur. *Appl. Environ. Microbe.*, 1999. **65**: p. 319-321.

324. Burton, E.D., R.T. Bush, and L.A. Sullivan, Acid-volatile sulfide oxidation in coastal flood plain drains: iron−sulfur cycling and effects on water quality. *Environ. Sci. Technol.*, 2006. **40**: p. 1217-1222.

325. Hampton, M.A., C. Plackowski, and A.V. Nguyen, Physical and chemical analysis of elemental sulfur formation during galena surface oxidation. *Langmuir*, 2011. **27**: p. 4190-4201.

326. Lukens, J.J. Bucher, N.M. Edelstein, and D.K. Shuh, Products of pertechnetate radiolysis in highly alkaline solution: structure of $TcO_2 \cdot xH_2O$. *Environ. Sci. Technol.*, 2002. **36**: p. 1124-1129.

327. Hu, Q.H., T.P. Rose, M. Zavarin, D.K. Smith, J.E. Moran, and P.H. Zhao, Assessing field-scale migration of radionuclides at the Nevada Test Site: “mobile” species. *J. Environ. Radioactiv.*, 2008. **99**: p. 1617-1630.

328. Jeong, H.Y., K. Sun, and K.F. Hayes, Microscopic and spectroscopic characterization of Hg(II) immobilization by mackinawite (FeS). *Environ. Sci. Technol.*, 2010. **44**: p. 7476-83.

329. Veeramani, H., A.C. Scheinost, N. Monsegue, N.P. Qafoku, R. Kukkadapu, M. Newville, A. Lanzirotti, A. Pruden, M. Murayama, and M.F. Hochella, Abiotic reductive immobilization of U(VI) by biogenic mackinawite. *Environ. Sci. Technol.*, 2013. **47**: p. 2361-2369.

330. Aller, R.C. and P.D. Rude, Complete oxidation of solid phase sulfides by manganese and bacteria in anoxic marine sediments. *Geochim. Cosmochim. Acta*, 1988. **52**: p. 751-765.

331. Zhang, Y.L. and V.P. Evangelou, Formation of ferric hydroxide-silica coatings on pyrite and its oxidation behavior. *Soil Science*, 1998. **163**: p. 53-62.

332. He, Y., C. Su, J.T. Wilson, R.T. Wilkin, C. Adair, T. Lee, P. Bradley, and M. Ferrey, Identification and characterization methods for reactive minerals responsible for natural attenuation of chlorinated organic compounds in ground water. 2009, U.S. EPA Office of Research and Development: Ada, Oklahoma.

333. Rügge, K., T.B. Hofstetter, S.B. Haderlein, P.L. Bjerg, S. Knudsen, C. Zraunig, H. Mosbæk, and T.H. Christensen, Characterization of predominant reductants in an anaerobic leachate-contaminated aquifer by nitroaromatic probe compounds. *Environ. Sci. Technol.*, 1998. **32**: p. 23-31.

334. Zhang, H., D. Colón, J.F. Kenneke, and E.J. Weber, The use of chemical probes for the characterization of the predominant abiotic reductants in anaerobic sediments, in *Aquatic Redox Chemistry*, P.G. Tratnyek, T.J. Grundl, and S.B. Haderlein, Editors. 2011, American Chemical Society: Washington, DC. p. 539-557.

335. Tratnyek, P., G., T. Grundl, J., and S. Haderlein, B., eds. *Aquatic Redox Chemistry*. ACS Symp. Ser. Vol. 1071. 2011, American Chemical Society. 0.

336. Strathmann, T.J. and A.T. Stone, Mineral surface catalysis of reactions between Fe II and oxime carbamate pesticides. *Geochim. Cosmochim. Acta*, 2003. **67**: p. 2775-2791.

337. O'Loughlin, E.J., Effects of electron transfer mediators on the bioreduction of lepidocrocite (γ-FeOOH) by *Shewanella putrefaciens* CN32. *Environ. Sci. Technol.*, 2008. **42**: p. 6876-6882.

338. Shi, Z., J.M. Zachara, L. Shi, Z. Wang, D.A. Moore, D.W. Kennedy, and J.K. Fredrickson, Redox reactions of reduced flavin mononucleotide (FMN), riboflavin (RBF), and anthraquinone-2,6-disulfonate (AQDS) with ferrihydrite and lepidocrocite. *Environ. Sci. Technol.*, 2012. **46**: p. 11644-11652.

339. Zhang, H. and E.J. Weber, Elucidating the role of electron shuttles in reductive transformations in anaerobic sediments. *Environ. Sci. Technol.*, 2009. **43**: p. 1042-1048.

340. Silvester, E., L. Charlet, C. Tournassat, A. Gehin, J.-M. GrenÈche, and E. Liger, Redox potential measurements and Mössbauer spectrometry of Fe II adsorbed onto Fe III (oxyhydr) oxides. *Geochim. Cosmochim. Acta*, 2005. **69**: p. 4801-4815.

341. Chen, S., D. Fan, and P.G. Tratnyek, Novel contaminant transformation pathways by abiotic reductants. *Environmental Science & Technology Letters*, 2014. **1**: p. 432-436.

342. Bishop, E., Indicators. 1st ed. 1972, Oxford: Pergamon. 746.

343. Maithreepala, R. and R.-a. Doong. Dechlorination of carbon tetrachloride by ferrous ion associated with iron oxide nano particles. in *The fourth academic sessions*. 2007.

344. Smolen, J.M., E.J. Weber, and P.G. Tratnyek, Molecular probe techniques for the identification of reductants in sediments: Evidence for reduction of 2-chloroacetophenone by hydride transfer. *Environ. Sci. Technol.*, 1999. **33**: p. 440-445.

345. Hofstetter, T.B., C.G. Heijman, S.B. Haderlein, C. Holliger, and R.P. Schwarzenbach, Complete reduction of TNT and other (poly) nitroaromatic compounds under iron-reducing subsurface conditions. *Environ. Sci. Technol.*, 1999. **33**: p. 1479-1487.

346. Johnson, R.L., G.O.B. Johnson, J.T. Nurmi, and P.G. Tratnyek, Natural organic matter enhanced mobility of nano zerovalent iron. *Environ. Sci. Technol.*, 2009. **43**: p. 5455-5460.

347. Saleh, N., K. Sirk, Y. Liu, T. Phenrat, B. Dufour, K. Matyjaszewski, R.D. Tilton, and G.V. Lowry, Surface modifications enhance nanoiron transport and NAPL targeting in saturated porous media. *Environ. Eng. Sci.*, 2006. **24**: p. 45-57.

348. He, F., M. Zhang, T. Qian, and D. Zhao, Transport of carboxymethyl cellulose stabilized iron nanoparticles in porous media: Column experiments and modeling. *Journal of Colloid and Interface Science*, 2009. **334**: p. 96-102.

349. Kocur, C.M., A.I. Chowdhury, N. Sakulchaicharoen, H.K. Boparai, K.P. Weber, P. Sharma, M.M. Krol, L. Austrins, C. Peace, and B.E. Sleep, Characterization of nZVI mobility in a field scale test. *Environ. Sci. Technol.*, 2014. **48**: p. 2862-2869.

350. Li, Y., J. Chen, Y. Ma, J. Zhao, Y. Qin, and L. Chang, Formation of bamboo-like nanocarbon and evidence for the quasi-liquid state of nanosized metal particles at moderate temperatures. *Chem. Commun.*, 1999: p. 1141-1142.

351. Huang, Y.H. and T.C. Zhang, Effects of dissolved oxygen on formation of corrosion products and concomitant oxygen and nitrate reduction in zero-valent iron systems with or without aqueous Fe^{2+}. *Water Res.*, 2005. **39**: p. 1751-1760.

352. Basnet, M., C. Di Tommaso, S. Ghoshal, and N. Tufenkji, Reduced transport potential of a palladium-doped zero valent iron nanoparticle in a water saturated loamy sand. *Water Res.*, 2015. **68**: p. 354-363.

353. Raychoudhury, T., N. Tufenkji, and S. Ghoshal, Aggregation and deposition kinetics of carboxymethyl cellulose-modified zero-valent iron nanoparticles in porous media. *Water Res.*, 2012. **46**: p. 1735-1744.

354. Filip, J., F. Karlický, Z. Marušák, P. Lazar, M. Černík, M. Otyepka, and R. Zbořil, Anaerobic reaction of nanoscale zerovalent iron with water: mechanism and kinetics. *J. Phys. Chem. C*, 2014. **118**: p. 13817-13825.

Appendix A Supporting Information to Chapter 2

A.1. Composition of Hanford artificial groundwater (HS300)

Table A.1. Recipe for Hanford artificial groundwater (HS300a).

Component	Concentration (mM)
$NaHCO_3$	1.44
$KHCO_3$	0.16
$MgCl_2•6H_2O$	0.51
$CaCl_2•2H_2O$	0.37
$CaSO_4•2H_2O$	0.63
NaH_2PO_4	1.50
NH_4Cl	4.70
HEPES	30.00[b]

[a] Modified from SGW1 medium in Lee et al.(*2*)
[b] 30 mM HEPES provides additional buffer capacity to neutralize pH increase from sodium sulfide.

A.2. Characterization and Properties of Pristine nZVI and Sulfidated nZVI

A.2.1. Methods

Micro X-ray Diffraction. Powders for diffraction analysis were loaded into 0.5 mm glass capillaries (Charles Supper Co., MA) under nitrogen atmosphere and sealed with wax. Diffraction data were recorded by the 2D image plate of a Rigaku D/Max Rapid II diffractometer. Cr Kα radiation (λ = 2.2910 Å) focused through a 300 μm diameter collimator was used, which avoids the high background produced from fluorescence of Fe-containing samples. The 2-dimensional diffraction data were integrated between 10 and 160° 2θ to give powder traces. Backgrounds were removed using the JADE software (Materials Data Inc. CA) by subtracting a trace from an empty capillary and additionally fitting a smooth spline curve.

Mössbauer Spectroscopy. Sample preparation for Mössbauer spectroscopy is identical to the procedures reported in Peretyazhko et al.(*3*) Mössbauer spectra of the samples were collected using either a WissEl Elektronik (Germany) or Web Research Company (St. Paul, MN) instruments that included a closed-cycle cryostat SHI-850 obtained from Janis Research (Wilmington, MA), a Sumitomo CKW-21 He compressor unit (Wilmington, MA), and an Ar-Kr proportional counter detector with WissEl setup or a Ritverc (St. Petersburg, Russia) NaI detection system. A ^{57}Co/Rh source (50 mCi to 75 mCi, initial strength) was used as the gamma energy source. With the WissEl setups, the transmitted counts were stored in a multichannel scalar (MCS) as a function of energy (transducer velocity) using a 1024-channel analyzer. The setups data were folded to 512 channels to provide a flat background and a zero-velocity position corresponding to the center shift (CS) of a metal Fe foil at room temperature (RT). Calibration spectra were obtained with a 25 μm thick Fe foil (Amersham, England) placed in the same position as the samples to minimize any geometry errors. The Mössbauer data were modeled with Recoil^{TM} software (University of Ottawa, Canada) using a Voigt-based structural fitting routine.

X-Ray Photoelectron Spectroscopy. The XPS analyses were conducted using a Physical Electronics Quantera Scanning ESCA Microprobe with a focused monochromatic Al Ka X-ray source (1486.7 eV) source and a spherical section analyzer. The mineral powder sample was mounted inside a nitrogen recirculated glove box operated at <0.5 ppm O_2. The samples were pressed onto double sided Scotch tape (#34-8507-5367-3) and supported by 1 cm x 3 cm clean flat Si (100) wafers. The individual Si wafer pieces were then mounted onto the standard Physical Electronics 75 mm x 75 mm sample holder using 2-56 stainless steel screws. The sample holder was then placed into the XPS vacuum introduction system and pumped to $<1 \times 10^{-6}$ Torr using a turbomolecular pumping system prior to introduction into the main ultra-high vacuum system. The main vacuum system pressure is maintained at $<5 \times 10^{-9}$ Torr during analysis and pumped using a series of sputter ion pumps and turbo-molecular pumps. For large collections of mineral particles, the X-ray beam was operated at approximately 100 W, focused to 100 µm diameter, and rastered over a 1.3 mm x 0.1 mm rectangle on the sample. The X-ray beam is incident normal to the sample and the photoelectron detector is at 45° off-normal. High energy resolution spectra were collected using a pass-energy of 69.0 eV with a step size of 0.125 eV. For the Ag 3d5/2 line, these conditions produced a FWHM of 0.91 eV. The sample experienced variable degrees of charging. Low energy electrons at ~1 eV, 20 µA and low energy Ar^+ ions were used to minimize this charging. The spectra were aligned to a carbon peak energy of 285.0 eV (adventitious carbon). The compositional results were obtained using the standard sensitivity factors in the Phi Multipak software package using peak area intensities after a Shirley background substation.

Transmission Electron Microscopy (TEM). The samples without exposure to Tc were prepared for TEM observations by dispersing a dry powder on a lacey-carbon coated 200 mesh Cu TEM grids under anaerobic conditions. In a subsequent step of loading the sample into the TEM, however, the samples were exposed to aerobic conditions for a period of few minutes. TEM conventional and high-resolution images were performed with spherical aberration corrected FEI Titan 80-300 operated at 300kV. The elemental analysis was performed with EDAX Si (Li) EDS detector and a subsequent analysis was performed with TIA software.

BET Surface Area Measurements. 100 to 200 mg of material was placed in a sealed BET vial and weighed (pre-drying weight). The sample in the BET vial was then placed in the VacPrep 061 in which the samples were heated under flowing UHP N_2 at 200°C. At selected times, the samples were allowed to cool and then weighed (after-drying weight). After samples were dried, surface area was measured by N_2 adsorption using a Micrometrics Gemini V surface area and pore size analyzer.

A.2.2. Results

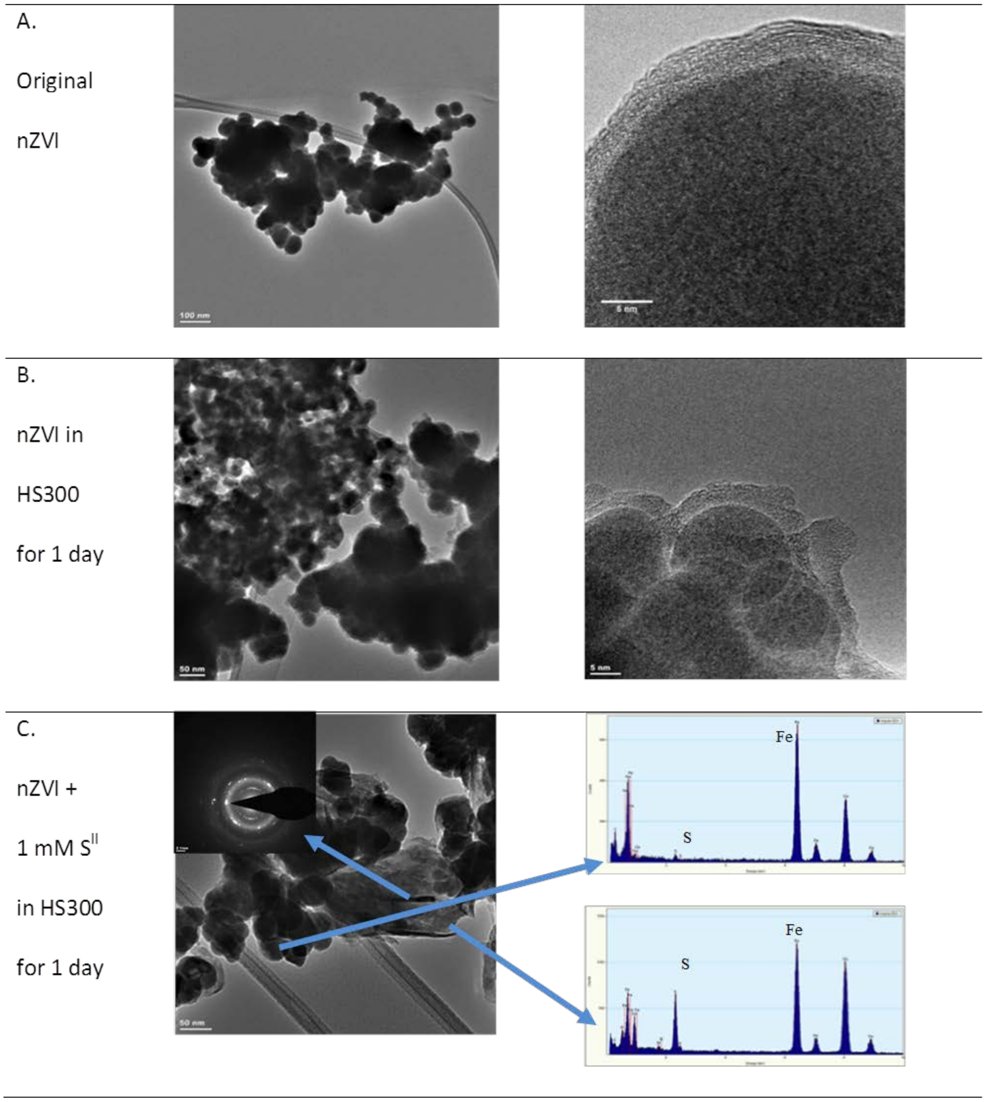

Figure A.1. Transmission electron micrographs of fresh and aged nZVI (**A**) freshly prepared nZVI: long chain structure connecting primary particles (left), primary particle with core-shell structure (right); (**B**) nZVI exposed in HS300 for 1 day: aggregated particles (left), core-shell structure upon exposure to HS300 (right); (**C**) nZVI exposed in 1 mM sulfide (S/Fe = 0.112) and HS300 for 1 day: co-presence of residual nZVI and FeS (left), EDX of residual nZVI (right top), and EDX of FeS (right bottom).

Table A.2. Surface element atomic percentage of pristine nZVI and nZVI exposed to incremental sulfide concentrations in HS300 for 1 day by XPS wide survey scan.

S/Fe ratio	**Atomic ratio %**									
	Fe2p	O1s	S2p	B1s	C1s	Ca2p	P2p	Si2p	Cu2p3	MgKLL
0 (Pristine nZVI)	27.8	27.4	N/D	19.2	25.6	N/D	N/D	N/D	N/D	N/D
0 (nZVI + HS300)	13.8	45.7	0.4	N/D	25.3	4.4	6.8	1.7	N/D	0.8
0.011 (nZVI + HS300 + 0.1 mM S^{2-})	15.1	42.0	0.8	N/D	29.7	4.0	6.4	1.1	N/D	0.8
0.112 (nZVI + HS300 + 1 mM S^{2-})	42.9	37.7	10.5	N/D	N/D	3.5	3.4	N/D	1.0	1.0
0.224 (nZVI + HS300 + 2 mM S^{2-})	51.5	26.6	10.9	N/D	N/D	3.8	2.4	N/D	1.1	1.9
1.12 (nZVI + HS300 + 10 mM S^{2-})	53.9	25.2	12.9	N/D	N/D	2.7	2.2	N/D	1.4	1.6

N/D: Not detectable above the signal background.

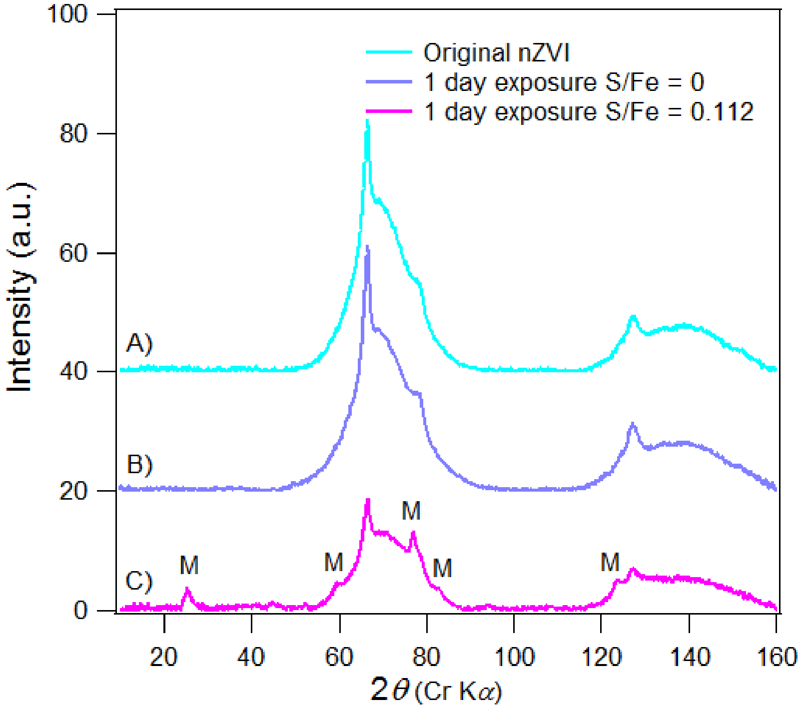

Figure A.2. Micro-XRD pattern of (**A**) pristine nZVI, (**B**) nZVI in HS300 for 1 day (S/Fe = 0) and (**C**) nZVI exposed to 1 mM sulfide in HS300 for 1 day (M stands for mackinawite).

Table A.3. Summary of µXRD and Mössbauer data of pristine nZVI with comparisons to previously reported studies.

Sources	This study	Prior studies[b] of related nZVI ($Fe^{BH\,a}$)	Prior studies[c] of Fe-boron alloys
(µ)XRD	Less than 10% of the phase matches face cubic center (FCC) γ-iron best (represented by sharp peak in **Figure A.2**). Broad humps represent poorly crystalline phase, which as smaller cell parameter than the sharp peak.	Predominantly body cubic center (BCC)-α iron	Amorphous
Mössbauer	Most consistent with amorphous iron(*4*)	BCC-α iron	Amorphous

[a] Fe^{BH} represents nZVI synthesized by borodydride reduction, adapted from Nurmi et al.(*5-7*); [b] ; [c] .

A.2.3. Discussion

Figure A.1B shows that the nZVI exposed to HS300 media for 1 day retains the chainlike morphology similar to pristine nZVI (**Figure A.1A**). The core-shell structure of individual particle is also preserved. However, the thickness of the shell is much less uniform and generally thicker compared to the pristine nZVI, evidently due to more extensive growth of the FeO passive layer. This interpretation is supported by XPS survey scan that shows the increasing oxygen amount in sample exposed to HS300 only (**Table A.2**). XPS survey scans also showed no boron in samples that were exposed to aqueous media, which can be attributed to the hydrolysis of Fe boride.(*5*, *7*)

Table A.3 summarizes differences in the μXRD and Mössbauer results between the present study and prior work. The μXRD pattern of the pristine nZVI contained sharp peaks that were most consistent with an FCC lattice (**Figure A.2A)**. By contrast, most of the prior XRD characterizations of nZVI synthesized by $NaBH_4$ reduction suggest BCC α-iron. In this study, it was estimated that the sharp peaks that match FCC lattice best (**Figure A.2A**) account for less than 10% of the total signal. The majority of the signal represented by the broad peaks cannot be identified with certainty, and could be amorphous or poorly crystalline material. Previous studies on Fe^{BH} also suggest that the XRD peak of Fe^{BH} is broader compared to typical α-iron, representing a distribution of crystallite size. Although the FCC lattice is typically found in γ-iron that is formed at high pressure and temperatures, FCC-modified iron may also arise as a result of alloying elements, most commonly carbon, at ambient conditions, especially when the particle size is small.(*3*) For the present nZVI samples, we speculate that boron incorporated into the nZVI shell has stabilized the FCC Fe lattice. The Mössbauer spectrum of the pristine nZVI exhibits broad features that are most consistent with amorphous Fe metal,(*6, 7*) which are clearly distinct from previously published Mössbauer spectra of nZVI made by borohydride reduction. However, in these two previous studies, the samples were prepared either by heat- or freeze-drying, which could easily be responsible for changing the crystallinity of the material.(*8, 10*) In fact, several earlier studies using borohydride reduction to synthesize ultrafine particles of Fe-metal (metalloid) alloys with recovery by filtration have reported broad Mössbauer features similar to this study, and they also interpreted their results as indication that the freshly prepared material was amorphous. After annealing at high temperature, however, the spectra obtained in these studies showed features indicating transformation to more crystalline ɑ-iron. Given that the flash drying protocol used in this study is essentially an anaerobic filtration,(*13*) the amorphous nature of the pristine nZVI observed here is reasonable.

In addition to post synthesis treatment, other experimental differences during the synthesis between our methods and those of previous studies could contribute to differences in the final product. One distinctive aspect of our method is the strong homogenization used during the introduction of $NaBH_4$ to $FeCl_3$ aqueous solution. This was done to mix the reagents rapidly and minimize aggregation of newly formed particles without the complications created by using a magnetic stir bar with magnetic nanoparticles. A variety of subjective, preliminary tests indicated that mixing with a homogenizer produced more reproducible dispersions of nZVI, but the specific effects of this on the particle composition and structure were not studied further.

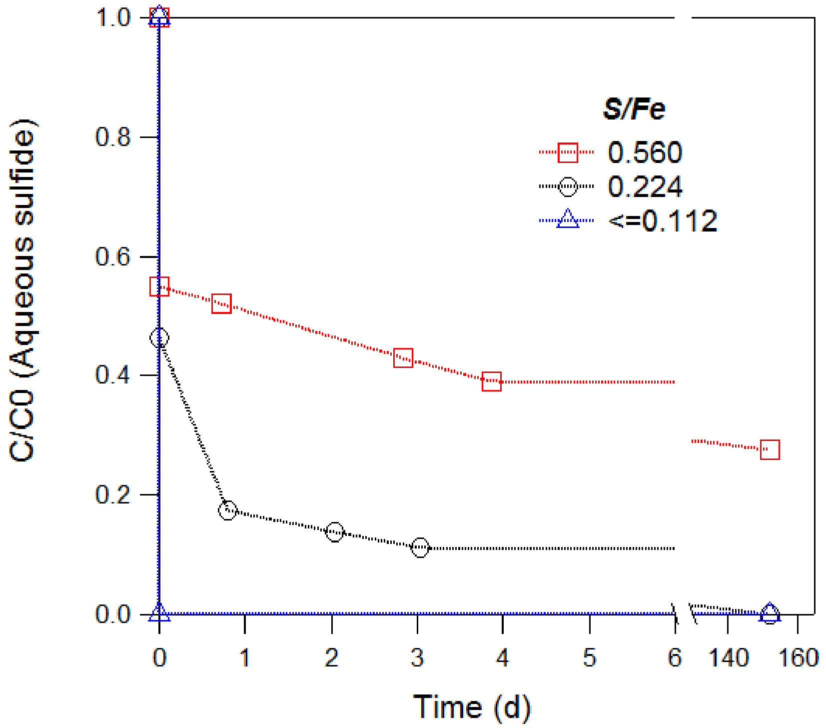

Figure A.3. The kinetics of sulfide uptake by nZVI at various S/Fe ratios in HS300 (nZVI concentration: 0.2 g L^{-1}, sulfide dose: 0, 0.04, 0.08, 0.16, 0.2, 0.4, 0.8, and 2 mM, pH = 7.9, temperature = 27±0.5 °C, aqueous sulfide concentrations in batches with sulfide dose below 0.8 mM were all below detection).

Control experiments without nZVI showed negligible changes of aqueous sulfide concentration over the sampling course (data not shown). At low S/Fe (≤ 0.112), aqueous sulfide was removed to below the detection limit within 5 min after sulfide addition (**Figure A.3**). However, at relatively high S/Fe (0.224 and 0.56), the kinetics of sulfide removal from solution exhibited two phases, with about half of the input sulfide removed rapidly followed by a gradual decrease over a much longer period (**Figure A.3**). The initial, fast stage likely corresponds to instantaneous sulfide adsorption onto the surface Fe oxides coating on nZVI, forming a surface complex of Fe(II)–HS^-.(*14, 15*) A similar process has been postulated to be the initial step in mackinawite formation on iron oxides in natural sulfidic environments. The later stage of sulfide removal reflects relatively slow formation of FeS precipitates. At S/Fe = 0.56, significant residual aqueous sulfide was detected even after 150 days of exposure, indicating incomplete transformation of nZVI to FeS.

A.3. Batch Tc Reduction Kinetics under High Fe dose (0.5 g/L)

A.3.1. Results

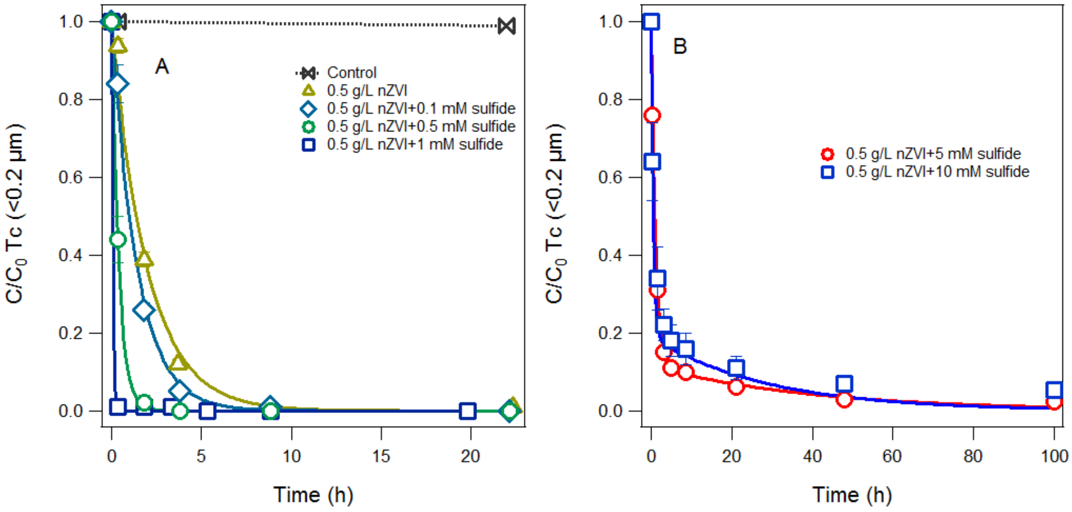

Figure A.4. Tc sequestration kinetics at high nZVI dose (0.5 g L^{-1}): (**A**) low S concentration (0.1 mM to 1 mM) and (**B**) high sulfide concentration (5 and 10 mM) (S/Fe ratio has the same range as **Figure 2.2**. Error bars represent the standard error from duplicates).

In these high nZVI dose experiments, the batch reactors were kept still without external mixing. Therefore, the reaction rate was significantly slower than the reaction rate presented in **Figure 2.4**, even though the nZVI and sulfide doses were higher. However, it is important to note that the general observation of these experiments is consistent with what was shown in **Figure 2.4**: at low S/Fe ratios, the reaction rate increased as S/Fe increased but higher S/Fe resulted inhibition of Tc removal. The higher residual Tc concentration (< 0.2 µm) observed at 5 and 10 mM sulfide concentrations were probably due to higher residual sulfide concentration.

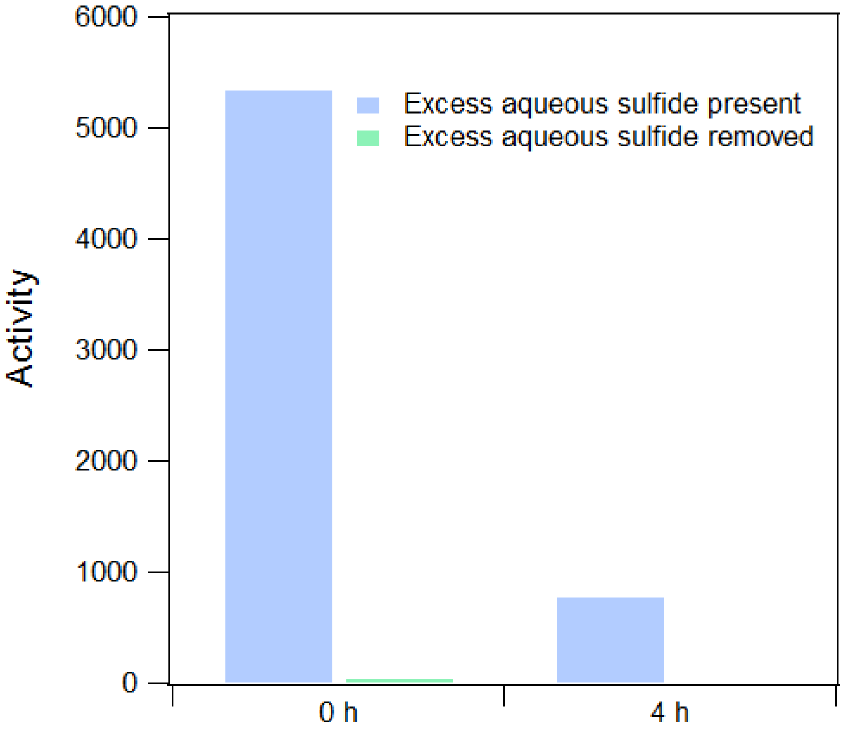

Figure A.5. Tc remaining in solution in the presence and absence of excess aqueous sulfide (Tc concentration is represented by counts per minute from liquid scintillation; Two batch reactors were prepared by exposing 0.5 g L^{-1} nZVI to 10 mM sulfide in HS300 for 1 day at pH = 7.9; Before Tc addition, excess of aqueous sulfide was removed in one of the bottles by filtration and the recovered solid was resuspended in HS300).

Figure A.5 shows the preliminary results where Tc removal rate was compared in the presence and absence of excess aqueous sulfide. Tc (< 0.2 µm) was quantified by using direct reading of the radioactivity (CPM). It clearly shows that when excess of aqueous sulfide was removed, Tc removal (blue bars) was much faster compared to the batch where excess of aqueous sulfide was present (green bars), and the removal rate is comparable to the lower S/Fe ratio cases (**Figure 2.4** and **Figure A.4A**). This suggests that the inhibition of Tc removal resulted from excess aqueous sulfide.

A.4. Evidence of Colloidal Tc Formation

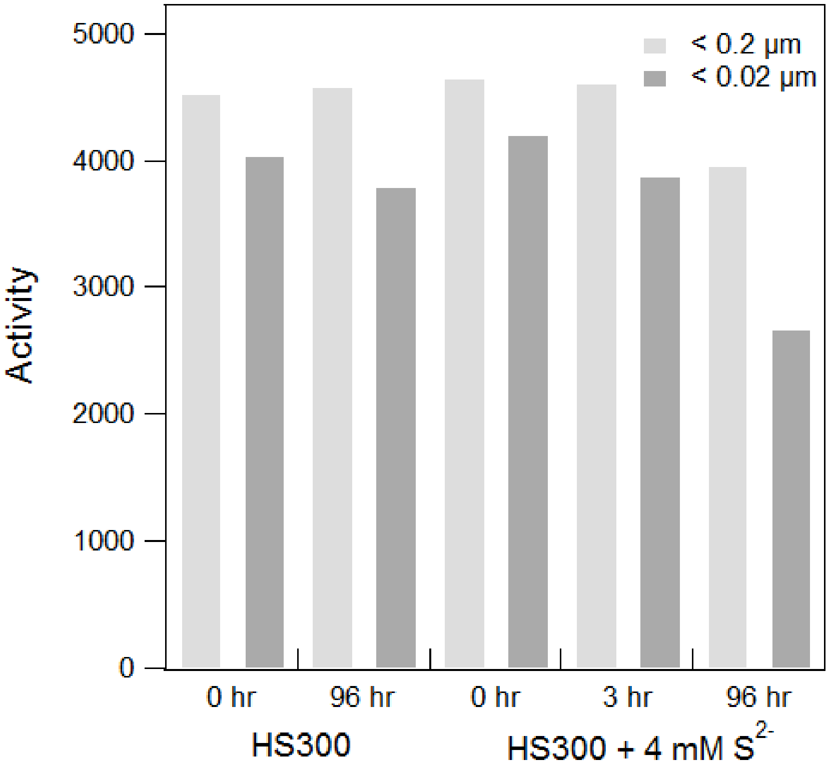

Figure A.6. Tc concentration in the presence and absence of sulfide (Activity in 0.2 and 0.02 µm filtrate was compared to differentiate colloidal Tc from dissolved TcO_4^-).

A.5. SEMs and TEMs of Sulfidated nZVI Exposed to TcO_4^-

A.5.1. Method

<u>*Scanning Electron Microscopy (SEM)*</u>. For Tc-containing material, a 5 µL drop was placed onto a silicon wafer and then anaerobically dried in the glove bag for scanning electron microscopy. The samples were coated using the Poloran carbon coater,

and ~5–10 nm carbon coating was applied to each sample. Samples were analyzed in a FEI Quanta 3DFEG scanning electron microscope equipped with an Oxford 80 mm^2 SDD detector and INCA software. Initially 20 keV was used to analyze the samples but later changed to 30 keV to pick up the Tc L 18.2 line to confirm Tc was present since the M line overlaps with sulfur which is between 2.3–2.5 keV. Surface tomography of the samples was obtained at 5 keV since 20–30 keV destroys any surface tomography of the material.

Transmission Electron Microscopy (TEM). For Tc-containing material, the sample preparation involved applying a 5 μL drop of material aqueous suspension to a 200-mesh copper TEM grid with carbon-coated formvar support film, (Electron Microscopy Sciences, Hatfield, PA). After 1 min, the excess liquid was removed by wicking, and the sample on a grid was anaerobically dried in the glove bag atmosphere (Coy Laboratories, Grass Lake, MI). The sample was anaerobically transferred to the TEM laboratory. Final loading of the sample on the holder required short period exposure to aerobic conditions. The prepared samples were imaged with JEOL 2010F transmission electron microscope operating at 200kV, coupled with INCA energy-dispersive spectroscopy (EDS) system (Oxford Instruments, UK) for elemental analysis.

A.5.2. Result

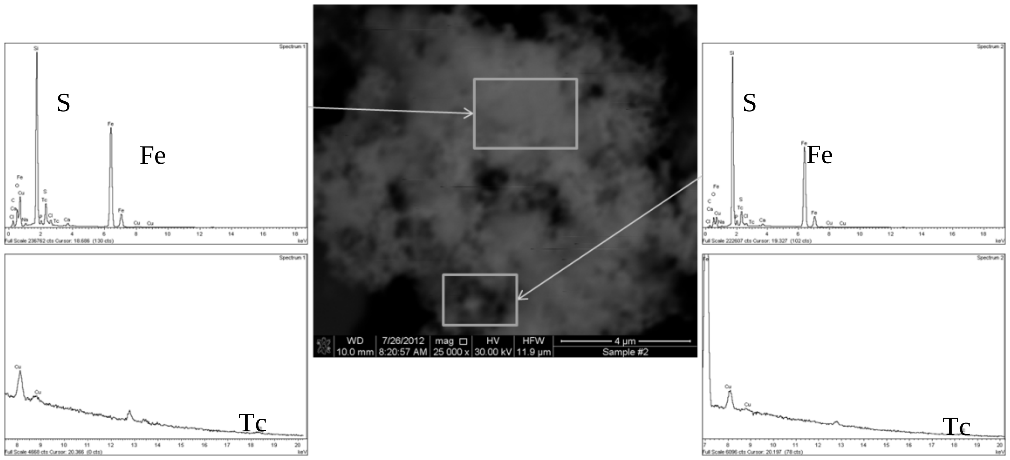

Figure A.7. A Back scattered scanning electron micrograph (middle) of sulfidated nZVI (S/Fe = 0.112) exposed to 50 μM TcO_4^- and corresponding energy dispersive x-ray spectra (EDX) (top left: spectra 1; bottom left: enlarged spectra 1; top right: spectra 2; bottom right: enlarged spectra 2).

The chemical heterogeneity shown at the scale of SEM was not as significant as that seen by TEM (**Figure 2.5**). S/Fe ratios measured at multiple areas by EDX (**Figure A.7** and other spectra (data not shown)) were around the input S/Fe ratio, which equals to 0.112. As a result, SEM did not show a significantly different Tc distribution pattern.

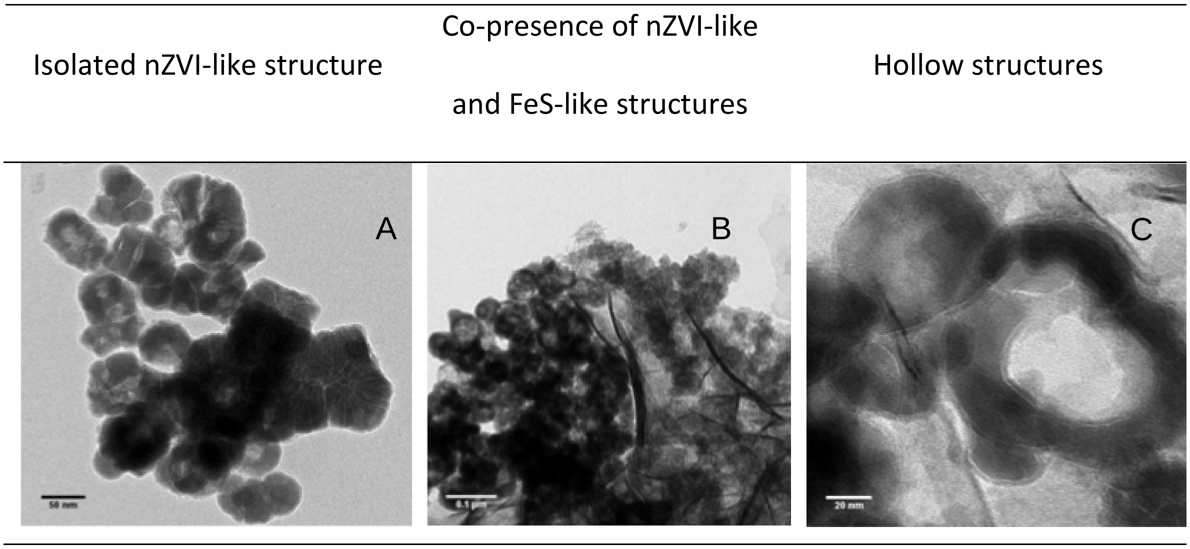

Figure A.8. Transmission electron micrographs of representative morphologies of sulfidated nZVI exposed to TcO_4^- (images were collected on the same sample in **Figure 2.5**: [TcO_4^-] = 50 µM, [nZVI] = 0.2 g L^{-1}, [S^{2-}] = 0.4 mM, S/Fe = 0.112, pH = 7.9).

A.6. Additional XAS information

A.6.1. Method

Tc XAS samples were prepared by reacting 8.4 µM TcO_4^- with 0.5 g L^{-1} nZVI pre-exposed to 0–10 mM sulfide. After greater than 99% Tc (< 0.2 µm) removal, Tc-containing solids were centrifuged and loaded as a concentrated slurry/paste into single slot Teflon holders. The holders were then sealed with a single layer of Kapton tape and further contained inside a heat-sealed polypropylene bag. Samples were kept in an anaerobic chamber prior to the measurements and under a continuous He purge while collecting the XAS spectra. XAS measurements were taken at the Tc K-edge and were collected at the Stanford Synchrotron Radiation Lightsource (SSRL) on beamline 4-1 and 11-2. Spectra were measured at room temperature in fluorescence mode using a 13 (30) element solid state detector (Ge), and a N_2-cooled Si (220) double crystal monochromator, detuned for 20% for harmonic rejection. Energy calibration was internally measured during each scan using a Mo metal foil (Mo K-edge energy 20 KeV).

Linear combination fitting of EXAFS was performed in ATHENA for samples with S/Fe ratios ranging from 0.0056 to 0.56 using samples with S/Fe = 0 and 1.12 as two end members, respectively. The values of each component were normalized to the total spectral weight sum from the components used in the linear combination. The total spectral weight sum ranged from 0.85 to 1 (without any constraining of the sum).

A.6.2. Additional results

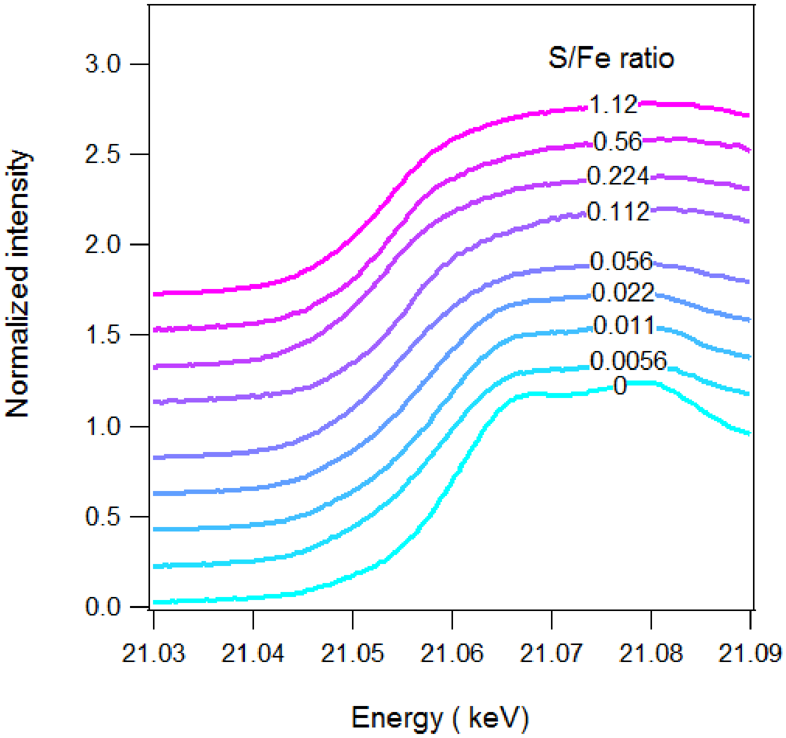

Figure A.9. Tc K-edge XANES of Tc immobilized at incremental S/Fe ratios (The spectra were collected on the same set of samples as in **Figure 2.7**).

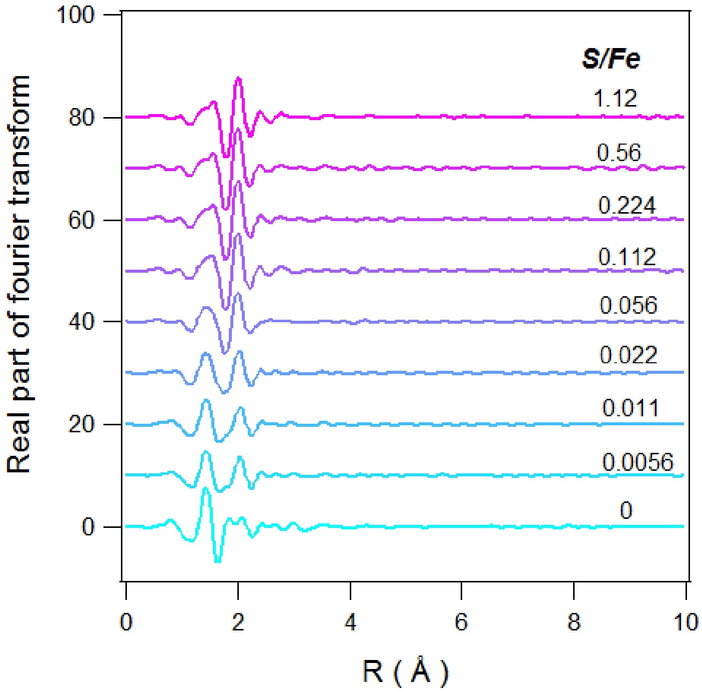

Figure A.10. Real part of Fourier transform of EXAFS of Tc reduced at incremental S/Fe ratios (The spectra were collected on the same set of samples in **Figure 2.7**)

Table A.4. Tc-EXAFS shell by shell fit for Tc reduced at S/Fe = 0 and 1.12 (*N*: coordination number; *D*: interatomic distance; σ^2: Debye-Waller factor; Standard deviation is in parenthesis)

		nZVI + Tc + 0 mM S^{2-}			**nZVI + Tc + 10 mM S^{2-}**
Tc-O1	*N*	†6	*Tc-S1*	*N*	‡2
	D (Å)	2.02(1)		*D* (Å)	2.30(2)
	σ^2 (Å^2)	0.006(1)		σ^2 (Å^2)	0.003(2)
Tc-Tc1		†1	*Tc-S2*		‡4
		2.44(3)			2.47(1)
		0.011(1)			0.003(2) [A]
Tc-Tc2		†1	*Tc-Tc1*		‡2
		3.19(4)			2.39(1)
		0.011(3) [a]			0.005(2) [†]
Tc-O2		†4	*Tc-Tc2*		‡1
		3.17(4)			2.58(2)
		0.009(2)			0.005(2) [B]
Tc-O3		†4	*Tc-S3*		‡2
		3.56(8)			3.13(1)
		0.009(2) [b]			0.005(2) [C]
Tc-Tc3		†4	*Tc-S4*		‡1
		3.71(2)			3.78(1)
		0.025(6)			0.005(2) [C]
Tc-O1-O1-		6 [d]	*Tc-S5*		‡1
		4.06(2) [d]			3.98(3)
		0.011(2) [d]			0.005(2) [C]
Tc-Tc4		†4	*Tc-Tc3*		‡2
		4.01(2)			3.63(1)
		0.025(6) [c]			0.007(2) [D]
			Tc-Tc4		‡1
					3.81(2)
					0.007(2) [D]

† Coordination numbers maintained to crystallographic value of TcO_2.

‡ Coordination numbers maintained to crystallographic value of TcS_2

[a] $\sigma_{Tc\text{-}Tc1} = \sigma_{Tc\text{-}Tc2}$, [b] $\sigma_{Tc\text{-}O3} = \sigma_{Tc\text{-}O3}$, [c] $\sigma_{Tc\text{-}Tc4} = \sigma_{Tc\text{-}Tc3}$,

[d] Multiple scattering N, σ, and d constrained to Tc-O1 shell distances.

[A] $\sigma_{Tc\text{-}S1} = \sigma_{Tc\text{-}S2}$, [B] $\sigma_{Tc\text{-}Tc1} = \sigma_{Tc\text{-}Tc2}$, [C] $\sigma_{Tc\text{-}S} = \sigma_{Tc\text{-}Tc1+0.002}$, [D] $\sigma_{Tc\text{-}Tc} = \sigma_{Tc\text{-}Tc1+0.002}$

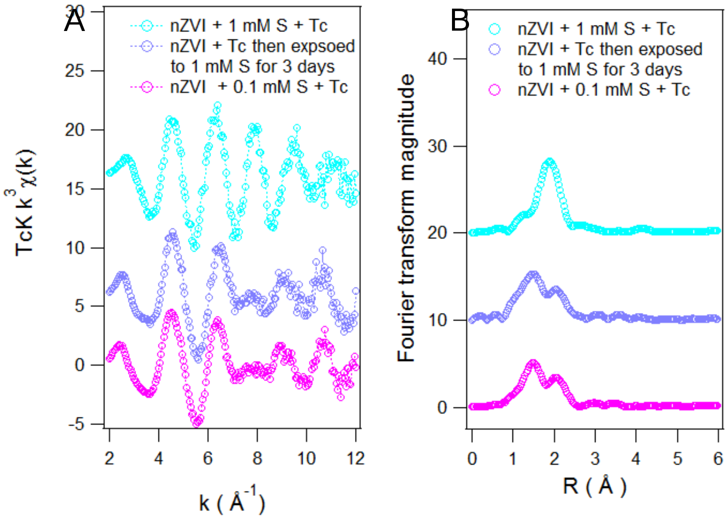

Figure A.11. (**A**) Tc K-edge EXAFS and (**B**) the respective Fourier transform of Tc reduced by nZVI first then exposed to 1 mM sulfide for 3 days (spectra for Tc reduced under S/Fe = 0.011 and 0.112 were used for comparison).

A.7. Geochemical Speciation Modeling of Tc/Fe/S system

A.7.1. Methods

Geochemical speciation modeling was performed using the ACT subset of the Geochemist's Workbench modeling package, release 8.0 (RockWare Inc., Golden, CO) with the thermodynamic constants given in the thermo.com.v8.r6+ dataset. Additional data for FeS was adapted from Davison et al.(*1*) and input into the dataset. Speciation diagrams for Fe/Tc/S in artificial Hanford groundwater system (HS300) were generated using the concentrations listed in **Table A.1.**. In the generation and interpretation of these diagrams, it was assumed that activity (α) was equal to concentration.

A.7.2. Results

The Fe/Tc speciation diagram was constructed in a way that is similar to the experimental design. $[HS^-]$ instead of $[H^+]$ was used as x-axis variable in order to represent the evolution of sulfidogenic conditions. Equilibrium approach was used to calculate Fe and Tc speciation and elucidate possible Tc sequestration pathways in the presence of nZVI and sulfide. The diagram suggested that the hypothetical Tc sequestration pathways presented in **Figure 2.1** are thermodynamically possible. $TcO_2{\bullet}nH_2O$ is the predominant reduced Tc phase when $\log a[HS^-]$ is less than −23. Beyond that value, TcS_2 becomes the dominant reduced Tc phases. The boundary line between Tc_2S_7 and TcS_2 has a negative slope with respect to $\log a[HS^-]$. As sulfide concentration further increases to the range of this study (shaded area), both TcS_2 and Tc_2S_7 are the dominant Tc phases, and this area coincidentally overlaps with the stability region of FeS. The diagram also indicates the possibility of transformation from $TcO_2{\bullet}nH_2O$ to TcS_2 or from Tc_2S_7 to TcS_2. The first pathway is especially important in real remedial practice because $TcO_2{\bullet}nH_2O$ is expected to be the dominant Tc reduced phase before sulfate reduction develops. This pathway has also been confirmed by XAS results (See **Figure A.11**).

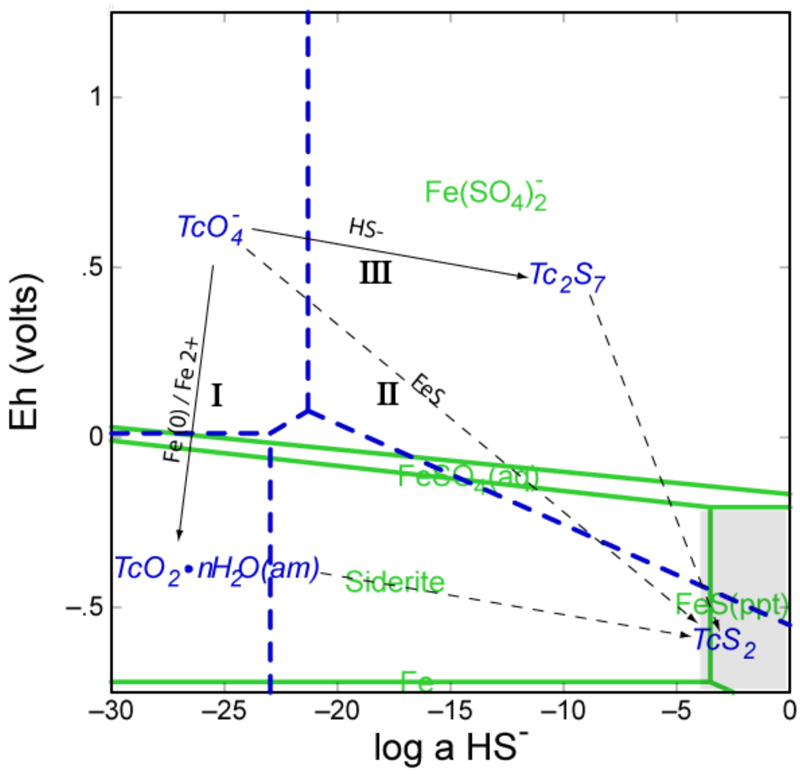

Figure A.12. Eh vs. log a(HS^-) of Fe/S/Tc speciation diagram in HS300 (Fe and Tc speciation diagrams were independently constructed and overlaid with each other: areas with green boundaries are the Fe stability regions and areas with blue boundaries are the Tc stability regions; shaded area represents the experimental conditions in terms of sulfide concentration and expected Eh range; Solid arrows represent the known reaction pathways whereas dashed arrows represents hypothetical reaction pathways; Process **I**, **II**, and **III** correspond to the reaction pathways in **Figure 2.1**; Model input: [TcO_4^-] = 10 μM, pH = 7.9, T = 25 °C).

A.8. References in Appendix Only

1. Lee, J.-H., J.K. Fredrickson, R.K. Kukkadapu, M.I. Boyanov, K.M. Kemner, X. Lin, D.W. Kennedy, B.N. Bjornstad, A.E. Konopka, D.A. Moore, C.T. Resch, and J.L. Phillips, Microbial reductive transformation of phyllosilicate Fe(III) and U(VI) in fluvial subsurface sediments. *Environ. Sci. Technol.*, 2012. **46**: p. 3721-3730.

2. Peretyazhko, T.S., J.M. Zachara, R.K. Kukkadapu, S.M. Heald, I.V. Kutnyakov, C.T. Resch, B.W. Arey, C.M. Wang, L. Kovarik, J.L. Phillips, and D.A. Moore, Pertechnetate (TcO_4^-) reduction by reactive ferrous iron forms in naturally anoxic, redox transition zone sediments from the Hanford Site, USA. *Geochim. Cosmochim. Acta*, 2012. **92**: p. 48-66.

3. Long, G.J., D. Hautot, Q.A. Pankhurst, D. Vandormael, F. Grandjean, J.P. Gaspard, V. Briois, T. Hyeon, and K.S. Suslick, Mössbauer-effect and X-ray absorption spectral study of sonochemically prepared amorphous iron. *Phys. Rev. B*, 1998. **57**: p. 10716-10716.

4. Nurmi, J.T., P.G. Tratnyek, V. Sarathy, D.R. Baer, J.E. Amonette, K. Pecher, C. Wang, J.C. Linehan, D.W. Matson, R.L. Penn, and M.D. Driessen, Characterization and properties of metallic iron nanoparticles: spectroscopy, electrochemistry, and kinetics. *Environ. Sci. Technol.*, 2005. **39**: p. 1221-1230.

5. Wang, Q., S. Snyder, J. Kim, and H. Choi, Aqueous ethanol modified nanoscale zerovalent iron in bromate reduction: synthesis, characterization, and reactivity. *Environ. Sci. Technol.*, 2009. **43**: p. 3292-3299.

6. Kanel, S.R., J.-M. Grenèche, and H. Choi, Arsenic(V) removal from groundwater using nano scale zero-valent iron as a colloidal reactive barrier material. *Environ. Sci. Technol.*, 2006. **40**: p. 2045-2050.

7. Glavee, G.N., K.J. Klabunde, C.M. Sorensen, and G.C. Hadjipanayis, Chemistry of borohydride reduction of iron(II) and iron(III) ions in aqueous and nonaqueous media - formation of nanoscale Fe, FeB, and Fe_2B powders. *Inorg. Chem.*, 1995. **34**: p. 28-35.

8. Forster, G.D., L. Fernάndez Barquín, R.L. Bilsborrow, Q.A. Pankhurst, I.P. Parkin, and W.A. Steer, Sodium borohydride reduction of aqueous iron–zirconium solutions: chemical routes to amorphous and nanocrystalline Fe–Zr–B alloys. *J. Mater. Chem.*, 1999. **9**: p. 2537-2544.

9. Corrias, A., G. Ennas, A. Musinu, G. Marongiu, and G. Paschina, Amorphous transition metal-boron ultrafine particles prepared by chemical methods. *Chem. Mater.*, 1993. **5**: p. 1722-1726.

10. Van Wonterghem, J., S. MØrup, C.J.W. Koch, S.W. Charles, and S. Wells, Formation of ultra-fine amorphous alloy particles by reduction in aqueous solution. *Nature*, 1986. **322**: p. 622-623.

11. Wei, B., M. Shima, R. Pati, S.K. Nayak, D.J. Singh, R. Ma, Y. Li, Y. Bando, S. Nasu, and P.M. Ajayan, Room-temperature ferromagnetism in doped face-centered cubic fe nanoparticles. *Small* 2006. **2**: p. 804-809.

12. Nurmi, J., V. Sarathy, P. Tratnyek, D. Baer, J. Amonette, and A. Karkamkar, Recovery of iron/iron oxide nanoparticles from solution: comparison of methods and their effects. *J. Nanopart. Res.*, 2011. **13**: p. 1937-1952.

13. Hansson, E.B., M.S. Odziemkowski, and R.W. Gillham, Formation of poorly crystalline iron monosulfides: surface redox reactions on high purity iron, spectroelectrochemical studies. *Corros. Sci.*, 2006. **48**: p. 3767-3783.

14. Rickard, D. and G.W. Luther III, Chemistry of iron sulfides. *Chem. Rev.*, 2007. **107**: p. 514-562.

15. Morse, J.W., F.J. Millero, J.C. Cornwell, and D. Rickard, The chemistry of the hydrogen sulfide and iron sulfide systems in natural waters. *Earth-Sci. Rev.*, 1987. **24**: p. 1-42.

16. Davison, W., N. Phillips, and B.J. Tabner, Soluble iron sulfide species in natural waters: reappraisal of their stoichiometry and stability constants. *Aquat. Sci.*, 1999. **61**: p. 23-43.

Appendix B Supporting Information to Chapter 3

B.1. Additional Information on Solid Phase Characterization

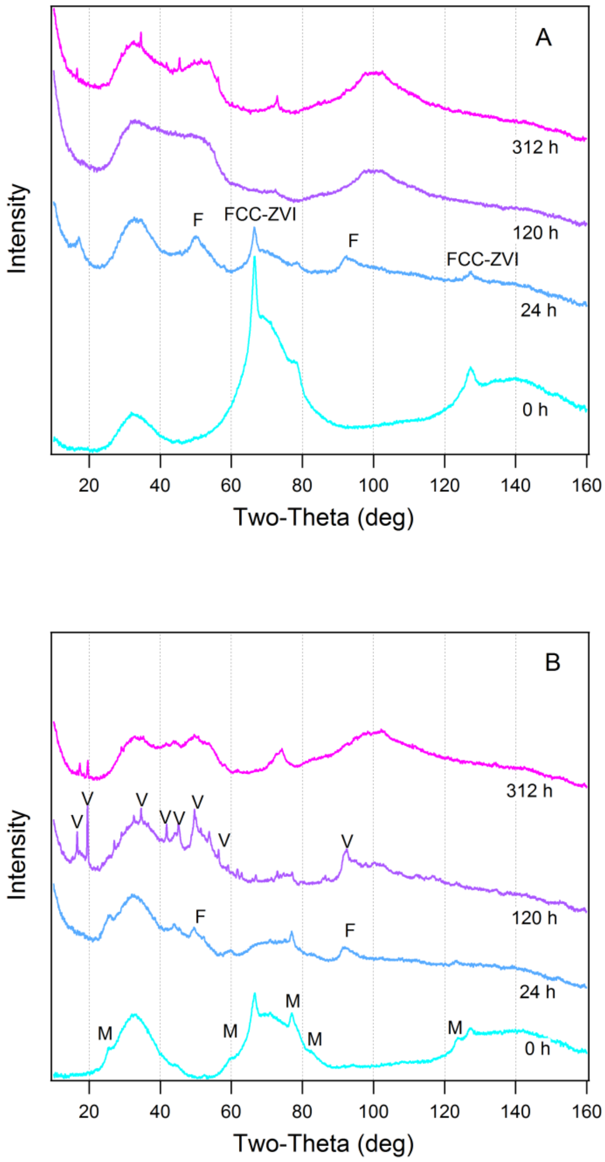

Figure B.1. Micro-XRD of nZVI (**A**) and sulfidated nZVI at S/Fe = 0.112 (**B**) after 0, 24, 120, and 312-h oxidation (F: ferrihydrite; V: vivianite; and M: mackinawite).

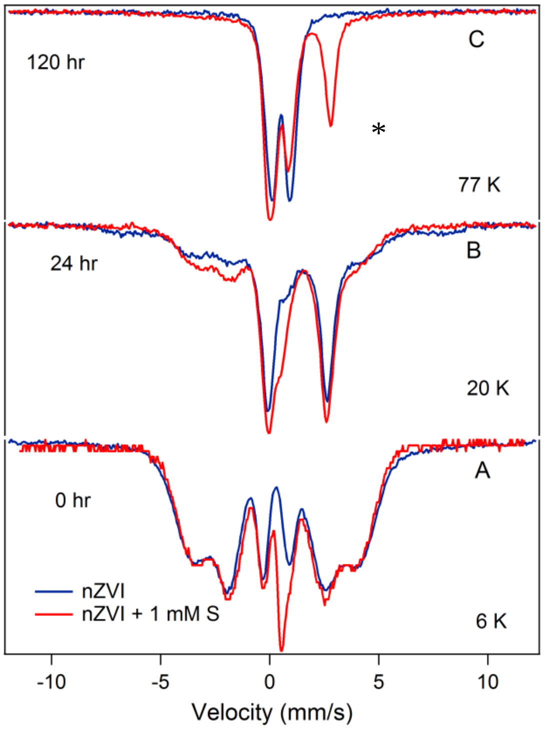

Figure B.2. Mössbauer spectra of unsulfidated nZVI (blue) and sulfidated nZVI (red) at (**A**) 0, (**B**) 24, and (**C**) 120-h oxidation. The spectra of two different S/Fe ratios at each time point were superimposed to facilitate direct visual comparison (the data for the 0-h oxidized samples are adopted from our previous Tc reduction study.(*2*)).

Mossbauer spectroscopy data for nZVI and sulfidated NZVI were compared to show the difference in effect of oxygen on these samples. Comparison of the spectra indicated that nZVI was relatively more oxidized in the non-sulfidated sample (for the same length of exposure), which is evident from: (*i*) lower amounts of nZVI in 24-h oxidized sample at S/Fe = 0, and (*ii*) absence of Fe(II) doublet in 120-h oxidized sample at S/Fe = 0 (high energy peak of the Fe(II) doublet is indicated by *). Also, the differences in 120-h spectra at 77 K (Figure B.2C) and 20 K spectrum (Figure 2C) is due to magnetic ordering of ferrihydrite at 20 K. Paramagnetic ferrihydrite transforms to sextet below 77 K.(*3*)

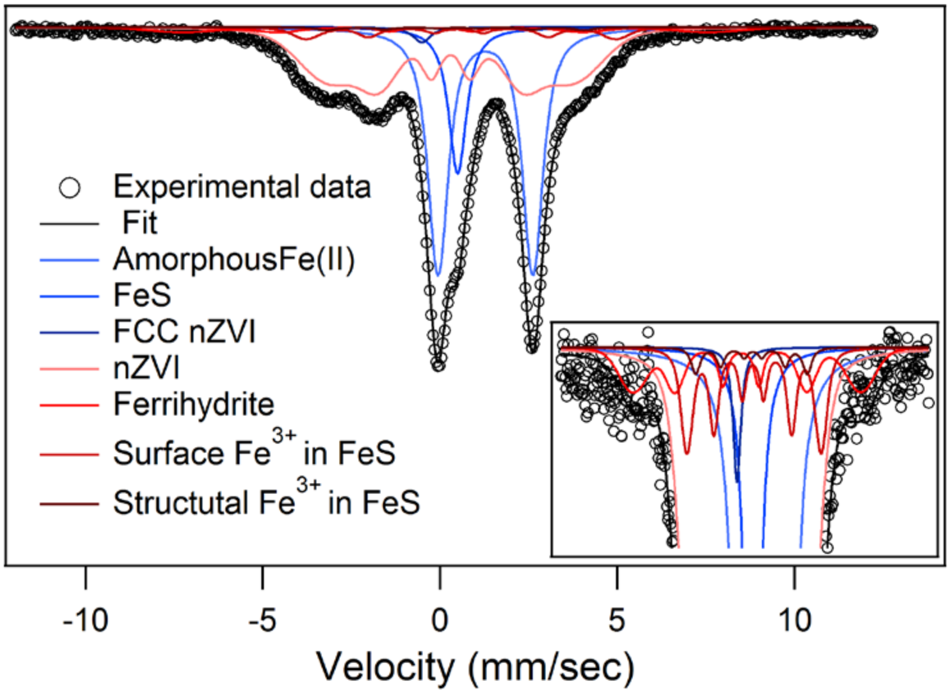

Figure B.3. A qualitative modeled fit showing sextet peaks due to structural and surface oxidized Fe^{3+} in mackinawite, as reported in Bi et al.(*4*). The fit is not optimum because statistically equivalent fits with different nZVI and oxidized Fe^{3+} are also possible. The fit is mainly shown to indicate oxidized Fe^{3+} in mackinawite sextet positions.

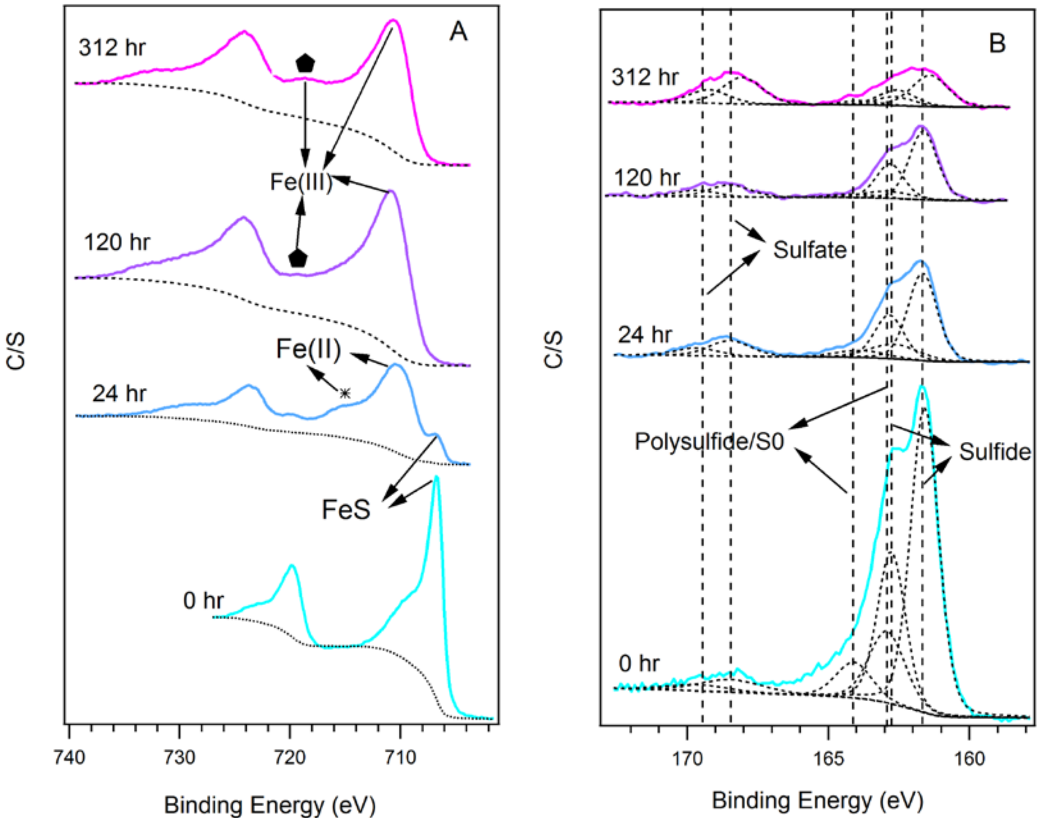

Figure B.4. XPS Fe2p (**A**) and S2p (**B**) narrow spectra of sulfidated nZVI (S/Fe = 0.112) after 0, 24, 120, and 312-h oxidation. In Figure B.2A, asterisk mark the Fe(II) satellite peak, solid diamonds mark the Fe(III) satellite peaks. Peak assignments are based on literature values obtained from Descostes et al.(*5*) and Mullet et al.(*6*) In Figure B.2B, spectra were fitted by the modeled individual components of sulfur species, whose binding energies are shown by dashed lines. Small sulfate peaks in 0-h oxidized sample is likely due to surface oxidation even though great care was taken to prevent contact with oxygen.

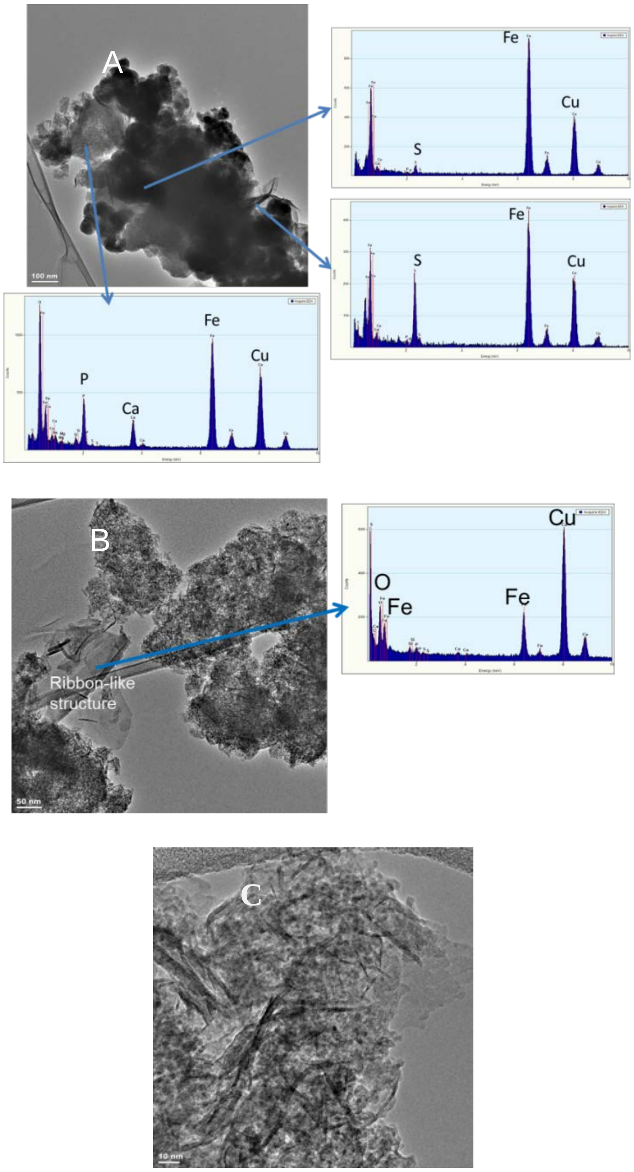

Figure B.5. TEM and associated EDX of sulfidated nZVI after (**A**) 24-h oxidation and (**B**) 120-h oxidation. (**C**) High resolution TEM of the ribbon-like structure.In Figure A, EDS spectra were taken in three regions with different morphologies but within the same aggregate.

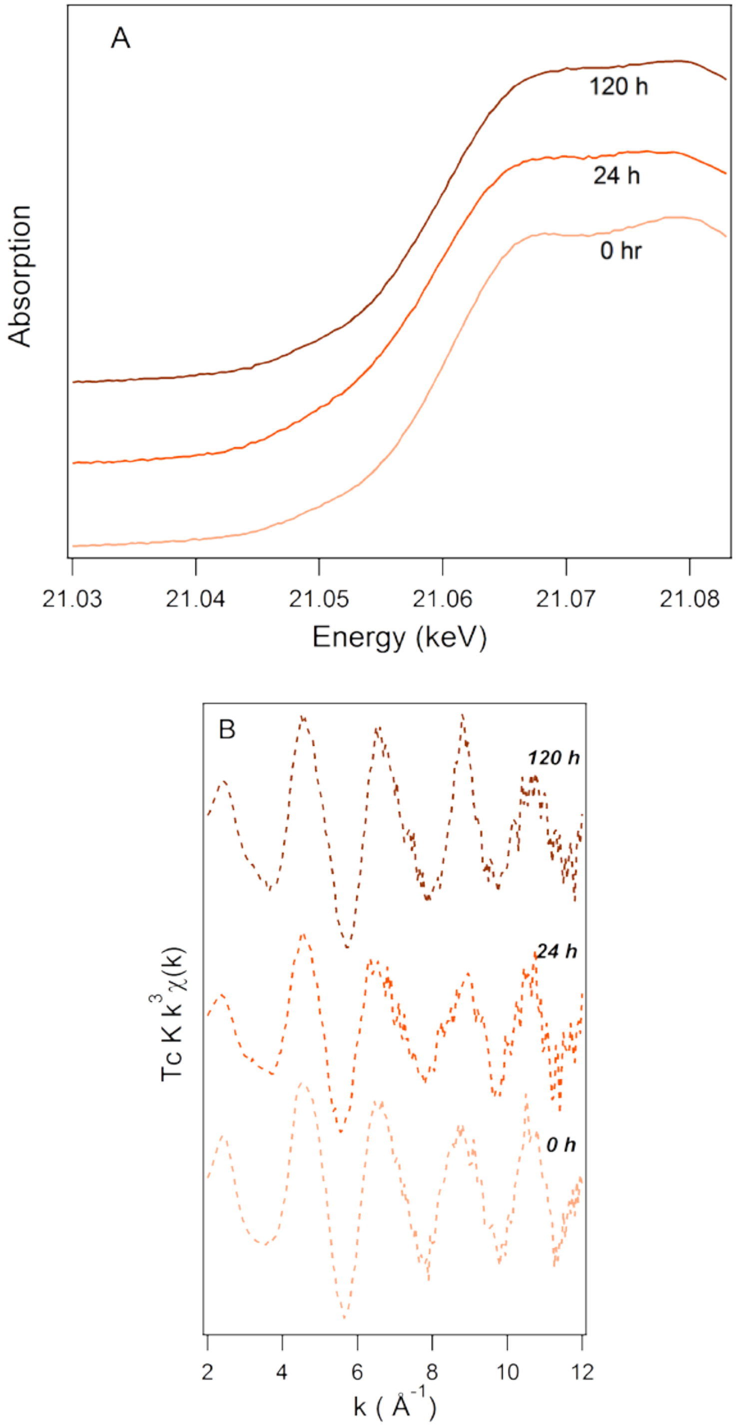

Figure B.6. Tc K-edge (**A**) XANES spectra and (**B**) EXAFS spectra of Tc reduced in the absence of sulfide oxidized at 0, 24, and 120 h (Data for the 0-h oxidized sample were adopted from our previous Tc reduction study.(*2*))

Table B.1. Fitting and calculated Mössbauer parameters for the Mössbauer spectra shown in Figure 2A─2D.

Oxidation time	Temp	Phase[1]	δ_o[2] mm/s	Δ or ε_o[3] mm/s	H[4] Tesla	σ_Δ (mm/s)[5] or σ_H (Tesla)	comp.(%)[6]	χ^2(7)	<CS>[8] mm/s	<Δ> or <ε>[9] mm/s	<H>[10] Tesla	σ_d <Δ> or <H>[11] mm/s	Phase, %[12]
0 h	6 K	nZVI-FCC	-0.5	0*	—[13]	0.1*	100	1.6	-0.5	0.08	—	0.06	1
		FeS	0.5	0.1*	—	7.00E-05	100		0.5	0.1	—	7.00E-05	8
		Amorphous-nZVI	0.28	0*	22.7	4.68	93.9		0.29	-0.02	22.01	5.32	92
					11.15	1.78	6.1						
24 h	20 K	Amorphous Fe(II)	1.29	2.68	—	0.24	100	1.5	1.29	2.68	—	0.24	39
		FeS	0.5	0.12*	—	0.001*	100		0.5	0.12	—	0.001	11
		nZVI-FCC	-0.5	0*	—	0.1*	100		-0.5	0.08	—	0.06	1
		nZVI-amorphous	0.32	0	22	4.78	100		0.32	-0.0003	22.03	4.78	45
		Ferrihydrite	0.05	0.2*	46*	5*	100		0.05	0.2	46	5	4
120 h	20 K	Vivianite	1.27	2.76	—	0	100	4.1	1.27	2.76	—	0	20
		Fe(III)-(oxyhdr)oxide	0.53	0.12*	—	0.25	100		0.53	0.22	—	0.17	7
		Ferrihydrite	0.47	-0.03	47.05	2.15	31.53		0.47	-0.03	35.4	13.35	73
					41.9	3.8	22						
					24.2	12.4	46.4						
312 h	12 K	Ferrihydrite	0.47	-0.014	47.21	2.01	43.15	1.4	0.47	-0.014	41	11.15	98
					43	3.3	37						
					22.4	16.2	19.7						
		Vivianite	1.38	2.79	—	0.1*	100		0.47	-0.014	—	0.1	2

[1] Spectral component; [2] center shift; [3] quadrupole splitting or quadruple shift parameter ; [4] hyperfine magnetic field; [5] std deviation of the component; [6] the weight of the Gaussian component; [7] reduced chi square; [8] average center shift; [9] average quadruple or average quadruple shift parameter; [10] average magnetic hyperfine field; [11] standard deviation; [12] spectral percent; [13] not applicable

Modeling was carried out using Voight-based fitting method of Rancourt and Ping (*1*) with RecoilTM Software; * These parameters are frozen during modeling; Lorentzian half widths at half maximum (HWHM) of all elemental Lorentzians in all elemetal doublet and sextets were ~0.2 mm/sec (0 h) and ~0.25 mm/sec (> 24 h samples); No coupling was allowed between CS, QS or e and average H; the A+/A- areas of doublet are fixed at 1; A1/A3 and A2/A3 areas are fixed at 2 and 3.

B.2. References in Appendix Only

1. Smith, A.H., E.O. Lingas, and M. Rahman, Contamination of drinking-water by arsenic in Bangladesh: a public health emergency. *Bulletin of the World Health Organization*, 2000. **78**: p. 1093-1103.

2. Fan, D., R.P. Anitori, B.M. Tebo, P.G. Tratnyek, J.S. Lezama Pacheco, R.K. Kukkadapu, M.H. Engelhard, M.E. Bowden, L. Kovarik, and B.W. Arey, Reductive sequestration of pertechnetate ($^{99}TcO_4^-$) by nano zerovalent iron (nZVI) transformed by abiotic sulfide. *Environ. Sci. Technol.*, 2013. **47**: p. 5302-5310.

3. Murad, E. and J. Cashion, Iron Oxides, in *Mössbauer Spectroscopy of Environmental Materials and Their Industrial Utilization*. 2004, Springer US. p. 159-188.

4. Bi, Y., S.P. Hyun, R. Kukkadapu, and K.F. Hayes, Oxidative dissolution of UO_2 in a simulated groundwater containing synthetic nanocrystalline mackinawite. *Geochim. Cosmochim. Acta*, 2012. **102**: p. 175-190.

5. Descostes, M., F. Mercier, N. Thromat, C. Beaucaire, and M. Gautier-Soyer, Use of XPS in the determination of chemical environment and oxidation state of iron and sulfur samples: constitution of a data basis in binding energies for Fe and S reference compounds and applications to the evidence of surface species of an oxidized pyrite in a carbonate medium. *Appl. Surf. Sci.*, 2000. **165**: p. 288-302.

6. Mullet, M., S. Boursiquot, M. Abdelmoula, J. Genin, and J. Ehrhardt, Surface chemistry and structural properties of mackinawite prepared by reaction of sulfide ions with metallic iron. *Geochim. Cosmochim. Acta*, 2002. **66**: p. 829-836.

Appendix C Supporting Information to Chapter 4

C.1. Experimental Details

C.1.1. Mineral Synthesis

Magnetite

Stoichiometric magnetite was synthesized based on the procedure described by Gorksi and Scherer (*1*). A 1:2 Fe(II):Fe(III) mixture was prepared from $FeSO_4$•$7H_2O$ and $FeCl_3$•$6H_2O$ in 200 mL DO/DI water in an anaerobic chamber filled with N2 (O2 < 0.8 ppm, no H2) with a total iron concentration of 0.19 M. The mixture was titrated with 10 M NaOH (prepared with DI/DO water) to above pH 10. The brownish mineral suspension was sealed under N_2 atmosphere and placed on an end-over-end rotator overnight. The black suspension was centrifuged, washed and resuspended in DO/DI water for probe experiments

Chloride green rust

The chloride green rust was prepared inside the anaerobic chamber following the coprecipitation procedure described by Refait et al. (*2*). 2.52 g $FeCl_2$ and 0.84 g $FeCl_3$•$6H_2O$ were dissolved in 60 mL DO/DI water. 4 g NaOH was dissolved in 40 mL DO/DI water. The two aqueous solutions were mixed, resulting a ratio of [Fe(II) + Fe(III)]/[NaOH] = 0.6 and a ratio of Fe(II) to Fe(III) of 3. The concentration of resulted green rust suspension is 150 mM, which equals to ~60 g/L if we assume the chemical formula of chloride green rust is $Fe(II)_3Fe(III)(OH)_8Cl \cdot 2H_2O$. The co-precipitation protocol was selected over partial oxidation methods—another commonly used approach to prepare green rust—for controlling Fe(II) to Fe(III) ratio to be exact.

C. 1.2. Thermodynamic CRPs

Table C.1. Properties of thermodynamic probes

Probe	Abbrev	E_m^7 (V)	λ_{max} Ox (nm)	λ_{max} Red (nm)	pKa
Resorufin	Rsf	-0.051[a]	571	Leuco	
5,5'-indigodisulfonate	I2S	-0.125[b]	610	407	[e]r1:7.3–7.5, r2:12.1, o1:12.3, o2:12.8
9,10-anthraquinone-2,6-disulfonate	AQDS	-0.184[c]	326	386	[f]r1: 7.5–8.1, r2:10.5
9,10-anthraquinone-2-sulfonate	AQS	-0.225[d]	326	403	

[a,b,e] ref (*3*), [c] ref (*4*), [d] ref (*5*), [f] refs(*4*, *6*)

Table C.2. Summary of the experimental conditions, the probes selected for calculating the E_{CRP} of each iron minerals, the calculated E_{CRP}, and measured E_{Pt} under each condition.

Iron Minerals	Mineral dose (g/L)	Fe(II) conc. (mM)	Used Probes	E_{CRP} (V vs SHE)	E_{Pt} (V vs SHE)
Goethite	3.0	0.2	N/A	N/A	N/A
Goethite	3.0	0.3	I2S	-0.124	0.1105
Goethite	3.0	0.5	AQDS	-0.195	0.0325
Goethite	3.0	1.0	AQS	-0.241	-0.0565
Goethite	3.0	1.0	AQS	-0.244	N/A
Goethite	2.25	1.0	AQS	-0.237	N/A
Goethite	1.2	1.0	AQDS	-0.207	N/A
Goethite	0.6	1.0	AQDS	-0.195	N/A
Goethite	0.3	1.0	AQDS(I2S)	-0.187(-0.178)	N/A
Goethite	7.5	1.0	AQDS	-0.198	N/A
Goethite	10	1.0	AQDS	-0.181	N/A
Goethite	3.0	1.0	AQS	-0.237	N/A
Goethite + 1 mg/L NOM	3.0	1.0	AQS	-0.236	N/A
Goethite + 10 mg/L NOM	3.0	1.0	AQS	-0.227	N/A
Goethite + 50 mg/L NOM	3.0	1.0	AQS	-0.209	N/A
Lepidocrocite	2.6	0.2	N/A	N/A	N/A
Lepidocrocite	2.6	0.3	I2S	-0.142	0.0645
Lepidocrocite	2.6	0.5	AQDS	-0.186	0.0195
Lepidocrocite	2.6	1.0	AQDS	-0.199	-0.0175
Lepidocrocite	2.6	1.0	AQDS	-0.199	N/A
Lepidocrocite	1.04	1.0	AQDS	-0.197	N/A
Lepidocrocite	0.52	1.0	AQDS	-0.195	N/A
Lepidocrocite	0.26	1.0	AQDS	-184	N/A
Lepidocrocite	7.5	1.0	AQDS	-180	N/A
Lepidocrocite	10	1.0	AQDS	-160	N/A
Hematite	2.8	0.2	N/A	N/A	0.1305
Hematite	2.8	0.3	N/A	N/A	0.1075
Hematite	2.8	0.5	N/A	N/A	0.0665
Hematite	2.8	1.0	I2S	-0.120	0.0345
Syn Magnetite	0.75	0.2	AQDS	-0.175	N/A
Syn Magnetite	075	0.3	AQS(AQDS)	-0.215 (-0.212)	-0.099
Syn Magnetite	0.75	0.5	AQS(AQDS)	-0.229 (-0.225)	-0.125
Syn Magnetite	0.75	1.0	AQS(AQDS)	-0.239 (-0.234)	-0.139
Syn Magnetite	0.75	0	AQDS	-0.182	N/A
Syn Magnetite	1.5	0	AQS	-0.213	N/A
Syn Magnetite	2.25	0	AQS	-0.226	N/A
Syn Magnetite	3	0	AQS	-0.228	N/A

C.1.3. Electrochemistry

Figure C.1A shows the ORP vs time profile for 1 mM aqueous Fe(II) only and four iron oxides pre-exposed to 1 mM aqueous Fe(II) for ~20 h. Three of the oxides exhibited similar response, wherein OPR decreased for several minutes, then slowly rebounded for 5-10 min, and became relatively stable by 15 min. The exceptions are goethite, where the ORP dropped and rebounded, but was continuously decreasing by 30 min, and magnetite, which dropped and became stable, without any rebound. The rebound is likely due to (*i*) oxygen intrusion into the electrochemical cell despite constant purging—an effect we documented in detail for OPR measurements on suspensions of low concentration of nZVI—based on similar pattern observed in the ORP measurement of low concentration of nZVI (*7*) or (*ii*) iron oxide accumulating onto the electrode surface, which we also described in prior on ORP measurement with nZVI (*7*) and confirmed by visual inspection of the electrode used in this study. The absence of rebound with magnetite could be because structural Fe(II) in magnetite provides redox buffer capacity to minimize the effect of oxygen intrusion and/or that the size and/or material properties of the magnetite resulted in less deposition onto the electrode surface.

Using the data in **Figure C.1A** and similar results for other concentrations of added Fe(II) (data not shown), we obtained the lowest ORP values (ORP_{min}) measured in each case and plotted ORP_{min} as a function of initial Fe(II) concentration in **Figure C.1B**. The figure shows that ORP_{min} became more negative as Fe(II) concentration increased for all four minerals. The slopes of ORP_{min} change with Fe(II) are similar for hematite, goethite, and magnetite but the trend for goethite is about 2-fold steeper. At 1 mM Fe(II) concentration, the $\mathrm{ORP}_{\mathrm{min}}$ for goethite is 50 mV more negative than lepidocrocite, and solid Fe(II) measurement after 24-h pre-equilibration showed 15% more Fe(II) associated with goethite than lepidocrocite (**Figure 4.4**). Given that electrode measurements of ORP in Fe(II)-iron oxide suspensions are mixed potentials that reflect contributions by both adsorbed and aqueous Fe(II) (*7*), it is possible that the more negative ORP obtained with goethite reflects the lower potential of the adsorbed Fe(II) compared to the aqueous Fe(II). However, this explanation would require that the sensitivity of the ORP electrode (i.e., the exchange current density) be similar for sorbed Fe(II) vs. aqueous Fe(II), and this would be difficult to quantify. Alleviating the challenges created by differential sensitive of electrodes to redox-active species is one of the expected benefits of redox characterization methods involving solution phase redox probes (the CRP method of this study).

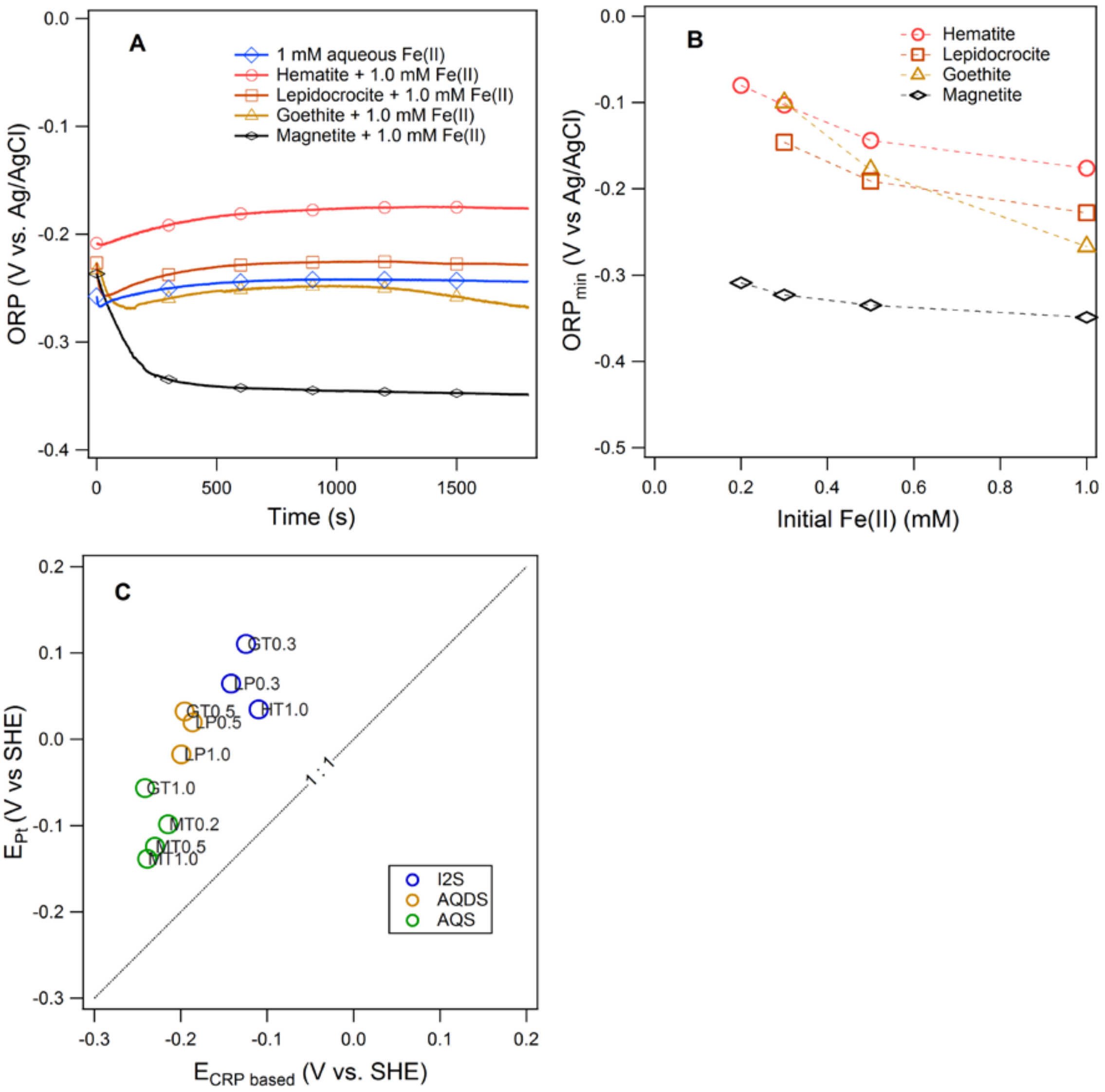

Figure C.1. (**A**) Oxidation-reduction potential (ORP) of four iron oxide suspension pre-exposed to 1 mM Fe(II) for 24 h, measured with a Pt RDE at 2000 rpm, vs. a Ag/AgCl as reference electrode, in 10 mM HEPES buffer at pH = 7.2. (**B**) Summary of ORP_{min} values for four iron oxides at different Fe(II) concentrations. (**C**) E_{Pt} converted from ORP_{min} vs. E_{CRP} calculated by probe speciation.

C.1.4. Batch Kinetics

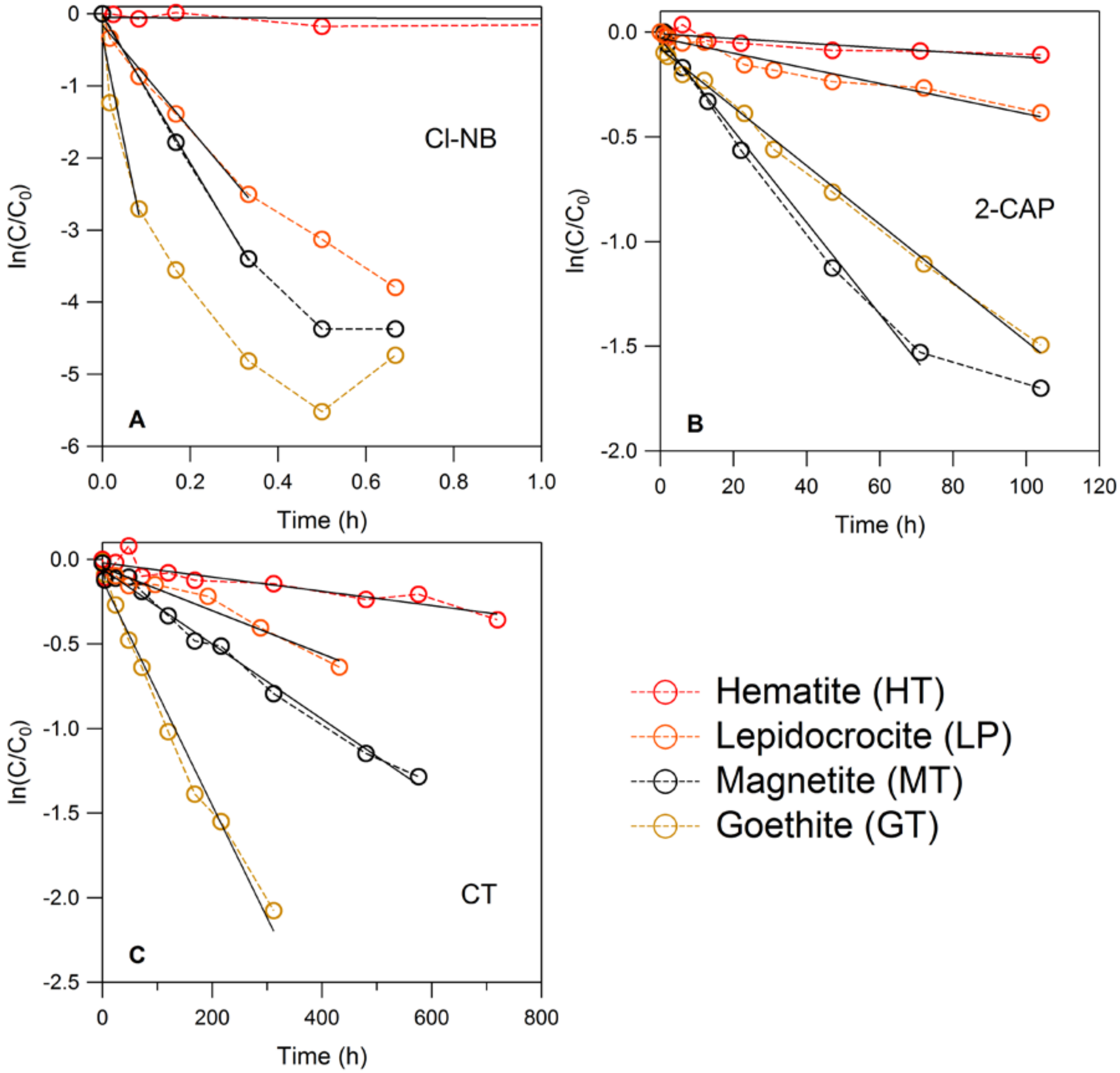

Figure C.2. Reduction kinetics of (**A**) 4-chloronitrobenzene (4Cl-NB), (**B**) 2-chloroacetophenone (2-CAP), and (**C**) carbon tetrachloride (CT) by four different iron oxides with 1 mM Fe(II) concentration (20 h preequilibration between the iron oxides and Fe(II), pH =7.2 with 10 mM HEPES, [4Cl-NB] = 50 µM, [2-CAP] = 50 µM, [CT] = 10 µM, reactions were all carried out in amber serum bottles crimped sealed with viton septum).

Table C.3. Observed pseudo-first order reduction rate constants (log k_{obs}) for three contaminants[a].

Mineral	Loading (g/L)	Fe(II) (mM)	log k_{obs} CT (h^{-1})	log k_{obs} 2CAP (h^{-1})	log k_{obs} 4Cl-NB (h^{-1})
GT	3.0	1 0	-2.18	-1.86	1.47
LP	2.8	1.0	-2.89	-2.44	0.857
MT	2.8	1.0	-2.65	-1.66	1
HT	0.75	1.0	-3.37	-2.95	-1.79

[a] All experiments were conducted in 10 mM HEPES buffer at pH 7.2 in amber serum vials crimp sealed at mixing rate of 45 rpm on an end-over-end rotator.

C.2. Summary of Reduction Rate Constants Reported in Literature

Table C.4. Published reduction rate constants for selected contaminants in well mixed magnetite[a] suspension.

Reference	Loading (g/L)	SA (m2/g)	log $k_{M\_}$ CE (L g^{-1} h^{-1})	log $k_{M\_}$ CA (L g^{-1} h^{-1})	log $k_{M\_}$ NAC (L g^{-1} h^{-1})	CoCs	Conditions
Ref (*8*)	2.6	19		-1.03		10 µM CT	2.3 mM Fe(II), pH 7.2 with 1.52 mM MOPs
Ref (*9*)	5	63.5		-1.24		110 µM CT	No Fe(II), pH 7.8 w 50 mM HEPES, 0.1 M NaCl
Ref (*9*)	5	14.5		-3.22		110 µM CT	No Fe(II), pH 7.8 w 50 mM HEPES, 0.1 M NaCl
Ref (*10*)	25	18.01		-3.44		20 µM CT	No Fe(II), pH 7, 24 h eq, 0.1 M NaCl
Ref(*11*)	8, 14, 18, 24	77		-2.54		19 µM CT	Aged Biogenic w 0.5 mM Fe(II), pH 7.0 w 10 mM MOPOS, 0.1 M NaClO$_4$
Ref (*12*)	63	57	-5.70			250 µM TCE	w/o Fe(II), pH 7 10 mM NaHCO$_3$
Ref (*12*)	63	57	-5.77			190 µM PCE	w/o Fe(II), pH 7 10 mM NaHCO$_3$
Ref (*1*)	1	62			1.08	40 µM NB	w/o Fe(II), pH 7.2 w 50 mM MOPs, near stoichiometric magnetite (Fe(II)/Fe(III) = 0.48)
Ref (*13*)	1.27	19		-3.23	 1.57	2.5 µM HCA 1.1 µM 4Cl-NB	w/o Fe(II), pH 7.2, 1.34 mM Fe(II) was released
Ref (*14*)	0.3	57			1.57	50 µM NB	w 2.3 mM Fe(II), pH 7, unspecified buffer
Ref (*14*)	0.3	57			1.65	50 µM 4Cl-NB	w 2.3 mM Fe(II), pH 7, unspecified buffer
Ref (*15*)	1	62			1.53	40 µM NB	w/o Fe(II), pH 7.2 w 50 mM MOPs, stoichiometric magnetite (Fe(II)/Fe(III) = 0.50)
Average log k_M			-5.73 ± 0.049	-2.45 ± 1.11	1.48 ± 0.23		

Table C.5. Published reduction rate constants for selected contaminants by Fe(II) sorbed onto various Fe(III) oxides.

Reference	Loading (g/L)	SA (m2/g)	log k_M CE (L g^{-1} h^{-1})	log k_M CA (L g^{-1} h^{-1})	log k_M NAC (L g^{-1} h^{-1})	CoCs	Oxides	Conditions
Ref (*8*)	3.1	17		-2.13		10 µM CT	BGT[a]	1.5 mM Fe(II), pH 7.2 w 5 mM MOPs
Ref (*8*)	3.1	17		-2.04		10 µM CT	BGT	1.5 mM Fe(II), pH 7.2
Ref (*16*)	3	17		-2.59		40 µM CT	BGT	Maintain 1 mM aq Fe(II), pH 7
Ref (*17*)	5	55		-1.66		1.5 µM CT	SGT[b]	3 mM Fe(II) pH 6.8-7.0 10 mM PIPES, 30C
Ref (*18*)	1.43	17.5		-1.96		CT	BGT	1 mM Fe(II), pH 7.2 w 25 mM MOPS
Ref (*19*)	6.9	15.4		-2.13		CT	BGT	1 mM Fe(II), pH 6.8 24 hr eq
Ref (*20*)	0.89	28.8		-1.39		CT	SGT	3 mM Fe(II), pH 7.0 50 mM HEPES, 20 hr eq
Ref (*18*)	1.43			-1.44		0.4 µM HCA	BGT	1 mM Fe(II), pH 7.2 w 25 mM MOPS
Ref (*13*)	1.54			-3.23	1.29	0.4 µM HCA 1.1 µM 4Cl-NB	BGT	1.24 mM Fe(II), pH 7.2
Ref (*21*)	0.64	17			0.092	50 µM NB	BGT	1.5 mM Fe(II), pH 7.2 w 25 mM MOPs, 48 hr eq
Ref (*22*)	0.64				0.0067	50 uM NB	BGT	1.5 mM Fe(II), pH 7.2 w 25 mM MOPs, 48 hr eq
Ref (*8*)	2.8			-2.61		10 µM CT	BLP[c]	1.9 mM Fe(II), pH 7.2 w 1 mM MOPs
Ref (*8*)	3.6			-3.56		10 µM CT	BHT[d]	1.5 mM Fe(II), pH 7.2 w 1 mM MOPs
Ref (*13*)	1.42			-3.89		2.5 µM HCA	BLP	1.14 mM Fe(II), pH 7.2 w 0.1 mM MOPS
Ref (*13*)	1.82			-4.08		2.5 µM HCA	BHT	1.04 mM Fe(II), pH 7.2 w 0.40 mM MOPS
Ref (*13*)	1.42				-0.032	1.1 µM 4Cl-NB	BLP	1.14 mM Fe(II), pH 7.2 w 0.1 mM MOPS
Ref (*13*)	1.82				-3.98	1.1 µM 4Cl-NB	BHT	1.04 mM Fe(II), pH 7.2 w 0.40 mM MOPS
GT Average log k_M				-2.06 ± 0.57	0.61 ± 0.65	[a] Bayferrox goethite, [b] Synthetic goethite, [c] Bayferrox lepidocrocite, [d] Bayferrox hematite		
LP Average log k_M				-3.25 ±0.64	-0.03			
HT Average log k_M				3.81 ± 0.26	-3.98			

Table C.6. Published reduction rate constants of selected contaminants by green rust suspension.

Reference	Loadin g (g/L)	SA (m2/g)	log k_{M}_ CE (L g^{-1} h^{-1})	log k_{M}_ CA (L g^{-1} h^{-1})	log k_{M}_ NAC (L g^{-1} h^{-1})	CoCs	Mineral	Fe(II)/ Fe(III)	Conditions
Ref (*23*)	15		-3.30	-1.27		17.8 µM TCE 20 µM CT	GR-Cl	3.2	No freeze dry, pH 7.2, HEPES, orbital 150 rpm, Teflon-lined rubber septa and aluminum crimp caps, 20 ml headspace
Ref (*24*)	5	14.1		-1.91		20 µM CT	GR-SO4	N/A	No freeze dry, pH 7.6
Ref (*25*)	10	19		-1.92		30 µM CT	GR-Cl	N/A	freeze dry, pH 8.0
Ref (*26*)	10	21	-5.31			22.5 µM PCE	GR-Cl	N/A	freeze dry, pH 8.0, ampules, shaker
Ref (*26*)	10	21	-4.59			22.5 µM TCE	GR-Cl	N/A	freeze dry, pH 8.0, ampules, shaker
Ref (*27*)	7	86.83	-3.24			250 µM TCE	GR-SO4	2.19	No freeze dry, pH 7, orbital 180 rpm, open-top cap and three-layered septum system
Ref (*27*)	7	86.83	-3.52			190 µM PCE	GR-SO4	2.19	No freeze dry, pH 7, orbital shaker 180 rpm, open-top cap and three-layered septum system
Ref (*28*)	5						GR-SO4	N/A	
Ref (*13*)	0.55	45.7		-0.47		2.5 µM HCA	GR-SO4		freeze dry, 1 mM Fe(II), pH 8
Ref (*29*)	4.17	28.4		-2.62		CT	GR-SO4	N/A	freeze dry, pH 7.9
Average log k_M			-3.99 ± 0.91	-1.63 ± 0.81					

Table C.7. Published reduction rate constants of selected contaminants by mackinawite suspension.

Reference	Loading (g/L)	SA (m2/g)	log $k_{M\_}$ CE (L g^{-1} h^{-1})	log $k_{M\_}$ CA (L g^{-1} h^{-1})	log $k_{M\_}$ NAC (L g^{-1} h^{-1})	CoCs	Conditions
Ref (*8*)	4	13		-0.22		8.2 µM CT	2.3 mM Fe(II), 0.76 mM MOPs, pH 7.2
Ref (*8*)	0.6	77		-0.98		11.5 µM CT	1.4 mM Fe(II), 0.76 mM MOPs, pH 7.2
Ref (*30*)	10	0.05		-2.19		20 µM CT	Freeze dry no Fe(II), pH 8.3 0.1 M tris buffer
Ref (*31*)	18			-0.65			
Ref (*32*)	10	0.05	-4.24			20 µM PCE	Freeze dry no Fe(II), pH 8.3 0.1 M tris buffer
Ref (*33*)	10	284	-4.12			15 µM PCE	Pretreat N/A, no Fe(II), pH 8.3 0.1 M tris buffer
Ref (*34*)	10	2.01	-5.28			30 µM PCE	Freeze dry, no Fe(II), pH 7, HEPES
Ref (*32*)	10	0.05	-3.83			20 µM TCE	Freeze dry no Fe(II), pH 8.3 0.1 M tris buffer
Ref (*35*)	10	0.05	-4.30			20 µM TCE	Freeze dry no Fe(II), pH 7.3 0.1 M tris buffer
Ref (*35*)	10	0.05	-3.70			20 µM TCE	Freeze dry no Fe(II), pH 9.3 0.1 M tris buffer
Ref (*34*)	10	2.01	-4.87			30 µM TCE	Freeze dry, no Fe(II), pH 7, HEPES
Ref (*34*)	10	2.01	-4.27			30 µM TCE	Freeze dry, no Fe(II), pH 8, HEPES
Ref (*33*)	10		-3.67			16 µM TCE	Pretreat NA no Fe(II), pH 8.3 0.1 M tris buffer
Ref (*36*)	20	178	-3.45			60 µM TCE	Non freeze dry, no Fe(II), 0.2 mM S2-,pH 7.2
Ref (*36*)	20	178	-4.77			60 µM TCE	Freeze dry, no Fe(II), pH 7.2, 0.2 mM S2-
Ref (*37*)	4.17	30.11	-3.51			100 µM PCE	No freeze dry, no Fe(II), pH 8.3, 50 mM tris
Ref (*13*)	1.98	12.6		-0.69	2.33	2.5 µM HCA 1.1 µM 4Cl-NB	1.25 mM Fe(II), pH 7.2, 1.0 mM MOPs
Ref (*38*)	10	0.05		-2.14		16 µM HCA	Freeze dry, no Fe(II), pH 8.3 0.1 M tris buffer
Ref (*30*)	10	0.05		-1.91		20 µM HCA	Freeze dry, no Fe(II), pH 8.3 0.1 M tris buffer
Ref (*39*)	10	0.05		-2.12		20 µM HCA	Freeze dry, no Fe(II), pH 8.3 0.1 M tris buffer
Ref (*40*)	33	NA		-2.423		1000 µM CT	No freeze dry, pH 7.5 tris buffer
Ref (*41*)	0.73	NA		-1.21			
Average log k_M			-4.16 ± 0.57	-1.45 ± 0.85	2.33		

C.3. References in Appendix Only

1. Gorski, C.A. and M.M. Scherer, Influence of magnetite stoichiometry on FeII uptake and nitrobenzene reduction. *Environ. Sci. Technol.*, 2009. **43**(10): p. 3675-3680.

2. Refait, P., M. Abdelmoula, and J.-M. Génin, Mechanisms of formation and structure of green rust one in aqueous corrosion of iron in the presence of chloride ions. *Corros. Sci.*, 1998. **40**(9): p. 1547-1560.

3. Bishop, E., *Indicators*. 1st ed. 1972, Oxford: Pergamon. 746.

4. Orsetti, S., C. Laskov, and S.B. Haderlein, Electron transfer between iron minerals and quinones: estimating the reduction potential of the Fe(II)-goethite surface from AQDS speciation. *Environ. Sci. Technol.*, 2013. **47**(24): p. 14161-14168.

5. Rau, J., H.-J. Knackmuss, and A. Stolz, Effects of different quinoid redox mediators on the anaerobic reduction of azo dyes by bacteria. *Environ. Sci. Technol.*, 2002. **36**(7): p. 1497-1504.

6. Aeschbacher, M., M. Sander, and R.P. Schwarzenbach, Novel electrochemical approach to assess the redox properties of humic substances. *Environ. Sci. Technol.*, 2009. **44**(1): p. 87-93.

7. Shi, Z., J.T. Nurmi, and P.G. Tratnyek, Effects of nano zero-valent iron (nZVI) on oxidation-reduction potential (ORP). *Environ. Sci. Technol.*, 2011. **45**(5): p. 1586-1592.

8. Zwank, L., M. Elsner, A. Aeberhard, R.P. Schwarzenbach, and S.B. Haderlein, Carbon isotope fractionation in the reductive dehalogenation of carbon tetrachloride at iron (hydr) oxide and iron sulfide minerals. *Environ. Sci. Technol.*, 2005. **39**(15): p. 5634-5641.

9. Vikesland, P.J., A.M. Heathcock, R.L. Rebodos, and K.E. Makus, Particle size and aggregation effects on magnetite reactivity toward carbon tetrachloride. *Environ. Sci. Technol.*, 2007. **41**(15): p. 5277-5283.

10. Danielsen, K.M. and K.F. Hayes, pH dependence of carbon tetrachloride reductive dechlorination by magnetite. *Environ. Sci. Technol.*, 2004. **38**(18): p. 4745-4752.

11. McCormick, M.L. and P. Adriaens, Carbon Tetrachloride Transformation on the Surface of Nanoscale Biogenic Magnetite Particles. *Environ. Sci. Technol.*, 2004. **38**(4): p. 1045-1053.

12. Lee, W. and B. Batchelor, Abiotic reductive dechlorination of chlorinated ethylenes by iron-bearing soil minerals. 1. pyrite and magnetite. *Environ. Sci. Technol.*, 2002. **36**(23): p. 5147-5154.

13. Elsner, M., R.P. Schwarzenbach, and S.B. Haderlein, Reactivity of Fe (II)-bearing minerals toward reductive transformation of organic contaminants. *Environ. Sci. Technol.*, 2004. **38**(3): p. 799-807.

14. Klausen, J., S.P. Troeber, S.B. Haderlein, and R.P. Schwarzenbach, Reduction of substituted nitrobenzenes by Fe (II) in aqueous mineral suspensions. *Environ. Sci. Technol.*, 1995. **29**(9): p. 2396-2404.

15. Gorski, C.A., J.T. Nurmi, P.G. Tratnyek, T.B. Hofstetter, and M.M. Scherer, Redox behavior of magnetite: Implications for contaminant reduction. *Environ. Sci. Technol.*, 2009. **44**(1): p. 55-60.

16. Elsner, M., S.B. Haderlein, T. Kellerhals, S. Luzi, L. Zwank, W. Angst, and R.P. Schwarzenbach, Mechanisms and products of surface-mediated reductive dehalogenation of carbon tetrachloride by Fe (II) on goethite. *Environ. Sci. Technol.*, 2004. **38**(7): p. 2058-2066.

17. Amonette, J.E., D.J. Workman, D.W. Kennedy, J.S. Fruchter, and Y.A. Gorby, Dechlorination of carbon tetrachloride by Fe (II) associated with goethite. *Environ. Sci. Technol.*, 2000. **34**(21): p. 4606-4613.

18. Pecher, K., S.B. Haderlein, and R.P. Schwarzenbach, Reduction of polyhalogenated methanes by surface-bound Fe (II) in aqueous suspensions of iron oxides. *Environ. Sci. Technol.*, 2002. **36**(8): p. 1734-1741.

19. Kenneke, J.F. and E.J. Weber, Reductive dehalogenation of halomethanes in iron- and sulfate-reducing sediments. 1. Reactivity pattern analysis. *Environ. Sci. Technol.*, 2003. **37**(4): p. 713-720.

20. Maithreepala, R. and R.-a. Doong, Synergistic effect of copper ion on the reductive dechlorination of carbon tetrachloride by surface-bound Fe (II) associated with goethite. *Environ. Sci. Technol.*, 2004. **38**(1): p. 260-268.

21. Hofstetter, T.B., C.G. Heijman, S.B. Haderlein, C. Holliger, and R.P. Schwarzenbach, Complete reduction of TNT and other (poly) nitroaromatic

compounds under iron-reducing subsurface conditions. *Environ. Sci. Technol.*, 1999. **33**(9): p. 1479-1487.

22. Rügge, K., T.B. Hofstetter, S.B. Haderlein, P.L. Bjerg, S. Knudsen, C. Zraunig, H. Mosbæk, and T.H. Christensen, Characterization of predominant reductants in an anaerobic leachate-contaminated aquifer by nitroaromatic probe compounds. *Environ. Sci. Technol.*, 1998. **32**(1): p. 23-31.

23. Maithreepala, R. and R.-a. Doong, Enhanced dechlorination of chlorinated methanes and ethenes by chloride green rust in the presence of copper (II). *Environ. Sci. Technol.*, 2005. **39**(11): p. 4082-4090.

24. O'Loughlin, E.J., K.M. Kemner, and D.R. Burris, Effects of AgI, AuIII, and CuII on the reductive dechlorination of carbon tetrachloride by green rust. *Environ. Sci. Technol.*, 2003. **37**(13): p. 2905-2912.

25. Liang, X. and E.C. Butler, Effects of natural organic matter model compounds on the transformation of carbon tetrachloride by chloride green rust. *Water Res.*, 2010. **44**(7): p. 2125-2132.

26. Liang, X., R. Paul Philp, and E.C. Butler, Kinetic and isotope analyses of tetrachloroethylene and trichloroethylene degradation by model Fe(II)-bearing minerals. *Chemosphere*, 2009. **75**(1): p. 63-69.

27. Lee, W. and B. Batchelor, Abiotic reductive dechlorination of chlorinated ethylenes by iron-bearing soil minerals. 2. green rust. *Environ. Sci. Technol.*, 2002. **36**(24): p. 5348-5354.

28. O'Loughlin, E.J. and D.R. Burris, Reduction of halogenated ethanes by green rust. *Environ. Toxicol. Chem.*, 2004. **23**(1): p. 41-48.

29. He, Y., C. Su, J.T. Wilson, R.T. Wilkin, C. Adair, T. Lee, P. Bradley, and M. Ferrey, *Identification and characterization methods for reactive minerals responsible for natural attenuation of chlorinated organic compounds in ground water*. 2009, U.S. EPA Office of Research and Development: Ada, Oklahoma.

30. Butler, E.C. and K.F. Hayes, Kinetics of the transformation of halogenated aliphatic compounds by iron sulfide. *Environ. Sci. Technol.*, 2000. **34**(3): p. 422-429.

31. Assaf-Anid, N. and K.-Y. Lin, Carbon tetrachloride reduction by Fe 2+, S 2-, and FeS with vitamin B 12 as organic amendment. *J. Environ. Eng.*, 2002. **128**(1): p. 94-99.

32. Butler, E.C. and K.F. Hayes, Kinetics of the transformation of trichloroethylene and tetrachloroethylene by iron sulfide. *Environ. Sci. Technol.*, 1999. **33**(12): p. 2021-2027.

33. Jeong, H.Y. and K.F. Hayes, Reductive dechlorination of tetrachloroethylene and trichloroethylene by mackinawite (FeS) in the presence of metals: reaction rates. *Environ. Sci. Technol.*, 2007. **41**(18): p. 6390-6396.

34. Liang, X., Y. Dong, T. Kuder, L.R. Krumholz, R.P. Philp, and E.C. Butler, Distinguishing abiotic and biotic transformation of tetrachloroethylene and trichloroethylene by stable carbon isotope fractionation. *Environ. Sci. Technol.*, 2007. **41**(20): p. 7094-7100.

35. Butler, E.C. and K.F. Hayes, Factors influencing rates and products in the transformation of trichloroethylene by iron sulfide and iron metal. *Environ. Sci. Technol.*, 2001. **35**(19): p. 3884-3891.

36. He, Y.T., J.T. Wilson, and R.T. Wilkin, Impact of iron sulfide transformation on trichloroethylene degradation. *Geochim. Cosmochim. Acta*, 2010. **74**(7): p. 2025-2039.

37. Amir, A. and W. Lee, Enhanced reductive dechlorination of tetrachloroethene during reduction of cobalamin (III) by nano-mackinawite. *J. Hazard. Mater.*, 2012. **235**: p. 359-366.

38. Butler, E.C. and K.F. Hayes, Effects of solution composition and pH on the reductive dechlorination of hexachloroethane by iron sulfide. *Environ. Sci. Technol.*, 1998. **32**(9): p. 1276-1284.

39. Jeong, H.Y. and K.F. Hayes, Impact of transition metals on reductive dechlorination rate of hexachloroethane by mackinawite. *Environ. Sci. Technol.*, 2003. **37**(20): p. 4650-4655.

40. Choi, J., K. Choi, and W. Lee, Effects of transition metal and sulfide on the reductive dechlorination of carbon tetrachloride and 1, 1, 1-trichloroethane by FeS. *J. Hazard. Mater.*, 2009. **162**(2): p. 1151-1158.

41. Devlin, J. and D. Müller, Field and laboratory studies of carbon tetrachloride transformation in a sandy aquifer under sulfate reducing conditions. *Environ. Sci. Technol.*, 1999. **33**(7): p. 1021-1027.

Appendix D Supporting Information to Chapter 5

D.1. Determining I2S and nZVI Concentration

If excess of I2S was present after I2S reduction by nZVI completed, the amount of nZVI consumption should be equal to the initial nZVI concentration. This was determined by the initial absorbance (Abs_{ini}) of the suspension before I2S addition using the calibration curve of nZVI (**Figure D.2**). Because there was ~10 second time lag between injection of I2S and the start of data recording by UV-VIS spectrophotometry, the initial absorbance of I2S was determined by reintroducing air into the suspension after the reduction step. The reoxidation of reduced I2S by air was much faster than Fe(II) oxidation by air therefore interference from Fe(II) oxidation on absorbance was minimized. The amount of I2S reduction can then be determined by calculating the difference between the absorbance of reoxidized suspension (Abs_{reox}) and plateau absorbance (Abs_{end}) using the calibration equation of I2S (**Figure D.2**), given that the absorbance of both oxidized nZVI and reduced I2S at 610 nm is negligible. If excess of nZVI was left, the amount of I2S consumption was considered to be equal to the initial I2S concentration, which, again, was determined by reoxidizing the suspension after reduction. The amount of nZVI consumption was determined calculating the difference between initial absorbance and end absorbance, which presumably is caused by residual nZVI.

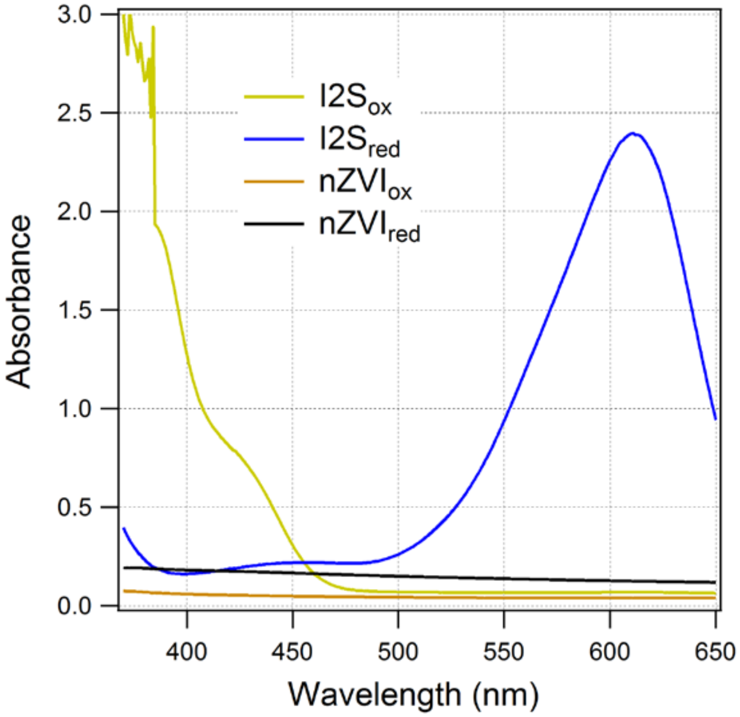

Figure D.1. Absorbance spectra of ~140 µM I2S$_{ox}$ and I2S$_{red}$ and 4 mg/L nZVI$_{ox}$ and nZVI$_{red}$ in 10 mM HEPES deoxygenated buffer at pH 7.2. (I2S was reduced by adding 1 drop of 1 M freshly-prepared sodium dithionite into the I2S$_{ox}$ solution; nZVI was oxidized by ambient air).

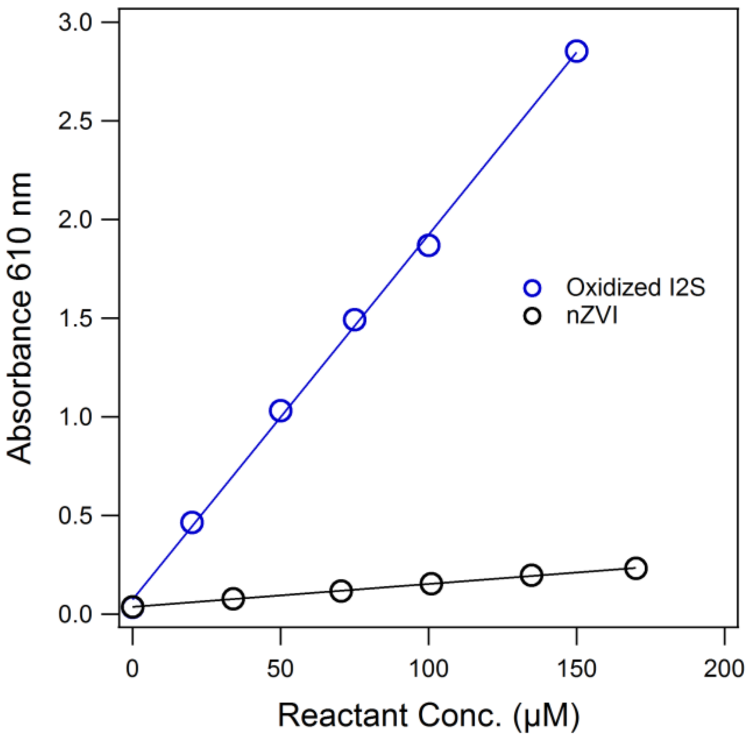

Figure D.2. Calibration curves for absorbance at 610 nm of oxidized I2S and CMC-nZVI in 10 mM HEPES buffer at pH 7.2, measured in a sealed glass cuvette with 1-cm path length.

D.2. Effects of Chemical Transformation on Absorbance Change

In prior work on characterizing CMC-nZVI, absorbance decrease over time is often interpreted as decreased physical stability of CMC-nZVI, such as aggregation and settling (*1*). This study suggested chemical transformation might be another contributor. **Figure D.3** shows absorbance change of nZVI suspension at three different concentrations and two pHs. At pH 7.2, all three nZVI concentrations show slight decrease in absorbance over time whereas at pH 8.5, less change occurred. Remixing the suspension did not bring the absorbance back to the initial values, suggesting the decrease of absorbance was not due to particle settling but corrosion in water. Although aggregation is a more likely explanation at higher nZVI concentrations that are typically used for characterizing physical stability, absorbance decrease should also be considered as evidence for Fe(0) loss as well.

The above results might suggest I2S reduction should be conducted at pH 8.5 due to less interference from parallel reaction with water. However, in the presence of 10 mg/L aqueous Fe(II), no I2S reduction was observed at pH 7.2 but a small amount of I2S reduction was observed at pH 8.5 (**Figure D.4**), which compromised the diagnostic response of I2S to Fe(0). The small amount of reduction might be due to increasing thermodynamic driving force of I2S reduction by aqueous Fe(II) at high pHs. The stoichiometric calculations indicate that not all Fe(II) was consumed by I2S reduction, suggesting that the system might reach thermodynamic equilibrium, with the redox couple of I2S accurately representing the redox potential of the system composed of Fe(II)/Fe(III) redox couple.

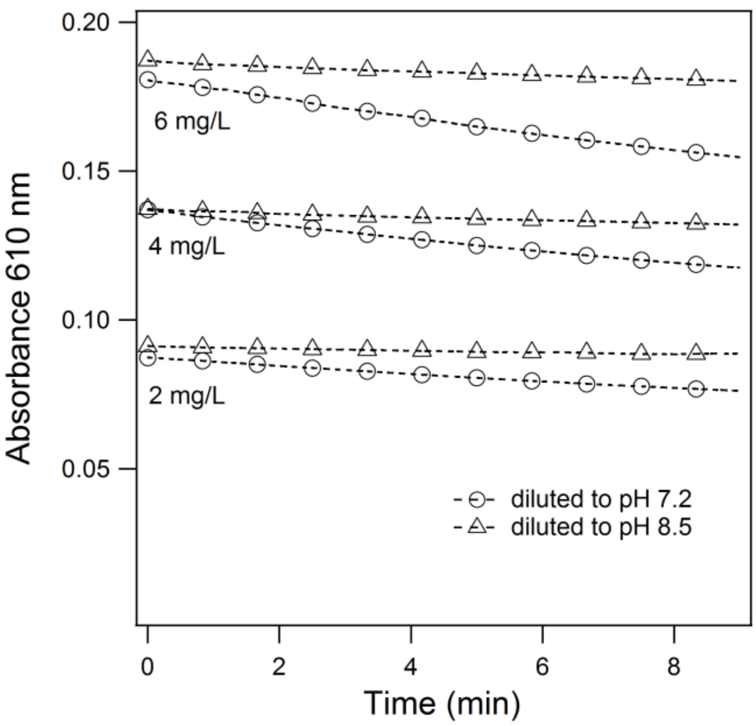

Figure D.3. Parallel reaction of CMC-nZVI with water during I2S reduction: change of absorbance of CMC-nZVI only with 2, 4, and 6 mg/L initial concentrations in 10 mM HEPES buffer at pH 7.2 and 8.5.

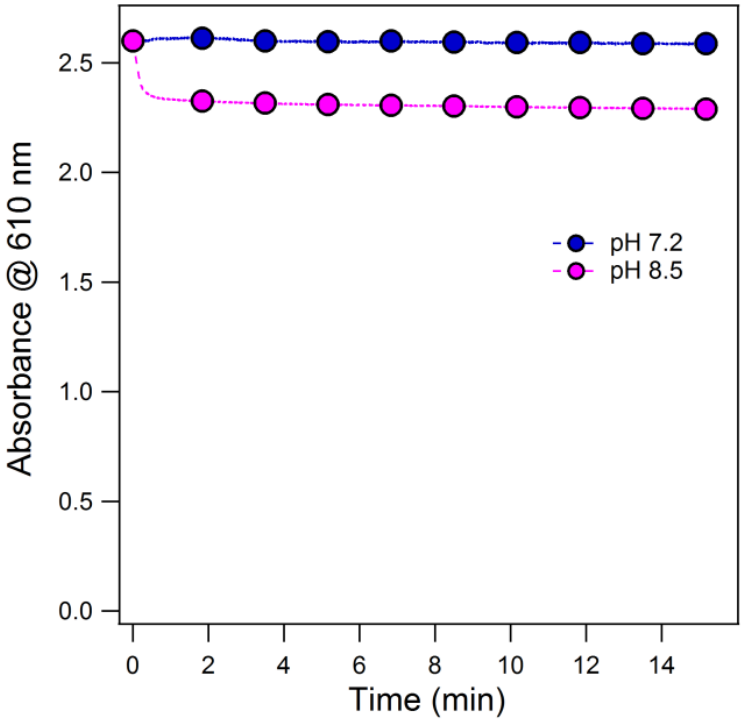

Figure D.4. Difference of absorbance due to I2S reduction by Fe(II) at high pH: reduction of I2S by 10 mg/L aqueous Fe(II) at pH 7.2 and 8.5, monitored by aqueous absorbance at 610 nm.

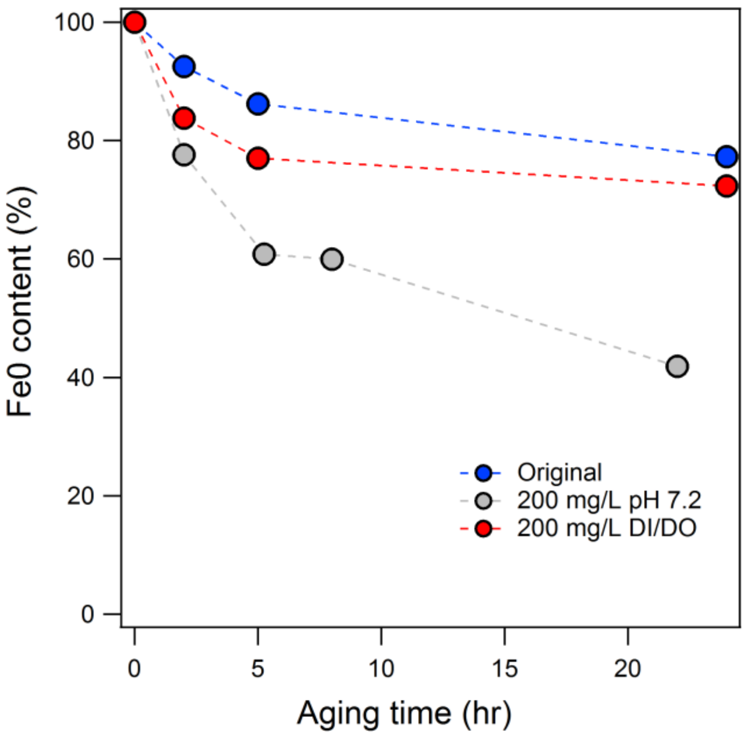

Figure D.5. The kinetics of Fe(0) loss in original synthesis solution and 200 mg/L nZVI in DI/DO water compared with 200 mg/L nZVI in pH 7.2 buffer shown in Figure 4B. The initial slopes were very similar between 200 mg/L nZVI in DI/DO water and pH 7.2 buffer indicating similar initial rate of Fe(0) loss. Inhibited dissolution was observed in DI/DO water (red) later but not in pH 7.2 buffer (grey).

D.3. Reference in Appendix Only

1. Kocur, C.M., D.M. O'Carroll, and B.E. Sleep, Impact of nZVI stability on mobility in porous media. *J. Contam. Hydro.*, 2013. **145**: p. 17-25.